Modelling multi-wavelength evolution of AGN across cosmic time

GRIFFIN, ANDREW,JAMES

Modelling multi-wavelength evolution of AGN across cosmic time

Andrew James Griffin

Submitted for the degree of Doctor of Philosophy
August 2019

Abstract

The evolution of Active Galactic Nuclei (AGNs) is crucial to galaxy evolution, given that AGNs affect their host galaxies via AGN feedback. In this thesis, I present predictions for the evolution of supermassive black holes (SMBHs) and AGNs from the semi-analytic model of galaxy formation GALFORM, over a range of redshift ($0 < z < 15$) and wavelength (from radio to X-ray). First, I compare SMBH masses and AGN optical to X-ray luminosities from the model for $z < 6$ to observations, and explore the evolution of typical SMBHs within the model. I find that the median SMBH spin evolves very little over this redshift range. Secondly, I present predictions for $z \geq 7$ for future surveys by JWST, EUCLID, ATHENA, and Lynx. I find that Lynx will detect the smallest SMBHs in the smallest host galaxies and host haloes, and that the predictions are generally insensitive to the SMBH seed mass. Thirdly, I predict the evolution of jet powers and (core-dominated) radio luminosities from the model for $z < 6$, and compare the evolution of these to observations. I predict the jet powers, halo masses, and fuelling mechanisms that dominate the model predictions. Finally, I present predictions of radio luminosities, lobe sizes and Fanaroff-Riley types of radio sources by combining a radio lobe evolution model appropriate for extended sources with the galaxy formation model. I find that this model generally is in good agreement with observed radio properties at $z = 0$, except for the fractions of Fanaroff-Riley sources, the number of low luminosity radio sources in high stellar mass galaxies, and the number of large sources. I explore the effect of varying different free parameters of this radio model, and suggest potential improvements.

Modelling multi-wavelength evolution of AGN across cosmic time

Andrew James Griffin

A Thesis presented for the degree of
Doctor of Philosophy

Institute for Computational Cosmology
Department of Physics
Durham University
United Kingdom

August 2019

Contents

List of Tables

List of Figures

Declaration

The work in this thesis is based on research carried out by the author between 2015 and 2019 at the Institute for Computational Cosmology, Durham University, whilst the author was a research student under the supervision of Prof. Cedric Lacey. No part of this thesis has been submitted elsewhere for any other degree or qualification.

Chapter 3 and Appendix A have been published in the form of an article in the Monthly Notices of the Royal Astronomical Society:

> *The evolution of SMBH spin and AGN luminosities for $z < 6$ within a semi-analytic model of galaxy formation*, Griffin, Andrew J.; Lacey, Cedric G.; Gonzalez-Perez, Violeta; Lagos, Claudia del P.; Baugh, Carlton M.; Fanidakis, Nikos, 2019, MNRAS, 487, 198

Chapter 4 and Appendix B has been submitted as an article to the Monthly Notices of the Royal Astronomical Society:

> *AGNs at the cosmic dawn: predictions for future surveys from a ΛCDM cosmological model*, Griffin, Andrew J.; Lacey, Cedric G.; Gonzalez-Perez, Violeta; Lagos, Claudia del P.; Baugh, Carlton M.; Fanidakis, Nikos

Chapter 5 will be submitted as an article to the Monthly Notices of the Royal Astronomical Society:

> *The evolution of radio jets across cosmic time*, Griffin, Andrew J.; Lacey, Cedric G.; Gonzalez-Perez, Violeta; Lagos, Claudia del P.

Chapter 6 and Appendix C will be submitted as an article to the Monthly Notices of the Royal Astronomical Society:

Acknowledgements

There are many people to thank for this thesis coming together. Firstly, I would like to thank my supervisor, Cedric Lacey, for sharing your comprehensive knowledge of astrophysics and for giving clear advice throughout my PhD. Thanks also to Carlton Baugh for helpful suggestions, and to Chris Done for accretion-based wisdom. Thanks also to Violeta Gonzalez-Perez for teaching me the ways of GALFORM, and to Claudia Lagos for fascinating plots to make.

Thank you to colleagues here at Durham who have asked brilliant questions and to those at conferences who have given me fresh insights into my work. Thank you to those who I have shared an office: Stuart, Helen, Sownak, Hou Jun, Flora, Anna, Jacob, Tom C, Lee and Jan. Thank you for helping with any coding issues and for asking how my weekend has been.

Thanks to those in Durham who have helped life outside of work be enjoyable, I thank housemates over the years: Piotr, Jamie, Cam, JP, Phil and Ali for late night McDonald's trips, Fifa sessions, and for brunch at the Duke. Thank you to those in Castle MCR and at Christchurch Durham who I've got to know over the years. Thank you to those from Oxford who have kept in touch, and for those from Holywell Church for keeping an interest in my wellbeing.

Thank you to Mum and Dad, for your continuous support and encouragement, and for teaching me to follow my passion. Thank you to David and Esther (and Daniel) for making me part of your life.

Finally, I thank the Lord Jesus Christ, whose sacrifice gives me purpose for life today, and who created the stars, galaxies, and black holes for us to understand.

Dedicated to

Mum and Dad, for your support

Chapter 1

Introduction

1.1 Introducing AGNs

1.1.1 A brief history of AGNs

The history of observations of Active Galactic Nuclei (AGNs) dates back just over a century, to 1908, when Edward Fath was performing optical spectroscopy on objects thought to be 'spiral nebulae' within the Milky Way. He found that one of them, NGC 1068, had an unusual spectrum, showing broad emission lines (Fath, 1909). These lines were confirmed by Vesto Slipher in 1917 (Slipher, 1917), who found that these emission lines were spread over a substantial range of wavelengths. Not that long after, Edwin Hubble determined that some of these nebulae, including NGC 1068, in fact reside outside of our own galaxy (Hubble, 1926). Extragalactic astronomy had been born.

A systematic study of these galaxies with these strong emission lines was conducted by Carl Seyfert in 1943 (Seyfert, 1943), but this was not enough to launch AGNs as a major focus of astronomical research. The end of World War II saw great developments in radio astronomy, as many radio engineers began to apply their expertise to astronomy, and the following decades saw many detections of radio sources, sometimes coincident with optical sources. An unusual class of object discovered were 'quasi-stellar sources' or 'quasars'. Optical observations of these objects showed broad emission lines at unfamiliar wavelengths, and more near-ultraviolet emission

than normal stars. The discovery by Maarten Schmidt in 1963 that the quasar associated with the radio source 3C273 has a redshift of 0.158 (Schmidt, 1963) - considered enormous at the time - revealed that quasars are of extragalactic origin, and launched the study of AGNs in a cosmological context.

The vast distances to AGNs implied very high optical luminosities, and hence there was interest in understanding the mechanism by which AGNs could produce such high luminosities. This mechanism was suggested by Edwin Salpeter in 1964 to be accretion of gas onto extremely massive objects of a small size (Salpeter, 1964; Lynden-Bell, 1969). It is now widely accepted that AGNs are powered by accretion onto a supermassive black hole (SMBH), with SMBHs observed in the centres of galaxies with masses, $M_{\rm BH} \sim 10^5 - 10^{10} M_\odot$. Black holes form when an amount of matter occupies a small enough volume so that no physical force can prevent its collapse under gravity, and the object is believed to collapse to form a singularity. The singularity is bounded by a surface, referred to as the event horizon, where the escape velocity from the black hole is equal to the speed of light. Evidence for SMBHs in the centres of galaxies has come from observations of the dynamics of the centre of the galaxy M87, which indicated a supermassive object of mass $M_{\rm BH} \sim 5 \times 10^9 M_\odot$ in the centre (Young et al., 1978; Sargent et al., 1978). More recently, the imaging of the accretion disc and event horizon of the supermassive black hole in the centre of the galaxy M87 using the Event Horizon Telescope (EHT - Event Horizon Telescope Collaboration et al., 2019), has provided good evidence for this picture, finding a mass of $M_{\rm BH} \approx 6.5 \times 10^9 M_\odot$. Future observations of the event horizon of the SMBH in our own galaxy using the EHT are planned, which will no doubt deepen our understanding of our closest SMBH.

1.1.2 The role of AGNs in galaxy formation

SMBHs in the centres of galaxies are believed to play an important role in galaxy formation and evolution. This is indicated by several pieces of evidence. First, X-ray observations of some clusters revealed the 'cooling flow problem'. From the X-ray emission of the hot intergalactic gas, a cooling time for the gas can be calculated, but for these objects, despite the cooling time being much shorter than the age of the

cluster, the gas in the centres is not observed to be condensing and turning into stars (Cowie & Binney, 1977; Fabian & Nulsen, 1977). These clusters therefore require some form of heating mechanism that could counterbalance the cooling. Secondly, giant elliptical galaxies are observed to have entirely old stellar populations. Within the standard paradigm of galaxy formation (i.e. hierarchical structure formation), one expects larger structures (and hence larger galaxies) to form later (Lacey & Cole, 1993), and therefore for these galaxies to have at least some young stars. While one could imagine scenarios where larger galaxies could have a lack of stars (e.g. if they are formed by mergers of gas-poor ellipticals), careful theoretical modelling shows we expect at least some young stars to form in the largest galaxies. Thirdly, observational studies have also measured correlations between the mass of the SMBH and the mass or the velocity dispersion of the host galaxy bulge (e.g. Magorrian et al., 1998; Häring & Rix, 2004; McConnell & Ma, 2013). These correlations suggest that there is some sort of 'co-evolution' occurring between SMBHs and their host galaxies. Fourthly, there is observed to be a sharp decrease in the number density of objects at the bright end of the galaxy luminosity function, which was hard to show using the understanding of the physical processes involved in galaxy formation in the early 2000s.

Combining these requirements, it was shown in theoretical models of galaxy formation that if a central SMBH heats the halo gas, such that it suppresses the cooling of the hot gas in the halo and shuts off star formation, that a match to the observed galaxy luminosity function can be obtained (e.g. Bower et al., 2006; Croton et al., 2006). This heating by an AGN addresses the observational puzzles described above. Examples of this 'AGN feedback' occurring can be observed in X-ray images of galaxy groups and clusters, where giant 'cavities' are seen at X-ray energies and coincide with the lobes of radio sources (e.g. Randall et al., 2011; Blanton et al., 2011). The SMBH is believed to provide the energy for the radio source, and therefore causes the evacuation of the gas in the host galaxy halo.

The inclusion of an AGN feedback prescription into theoretical models of galaxy formation also allowed other open questions in galaxy evolution to be addressed. The colour distribution of galaxies is observed to be bimodal, with a population of blue,

star-forming galaxies and a population of red, quiescent galaxies. The bimodality implies that the mechanism by which galaxies transition from the former to the latter is relatively fast. While mergers had been proposed as a mechanism for this transition, feedback from AGNs is thought to be able to terminate star formation and redden galaxies much faster (Springel et al., 2005).

Overall, the evidence from observations and theoretical models suggests a connection between SMBHs and their host galaxies. I now turn to consider our current understanding of galaxy formation.

1.2 Galaxy formation

Decades of observations of galaxies and the development of state-of-the-art theoretical galaxy formation models have greatly advanced our understanding of the wide variety of galaxies observed. The theoretical models are generally developed within the currently accepted cosmological paradigm, ΛCDM.

1.2.1 The ΛCDM Paradigm

In the ΛCDM paradigm, the energy density of the Universe today is dominated by dark energy (a vacuum energy density), and cold dark matter, which is non-baryonic matter with negligible thermal velocity at decoupling. Dark energy constitutes about 70 per cent of the energy density, and cold dark matter constitutes about 26 per cent of the energy density. The other 4 per cent is composed of baryons, which constitute the stars and gas in the Universe, and radiation, which contributes a negligible fraction of the Universe today.

The idea that the Universe contains a dark matter component dates back to the work of Oort (1932) analysing the orbits of stars in the Milky Way, and Zwicky (1933) analysing the orbits of galaxies in the Coma cluster. The velocities of the orbits of these objects were found to imply total masses above the masses from the observed luminous matter. This analysis was subsequently complemented by measurements of the rotation curves of galaxies, which were showed to be flat out to large radii (Roberts & Rots, 1973; Rubin et al., 1980).

The nature of dark matter is yet to be clarified. Initially, dark matter was thought to consist of faint, compact objects, that are composed of baryons, such as black holes and brown dwarfs. However, there have been insufficient micro-lensing signatures from such objects to provide the mass required (Alcock et al., 2000). Constraints on the baryon energy density, Ω_b, can be obtained from the abundance of light elements produced in Big Bang nucleosynthesis (e.g. Alpher et al., 1948), which occurs $\sim 100s$ after the Big Bang. When compared to values of the matter energy density, Ω_m, obtained from the abundances of clusters (e.g. Vikhlinin et al., 2009), it is found that $\Omega_b \ll \Omega_m$. Dark matter therefore cannot be baryonic.

Many different elementary particles have been suggested to be dark matter, although some have been ruled out by cosmological constraints, such as neutrinos. Neutrinos have a small rest mass ($\sim 100eV$), causing them to travel at relativistic velocities, and hence they free-stream out of perturbations, erasing structure on scales smaller than superclusters ($\sim 10^{15} M_{\odot}$). Current possible candidates for dark matter include exotic particles such as axions, or weakly-interacting massive particles, such as sterile neutrinos.

Evidence for the Universe's dark energy component has only emerged more recently. A rare type of supernova, type Ia, occurs when a white dwarf explodes after having accreted material from a companion star. As the white dwarf accretes material, it eventually accretes sufficient mass that the electron degeneracy pressure can no longer prevent its collapse. The luminosity of type Ia supernovae is a known quantity (given a measured light curve), and so from the luminosities and redshifts of these objects, cosmological parameters can be inferred. Observations of these supernovae in other galaxies found that they were fainter than would be expected in a matter dominated universe, and so the expansion of the Universe must be accelerating (Riess et al., 1998; Perlmutter et al., 1999).

Other evidence for dark energy comes from temperature fluctuations in the Cosmic Microwave Background (CMB). The CMB, disovered by Penzias & Wilson (1965), is a relic of the early Universe from the era of recombination, which occured when the Universe was about 380,000 years old. Prior to recombination, the Universe was ionised and Thomson scattering was the dominant interaction

between matter and radiation, which were in thermal equilibrium. After recombination, matter and radiation were able to evolve separately, with photons able to propagate freely through the Universe. The CMB is generally isotropic, and can be well fit by a blackbody of temperature $\sim 3K$, but there are some deviations from this uniform temperature of $30\mu K$. From the angular power spectrum of these fluctuations, cosmological parameters can be constrained. These analyses indicate that the Universe is described by a flat geometry. To close the Universe to a flat geometry, a dark energy component is required in addition to the mass provided by baryons and dark matter.

The Universe therefore is such that most of its mass is in dark energy and dark matter, while the majority of the luminosity is provided by main sequence stars, despite only contributing $\sim 0.16\%$ of the total density (e.g. Fukugita & Peebles, 2004). The Universe is also remarkably inefficient at forming stars, with only 6% of the baryons forming stars, the rest being in the form of warm intergalactic plasma, or intracluster plasma (Fukugita & Peebles, 2004). Understanding why such a small fraction of baryons form stars is one of the motivations for understanding galaxy formation. I now proceed to outline a theoretical picture of galaxy formation.

1.2.2 Theoretical Models of Galaxy Formation

Quantum fluctuations in the scalar field that drives inflation, that are then expanded to galaxy and larger scales by inflation, are thought to seed structure formation. These perturbations are observed in the CMB. While the initial, linear growth of these density perturbations can be calculated analytically, the collapse of these fluctuations and the build up of structure is a highly non-linear process. However, empirical arguments (Sheth et al., 2001), and N-body simulations (Springel et al., 2005) have allowed this non-linear evolution to be generally well understood.

Once the density of a perturbation is such that its self-gravity can overcome the expansion of the Universe, the dark matter undergoes dissipationless gravitational collapse, to form a dark matter halo. It is within these dark matter haloes that baryons condense to form galaxies. These dark matter haloes assemble hierarchically, with smaller haloes forming first, and larger haloes forming later. This

is because the shape of the matter power spectrum is such that the variance of fluctuations is larger on small scales, and so small scale fluctuations collapse first.

It is thought that the photon-baryon fluid should trace the dark matter distribution at early times. However, once recombination has occured, the photons and baryons are no longer coupled. The baryons therefore fall into the potential wells provided by the dark matter perturbations. As this gas falls inwards, it is compressed, which cause shocks to form, thus heating the gas. The gas within haloes is thought to be shock heated to around the virial temperature. Any further gas being added to the halo shocks upon reaching the virial radius of the dark matter halo.

This gas can then cool, radiating away energy through a variety of atomic and molecular processes, falling further into the gravitational potential well of the dark matter halo. As this gas cools, it eventually can become self-gravitating, and therefore form a galactic disc (Fall & Efstathiou, 1980; Mo et al., 1998). The angular momentum of the gas that collapses to discs is provided by the tidal torques from the anisotropic distribution of structure.

The cold gas in the galaxy is then able to form stars. How star formation occurs from gas is not a process that is well understood in detail, partly due to the vast range of scales involved, but the relationship between star formation rate surface density and the surface density of gas within galaxies (Kennicutt, 1998) is well established. More recent studies show correlations between the star formation rate density and the surface density of molecular hydrogen, rather than of the total gas (Kennicutt et al., 2007; Bigiel et al., 2008).

Once populations of stars form, the evolutionary paths of stars is generally well understood, thanks to years of investigation into stellar evolution in the Milky Way and nearby galaxies. Lower mass stars are fainter, but have long lifetimes, whereas higher mass stars are brighter, and end their relatively short lifetimes dramatically, as supernova explosions. These supernova explosions inject energy into the ISM, and drive the gas out of galaxies (Larson, 1974).

The above picture of galaxies forming as baryons condense within dark matter haloes was originally developed by White & Rees (1978). These early theoretical models suffered from the ‘overcooling problem’, where too many faint galaxies were

predicted by the models. Fundamentally, this issue arises because the shape of the halo mass function is a different shape to that of the galaxy luminosity function. Therefore, in a model where all galaxies have the same mass to light ratio, it is not possible to simultaneously reproduce the halo mass function and the galaxy luminosity function. The models therefore needed to account for the relative lack of galaxies at the faint and bright end of the luminosity function.

At the faint end, this can be explained by including feedback from supernovae into the models, such as via the 'disc reheating' method of Cole et al. (2000), where the gas is reheated and ejected from the galaxy by supernova feedback. The gas rises out of the potential well of the dark matter halo, and therefore is unavailable for star formation. While this can provide the models with a satisfactory fit to the faint end slope of the galaxy luminosity function, this effect causes problems at the bright end. This is because in larger haloes, the massive reservoir of gas ejected by supernova feedback eventually cools onto the galaxy, due to the larger gravitational potential of the halo. This gas cooling fuels star formation, and causes the number density of galaxies at the bright end to be too high.

Benson et al. (2003) explored the effect of different physical processes on the galaxy luminosity function using the semi-analytic model of galaxy formation GALFORM. To provide a match to the bright end of the luminosity function, a mechanism by which cooling could be suppressed in the most massive haloes was required. Thermal conduction was found to be a potential mechanism for this. In this mechanism, conduction in the ionised gas transports energy into the inner regions of the halo, which increases the gas cooling time, and therefore decreases the cooling radius. However, this required an uncomfortably high conduction efficiency. Alternatively, a high energy 'superwind', where gas is ejected completely from the dark matter halo, could suppress cooling as required, but the energy required was found to exceed the energy available from star formation. The supermassive black hole at the centre of the galaxy accreting gas could provide the energy required.

The models could therefore account for the lack of galaxies at the faint and bright end of the luminosity function, and feedback from supernovae and AGNs is now commonly used in theoretical models and simulations of galaxy formation.

1.3 Modelling galaxy formation

There are a variety of ways to model galaxy formation in a cosmological context. Two of the more physically-based approaches are semi-analytic models and hydrodynamical simulations (for a review, see Somerville & Davé, 2015). I use the semi-analytic model GALFORM for the predictions in this thesis, and I compare to a few results from hydrodynamical simulations. Both can provide important insights into galaxy formation.

In semi-analytic models, baryonic processes such as gas cooling, star formation and feedback are modelled analytically, evolving through the merging history of dark matter haloes. Typically, these dark matter merger trees are extracted from dark matter N-body simulations. Semi-analytic models have the advantage of being computationally inexpensive, which allows large volumes to be simulated, and allows large parameter spaces to be explored. However, semi-analytic models have the disadvantage that they often need to make certain simplifying assumptions, such as that of spherical symmetry. Some other semi-analytic models of galaxy formation are the model presented in Somerville et al. (2008), L-Galaxies (Guo et al., 2011), SAGE (Croton et al., 2016), ν^2GC (Shirakata et al., 2018), SAG (Cora et al., 2018), and SHARK (Lagos et al., 2018).

Hydrodynamical simulations solve the equations of gravity and hydrodynamics in a cosmological context, incorporating physical processes such as gas cooling and feedback, and trace the properties of dark matter, stars and gas in given resolution elements through time. To model physical processes occurring below the resolution of the simulation (e.g. star formation, black hole accretion and energy injection by supernovae and AGNs), 'subgrid' models are adopted, which are then calibrated to observed galaxy properties. Hydrodynamical simulations have the advantage that the anisotropic distributions of matter, and the impact of baryonic effects on dark matter can be calculated, but are more computationally expensive. Some hydrodynamical galaxy formation simulations are EAGLE (Schaye et al., 2015), Illustris-TNG (Springel et al., 2018), Horizon-AGN (Dubois et al., 2014), and the BlueTides simulation (Feng et al., 2016).

Comparing these two approaches, semi-analytic models are less computationally

expensive, allowing larger volumes and parameter spaces to be probed. This means that large volume mock catalogues for surveys can be produced. On the other hand, hydrodynamical simulations require fewer approximations to be made, and allow anisotropic distributions of structure to be simulated, and allow the effect of baryons on dark matter to be understood.

The work presented in this thesis is well suited to using a semi-analytic model of galaxy formation for several reasons. First, in this thesis we extensively explore the effect of varying different input parameters on the predictions, such as the effect of the SMBH spin model on the AGN luminosity function, and the effect of radio lobe parameters on the radio AGN predictions. The relatively short computational time required to run semi-analytic models allows predictions with different parameters to be made. Secondly, the volumes that we are able to simulate by using a semi-analytic model allow us to make predictions down to low number densities, such as in the AGN luminosity function. Thirdly, the relative simplicity with which changes can be made to a semi-analytic model (as galaxy components within a galaxy evolve analytically) means detailed subgrid models can be developed (in this case for SMBH spin and radio lobe evolution), so a wide range of properties can be compared to the observations.

The implementation of AGN feedback is different in different semi-analytic models. In GALFORM, AGN feedback is implemented only as 'radio mode' feedback. Here, if the halo is in the quasi-hydrostatic cooling regime and if the SMBH is accreting with a low Eddington accretion rate, the gas cooling is assumed to be exactly balanced by the heating from the AGN jet (Bower et al., 2006). This model of AGN feedback is also used in ν^2GC (Shirakata et al., 2018), and is one two available options of AGN feedback in SHARK (Lagos et al., 2018). In L-Galaxies (Guo et al., 2011), AGN feedback is also implemented only in the radio mode, but rather than the gas cooling being completely balanced by the AGN heating if certain conditions are met, the mass cooling rate is reduced by the AGN heating. In the model in Somerville et al. (2008), AGN feedback is in two modes: a merger driven 'bright mode' where radiative energy from the AGN drives a wind, and a radio mode where the mass accretion rate is the Bondi (1952) mass accretion rate.

1.4 SMBH spin

While AGN jets are understood to be important for galaxy formation, a precise physical mechanism for the production of AGN jets has not yet been determined. The most widely accepted models for these jets postulate that the jet energy source is either the rotational energy of the black hole (Blandford & Znajek, 1977), or the rotational energy of the accretion disc (Blandford & Payne, 1982). Therefore, an understanding of SMBH spin has the potential to provide clues to how AGN feedback proceeds in galaxy formation.

The spin of the black hole is characterised by the dimensionless spin parameter, a, given by:

$$a = cJ_{\rm BH}/GM_{\rm BH}^2, \tag{1.4.1}$$

where $M_{\rm BH}$ and $J_{\rm BH}$ are the mass and angular momentum of the SMBH. a takes values in the range $-1 \leq a \leq 1$, where $a = 0$ denotes a non-rotating black hole, and $a = 1$ denotes a maximally spinning black hole.

SMBH spin depends on the gas accretion and merger histories of SMBHs, because SMBH spins change either when gas is accreted, or when merging with another SMBH occurs. These processes are determined by the evolution of the host galaxy, as its gas content evolves and it merges with other galaxies. This has motivated predictions for SMBH spin evolution within cosmological simulations (e.g. Fanidakis et al., 2011; Barausse, 2012; Bustamante & Springel, 2019). In these models the evolution of the host galaxies is determined a physical galaxy formation model.

SMBH spins are difficult to measure observationally, but some studies have constrained spin values, either using the iron Kα line profile (e.g. Brenneman & Reynolds, 2006; Chiang & Fabian, 2011), or by fitting multiwavelength observations to accretion disc models (e.g. Done et al., 2013). For stellar mass black holes, detections of gravitational waves following black hole mergers can put constraints on black hole spin values both before and after the merger, such as from the gravitational wave measurement of Abbott et al. (2016). Similarly, SMBH spin values may be able to be constrained with future instruments such as Evolved Laser Interferometer

Space Antenna (eLISA), which are planned to be able to detect gravitational wave signals from merging SMBHs.

1.5 Radio emission from AGNs

AGN jets provide the energy for producing large lobes of relativistic plasma which then emit at radio frequencies via synchrotron emission. These radio sources can have a wide variety of sizes, luminosities and morphologies, with some sources having sizes up to several Mpc (see Muxlow & Garrington, 1991, for a review). One way to classify the morphologies of these extended radio sources is that of Fanaroff & Riley (1974), in which sources are split into two classes according to their radio brightness distribution. Sources that are brighter in the core than at the edges are classified as type I (FRI), whereas sources that are brighter at the edges than at the core are classified as type II (FRII).

While the physical reason for the dichotomy between FRIs and FRIIs is currently not well understood, observational studies have suggested potential mechanisms that cause the two types. Radio luminosity could be responsible, with a gradual switch between the two types observed around $P_{1.4\mathrm{GHz}} \sim 10^{24}\mathrm{WHz}^{-1}\mathrm{Sr}^{-1}$ (Gendre et al., 2010, 2013), and jet powers have also been suggested (e.g. Rawlings & Saunders, 1991). The environments of the two types appear to be different (e.g. Prestage & Peacock, 1988; Gendre et al., 2013) with FRIs observed in richer clusters, but with a large overlap between the two classes. Observational studies have also found different correlations between properties for the two types, with Owen & Ledlow (1994) reporting a separation in FRIs and FRIIs in the radio versus optical luminosity plane, although more recent studies do not show that separation (Best, 2009).

Another commonly used classification of AGNs is into High Excitation Radio Galaxies (HERGs), and Low Excitation Radio Galaxies (LERGs). HERGs and LERGs are typically classified based on optical emission line strength, with HERGs having stronger emission lines. HERGs are believed to correspond to AGNs accreting gas via a physically thin, optically thick accretion disc (Shakura & Sunyaev, 1973), whereas LERGs are believed to accrete gas via a physically thick, optically thin

Advection Dominated Accretion Flow (ADAF - Yuan & Narayan, 2014).

Observational studies of the radio luminosity function of HERGs and LERGs (Best et al., 2014) and Pracy et al. (2016) both find that these two populations evolve differently. Best et al. (2014) and Pracy et al. (2016) both find that the number density of HERGs increases with redshift at all radio luminosities from $z = 0$ to $z = 1$. For LERGs, Best et al. (2014) report an increase in space density at high radio luminosities over this redshift increase, and a decrease at low radio luminosities. However, Pracy et al. (2016) report little evolution for LERGs over this redshift range.

These observational studies of radio AGNs are made possible because of large surveys at radio frequencies, such as the Faint Images of the Radio Sky at Twenty centimetres (FIRST - Becker et al., 1995), the 1.4 GHz National Radio Astronomy Observatory VLA Sky Survey (NVSS - Condon et al., 1998), and more recently the LOFAR Two Metre Sky Survey (LoTSS - Shimwell et al., 2017). These surveys can be cross compared with optical surveys to study radio AGNs and galaxies together. Alongside some of the discoveries detailed above, some other findings have been: a dependence of radio AGN activity on galaxy stellar mass (Best et al., 2005b), the effect of radio AGN activity on star formation in the most massive galaxies (Chen et al., 2013), and that for sufficiently low radio luminosities and high stellar masses, all galaxies host a radio AGN (Sabater et al., 2019).

Our understanding will be deepened further by planned radio surveys with new telescopes such as MeerKAT (Jonas & MeerKAT Team, 2016), the Australian Square Kilometre Array Pathfinder (ASKAP - Johnston et al., 2008), and the Square Kilometre Array (SKA - Schilizzi et al., 2008).

1.6 Thesis Outline

The outline of this thesis is as follows. In Chapter 2 I describe the modelling of physical processes in the semi-analytic galaxy formation model GALFORM, that I will use for this thesis.

In Chapter 3, I present the SMBH spin evolution model, and the method by which

AGN luminosities are calculated. I present black hole mass functions, accretion rate distributions, and relations between SMBH mass and bulge/galaxy stellar mass. I present the AGN bolometric luminosity function and analyse the contributions from different accretion disc states and fuelling modes. I then compare AGN luminosity functions in different bands (from optical to X-ray) to observations for $0 \leq z \leq 6$.

In Chapter 4, I extend the model to make predictions for $z \geq 7$, for future surveys with the space-based telescopes JWST and EUCLID (in the optical and near-infrared), and ATHENA and Lynx (in X-rays). I predict the number of objects that should be detected by possible surveys conducted by these telescopes, as well as the properties of objects detected (black hole masses, mass accretion rates, stellar masses, halo masses).

In Chapter 5, I present predictions for AGN jet powers and (core-dominated) radio luminosities. This model uses a Blandford-Znajek type model for the jet powers, and a published scaling relation for determining the radio luminosities from the jet powers. I present predictions for the evolution of jet powers and radio luminosities, and compare to observations for $0 \leq z \leq 6$.

In Chapter 6, I present predictions at $z = 0$ using a model of radio emission for extended sources. The analytic model for radio emission that I couple to GALFORM tracks the evolution of radio lobe luminosity, size, and Fanaroff-Riley type. I compare the predictions from the model to observational radio luminosity functions, fractions of each Fanaroff-Riley type, and radio source sizes and finally explore the effect on the model predictions of varying free parameters of the radio lobe model.

Finally, I summarise the main findings of this thesis, and give suggestions for future work in Chapter 7.

Chapter 2

The galaxy formation model

The work described in this thesis makes use of the Durham semi-analytic model of galaxy formation GALFORM. The GALFORM model builds on the principles outlined in White & Rees (1978), White & Frenk (1991), and Cole et al. (1994), and was introduced in Cole et al. (2000).

In GALFORM galaxies form from baryons condensing within dark matter haloes, with the evolution of the dark matter haloes described by the dark matter merger trees. The baryonic physics is modelled by a series of coupled differential equations, which track the exchange of baryons between different galaxy components. Physical processes modelled in GALFORM include i) the merging of dark matter haloes, ii) shock heating and radiative cooling of gas in haloes, iii) the collapse of cooled gas to a rotationally supported disc, iv) a two-phase interstellar medium with star formation from molecular gas, v) feedback from photoionisation, supernovae, and AGNs, vi) the chemical evolution of gas and stars, vii) galaxies merging in haloes due to dynamical friction, viii) bar instabilities in galaxy discs, ix) the growth of SMBHs by gas accretion and galaxy mergers, x) the evolution of stellar populations, and xi) the extinction and reprocessing of stellar radiation by dust.

There are several different versions of the GALFORM model, the most recent of these being those of Lacey et al. (2016), Gonzalez-Perez et al. (2018), and Baugh et al. (2019). These different models all follow the same overall methodology. For the work presented in this thesis, I am using the model of Lacey et al. (2016), as recalibrated by Baugh et al. (2019). I give the values of the free parameters used

in this model in Tables 2.1 and 2.2. Below, I describe how the different physical processes of galaxy formation are modelled. The description of GALFORM presented here is based on those given in Cole et al. (2000), Lacey et al. (2016), and Baugh et al. (2019).

2.1 Dark matter haloes

In GALFORM galaxies evolve within dark matter merger trees, which describe the merging histories of dark matter haloes, from their progenitors down to the desired output redshift. Dark matter merger trees can be calculated either using a Monte-Carlo technique that is based on the Extended Press-Schechter model (Lacey & Cole, 1993; Cole et al., 2000; Parkinson et al., 2008), or can be extracted directly from N-body simulations (Helly et al., 2003). The former has the advantage that it is computationally inexpensive to generate these merger trees, and any desired halo mass resolution can be input, whereas the latter has the advantage that it allows the spatial distribution of galaxies to be studied. For this thesis, I am using merger trees generated by the latter procedure.

To generate the merger trees, first a dark matter N-body simulation is run from high-redshift (e.g. $z = 127$ in the P-Millennium simulation used in this thesis) down to the present day, and the particle data is output at several 'snapshots'. Groups of dark matter particles are identified in the simulation snapshots using the *Friends of Friends* algorithm (FoF - Davis et al., 1985). The SUBFIND algorithm (Springel et al., 2001) is then used to identify self-bound, locally overdense sub-groups within the FoF groups. The merger trees are generated using the 'Dhaloes' algorithm (Jiang et al., 2014). When they form, haloes are assumed in GALFORM to have a virial radius given by:

$$r_{\rm vir} = \left(\frac{3 M_{\rm halo}}{4\pi \Delta_{\rm vir} \bar{\rho}} \right)^{1/3}, \tag{2.1.1}$$

where $M_{\rm halo}$ is the halo mass, $\bar{\rho}$ is the cosmological mean density at that redsift, and $\Delta_{\rm vir}$ is the overdensity, which is calculated from the spherical top-hat collapse model (e.g. Eke et al., 1996). The dark matter density profiles of haloes are assumed to

Table 2.1: The cosmological and galaxy formation parameters relevant for star formation for the Baugh et al. (2019) recalibration of the Lacey et al. (2016) model used in this thesis.

Parameter	Description	Value
Cosmology		
$\Omega_{\rm m0}$	Matter density	0.307
$\Omega_{\rm v0}$	Vacuum energy density	0.693
$\Omega_{\rm b0}$	Baryon density	0.0483
h	Reduced Hubble parameter	0.678
σ_8	Power spectrum normalization	0.829
n_s	Power spectrum slope	0.961
IMF: quiescent		
x	Initial mass function slope	$x = 0.4$ for $m < M_\odot$ and $x = 1.5$ for $m > M_\odot$
p	Yield	0.021
R	Recycled fraction	0.44
IMF: starburst		
x	Initial mass function slope	1
p	Yield	0.048
R	Recycled fraction	0.54
Quiescent star formation		
$\nu_{\rm SF}$	Molecular gas efficiency factor	0.74 $\rm Gyr^{-1}$
P_0	Pressure relation normalisation	1.7×10^4 $k_B \rm cm^{-3} K$
α_P	Pressure relation slope	0.8
Burst star formation		
f_{dyn}	Dynamical time multiplier	20
$\tau_{\rm burst,min}$	Minimum burst timescale	100Myr

Table 2.2: The galaxy formation parameters for feedback, dynamical processes and dust for the Baugh et al. (2019) recalibration of the Lacey et al. (2016) model used in this thesis.

Parameter	Description	Value
Photoionisation feedback		
$z_{\rm reion}$	Redshift of reionisation	10
$V_{\rm crit}$	Threshold circular velocity	$30{\rm kms}^{-1}$
SN feedback		
$V_{\rm SN}$	Pivot velocity	$320{\rm kms}^{-1}$
$\gamma_{\rm SN}$	Slope of mass loading	3.4
$\alpha_{\rm ret}$	Gas reincorporation timescale	1.0
AGNs and SMBHs		
$f_{\rm BH}$	Fraction of mass accreted onto SMBH in a starburst	0.005
$\alpha_{\rm cool}$	AGN feedback threshold	0.8
$f_{\rm Edd}$	Maximum BH heating rate	0.01
$\epsilon_{\rm heat}$	SMBH heating efficiency	0.02
Disc stability		
$F_{\rm stab}$	Disc instability threshold	0.9
Galaxy merger timescale		Simha & Cole (2017)
Size of merger remnants		
$f_{\rm orbit}$	Orbital energy contribution	0
$f_{\rm DM}$	DM fraction in galaxy mergers	2
Starbursts in mergers		
$f_{\rm ellip}$	Major merger mass ratio threshold	0.3
$f_{\rm burst}$	Mass ratio threshold for burst	0.05
Dust model		
$f_{\rm cloud}$	Fraction of dust in clouds	0.5
$t_{\rm esc}$	Escape time of young stars	1Myr

have the NFW form (Navarro et al., 1997):

$$\rho_{\rm DM}(r) \propto \frac{1}{(r/r_{\rm s})(1+r/r_{\rm s})^2}, \tag{2.1.2}$$

where $r_{\rm s}$, the scale radius, relates to the virial radius by, $r_{\rm s} = r_{\rm vir}/c_{\rm NFW}$, where $c_{\rm NFW}$ is calculated using the analytical prescription of Navarro et al. (1997).

In the simulation, haloes can grow either by mergers or by accretion. The virial velocity, $V_{\rm vir} = (GM_{\rm halo}/r_{\rm vir})^{1/2}$, and $c_{\rm NFW}$ are updated at 'halo formation events', which are defined as occurring either when a halo appears without a progenitor, or when a halo has grown in mass by a factor of two since the last halo formation event.

Haloes acquire angular momentum from tidal torques during their formation. At each halo formation event, a value of the dimensionless spin parameter of the halo:

$$\lambda_H = \frac{J_{\rm halo}|E_{\rm halo}|^{1/2}}{GM_{\rm halo}^{5/2}}, \tag{2.1.3}$$

is drawn from a lognormal distribution, with median $\lambda_{\rm H,median} = 0.039$, and dispersion $\sigma_{\lambda_H} = 0.53$ in $\ln \lambda_H$. These values are obtained from the N-body simulations of Cole & Lacey (1996).

2.2 Gas in haloes

Each halo is initially given the cosmological fraction of baryons - $(\Omega_b/\Omega_M)M_{\rm halo}$. It is assumed that the gas in haloes is shock heated to the virial temperature:

$$T_{\rm vir} = \frac{\mu m_H}{2k_B} V_{\rm vir}^2, \tag{2.2.4}$$

where m_H is the mass of a hydrogen atom and μ is the mean molecular weight. The hot gas is assumed to settle in a spherically symmetric distribution with density profile:

$$\rho_{\rm hot}(r) \propto \frac{1}{r_c^2 + r^2}, \tag{2.2.5}$$

with a core radius, $r_c = 0.1 r_{\rm vir}$ (following Lacey et al., 2016). The thermal energy per unit volume of the gas at a radius r is:

$$U_{\rm hot}(r) = \frac{3}{2}\frac{k_B T_{\rm vir}}{\mu m_H}\rho_{\rm hot}(r). \tag{2.2.6}$$

The hot gas then loses its thermal energy through atomic processes, such that its cooling luminosity per unit volume is:

$$L_{\rm cool}(r) = \rho^2_{\rm hot}(r)\Lambda(T_{\rm vir}, Z_{\rm hot}), \tag{2.2.7}$$

where $\Lambda(T_{\rm vir}, Z_{\rm hot})$ is the temperature and metallicity dependent cooling function tabulated by Sutherland & Dopita (1993). The ratio of these two quantities gives a cooling time, which is the timescale for the gas to radiate its thermal energy:

$$\tau_{\rm cool} = \frac{3}{2}\frac{k_B}{\mu m_H}\frac{T_{\rm vir}}{\rho_{\rm hot}(r)\Lambda(T_{\rm vir}, Z_{\rm hot})}. \tag{2.2.8}$$

From this, a cooling radius can be calculated, at which the cooling time of the gas is equal to the age of the halo: $\tau_{\rm cool}(r_{\rm cool}) = t - t_{\rm form}$. This propagates outwards with time. Gas with $r < r_{\rm cool}$ is assumed to have cooled.

For gas to form a galactic disc, it also needs to have time to fall down the potential well produced by the dark matter halo. The free-fall time of a test particle for a given mass distribution is:

$$t_{\rm ff}(r) = \int_0^r \left[\int_r^{r''} -\frac{GM(r')}{r'^2}dr'\right]^{-1/2} dr'', \tag{2.2.9}$$

and from this, the free-fall radius, $r_{\rm ff}$, can be calculated via $t_{\rm ff}(r_{\rm ff}) = t - t_{\rm form}$. A particle at $r < r_{\rm ff}$ will have had sufficient time to fall to the centre of the potential well. For gas to become available to be accreted onto a galactic disc it needs to have sufficient time to cool, and sufficient time to fall to the centre of the potential well. Therefore, an accretion radius for the halo gas is defined by:

$$r_{\rm acc}(t) = \min[r_{\rm cool}(t), r_{\rm ff}(t)]. \tag{2.2.10}$$

The accretion rate of hot gas onto the cold disc is given by:

$$\dot{M}_{\rm acc} = 4\pi r^2_{\rm acc}\rho_{\rm hot}(r_{\rm acc})\frac{dr_{\rm acc}}{dt}. \tag{2.2.11}$$

The angular momentum of the gas is conserved, and forms a disc. We assume that gas only accretes onto a central galaxy, and not onto satellite galaxies. Once a galaxy becomes a satellite, it is assumed that the hot gas of the satellite is instantly stripped by ram pressure stripping, so no gas can cool onto satellite galaxies.

2.3 Star formation

Gas that cools from the halo is added to the disc, and this cold gas is available to form stars. The galaxy has disc and spheroid components, and both contain gas and stars. Star formation is assumed to occur in a quiescent mode in the disc, and in a starburst mode in the spheroid. Stars and gas can be transferred from the disc to the spheroid by galaxy mergers and disc instabilities.

2.3.1 Star formation in the disc

Star formation in the disc is calculated using the Blitz & Rosolowsky (2006) empirical law, which was implemented into GALFORM in Lagos et al. (2011). The gas is in atomic and molecular phases, with the ratio of the surface densities, $\Sigma_{\rm atom}$ and $\Sigma_{\rm mol}$, depending on the gas pressure at the midplane, P, as:

$$R_{\rm mol} = \frac{\Sigma_{\rm mol}}{\Sigma_{\rm atom}} = \left(\frac{P}{P_0}\right)^{\alpha_P}, \tag{2.3.12}$$

where $\alpha_P = 0.8$ and $P_0/k_B = 1700{\rm cm}^{-3}K$, based on observations from Leroy et al. (2008). The star formation rate in the galaxy disc is then assumed to be proportional to the mass of molecular gas:

$$\psi_{\rm disc} = \nu_{\rm SF} M_{\rm mol,disc} = \nu_{\rm SF} f_{\rm mol} M_{\rm cold,disc}, \tag{2.3.13}$$

where $f_{\rm mol} = R_{\rm mol}/(1 + R_{\rm mol})$ and $\nu_{\rm SF}$ is a free parameter. For the model used in this thesis, $\nu_{\rm SF} = 0.74$, as in Lacey et al. (2016).

2.3.2 Star formation in bursts

For star formation in bursts (which occur in the bulge/spheroid), we assume that $f_{\rm mol} \approx 1$, and that the star formation rate depends on a star formation timescale, $\tau_{\star,\rm burst}$, as:

$$\psi_{\rm burst} = \nu_{\rm SF,burst} M_{\rm cold,burst} = \frac{M_{\rm cold,burst}}{\tau_{\star,\rm burst}}. \tag{2.3.14}$$

$\tau_{\star,\rm burst}$ depends on the dynamical timescale of the bulge, $\tau_{\rm dyn,bulge}$ as:

$$\tau_{\star,\rm burst} = \max[f_{\rm dyn}\tau_{\rm dyn,bulge}, \tau_{\rm burst,min}], \tag{2.3.15}$$

where $\tau_{\rm dyn,bulge}$ is the dynamical timescale of the bulge, calculated as $r_{\rm bulge}/V_C(r_{\rm bulge})$, and $f_{\rm dyn}$ and $\tau_{\rm burst,min}$ are parameters of the model. In the above expression the star formation timescale scales with the dynamical timescale of the bulge ($f_{\rm dyn} = 20$) at large dynamical times, and has a floor value ($\tau_{\rm burst,min} = 100$Myr) at small dynamical times. These are the values from Lacey et al. (2016).

2.4 Feedback processes

2.4.1 Photoionisation feedback

The Intergalactic Medium (IGM) is reionised and photo-heated by ionising photons produced by stars and AGNs. This inhibits galaxy formation because i) the increased IGM pressure inhibits the collapse of gas into dark matter haloes, and ii) the photo-heating of gas in haloes from the UV background inhibits gas cooling within haloes. In the model, reionisation is assumed to occur instantly at $z = z_{\rm reion}$. After the IGM is reionised at $z = z_{\rm reion}$, no cooling occurs for haloes with circular velocities, $V_C < V_{\rm crit}$ (Benson et al., 2003). A value of $z_{\rm reion} = 10$ is adopted here (Dunkley et al., 2009), and a value of $V_{\rm crit} = 30{\rm kms}^{-1}$ based on the gas-dynamical simulations of Okamoto et al. (2008). This prescription has been shown to agree with more detailed treatments quite well (e.g. Font et al., 2011).

2.4.2 Supernova feedback

The most massive stars end their lives as supernova (SN) explosions, which inject energy into the ISM, and expel cold gas from the galaxy. These massive stars are short lived, and so in the model, the gas ejection rate from the galaxy due to SNe is assumed to be proportional to the instantaneous star formation rate, ψ:

$$\dot{M}_{\rm eject} = \beta\psi. \tag{2.4.16}$$

The factor β depends on the circular velocity of the halo, V_c, taking into account that the mass ejection rate should depend on the gravitational potential of the halo, and is given by:

$$\beta = \left(\frac{V_c}{V_{\rm SN}}\right)^{-\gamma_{\rm SN}}, \tag{2.4.17}$$

where $V_{\rm SN}$ and $\gamma_{\rm SN}$ are free parameters, with the values $V_{\rm SN} = 320{\rm kms}^{-1}$ and $\gamma_{\rm SN} = 3.4$ adopted here. These values are obtained from calibration to galaxy properties in Lacey et al. (2016) and Baugh et al. (2019) respectively. $V_c = V_c(r_{\rm disc})$ for quiescent star formation in the disc, and $V_c = V_c(r_{\rm bulge})$ for starbursts in the bulge. The ejection rate is calculated separately for the disc and for the bulge, and then combined to give a total mass ejection rate.

This gas is assumed to be ejected beyond the virial radius of the dark matter halo to a reservoir of gas with mass $M_{\rm res}$. This gas is assumed to return to the hot gas reservoir within the virial radius, at a rate:

$$\dot{M}_{\rm return} = \alpha_{\rm ret}\frac{M_{\rm res}}{\tau_{\rm dyn,halo}}, \tag{2.4.18}$$

where $\tau_{\rm dyn,halo} = r_{\rm vir}/V_{\rm vir}$ is the halo dynamical time, and $\alpha_{\rm ret}$ is a free parameter. In this thesis, $\alpha_{\rm ret} = 1$. This value is obtained in Baugh et al. (2019) by calibration to galaxy properties.

2.4.3 AGN feedback

Supermassive black holes accrete gas, and subsequently release energy into their surrounding environment. There are generally thought to be two modes of AGN

feedback - quasar mode feedback and radio mode feedback. Quasar mode feedback occurs as rapidly growing AGNs drive wide-angle outflows, at velocities $\sim 10^2 - 10^3 \mathrm{kms}^{-1}$. It has been suggested that these outflows may establish the observed correlations between black hole mass and bulge properties (King & Pounds, 2015). Feedback in the radio mode involves a relativistic jet depositing energy in hot gas haloes to balance radiative cooling. In GALFORM, only feedback in the radio mode is included, with the jet energy released by gas accreting onto the SMBH from hot halo gas. We assume that the heating from the jet balances radiative cooling if the following two conditions are met (Bower et al., 2006). First, the cooling time of the gas, $t_{\rm cool}$, needs to be sufficiently long compared to the free-fall time, $t_{\rm ff}$, as cooling needs to be in the quasi-hydrostatic cooling regime for the gas to be heated effectively:

$$t_{\rm cool}(r_{\rm cool})/t_{\rm ff}(r_{\rm cool}) > 1/\alpha_{\rm cool}, \tag{2.4.19}$$

where $r_{\rm cool}$ is the cooling radius calculated using the procedure in Lacey et al. (2016) Section 3.3, and $\alpha_{\rm cool}$ is a free parameter, where a value of $\alpha_{\rm cool} = 0.8$ is adopted here. This value is obtained from the calibration to galaxy properties in Lacey et al. (2016). Secondly, the cooling luminosity, $L_{\rm cool}$ needs to be below a fraction of the Eddington luminosity, as jet production is assumed to occur for SMBHs accreting at low Eddington accretion rates:

$$L_{\rm cool} < f_{\rm Edd} L_{\rm Edd}(M_{\rm BH}), \tag{2.4.20}$$

where $f_{\rm Edd}$ is a free parameter, with $f_{\rm Edd} = 0.01$ adopted here, as in Fanidakis et al. (2011) and Lacey et al. (2016). When AGN feedback is active, the SMBH accretes gas from the hot halo by 'hot halo accretion'.

2.5 Galaxy mergers

Galaxies are either central galaxies, which sit at the centre of the dark matter halo, or satellite galaxies, which orbit within the dark matter halo. When haloes merge, we assume that the central galaxy of the most massive progenitor halo becomes the

new central galaxy, while the other galaxies become satellites within the dark matter halo. It is assumed that the satellites are stripped of their hot gas haloes (which is then added to the central galaxy) through ram pressure stripping, and no further gas can cool onto them.

These satellite galaxies may then merge with the central galaxy. The timescale on which the satellites merge is calculated as in the treatment of Simha & Cole (2017), in which satellite galaxies track the positions of their associated subhaloes in the N-body simulation. When the subhalo hosting the satellite can no longer be tracked in the simulation, the position and the velocity of the subhalo when it was last tracked are used to calculate the dynamical friction timescale analytically. Dynamical friction is the process of a satellite galaxy accelerating stars and dark matter in its wake, which slows down the satellite. The timescale for dynamical friction is calculated here by:

$$T_{\rm DF} = \left(\frac{R_{\rm vir}}{R_C}\right)^{\alpha} \left(\frac{J}{J_C}\right)^{\beta} \frac{\tau_{\rm dyn,halo}}{2B(1)\ln\Lambda} \left(\frac{M_{\rm halo}}{M_{\rm sat}}\right), \tag{2.5.21}$$

where R_C is the radius of a circular orbit with the same energy as the actual orbit, and J/J_C is the ratio of the angular momentum of the actual orbit to the angular momentum of a circular orbit with the same energy. α and β are parameters that are determined numerically in Simha & Cole (2017) as $\alpha = -1.8$ and $\beta = 0.85$. $\tau_{\rm dyn,halo}$ is the dynamical time of the halo, and $B(x)$ is given by:

$$B(x) = \mathrm{erf}(x) - \frac{2x}{\sqrt{\pi}} \exp(-x^2). \tag{2.5.22}$$

Following Simha & Cole (2017), $\ln\Lambda$ is taken to be $\ln(M_{\rm halo}/M_{\rm sat})$. The result of the galaxy merger depends on the ratio of the baryonic mass of the satellite to that of the central. If $M_{\rm sat}/M_{\rm cent} > f_{\rm ellip}$, then the merger is classified as a major merger, in which the stellar discs of the central and satellite are destroyed, and the gas and stars are added to the resultant spheroid. Other mergers are classified as minor, in which the stars from the satellite are added to the spheroid of the central, and the gas from the satellite is added to the disc of the central, without changing its specific angular momentum. Mergers with $M_{\rm sat}/M_{\rm cent} > f_{\rm burst}$ trigger starbursts

in which all of the cold gas from the merging galaxies is transferred to the spheroid, to form stars or be ejected by the resulting SN feedback. Some of this gas is then available to feed the central SMBH (Kauffmann & Haehnelt, 2000; Malbon et al., 2007). $f_{\rm ellip}$ and $f_{\rm burst}$ are free parameters with values 0.3 and 0.05 respectively.

2.6 Disc instabilities

Galaxy discs are susceptible to bar instabilities, which can change the galaxy morphology, and drive gas to the centre of the galaxy. Galaxy discs become unstable to bar formation when they are sufficiently self-gravitating. To model this we use the Efstathiou et al. (1982) disc stability criterion, where discs are dynamically unstable if:

$$F_{\rm disc} \equiv \frac{V_c(r_{\rm disc})}{(1.68GM_{\rm disc}/r_{\rm disc})^{1/2}} < F_{\rm stab}, \tag{2.6.23}$$

where $M_{\rm disc}$ is the disc mass (gas and stars), and $r_{\rm disc}$ is the disc half-mass radius. $F_{\rm disc}$ quantifies the contribution of disc self-gravity to its circular velocity, so higher values of $F_{\rm disc}$ correspond to less self-gravity, and therefore greater disc stability. $F_{\rm stab}$ is a parameter of the model. The N-body simulations of Efstathiou et al. (1982) found $F_{\rm stab} \approx 1.1$ for purely stellar discs embedded in dark matter haloes, whereas Christodoulou et al. (1995) found $F_{\rm stab} \approx 0.9$ for purely gaseous discs. If $F_{\rm disc} < F_{\rm stab}$ at any timestep, we assume that the disc forms a bar, which then thickens due to buckling instabilities, and forms a spheroid. This transition from disc to spheroid is assumed to happen instantaneously, and this disc instability triggers a starburst. A value of $F_{\rm stab} = 0.9$ is used here.

Disc instabilities also transfer gas to the centre of the galaxy to be fed into the SMBH. Disc instabilities driving gas into the centres of galaxies is an effect seen in various hydrodynamical simulations (e.g. Hohl, 1971; Bournaud et al., 2005; Younger et al., 2008), and treated as a channel of black hole/bulge growth in many semi-analytic models of galaxy formation (e.g. De Lucia et al., 2011; Hirschmann et al., 2012; Menci et al., 2014; Croton et al., 2016; Lagos et al., 2018), although the implementation of these disc instabilities varies between models. Most models also

use the disc instability criterion of Efstathiou et al. (1982), however different models apply this condition differently. For example, in the model of Hirschmann et al. (2012), if a disc is unstable, then enough gas and stars are transferred from the disc to the bulge to completely stabilise the disc, while in GALFORM, we assume that if a disc is unstable, then it is completely destroyed and forms a bulge. Numerical simulations of isolated disks show that disc instabilities can transfer large fractions of gas and stars into the bulge in some situations (e.g. Bournaud et al., 2007; Elmegreen et al., 2008; Saha & Cortesi, 2018).

2.7 SMBH growth

The starting point for the treatment of SMBHs in the model is SMBH seeds that eventually grow by accretion of gas and by merging with other SMBHs to form the objects in the Universe today. The processes for SMBH seed formation are uncertain (see e.g. Volonteri 2010, and references therein) and so we simply add a seed SMBH of mass $M_{\rm seed}$ into each halo, where $M_{\rm seed}$ is a parameter that we can vary. Unless otherwise stated, this parameter has the value $M_{\rm seed} = 10h^{-1}M_{\odot}$ - representative of the SMBH seeds formed by stellar collapse. SMBHs in GALFORM grow in three different ways.

2.7.1 Starburst mode gas accretion

First, SMBHs can accrete gas during starbursts, which are triggered by either galaxy mergers or disc instabilities. In both of these cases, all of the remaining cold gas in a galaxy is consumed in a starburst and a fixed fraction of the mass of stars formed from the starburst feeds the SMBH, such that the accreted mass is given by:

$$M_{\rm acc} = f_{\rm BH} M_{\star,\rm burst}, \tag{2.7.24}$$

where $M_{\star,\rm burst}$ is the mass of stars formed in the starburst and $f_{\rm BH}$ is a free parameter, which takes the value $f_{\rm BH} = 0.005$ here, as adopted in Lacey et al. (2016). Note that the mass of the stars formed is less than the initial mass of the gas in the starburst due to the ejection of gas by supernova feedback.

It is assumed that that during an accretion episode the accretion rate is constant over a time $f_{\rm q}\tau_{\rm dyn,bulge}$, where $\tau_{\rm dyn,bulge}$ is the dynamical timescale of the bulge (calculated in Section 2.8), and $f_{\rm q}$ is a free parameter, given in Table 3.1. The value of $f_{\rm q}$ is calibrated on the AGN luminosity functions as shown in Figure A.9. Therefore, the mass accretion rate is given by:

$$\dot{M} = \frac{f_{\rm BH} M_{\star,\rm burst}}{f_q \tau_{\rm dyn,bulge}}. \tag{2.7.25}$$

2.7.2 Hot halo mode gas accretion

In GALFORM we assume that SMBHs can also accrete gas from the hot gas atmospheres of massive haloes. When the cooling time of the gas is longer than its free-fall time, the SMBH is fed with a slow inflow from the halo's hot atmosphere - 'hot halo mode accretion' (Bower et al., 2006), which occurs when AGN feedback is active (see Section 2.4.3). The energy input from the relativistic jet is assumed to balance radiative cooling in the halo, with the mass accretion rate onto the black hole $\dot{M}$ being determined by this energy balance condition:

$$\dot{M} = \frac{L_{\rm cool}}{\epsilon_{\rm heat} c^2}, \tag{2.7.26}$$

where $L_{\rm cool}$ is the radiative cooling luminosity of the hot halo gas from Section 2.4.3, and $\epsilon_{\rm heat}$ is the efficiency of halo heating, which is treated as a free parameter, with value 0.02, as adopted in Lacey et al. (2016).

2.7.3 SMBH mergers

SMBHs can also be built up by SMBH-SMBH mergers. When galaxies merge, dynamical friction from gas, stars and dark matter causes the SMBH of the smaller galaxy to sink towards the other SMBH. Then, as the separation decreases, gravitational radiation provides a mechanism by which the SMBHs can lose angular momentum and spiral in to merge and form a larger SMBH. In the model, we assume the timescale on which the SMBHs merge is short, so that the SMBHs merge when the galaxies merge.

2.8 Galaxy Sizes

The size of a galaxy disc is determined by conservation of angular momentum and centrifugal equilibrium. The following derivation follows Appendix C of Cole et al. (2000). Galaxy sizes are calculated in GALFORM such that as the gas condenses to form a galaxy at the centre of the dark matter halo, the lengthscales of the disc and bulge and the mass distribution in the halo respond adiabatically to each other. A fraction $1 - f_H$ of the total mass condenses to form a galaxy at the centre of the halo, with a fraction f_H of mass still in the halo component. f_H is determined by the sum of the disc and bulge masses. It is assumed that the pseudo-specific angular momentum, $rV_c(r)$ is conserved for each shell of the halo. Under this assumption:

$$r_0 V_{c,0}(r_0) = r V_c(r), \tag{2.8.27}$$

where r_0 and r are the initial and final radii of the shell (before and after the galaxy condensation), and $V_{c,0}$ and V_c are the initial and final circular velocities of the halo. The initial and final masses interior to the shell are related by:

$$M_H(r) = f_H M_{H,0}(r_0), \tag{2.8.28}$$

where $M_H(r)$ is the halo mass profile. V_c for halo mass shells is then given by:

$$V_c^2(r) = G[M_H(r) + M_D(r) + M_B(r)]/r, \tag{2.8.29}$$

where $M_D(r)$ and $M_B(r)$ are the disc and bulge masses, interior to the radius r. Equations (2.8.27), (2.8.28), and (2.8.29), can then be combined to give:

$$r_0 M_{H,0}(r_0) = r[f_H M_{H,0}(r_0) + M_D(r) + M_B(r)], \tag{2.8.30}$$

which relates the final radius of a halo shell to its initial radius, given known disc and bulge profiles. In the model, the disc is assumed to have an exponential surface density profile:

$$\Sigma_D(r) = \frac{M_D}{2\pi h_D^2} \exp(-r/h_D), \tag{2.8.31}$$

where:

$$M_D(r) = M_D[1 - (1 + r/h_D)\exp(-r/h_D)], \tag{2.8.32}$$

where h_D is the radial scale length of the disc. This is related to the disc half-mass radius, r_D by $r_D = 1.68h_D$. The specific angular momentum of the disc, j_D, is given by:

$$j_D = k_D r_D V_{cD}(r_D), \tag{2.8.33}$$

where V_{cD} is the circular velocity in the disc plane at the half-mass radius and k_D is a constant. For a flat rotation curve ($V_{cD}(r) = V_{cD}(r_D)$), $k_D = 1.19$, and the value of k_D only weakly depends on the assumed rotation curve. GALFORM uses $k_D = 1.19$. From equation (2.8.33), the angular momentum of the disc is then given by:

$$\begin{aligned} j_D^2 =& k_D^2 r_D^2 V_{cD}^2(r_D) \\ =& k_D^2 G r_D \left[f_H M_{H,0}(r_{D,0}) + \frac{1}{2} k_H M_D + M_B(r_D) \right], \end{aligned} \tag{2.8.34}$$

where $M_D(r_D) = \frac{1}{2}M_D$ by construction. The constant k_H arises from the fact that the disc is not spherically symmetric. For an exponential disc, $k_H = 1.25$. Therefore, to calculate the disc half-mass radius, equation (2.8.34) evaluated at r_D, must be satisfied, and equation (2.8.30) evaluated at r_D:

$$r_{D0} M_{H,0}(r_{D,0}) = r_D[f_H M_{H,0}(r_{D,0}) + \frac{1}{2} M_D + M_B(r_D)], \tag{2.8.35}$$

must be satisfied. A similar procedure can then be followed to determine the size of the spheroid (see Appendix C of Cole et al., 2000). The mass density profile for the spheroid in projection is given by (de Vaucouleurs, 1948):

$$\Sigma_B(r) = \Sigma_0 \exp\left[7.676 \left(\left(\frac{r}{r_e} \right)^{1/4} - 1 \right) \right], \tag{2.8.36}$$

where r_e is the half-mass radius of the bulge in projection, which relates to r_B by $r_e = r_B/1.35$.

In GALFORM, a spheroid is formed after a merger or a disc instability. In the case of a merger, once the separation between the galaxies equals the sum of their half-mass radii, the galaxies are assumed to merge. Using the virial theorem, the internal energy of a galaxy relates to the gravitational self-binding energy of the galaxy and hence the total mass, M, and the half-mass radius, r, by:

$$E_{\rm int} = -\frac{1}{2}E_{\rm bind} = -\frac{c_{\rm bind}}{2}\frac{GM^2}{r}, \tag{2.8.37}$$

where $c_{\rm bind}$ is a constant that depends on the assumed density profile. For a spheroid with the mass density considered here, $c_{\rm bind} = 0.45$ (which I refer to as c_B), whereas for an exponential disc, $c_{\rm bind} = 0.49$ (which I refer to as c_D). For simplicity, in the model, a single value of $c_{\rm bind} = 0.5$ is adopted. The energy of the relative orbital motion between the two galaxies just prior to the merger is:

$$E_{\rm orbit} = -\frac{f_{\rm orbit}}{2}\frac{GM_1M_2}{r_1 + r_2}, \tag{2.8.38}$$

where M_1 and M_2 are the total (dark matter and gas and stars) masses, and r_1 and r_2 are the half-mass radii of the galaxies. The value of the parameter $f_{\rm orbit}$ depends on the orbital parameters of the galaxy pair. For two point masses on circular orbits, $f_{\rm orbit} = 1$, whereas for a parabolic trajectory, $f_{\rm orbit} = 0$. $f_{\rm orbit}$ is treated as an adjustable parameter in the range $0 \leq f_{\rm orbit} \lesssim 1$, and a value of $f_{\rm orbit} = 0$ is adopted here, following Lacey et al. (2016). By conservation of energy, the binding energy of the new spheroid is given by:

$$E_{\rm int,new} = E_{\rm int,1} + E_{\rm int,2} + E_{\rm orbit}. \tag{2.8.39}$$

By combining equations (2.8.37), (2.8.38), and (2.8.39), I obtain the expression:

$$\frac{(M_1 + M_2)^2}{r_{\rm new}} = \frac{M_1^2}{r_1} + \frac{M_2^2}{r_2} + \frac{f_{\rm orbit}}{c_{\rm bind}}\frac{M_1M_2}{r_1 + r_2}, \tag{2.8.40}$$

which can be solved for the half-mass radius of the new spheroid, $r_{\rm new}$. For disc instabilities, a similar expression to equation (2.8.40) can be computed:

$$\frac{c_B(M_D + M_B)^2}{r_{\rm new}} = c_B\frac{M_B^2}{r_B} + c_D\frac{M_D^2}{r_D} + f_{\rm int}\frac{M_DM_B}{r_D + r_B}, \tag{2.8.41}$$

where c_B and c_D are defined as above. The masses M_B and M_D are the masses of the baryonic (stars and gas) components of the bulge and disc. The final term represents the gravitational interaction energy of the disc and the bulge, with $f_{\rm int}$ reasonably well approximated by $f_{\rm int} = 2$. This value follows Cole et al. (2000) and Lacey et al. (2016).

From these calculations the half-mass radius of the bulge, r_B has been obtained. From r_B and the circular velocity at r_B, the dynamical timescale of the bulge can be calculated via:

$$\tau_{\rm dyn,bulge} = r_B/V_c(r_B), \tag{2.8.42}$$

which is then used for calculating the timescale over which an SMBH growth epsiode in the starburst mode occurs in Section 2.7.1.

2.9 Chemical evolution and IMF

2.9.1 The evolution of mass and metals

The above processes of gas cooling, star formation and feedback can be expressed as a series of coupled differential equations, describing the evolution of the hot gas in haloes ($M_{\rm hot}$), cold gas in galaxies ($M_{\rm cold}$), stars in galaxies ($M_\star$), and the reservoir of ejected gas outside haloes ($M_{\rm res}$). I illustrate these differential equations in Figure 2.1, and give the equations below (ignoring SMBH terms which are much smaller):

$$\dot{M}_{\rm hot} = -\dot{M}_{\rm halo,acc} + \alpha_{\rm ret}\frac{M_{\rm res}}{\tau_{\rm dyn,halo}}, \tag{2.9.43}$$

$$\dot{M}_{\rm cold} = \dot{M}_{\rm halo,acc} - (1 - R + \beta)\psi, \tag{2.9.44}$$

$$\dot{M}_\star = (1 - R)\psi, \tag{2.9.45}$$

$$\dot{M}_{\rm res} = \beta\psi - \alpha_{\rm ret}\frac{M_{\rm res}}{\tau_{\rm dyn,halo}}. \tag{2.9.46}$$

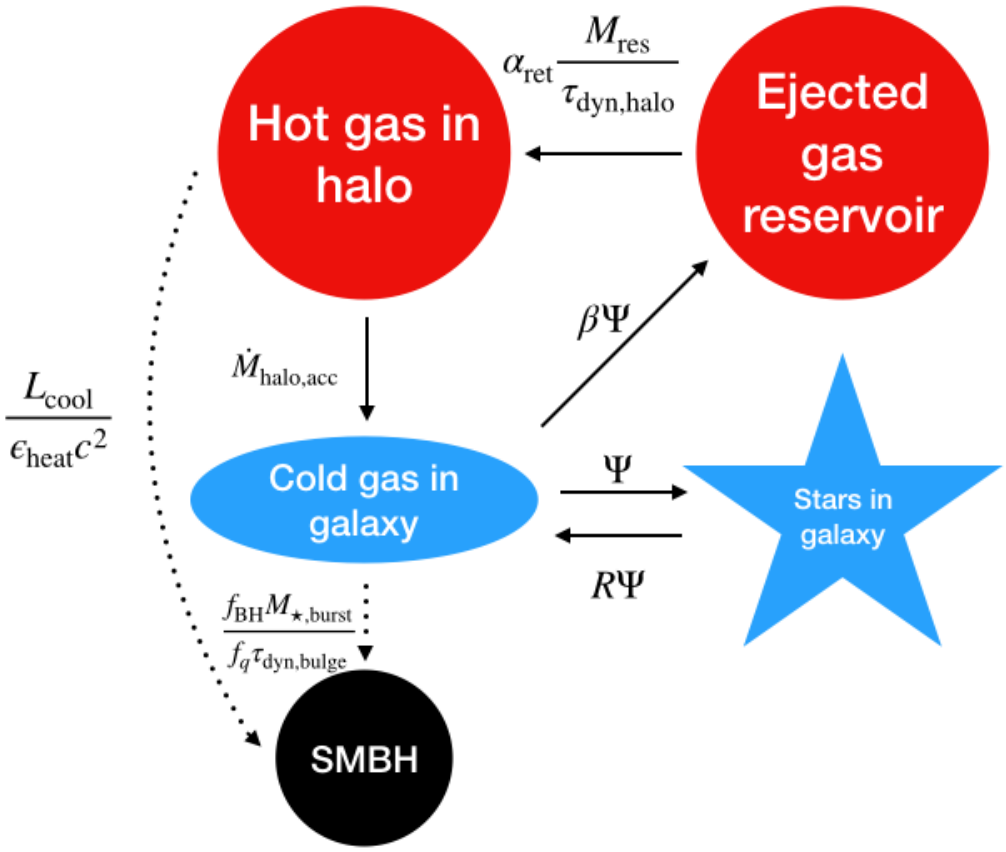

Figure 2.1: A schematic showing the exchange of baryons between the different halo components, including the SMBH. The mass accretion rates for the exchange between each components are shown next to each arrow. Accretion onto the SMBH requires either a starburst or hot halo accretion, which may not be occurring at a certain timestep, and so are given by dotted lines.

The masses of the metals obey a similar set of differential equations:

$$\dot{M}^Z_{\rm hot} = -Z_{\rm hot}\dot{M}_{\rm halo,acc} + \alpha_{\rm ret}\frac{M^Z_{\rm res}}{\tau_{\rm dyn,halo}}, \tag{2.9.47}$$

$$\dot{M}^Z_{\rm cold} = Z_{\rm hot}\dot{M}_{\rm halo,acc} - [p - (1 - R + \beta)Z_{\rm cold}]\psi, \tag{2.9.48}$$

$$\dot{M}^Z_\star = (1 - R)Z_{\rm cold}\psi, \tag{2.9.49}$$

$$\dot{M}^Z_{\rm res} = \beta Z_{\rm cold}\psi - \alpha_{\rm ret}\frac{M^Z_{\rm res}}{\tau_{\rm dyn,halo}}, \tag{2.9.50}$$

where $Z_{\rm hot}$ is the metallicity of the hot gas component, given by $Z_{\rm hot} = M^Z_{\rm hot}/M_{\rm hot}$. This is similarly defined for the other components. R is the returned fraction, and p is the yield. The two quantities depend on the initial mass function, and are defined below.

2.9.2 Initial Mass Function

The initial mass function (IMF) is defined as the distribution of stars in mass m when a stellar population is formed, normalised to unit solar mass:

$$\int_{m_L}^{m_U} m\Phi(m)d\ln m = 1, \tag{2.9.51}$$

where $\Phi(m)d\ln m$ is the number of stars formed with masses between $\ln(m)$ and $\ln(m) + d\ln(m)$ per unit total mass of stars formed, and m_L and m_U are lower and upper limits of the IMF. The returned fraction, R, which is the fraction of the initial mass of a stellar population that is returned to the ISM by mass loss from dying stars, is given by:

$$R = \int_{1M_\odot}^{m_U}(m - m_{\rm rem}(m))\Phi(m)d\ln m, \tag{2.9.52}$$

where $m_{\rm rem}(m)$ is the mass of the remnant (white dwarf, neutron star, black hole) left by a star of mass m. This calculation assumes the 'instantaneous recycling

approximation', which assumes that all stars with masses above $1M_{\odot}$ die immediately, whereas stars of lower mass live forever. This approximation is reasonable as the lifetimes of massive stars is short compared to the timescales on which galaxies evolve.

The yield, p, which is the fraction of the initial mass of a stellar population that is synthesised into new metals and then ejected, is given by:

$$p = \int_{1M_{\odot}}^{m_U} p_Z(m) m \Phi(m) d\ln m, \tag{2.9.53}$$

where $p_Z(m)$ is this fraction for a single star of initial mass, m, as obtained from stellar evolution calculations. The IMF is assumed to be a power law, or a piecewise power law, in mass:

$$\Phi(m) = \frac{dN}{d\ln m} \propto m^{-x}, \tag{2.9.54}$$

where x is the IMF slope. For a Salpeter (1955) IMF, $x = 1.35$. The model uses different IMFs for the different modes of star formation. For the quiescent mode of star formation, a Kennicutt (1983) IMF is assumed, where $x = 0.4$ for $m < 1M_{\odot}$, and $x = 1.5$ for $m > 1M_{\odot}$, whereas for the burst mode of star formation, a single power law IMF is used, with $x = 1$.

2.10 Stellar populations and Dust

2.10.1 Stellar population synthesis

From the previous calculations, the evolution of stellar mass and metallicity of each galaxy is obtained. These can be combined with a stellar population synthesis (SPS) model to determine the spectral energy distribution (SED) of each galaxy. The SED of a stellar population with a mixture of ages and metallicities at a time t can be written as:

$$L_{\lambda}(t) = \int_0^t dt' \int_0^{\infty} dZ' \Psi(t', Z') L_{\lambda}^{\mathrm{SSP}}(t - t', Z'; \Phi), \tag{2.10.55}$$

where $\Psi(t', Z')dt'dZ'$ is the mass of stars formed between t' and $t'+dt'$ and metallicity between Z' and $Z'+dZ'$. $L_\lambda^{\rm SSP}(t-t', Z'; \Phi)$ is the SED of a single stellar population (SSP) of unit mass, with an age $t-t'$, metallicity Z', and formed with an IMF $\Phi(m)$. $L_\lambda^{\rm SSP}(t, Z; \Phi)$ can be calculated from the SED of a single star (of age t, metallicity Z and mass m), $L_\lambda^{\rm (star)}(t, Z, m)$ using:

$$L_\lambda^{\rm SSP}(t, Z; \Phi) = \int_{m_L}^{m_U} L_\lambda^{\rm (star)}(t, Z, m)\Phi(m) d\ln m. \tag{2.10.56}$$

As separate IMFs are assumed for the disc and for the spheroid, these are calculated separately. The SPS model adopted in the Lacey et al. (2016) model is that of Maraston (2005).

2.10.2 Dust extinction

The light from stars is absorbed by dust, which re-emits the radiation at longer wavelengths. The dust is assumed to be in two components, (i) dense molecular clouds, which surround young stars and star forming regions, and (ii) diffuse dust with an exponential vertical and radial distribution in a disc. The fraction of the dust in molecular clouds is $f_{\rm cloud}$, while the rest of the dust is in the diffuse medium. A value of $f_{\rm cloud} = 0.5$ is adopted in Lacey et al. (2016).

For the dense molecular component, stars are assumed to form surrounded by uniform density dust clouds with a constant mass ($m_{\rm cloud}$) and radius ($r_{\rm cloud}$), and then gradually leave these clouds over a timescale of $t_{\rm esc}$. The clouds cause extinction of the light from the stars inside them, with an optical depth proportional to the amount of dust (proportional to $Z_{\rm cloud}$) and the projected density (proportional to $m_{\rm cloud}/r_{\rm cloud}^2$):

$$\tau \propto Z_{\rm cold} \frac{m_{\rm cloud}}{r_{\rm cloud}^2}. \tag{2.10.57}$$

The diffuse dust component also obscures starlight. To model this component, GALFORM uses the tabulated radiative transfer models of Ferrara et al. (1999). This component produces extinction with optical depth:

$$\tau \propto (1 - f_{\rm cloud}) Z_{\rm cold} \frac{M_{\rm cold}}{r_{\rm diff}^2}, \tag{2.10.58}$$

where $r_{\rm diff} = r_{\rm disc}$ for quiescent star formation, and $r_{\rm diff} = r_{\rm bulge}$ for starbursts.

2.11 The Lacey et al. (2016) model

There exist several different published GALFORM models. Starting with the original Cole et al. (2000) model, two different variants were developed: (i) a model using supernova-driven superwinds and a varying IMF to match the abundances of submillimetre and Lyman-break galaxies (Baugh et al., 2005), and (ii) a model including AGN feedback (Bower et al., 2006). The Lacey et al. (2016) model brought these branches together into a model including both AGN feedback and a varying IMF, and hence can be thought of as a 'unifying' model.

This model used cosmological parameters from the WMAP cosmology (Komatsu et al., 2011). It used the Millennium-WMAP7 (MW7) simulation, which has a box size of side $500h^{-1}$Mpc, and has a halo mass resolution of $1.87 \times 10^{10} h^{-1} M_{\odot}$. This corresponds to a dark matter particle resolution of $9.36 \times 10^{8} h^{-1} M_{\odot}$ (haloes are defined to have a minimum of 20 particles).

The Lacey et al. (2016) model compares well to a wide range of observational constraints, across a range of wavelengths (from 850μm number counts to far-UV luminosity functions) and across a range in redshift (from $z = 0$ out to $z = 6$).

2.12 The Baugh et al. (2019) model

The model I am using for this thesis is the recalibration of the Lacey et al. (2016) GALFORM model by Baugh et al. (2019). This model uses a higher resolution dark matter only simulation, P-Millennium (Baugh et al., 2019), which has a box size of side 800Mpc and a halo mass resolution of $2.12 \times 10^{9} h^{-1} M_{\odot}$, which corresponds to a dark matter particle mass of $1.06 \times 10^{8} h^{-1} M_{\odot}$ (haloes are defined to have a minimum of 20 particles). The P-Millennium also has an increased number of snapshots output - 270 instead of 64 for the MW7 simulation used in Lacey et al.

(2016). The new model also includes a more accurate calculation of the timescale for galaxies to merge within a halo (Simha & Cole, 2017), as I described in Section 2.5.

Because of the changed cosmological parameters and an improved halo mass resolution in P-Millennium compared to the simulation used in Lacey et al. (2016), some of the galaxy formation parameters were recalibrated compared to Lacey et al. (2016). Only two GALFORM parameters were changed, both relating to supernova feedback ($\gamma_{\rm SN}$) and the return of ejected gas ($\alpha_{\rm ret}$). This P-Millennium based model has already been used in Cowley et al. (2018) to make predictions for galaxies for JWST in near- and mid-IR bands, and a model using P-Millennium and the model of Gonzalez-Perez et al. (2018) was used to study the effect of AGN feedback on halo occupation distribution models in McCullagh et al. (2017).

Chapter 3

The evolution of SMBH spin and AGN luminosity for $0 < z < 6$

3.1 Introduction

Ever since quasars were first identified to be cosmological sources (Schmidt, 1968), a key aim has been to to understand their evolution through cosmological time. Early studies showed that the number density of quasars shows strong evolution, with more luminous quasars present at $z \approx 2$ than at $z \approx 0$, leading to the suggestion that quasars evolve by 'pure luminosity evolution' (PLE). In this scenario, quasars are long lived and fade through cosmic time, leading to an evolution in the luminosity function of only the characteristic luminosity (e.g. Boyle et al., 1990). However, more recent optical surveys, which can probe both the faint and bright end of the luminosity function, have shown not only that the slope of the luminosity function evolves (e.g. Richards et al., 2006; Croom et al., 2009), but also that the number density decreases at high redshift (e.g. Fan et al., 2001; Jiang et al., 2016). Surveys at X-ray wavelengths, show an evolution in the shape of the luminosity function (e.g. Ueda et al., 2014) as well as differences between the absorbed and unabsorbed populations (e.g. Aird et al., 2015; Georgakakis et al., 2015). Clearly, the full picture of supermassive black holes (SMBHs) and Active Galactic Nuclei (AGNs) evolving through cosmological time is complicated, and requires detailed investigation. Theoretical models and cosmological simulations have allowed us to

try to quantify the role of different contributing black hole fuelling mechanisms (e.g. mergers, disc instabilities) and obscuration to the AGN luminosity function (e.g. Fanidakis et al., 2012; Hirschmann et al., 2012), but we do not yet fully understand the reasons for the different features of the evolution.

In this Chapter, we present predictions for the evolution of SMBH and AGN properties in the redshift range $0 < z < 6$, using an updated prescription for the evolution of SMBH spin within GALFORM, as we now describe. This Chapter is organised as follows. In Section 3.2 we outline the spin evolution model and in Section 3.3 we outline the calculation of AGN luminosities. In Section 3.4 we present predictions for black hole masses and spins for the model, as well as the dependence of AGN luminosities on galaxy properties. In Section 3.5 we show the evolution of the AGN luminosity function at different wavelengths for $0 < z < 6$. In Section 3.6 we give concluding remarks.

3.2 SMBH spin evolution

In this Section, we update/modify the model for SMBHs and AGNs presented in Fanidakis et al. (2011), superceding the equations in that paper, which contained some typographical errors, and also putting special emphasis on improving the model for the obscuration of AGNs at X-ray and optical wavelengths. We calculate expressions for accretion disc quantities (e.g. warp radius, self-gravity radius) only using the accretion disc solutions of Collin-Souffrin & Dumont (1990), which are appropriate for AGN discs, rather than using different expressions from different studies.

3.2.1 SMBH mass growth and spinup by gas accretion

In this model, SMBHs can change spin in two ways: (i) by accretion of gas or (ii) by merging with another SMBH. The SMBH spin is characterised by the dimensionless spin parameter, $a = cJ_{\rm BH}/GM_{\rm BH}^2$, within the range $-1 \leq a \leq 1$, where $J_{\rm BH}$ is the angular momentum of the SMBH, and $M_{\rm BH}$ is the mass of the SMBH. $a = 0$ represents a black hole that is not spinning and $a = 1$ or $a = -1$ represents a

maximally spinning black hole. The sign of a is defined by the direction of the angular momentum of the black hole relative to that of the innermost part of the accretion disc, so for $a > 0$ the black hole is spinning in the same direction as the inner accretion disc and for $a < 0$ the black hole is spinning in the opposite direction to the inner accretion disc. To calculate the SMBH spin, a^f after an accretion episode, we use the expression in Bardeen (1970)[1]:

$$a^f = \frac{1}{3}\sqrt{\hat{r}_{\rm lso,i}}\frac{M_{\rm BH,i}}{M_{\rm BH,f}}\Big(4 - \Big[3\hat{r}_{\rm lso,i}\Big(\frac{M_{\rm BH,i}}{M_{\rm BH,f}}\Big)^2 - 2\Big]^{1/2}\Big), \tag{3.2.1}$$

where $\hat{r}_{\rm lso}$ is the radius of the last stable circular orbit in units of the gravitational radius, $R_{\rm G} = GM_{\rm BH}/c^2$, and the subscripts i and f indicate values at the start and end of an accretion event. The black hole mass before and after an accretion event are related by:

$$M_{\rm BH,f} = M_{\rm BH,i} + (1 - \epsilon_{\rm TD})\Delta M, \tag{3.2.2}$$

where ΔM is the mass accreted from the disc in this accretion episode (from the fuelling modes outlined in Scetion 2.7) and $\epsilon_{\rm TD}$, the radiative accretion efficiency for a thin accretion disc, is given by:

$$\epsilon_{\rm TD} = 1 - \Big(1 - \frac{2}{3\hat{r}_{\rm lso}}\Big)^{1/2}. \tag{3.2.3}$$

$\hat{r}_{\rm lso}$ is calculated from the spin a, as in Bardeen et al. (1972):

$$\hat{r}_{\rm lso} = 3 + Z_2 \mp \sqrt{(3 - Z_1)(3 + Z_1 + 2Z_2)}, \tag{3.2.4}$$

with the minus sign for $a > 0$ and the positive sign for $a < 0$. The functions Z_1 and Z_2 are given by:

$$Z_1 = 1 + (1 - |a|^2)^{1/3}[(1 + |a|)^{1/3} + (1 - |a|)^{1/3}], \tag{3.2.5}$$

$$Z_2 = \sqrt{3|a|^2 + Z_1^2}. \tag{3.2.6}$$

[1]Note that equation (3.2.1) is corrected from a typographical error in Fanidakis et al. (2011) equation (6).

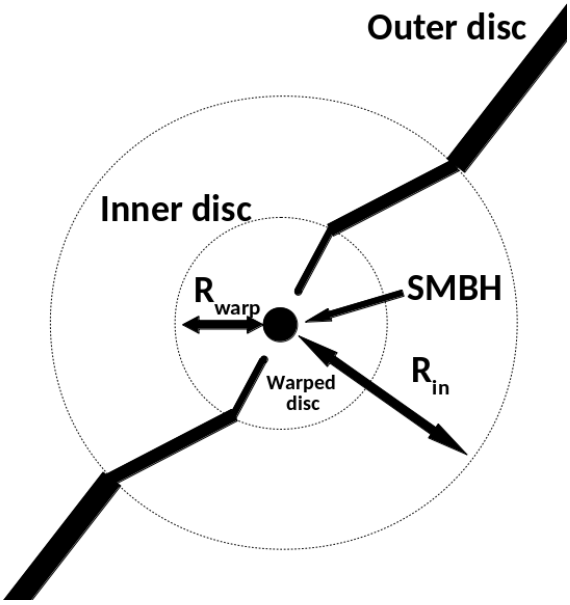

Figure 3.1: A diagram showing the various scales involved in the gas accretion - the warp radius $R_{\rm warp}$ and the inner radius $R_{\rm in}$. We refer to the region within $R_{\rm in}$ as the inner disc and the region outside of $R_{\rm in}$ as the outer disc. For typical parameters (i.e. $a = 0.4$, $\alpha_{\rm TD} = 0.1$, $\dot{m} = 0.1$, $M_{\rm BH} = 10^6 M_\odot$, $\nu_2/\nu_1 = 1$, with these variables defined below) using equations (3.2.11) and (3.2.16), $R_{\rm warp} = 0.0006$pc and $R_{\rm in} = 0.02$pc.

We consider the accretion disc in three separate parts as shown in Figure 3.1 - an outer disc at radii greater than an inner radius, $R_{\rm in}$, an inner disc for radii less than $R_{\rm in}$, and a warped disc for radii less than the warp radius, $R_{\rm warp}$. The SMBH has an angular momentum $\vec{J}_{\rm BH}$, and the angular momentum of the disc within $R_{\rm in}$ is $\vec{J}_{\rm in}$. If $\vec{J}_{\rm BH}$ is not in the same direction as $\vec{J}_{\rm in}$ a spinning black hole induces a Lense-Thirring precession in the misaligned disc elements. Because the precession rate falls off as R^{-3}, at smaller radii the black hole angular momentum and the accretion disc angular momentum vectors will become exactly aligned or anti-aligned, whereas at sufficiently large radii there will still be a misalignment (Bardeen & Petterson, 1975). The transition between these two regions occurs at the so-called 'warp radius', $R_{\rm warp}$. The angular momentum of the disc within the warp radius is $\vec{J}_{\rm warp}$. At the start of an accretion event, the angular momentum $\vec{J}_{\rm warp}$ within $R_{\rm warp}$ is assumed to be aligned with $\vec{J}_{\rm in}$. As a result of the torques, $\vec{J}_{\rm BH}$

then aligns with $\vec{J}_{\rm tot} = \vec{J}_{\rm BH} + \vec{J}_{\rm warp}$ (which remains constant during this alignment process) and $\vec{J}_{\rm warp}$ either anti-aligns or aligns with $\vec{J}_{\rm BH}$ (King et al., 2005). The gas within $R_{\rm warp}$ is then assumed to be accreted onto the SMBH from the aligned/anti-aligned disc. As more gas is accreted, $\vec{J}_{\rm BH}$ eventually aligns with the rest of the inner disc, as the gas in the inner disc is consumed.

We consider two alternative scenarios for how the angular momentum directions of the inner and outer disc are related. In the 'prolonged mode' accretion scenario, the angular momentum of the inner disc is in the same direction as the angular momentum of the outer disc, $\vec{J}_{\rm out}$, but in the 'chaotic mode' accretion scenario introduced in King et al. (2008), the orientation of the angular momentum of the inner disc is randomly oriented with respect to the angular momentum of the outer disc. King et al. (2008) propose that $R_{\rm in}$ is the self-gravity radius of the disc, and we assume this in our model.

The motivation for chaotic mode accretion is twofold. First, the Soltan (1982) argument, a comparison of the integral of the quasar luminosity function over luminosity and redshift to the integral over the black hole mass function in the local Universe, implies an average radiative efficiency of SMBH growth of $\epsilon \approx 0.1$ (which corresponds to a spin value of $a \approx 0.67$), suggesting that SMBHs in the Universe are typically not maximally spinning, as we would expect from SMBHs that have been spun up by the accretion of gas that is aligned in the same direction, as in the prolonged accretion scenario. However, there are uncertainties in the value of ϵ from the Soltan (1982) argument, due to uncertainties in the derived quasar luminosity function and black hole mass function (the latter is generally determined using scaling relations with σ, $M_{\rm bulge}$ or $L_{\rm bulge}$). Secondly, AGN jets seem to be misaligned with their host galaxies (e.g. Kinney et al., 2000; Sajina et al., 2007), suggesting a misaligned accretion of material onto the SMBH.

Accretion continues in this manner until the gas in the outer disc has been consumed. For this analysis, we adopt chaotic mode accretion as our standard choice.

3.2.2 Warped accretion discs

To obtain the warp radius, $R_{\rm warp}$, of an accretion disc, we need expressions for the structure of the accretion disc. There are two different types of accretion discs: i) physically thin, optically thick, radiatively efficient 'thin discs' (Shakura & Sunyaev, 1973) and ii) physically thick, optically thin, radiatively inefficient Advection Dominated Accretion Flows (ADAFs - see Yuan & Narayan, 2014, for a review). Shakura & Sunyaev (1973) introduced the 'α-prescription' to solve the accretion disc equations for a thin disc, where the viscosity, ν, is given by $\nu = \alpha_{\rm TD} c_s H$, where $\alpha_{\rm TD}$ is the dimensionless Shakura & Sunyaev (1973) parameter, c_s is the sound speed and H is the disc semi-thickness. In this analysis, we use the solutions of Collin-Souffrin & Dumont (1990), in which the accretion disc equations are solved for AGN discs, assuming this α-prescription. We use their solution for the regime where the opacity is dominated by electron scattering and where gas pressure dominates over radiation pressure.

The disc surface density, Σ, is then given by:

$$\Sigma = 6.84 \times 10^5 \, {\rm g \, cm^{-2}} \, \alpha_{\rm TD}^{-4/5} \dot{m}^{3/5} \Big(\frac{M_{\rm BH}}{10^8 M_\odot} \Big)^{1/8} \Big(\frac{R}{R_{\rm S}} \Big)^{-3/5}, \tag{3.2.7}$$

where $\dot{m} = \dot{M}/\dot{M}_{\rm Edd}$ is the dimensionless mass accretion rate, R is the radius from the centre of the disc and $R_{\rm S} = 2GM_{\rm BH}/c^2$ is the Schwarzschild radius. The value we use for $\alpha_{\rm TD}$ is given in Table 3.1. The disc semi-thickness H is given by[2]:

$$\frac{H}{R} = 1.25 \times 10^{-3} \, \alpha_{\rm TD}^{-1/10} \dot{m}^{1/5} \left(\frac{M_{\rm BH}}{10^8 M_\odot} \right)^{-1/10} \left(\frac{R}{R_{\rm S}} \right)^{1/20}. \tag{3.2.8}$$

We calculate the Eddington luminosity using:

$$L_{\rm Edd} = \frac{4\pi G M_{\rm BH} c}{\kappa} = 1.26 \times 10^{46} \left(\frac{M_{\rm BH}}{10^8 M_\odot} \right) {\rm ergs^{-1}}, \tag{3.2.9}$$

where κ is the opacity, for which we have used the electron scattering opacity for pure hydrogen gas. We calculate the Eddington mass accretion rate $\dot{M}_{\rm Edd}$ from

[2]Note that equation (3.2.8) is different to Fanidakis et al. (2011) equation (25), as we are using the accretion disc solutions of Collin-Souffrin & Dumont (1990).

$L_{\rm Edd}$ using a nominal accretion efficiency $\epsilon = 0.1$ (as used in Yuan & Narayan, 2014) chosen so that the Eddington normalised mass accretion rate $\dot{m}$ does not depend on the black hole spin:

$$\dot{M}_{\rm Edd} = \frac{L_{\rm Edd}}{0.1c^2}. \tag{3.2.10}$$

Note that for the calculation of the luminosities, we do use the spin-dependent radiative efficiency. We then follow the method of Natarajan & Pringle (1998) and Volonteri et al. (2007) and take the warp radius as the radius at which the timescale for radial diffusion of the warp due to viscosity is equal to the local Lense-Thirring precession timescale. This then gives an expression for the warp radius[3]:

$$\frac{R_{\rm warp}}{R_S} = 3410\, a^{5/8} \alpha_{\rm TD}^{-1/2} \dot{m}^{-1/4} \left(\frac{M_{\rm BH}}{10^8 M_\odot}\right)^{1/8} \left(\frac{\nu_2}{\nu_1}\right)^{-5/8}, \tag{3.2.11}$$

where $\nu_{1,2}$ are the horizontal and vertical viscosities respectively. For this analysis, we assume that $\nu_1 = \nu_2$ (e.g. King et al., 2008). The warp mass can then be calculated using:

$$M_{\rm warp} = \int_0^{R_{\rm warp}} 2\pi \Sigma(R) R^2 dR, \tag{3.2.12}$$

to give an expression[4]:

$$M_{\rm warp} = 1.35\, M_\odot \alpha_{\rm TD}^{-4/5} \dot{m}^{3/5} \left(\frac{M_{\rm BH}}{10^8 M_\odot}\right)^{11/5} \left(\frac{R_{\rm warp}}{R_{\rm S}}\right)^{7/5}. \tag{3.2.13}$$

3.2.3 Self-gravitating discs

In the chaotic mode accretion scenario of King et al. (2008), the inner radius, $R_{\rm in}$, is assumed to be equal to the disc self-gravity radius, $R_{\rm sg}$. The self-gravity radius of the accretion disc is the radius at which the vertical gravity due to the disc equals

[3]Note that equation (3.2.11) is different to Fanidakis et al. (2011) equation (15), as we are using the accretion disc solutions of Collin-Souffrin & Dumont (1990).

[4]Note that equation (3.2.13) is different to Fanidakis et al. (2011) equation (18), as we integrate the disc surface density, which is not the method followed in Fanidakis et al. (2011).

Table 3.1: The values for the SMBH/AGN free parameters in the model. The upper part of the table shows parameters where the values adopted are from other studies, whereas the lower part of the table gives parameters which have been calibrated on the luminosity functions in Section 3.4.4.

Parameter	Fanidakis et al. (2012)	Adopted here	Significance
$\alpha_{\rm ADAF}$	0.087	0.1	Shakura & Sunyaev (1973) viscosity parameter for ADAFs
$\alpha_{\rm TD}$	0.087	0.1	Shakura & Sunyaev (1973) viscosity parameter for TDs
$\delta_{\rm ADAF}$	2000^{-1}	0.2	Fraction of viscous energy transferred to electrons in ADAF
$\dot{m}_{\rm crit,ADAF}$	0.01	0.01	Boundary between thin disc and ADAF accretion
$\eta_{\rm Edd}$	4	4	Super-Eddington suppression factor
$f_{\rm q}$	10	10	Ratio of lifetime of AGN episode to bulge dynamical timescale

the vertical gravity of the central SMBH at the disc midplane. For thin discs (where $\dot{m} > \dot{m}_{\rm crit,ADAF}$), the self-gravity condition is (Pringle, 1981):

$$M_{\rm sg} = M_{\rm BH}\frac{H}{R}, \tag{3.2.14}$$

where $M_{\rm sg}$ is the disc mass within the radius $R_{\rm sg}$. For ADAFs (where $\dot{m} < \dot{m}_{\rm crit,ADAF}$), $H \sim R$, so the self-gravity condition is:

$$M_{\rm sg} = M_{\rm BH}. \tag{3.2.15}$$

Using the accretion disc solutions of Collin-Souffrin & Dumont (1990), we derive an expression for the self-gravity radius for thin discs[5]:

$$\frac{R_{\rm sg}}{R_{\rm S}} = 4790\,\alpha_{\rm TD}^{14/27}\dot{m}^{-8/27}\left(\frac{M_{\rm BH}}{10^8 M_\odot}\right)^{-26/27}, \tag{3.2.16}$$

and using an integral similar to equation (3.2.12), the self-gravity mass for the thin disc is given by[6]:

$$M_{\rm sg} = 1.35\,M_\odot\alpha_{\rm TD}^{-4/5}\dot{m}^{3/5}\left(\frac{M_{\rm BH}}{10^8 M_\odot}\right)^{11/5}\left(\frac{R_{\rm sg}}{R_{\rm S}}\right)^{7/5}. \tag{3.2.17}$$

3.2.4 Numerical procedure for modelling SMBH accretion

We have calculated results for both the prolonged and chaotic scenario, and for gas accreted in increments of the self-gravity mass or warp mass. We present predictions mostly for our standard case in which mass is accreted in increments of the self-gravity mass and assuming the chaotic mode of accretion. We find that the predicted spin distribution of the SMBHs is the same if we use increments of the self-gravity mass or the warp mass (cf. Figure 3.8) and so we use increments of the self-gravity mass as it is computationally faster. This is because when gas is accreted onto the SMBH in increments of the warp mass, for small SMBHs the warp mass is very

[5]Note that equation (3.2.16) is different to Fanidakis et al. (2011) equation (24), because we are using the accretion disc solutions of Collin-Souffrin & Dumont (1990).

[6]Note that equation (3.2.17) is different to Fanidakis et al. (2011) equation (26), as we integrate the disc surface density, unlike the method followed in Fanidakis et al. (2011).

small, and so in each accretion event the SMBH grows by a very small amount in each accretion event. First, we present the numerical procedure when mass is accreted in increments of the warp mass (cf. Volonteri et al., 2007; Fanidakis et al., 2011), and then the case where mass is accreted in increments of the self-gravity mass (cf. King et al., 2008).

Accretion in increments of the warp mass

For the first warp mass of gas, the angular momentum of the SMBH, $\vec{J}_{\rm BH}$, and the angular momentum of the inner disc, $\vec{J}_{\rm in}$, are assigned a random angle, θ_i, in the range $[0, \pi]$ radians. In the chaotic mode, each time the inner disc is consumed, θ_i is assigned a new random angle. The gas with $R < R_{\rm warp}$ initially has angular momentum $\vec{J}_{\rm warp}$ aligned with $\vec{J}_{\rm in}$, so θ_i is also the initial angle between $\vec{J}_{\rm BH}$ and $\vec{J}_{\rm warp}$. $\vec{J}_{\rm BH}$ and $\vec{J}_{\rm warp}$ are then evolved according to the Lense-Thirring effect described in Section 3.2.1, with $\vec{J}_{\rm BH}$ and $\vec{J}_{\rm warp}$ respectively aligning and aligning/anti-aligning with $\vec{J}_{\rm tot}$. The magnitude of $\vec{J}_{\rm BH}$ remains constant during this process, but the magnitude of $\vec{J}_{\rm warp}$ changes. This is treated as happening before the mass consumption onto the SMBH starts.

We calculate the angular momentum of the material within the warped disc as $J_{\rm warp} = M_{\rm warp}\sqrt{GM_{\rm BH}R_{\rm warp}}$ and the angular momentum of the black hole, $J_{\rm BH} = 2^{-1/2}M_{\rm BH}a\sqrt{GM_{\rm BH}R_{\rm S}}$. Then the ratio of these two quantities is:

$$\frac{J_{\rm warp}}{2J_{\rm BH}} = \frac{M_{\rm warp}}{\sqrt{2}aM_{\rm BH}}\Big(\frac{R_{\rm warp}}{R_{\rm S}}\Big)^{1/2}. \tag{3.2.18}$$

Whether $\vec{J}_{\rm warp}$ and $\vec{J}_{\rm BH}$ align or anti-align with each other depends on this ratio and on the angle θ_i. Following King et al. (2005), if $\cos\theta_i > -J_{\rm warp}/2J_{\rm BH}$, $\vec{J}_{\rm warp}$ and $\vec{J}_{\rm BH}$ become aligned (prograde accretion), whereas if $\cos\theta_i < -J_{\rm warp}/2J_{\rm BH}$, $\vec{J}_{\rm warp}$ and $\vec{J}_{\rm BH}$ become anti-aligned (retrograde accretion). The angle between $\vec{J}_{\rm BH}$ and $\vec{J}_{\rm in}$ after the accretion event, θ_f, is determined by conservation of $\vec{J}_{\rm tot}$ and $|\vec{J}_{\rm BH}|$ and is given by:

$$\cos\theta_f = \frac{J_{\rm warp} + J_{\rm BH}\cos\theta_i}{\sqrt{J_{\rm BH}^2 + J_{\rm warp}^2 + 2J_{\rm warp}J_{\rm BH}\cos\theta_i}}. \tag{3.2.19}$$

When a new warp mass $M_{\rm warp}$, is then consumed, the gas is given a new $\vec{J}_{\rm warp}$ pointing in the same direction as the inner disc and the same process happens again. This repeated process has the effect that $\vec{J}_{\rm BH}$ gradually aligns with the angular momentum of the inner accretion disc, $\vec{J}_{\rm in}$ as more gas is accreted. Eventually the gas in the inner disc is completely consumed.

In the prolonged mode, this process continues until all of the gas in the outer disc has also been consumed, whereas in the chaotic mode, once a self-gravity mass of gas has been consumed, the angle between $\vec{J}_{\rm in}$ and $\vec{J}_{\rm out}$ is randomised again.

Accretion in increments of the self-gravity mass

In the scenario where gas is being accreted in increments of the self-gravity mass of gas, the above procedure is followed, but only once for each inner disc of gas consumed. For this case, the ratio of angular momenta is given by:

$$\frac{J_{\rm in}}{2J_{\rm BH}} = \frac{M_{\rm sg}}{\sqrt{2}aM_{\rm BH}}\Big(\frac{\min(R_{\rm warp}, R_{\rm sg})}{R_{\rm S}}\Big)^{1/2}. \tag{3.2.20}$$

In the future we plan a more thorough analysis of the effect on the spin evolution of accreting in increments of self-gravity mass compared to increments of warp mass. The AGN luminosities are not affected by this choice as they depend on the accreted mass and the SMBH spin as we describe in Section 3.3.1.

3.2.5 Spinup by SMBH mergers

The other way in which an SMBH can change its spin is by merging with another SMBH. The spin of the resulting SMBH depends on the spins of the two SMBHs that merge and on the angular momentum of their binary orbit. To determine the final spin, $\mathbf{a}_f$, we use the expressions obtained from numerical simulations of BH-BH mergers in Rezzolla et al. (2008):

$$\begin{aligned}|\mathbf{a}_f| = \frac{1}{(1+q)^2}\Big(&|\mathbf{a}_1^2| + |\mathbf{a}_2^2|q^4 + 2|\mathbf{a}_1||\mathbf{a}_2|q^2\cos\phi + \\ &2(|\mathbf{a}_1|\cos\theta + |\mathbf{a}_2|q^2\cos\xi)|\mathbf{l}|q + |\mathbf{l}|^2q^2\Big)^{1/2},\end{aligned} \tag{3.2.21}$$

where $\mathbf{a}_{1,2}$ are the spins of the SMBHs, q is the mass ratio M_1/M_2, with M_1 and M_2 chosen such that $q \leq 1$, μ is the symmetric mass ratio $q/(q+1)^2$, and $\mathbf{l}$ is the contribution of the orbital angular momentum to the spin angular momentum of the final black hole. It is assumed that the direction of $\mathbf{l}$ is that of the initial orbital angular momentum, while its magnitude is given by:

$$\begin{aligned} |\mathbf{l}| = \frac{s_4}{(1+q^2)^2}(|\mathbf{a}_1|^2 + |\mathbf{a}|_1^2 q^4 + 2|\mathbf{a}_1||\mathbf{a}_2|q^2\cos\phi) + \\ \Big(\frac{s_5\mu + t_0 + 2}{1+q^2}\Big)(|\mathbf{a}_1|\cos\theta + |\mathbf{a}_2|q^2\cos\xi) + \\ 2\sqrt{3} + t_2\mu + t_3\mu^2, \end{aligned} \tag{3.2.22}$$

where $s_4 = -0.129$, $s_5 = -0.384$, $t_0 = -2.686$, $t_2 = -3.454$, $t_3 = 2.353$ are values obtained in Rezzolla et al. (2008). The angles ϕ, θ and ξ are the angles between the spins of the two black holes and their orbital angular momentum, and are given by:

$$\cos\phi = \hat{\mathbf{a_1}} \cdot \hat{\mathbf{a_2}}, \tag{3.2.23}$$

$$\cos\theta = \hat{\mathbf{a_1}} \cdot \hat{\mathbf{l}}, \tag{3.2.24}$$

$$\cos\xi = \hat{\mathbf{a_2}} \cdot \hat{\mathbf{l}}. \tag{3.2.25}$$

When we consider two SMBHs merging, we calculate the angles between the three different vectors by randomly selecting directions for $\mathbf{a_1}$, $\mathbf{a_2}$ and $\mathbf{l}$ uniformly over the surface of a sphere. This prescription makes the assumption that the radiation of gravitational waves does not affect the direction of the orbital angular momentum as the binary orbit shrinks, and we also assume that the mass lost to gravitational radiation is negligible.

3.3 Calculating AGN luminosities

3.3.1 AGN bolometric luminosities

From the mass of gas that is accreted onto the SMBH, we can calculate a radiative bolometric luminosity as follows. The mass accretion rates are calculated for the starburst and hot halo modes in Section 2.7. We then calculate the bolometric luminosity for a thin accretion disc using:

$$L_{\rm bol,TD} = \epsilon_{\rm TD}\dot{M}c^2, \tag{3.3.26}$$

where the radiative efficiency $\epsilon_{\rm TD}$ for the thin disc case depends on the black hole spin, as given by equation (3.2.3). However, the radiative efficiency is not the same for all regimes of the accretion flow. As well as the thin disc and the ADAF case, there are also AGNs accreting above the Eddington accretion rate. Such objects are generally understood to be advection dominated and to have optically thick flows (Abramowicz et al., 1988).

For the ADAF regime we use the expressions for bolometric luminosity from Mahadevan (1997). There are two cases within this regime. For lower accretion rate ADAFs ($\dot{m} < \dot{m}_{\rm crit,visc}$), heating of the electrons is dominated by viscous heating, whereas for higher accretion rate ADAFs ($\dot{m}_{\rm crit,visc} < \dot{m} < \dot{m}_{\rm crit,ADAF}$), the ion-electron heating dominates the heating of the electrons. In the super-Eddington regime, the radiative efficiency is lower than the corresponding thin disc radiative efficiency, and so a super-Eddington luminosity suppression is introduced (Shakura & Sunyaev, 1973). This expression includes a free parameter, $\eta_{\rm Edd}$, the value for which is given in Table 3.1,

Hence, the bolometric luminosities in the model are given by the following expressions[7]. For the low accretion rate ADAF regime, where $\dot{m} < \dot{m}_{\rm crit,visc}$:

$$L_{\rm bol} = 0.0002\epsilon_{\rm TD}\dot{M}c^2\Big(\frac{\delta_{\rm ADAF}}{0.0005}\Big)\Big(\frac{1-\beta}{0.5}\Big)\Big(\frac{6}{\hat{r}_{\rm lso}}\Big), \tag{3.3.27}$$

[7]Note that the coefficients of the ADAF luminosities are derived in Mahadevan (1997) and not free parameters.

where β and $\delta_{\rm ADAF}$ are defined below.

For the higher accretion rate ADAF regime, where $\dot{m}_{\rm crit,visc} < \dot{m} < \dot{m}_{\rm crit,ADAF}$, we have:

$$L_{\rm bol} = 0.2\epsilon_{\rm TD}\dot{M}c^2\Big(\frac{\dot{m}}{\alpha^2_{\rm ADAF}}\Big)\Big(\frac{\beta}{0.5}\Big)\Big(\frac{6}{\hat{r}_{\rm lso}}\Big). \tag{3.3.28}$$

For the thin disc regime, where $\dot{m}_{\rm crit,ADAF} < \dot{m} < \eta_{\rm Edd}$, $L_{\rm bol} = L_{\rm bol,TD}$. Finally, for the super-Eddington regime, where $\dot{m} > \eta_{\rm Edd}$, we have:

$$L_{\rm bol} = \eta_{\rm Edd}(1 + \ln(\dot{m}/\eta_{\rm Edd}))L_{\rm Edd}. \tag{3.3.29}$$

The value of $\eta_{\rm Edd}$ adopted gives a similar luminosity at a given mass accretion rate in the super-Eddington regime to the model of Watarai et al. (2000) who model super-Eddington sources as advection dominated slim discs.

In the above, $\alpha_{\rm ADAF}$ is the viscosity parameter in the ADAF regime (the value is given in Table 3.1). $\delta_{\rm ADAF}$ is the fraction of viscous energy transferred to the electrons (the value is given in Table 3.1). The current consensus for the value of $\delta_{\rm ADAF}$ is a value between 0.1 and 0.5, (cf. Yuan & Narayan, 2014). Therefore, for this study we adopt a value $\delta_{\rm ADAF} = 0.2$, more in line with observational (Yuan et al., 2003; Liu et al., 2013) and theoretical (Sharma et al., 2007) constraints, as opposed to the value of $\delta_{\rm ADAF} = 2000^{-1}$ adopted in Fanidakis et al. (2012). Changing the value of $\delta_{\rm ADAF}$ makes no discernible difference to the luminosity functions shown in this paper. β is the ratio of gas pressure to total pressure (total pressure being the sum of gas pressure and magnetic pressure). Following Fanidakis et al. (2012), we use the relation $\beta = 1 - \alpha_{\rm ADAF}/0.55$, which is based on MHD simulations in Hawley et al. (1995).

The boundary between the two ADAF regimes is:

$$\dot{m}_{\rm crit,visc} = 0.001\left(\frac{\delta_{\rm ADAF}}{0.0005}\right)\left(\frac{1-\beta}{\beta}\right)\alpha^2_{\rm ADAF}, \tag{3.3.30}$$

which is a value chosen so that $L_{\rm bol}$ is continuous in the ADAF regime. The boundary between the ADAF and thin disc regimes is assumed to be $\dot{m}_{\rm crit,ADAF} = 0.01$ (Yuan & Narayan, 2014). $f_{\rm q}$ and $\eta_{\rm Edd}$ are free parameters that we calibrate on observed AGN luminosity functions, as described in Section 3.5.1.

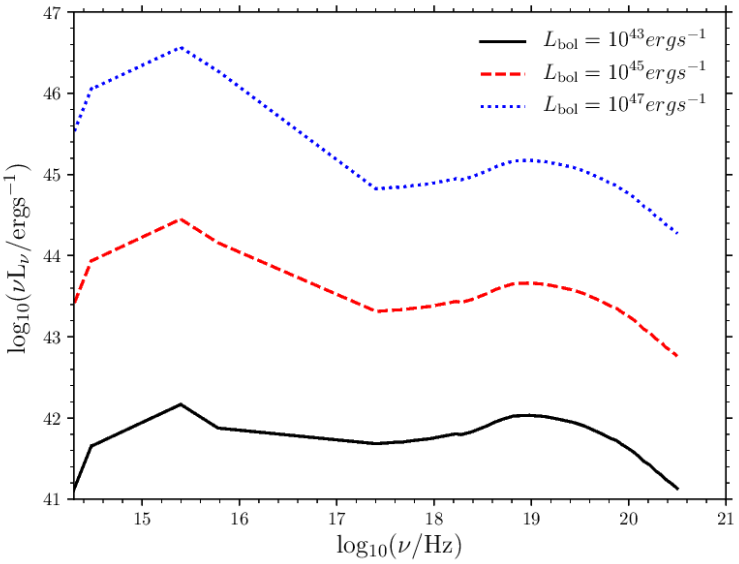

Figure 3.2: The Marconi et al. (2004) SED used for calculating luminosities in different wavebands in this Chapter. Shown is the SED for $L_{\rm bol} = 10^{43}{\rm ergs}^{-1}$ (black solid line), $L_{\rm bol} = 10^{45}{\rm ergs}^{-1}$ (red dashed line) and for $L_{\rm bol} = 10^{47}{\rm ergs}^{-1}$ (blue dotted line).

3.3.2 Converting from bolometric to optical and X-ray AGN luminosities

To convert from AGN bolometric luminosity to luminosities in other wavebands we use bolometric corrections derived from the empirical AGN SED template in Marconi et al. (2004). We show this SED for three different luminosities in Figure 3.2. The rest-frame bolometric corrections calculated from this SED are[8]:

$$\log_{10}(L_{\rm HX}/L_{\rm bol}) = -1.54 - 0.24\mathcal{L} - 0.012\mathcal{L}^2 + 0.0015\mathcal{L}^3, \tag{3.3.31}$$

$$\log_{10}(L_{\rm SX}/L_{\rm bol}) = -1.65 - 0.22\mathcal{L} - 0.012\mathcal{L}^2 + 0.0015\mathcal{L}^3, \tag{3.3.32}$$

[8]Note that equations (3.3.31) and (3.3.32) are corrected from a typographical error in Fanidakis et al. (2012) equation (10).

$$\log_{10}(\nu_B L_{\nu B}/L_{\rm bol}) = -0.80 + 0.067\mathcal{L} - 0.017\mathcal{L}^2 + 0.0023\mathcal{L}^3, \quad (3.3.33)$$

where $\mathcal{L} = \log_{10}(L_{\rm bol}/10^{12}L_{\odot})$, $L_{\rm HX}$ is the hard X-ray (2-10 keV) luminosity, $L_{\rm SX}$ is the soft X-ray (0.5-2 keV) luminosity, $\nu_B = c/4400$Å is the frequency of the centre of the B-band, and $L_{\nu B}$ is the luminosity per unit frequency in the B-band.

To calculate B-band magnitudes we use the expression[9]:

$$M_{B,AB} = -11.33 - 2.5\log_{10}\Big(\frac{\nu_B L_{\nu B}}{10^{40}{\rm ergs}^{-1}}\Big), \quad (3.3.34)$$

for magnitudes in the AB system, from the definition of AB magnitudes (Oke & Gunn, 1983). Using the Marconi et al. (2004) SED template, we convert from rest-frame B-band magnitudes to rest-frame 1500Å band magnitudes using a relation similar to equation (A.2.8) to give:

$$M_{1500,AB} = M_{B,AB} + 0.514. \quad (3.3.35)$$

The Marconi et al. (2004) SED is based on observations of quasars, with the UV part of the SED based on observations at $L_{UV} \sim 10^{42.5-47}{\rm ergs}^{-1}$ and the X-ray part of the SED based on observations at $L_{HX} \sim 10^{41-44}{\rm ergs}^{-1}$. Therefore, this SED is likely to be most appropriate for AGN in the thin disc and super-Eddington regime. For $z > 6$ and for the luminosities that we are considering, the AGN are in the thin disc or super-Eddington regime, so this SED is appropriate, although in future work we plan to include a wider variety of SEDs for AGN in different accretion regimes.

3.3.3 AGN obscuration and unobscured fractions

AGN are understood to be surrounded by a dusty torus, which causes some of the radiation to be absorbed along some sightlines, and re-emitted at longer wavelengths. For simplicity, we assume that at a given wavelength, AGN are either completely obscured or completely unobscured. The effect of obscuration can therefore be

[9]Note that equation (3.3.34) is different to Fanidakis et al. (2012) equation (13), which may have been caused by a typographical error.

expressed as an unobscured fraction (visible fraction), which is the fraction of objects that are unobscured in a certain waveband at a given luminosity and redshift.

The fraction of obscured objects in the hard X-ray band is thought to be small, so for this thesis we assume that there is no obscuration at hard X-ray wavelengths. There is a population of so-called 'Compton-thick' AGNs for which the column density of neutral hydrogen exceeds $N_H \approx 1.5 \times 10^{24}\mathrm{cm}^{-2}$, which is the unit optical depth corresponding to the Thomson cross section. Such objects are difficult to detect, even at hard X-ray wavelengths. The number of such objects is thought to be small, so we ignore their contribution for this thesis.

We calculate the unobscured fractions in the soft X-ray and optical bands using one of three observationally determined empirical relations from the literature, and also two more introduced here.

1. The unobscured fraction of Hasinger (2008) is:

$$f_{\mathrm{vis}} = 1 + 0.281\big[\log_{10}\Big(\frac{L_{\mathrm{HX}}}{10^{43.75}\mathrm{ergs}^{-1}}\Big)\big] - A(z), \tag{3.3.36}$$

where

$$A(z) = 0.279(1+z)^{0.62}. \tag{3.3.37}$$

L_{HX} is the hard X-ray luminosity in the observer frame and z is the redshift[10]. The redshift dependence of the visible fraction in this model saturates at $z \geq 2.06$ and the visible fraction is not allowed to have values below 0 or above 1. Because the observational data on which this obscuration model is based only extend to $z = 2$, we extrapolate the model to $z > 2$ using L_{HX} as the rest-frame hard X-ray band at $z = 2$, i.e. 6-30 keV. For this obscuration model, if an object is obscured at soft X-ray wavelengths, then it is also assumed to be obscured at optical/UV wavelengths.

[10]This empirical model and others we use from observational studies were derived using a slightly different cosmology from the one used in the P-Millennium, for simplicity we ignore the effect of this here.

2. Hopkins et al. (2007) derive an unobscured fraction of the form:

$$f_{\rm vis} = f_{46}\Big(\frac{L_{\rm bol}}{10^{46}{\rm ergs}^{-1}}\Big)^{\beta}, \tag{3.3.38}$$

where f_{46} and β are constants for each band. For the B-band, [f_{46}, β] are [0.260, 0.082] and for the soft X-ray band, [f_{46}, β] are [0.609, 0.063]. This model does not require a high redshift extrapolation, as it depends only on bolometric luminosity.

3. Aird et al. (2015) observationally determine an unobscured fraction for soft X-rays of the form:

$$f_{\rm vis} = \frac{\phi_{\rm unabs}}{\phi_{\rm unabs} + \phi_{\rm abs}}, \tag{3.3.39}$$

where $\phi_{\rm unabs}$, the number density of unabsorbed sources, and $\phi_{\rm abs}$, the number density of absorbed sources, are given by:

$$\phi = \frac{K}{(\frac{L_{\rm HX}}{L_{\star}})^{\gamma_1} + (\frac{L_{\rm HX}}{L_{\star}})^{\gamma_2}}, \tag{3.3.40}$$

where the constants for both cases are given in Table 3.2. As for the Hasinger (2008) obscuration model, if the object is obscured at soft X-ray wavelengths, then we assume that it is also obscured at optical/UV wavelengths. For this obscuration model, we extrapolate to high redshift such that for $z > 3$, the $L_{\rm HX}$ hard X-ray band is the rest-frame band for $z = 3$.

4. We also use unobscured fractions that are modified versions of Hopkins et al. (2007). These unobscured fractions also depend solely on $L_{\rm bol}$, but with different coefficients. These coefficients were derived by constructing a bolometric luminosity function from the luminosity functions at optical, UV, and X-ray wavelengths. We used the Marconi et al. (2004) bolometric corrections and selected coefficients for the visible fraction so as to create a resultant bolometric luminosity function with the scatter between points minimised. This is described in Appendix A.3. The first of these new obscuration relations, the

Table 3.2: The parameters that correspond to the best fit visible fraction from Aird et al. (2015) where $\zeta = \log(1+z)$. These parameter values have been obtained by private communication. See equations (3.3.39) and (3.3.40).

	absorbed	unabsorbed
$\log(\mathrm{K}\ /\mathrm{Mpc}^{-3})$	$-4.48 + 3.38\zeta - 7.29\zeta^2$	$-5.21 + 3.21\zeta - 5.17\zeta^2$
$\log(\mathrm{L}_\star/\mathrm{ergs}^{-1})$	$43.06 + 3.24\zeta - 1.59\zeta^2 + 0.43\zeta^3$	$43.80 - 0.57\zeta + 9.70\zeta^2 - 11.23\zeta^3$
$\log\gamma_1$	$-0.28 - 0.67\zeta$	$-0.44 - 1.25\zeta$
γ_2	2.33	2.32
β_{CT}	0.34	0.34

'low-z modified Hopkins', (LZMH) visible fraction for rest-frame 1500Å has the form:

$$f_{\mathrm{vis,LZMH}} = 0.15\Big(\frac{L_{\mathrm{bol}}}{10^{46}\mathrm{ergs}^{-1}}\Big)^{-0.1}, \tag{3.3.41}$$

and for the soft X-ray band it has the form:

$$f_{\mathrm{SX,LZMH}} = 0.4\Big(\frac{L_{\mathrm{bol}}}{10^{46}\mathrm{ergs}^{-1}}\Big)^{0.1}. \tag{3.3.42}$$

5. The second of these modified Hopkins unobscured fractions, the '$z = 6$ modified Hopkins' (Z6MH) visible fraction was derived by fitting the GALFORM $z = 6$ luminosity functions at 1500Å and in the soft X-ray band to the observational estimates. This visible fraction is:

$$f_{\mathrm{vis,Z6MH}} = 0.04, \tag{3.3.43}$$

for both rest-frame 1500Å and soft X-rays.

3.3.4 Calculating model AGN luminosity functions

Typically when one constructs a luminosity function from a simulation, only the AGNs that are switched on at each snapshot are included. However, if one does this, rarer objects with higher luminosities but which are only active for a short

time are not sampled well. To probe the luminosity function for such objects, we average over a time window, $\Delta t_{\rm window}$. The time window should not be too large, as then we may miss the effect of multiple starbursts within the time window, because the simulation only outputs information on the most recent starburst. We select a time window for which the luminosity function using the time average method is converged to the luminosity function using only the AGNs switched on at the snapshots. For the predictions here we set $\Delta t_{\rm window} = t_{\rm snapshot}/10$, where $t_{\rm snapshot}$ is the age of the Universe at that redshift.

Each object is assigned a weight, w, given by:

$$w = t_Q/\Delta t_{\rm window}, \tag{3.3.44}$$

where $t_Q = f_{\rm q} t_{\rm bulge}$ is the lifetime of the most recent quasar episode occurring within the time interval Δt_{window} as in Section 3.3.1. This weight is then applied to the number densities counting all AGN occurring within the time interval Δt_{window} which then allows us to include higher luminosity events at lower number densities in the luminosity function. We show the effect of changing the value of Δt_{window}, as well as the effect of simply using snapshot quantities on the predicted luminosity functions in Appendix A.4.

3.4 SMBH Masses, accretion rates and spins

We start by showing some basic predictions from the new model for SMBH masses, accretion rates and spins.

3.4.1 Black hole masses

In the left panel of Figure 3.3 we show the black hole mass function at $z = 0$ predicted by our model compared to observational estimates. The observations use indirect methods to estimate the black hole mass function, because of the lack of a large sample of galaxies with dynamically measured black hole masses. In Marconi et al. (2004) and Shankar et al. (2004, 2009) galaxy luminosity/velocity dispersion functions are combined with relations between black hole mass and host galaxy

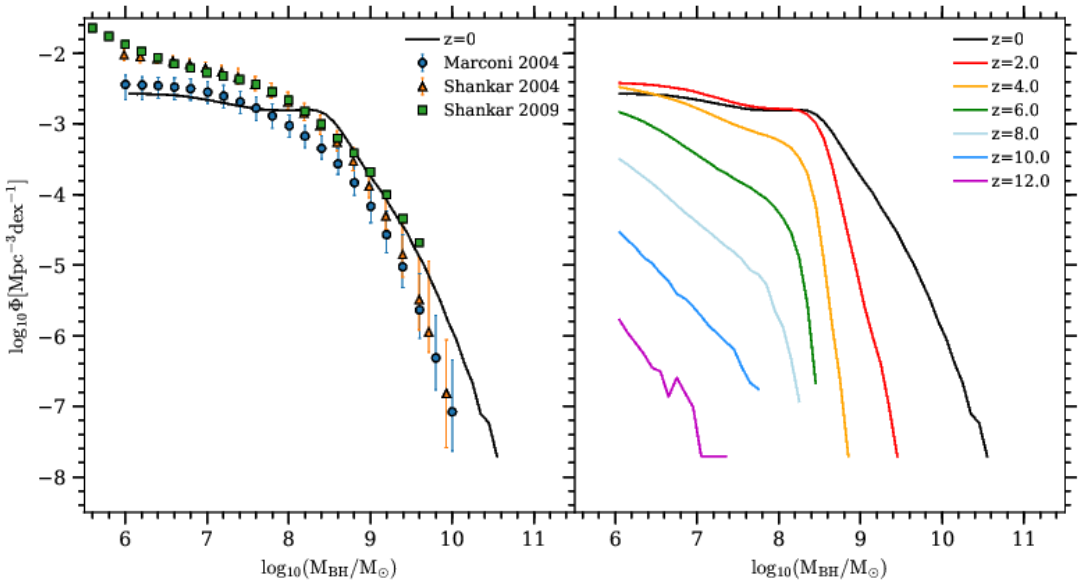

Figure 3.3: The black hole mass function. *Left panel*: the predicted black hole mass function at $z = 0$ compared to observational estimates by Marconi et al. (2004); Shankar et al. (2004, 2009). *Right panel*: the evolution of the black hole mass function over the range $0 < z < 12$.

properties to estimate black hole mass functions. The predictions of the model fit well to the observational estimates within the observational errors, especially given that there will also be uncertainties on the black hole mass measurements and given the discrepancies between the observational estimates. The former means the predictions could still be consistent with observations at the high mass end ($M_{\rm BH} \geq 10^9 M_{\odot}$).

The evolution of the black hole mass function for $0 < z < 12$ is shown in the right panel of Figure 3.3. Most of the SMBH mass is formed by $z \sim 2$, as the mass density of black holes is dominated by objects around the knee of the black hole mass function, and this knee is in place by $z \sim 2$. The dominant fuelling mechanism for growing the black hole mass density across all redshifts is gas accretion in starbursts triggered by disc instabilities, and disc instabilities play an important role in shaping the black hole mass function for $M_{\rm BH} < 10^8 M_{\odot}$. However, SMBH mergers are more important for determining the shape of the black hole mass function for $M_{\rm BH} > 10^8 M_{\odot}$, as they are the mechanism by which the largest SMBHs are formed. AGN feedback also plays an important role in shaping the black hole mass function at this high mass end, by suppressing gas cooling and so slowing down the rate at which the SMBHs grow by cold gas accretion.

In Figure 3.4, we show the 'active' black hole function at $z = 0$ compared to observational estimates from Schulze & Wisotzki (2010). In this observational estimate, active SMBHs are defined as AGN radiating above a certain Eddington ratio ($L_{\rm bol}/L_{\rm Edd} > 0.01$). The flux limit in the observations results in the observational sample being incomplete for $M_{B_J} > -19$. The observational sample also only includes type 1 (unobscured) AGNs. Therefore, we apply these selections to the model predictions, using the LZMH visible fraction, to compare with this observational estimate of the active black hole mass function. We also present predictions where the selection on M_{B_J} has not been applied. The effect of the selection on M_{B_J} can be seen at the low mass end ($M_{\rm BH} < 10^8 M_{\odot}$), where the dashed and solid lines diverge. While the model is in reasonable agreement with the observations at $M_{\rm BH} \sim 10^{8.5} M_{\odot}$, the model generally underpredicts the active black hole mass function, although the model does reproduce the overall shape of the shape of the

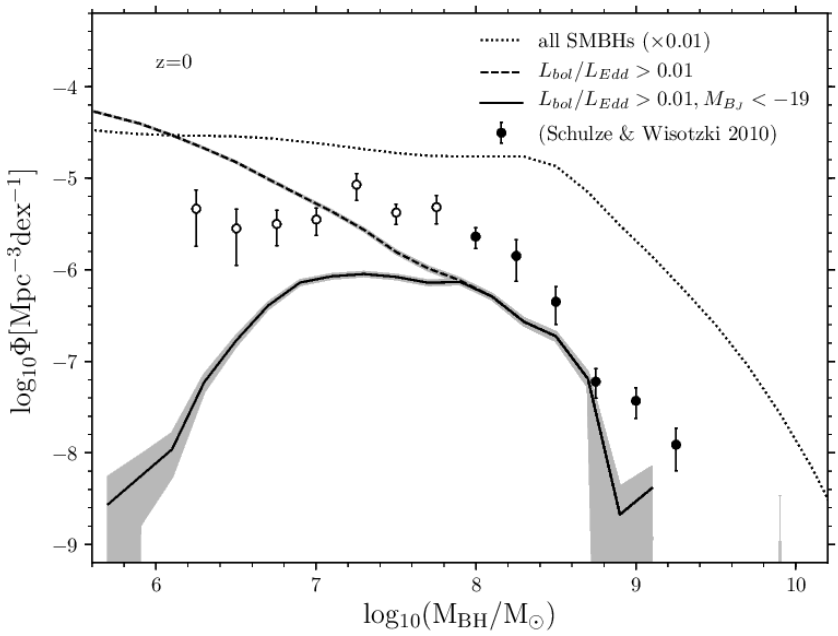

Figure 3.4: The active black hole mass function (solid line) at $z = 0$, compared to observational estimates from Schulze & Wisotzki (2010). We show predictions where active SMBHs are defined as AGNs brighter than a threshold Eddington ratio ($L_{\rm bol}/L_{\rm Edd} > 0.01$), using the LZMH visible fraction (cf. Section 3.3.3) (dashed line), and predictions also brighter than a threshold AGN absolute magnitude ($M_{\rm B_J} < -19$) (solid line). This is for appropriate comparison with the active black hole mass function in Schulze & Wisotzki (2010), where the open circles are the data points that suffer from incompleteness, while the filled circles are the data points that do not. We also show the total black hole mass function (dotted line) with the number density divided by 100, for comparison.

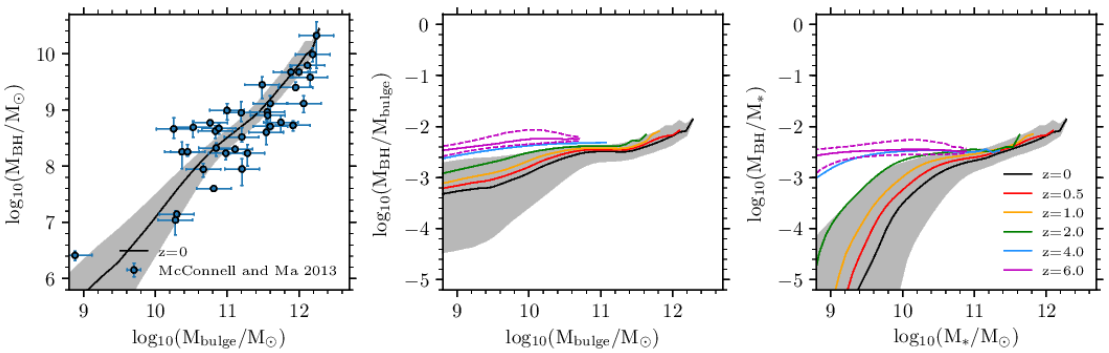

Figure 3.5: *Left panel*: the predicted SMBH mass versus bulge stellar mass relation at $z = 0$ compared to observational data from McConnell & Ma (2013). The line represents the median of the predicted SMBH mass in bins of bulge mass and the shading denotes the 10-90 percentiles of the predicted distribution. *Middle panel*: the evolution of the median of the ratio of SMBH mass to bulge mass versus bulge mass relation with redshift for $z = 0$, 0.5, 1, 2, 4, 6. As in the left panel, the grey shaded band is the 10-90 percentiles of the distribution for $z = 0$ and the purple dashed lines are the 10-90 percentiles of the distribution for $z = 6$. *Right panel*: the evolution of the median of the ratio of SMBH mass to galaxy stellar mass versus galaxy stellar mass relation, with the lines representing the same redshifts as the middle panel as indicated by the legend.

observational active black hole mass function. We found similar results when comparing with other studies, such as those from SDSS (e.g. Vestergaard & Osmer, 2009).

Figure 3.5 shows the relation between SMBH mass and bulge or total stellar mass. In the left panel of Figure 3.5 we show the predicted SMBH mass versus bulge mass relation compared to observational data from McConnell & Ma (2013). The predictions follow the observations well, with the scatter decreasing towards higher masses. BH-BH mergers contribute towards this decrease in scatter, as seen in Jahnke & Macciò (2011), although they are not the only contributing mechanism, with AGN feedback also affecting the scatter at the high mass end.

In the middle panel of Figure 3.5, we show the evolution of the ratio of SMBH mass to bulge mass ($M_{\rm BH}/M_{\rm bulge}$) versus bulge stellar mass for $0 < z < 6$, showing

the scatter of the distribution for $z = 0$ and $z = 6$. As we go to higher redshift, the ratio $M_{\rm BH}/M_{\rm bulge}$ increases, as also seen in observations (e.g. Peng et al., 2006). The ratio $M_{\rm BH}/M_{\rm bulge}$ reflects the mechanism by which these two galaxy components form. At higher redshift, bulges grow mainly by starbursts, which also feeds the growth of SMBHs and so the distribution of the ratio $M_{\rm BH}/M_{\rm bulge}$ peaks at $f_{\rm BH}$ (the fraction of the mass of stars formed in a starburst accreted onto a black hole), with some scatter caused by mergers. At lower redshift the ratio $M_{\rm BH}/M_{\rm bulge}$ decreases, as galaxy mergers cause bulges to form from discs, but without growing the SMBHs. We also note how the scatter of the relation is lower at $z = 6$ than at $z = 0$ for all masses - by $z = 0$ galaxies have had more varied formation histories compared to the $z = 6$ population.

In the right panel of Figure 3.5 we show the evolution of the ratio of the SMBH mass to the galaxy stellar mass ($M_{\rm BH}/M_{\star}$) versus galaxy stellar mass for the redshift range $0 < z < 6$. Galaxies of larger stellar mass and the largest SMBHs form at late times, and at lower masses ($M_{\star} < 10^{11} M_{\odot}$), $M_{\rm BH}/M_{\star}$ is smaller at later times. At lower masses, the ratio $M_{\rm BH}/M_{\star}$ decreases with time because the fraction of the stellar mass that is in the bulge decreases. This evolution slows down at $z < 1$. At higher masses ($M_{\star} > 10^{11} M_{\odot}$), the stellar mass and SMBH mass stay on the same relation independent of redshift. It is in this regime that the AGN feedback is operational: in our model we use the AGN feedback prescription of Bower et al. (2006) in which AGN feedback is only active where the hot gas halo is undergoing 'quasistatic' (slow) cooling. This has the effect that AGN feedback is only active for haloes of mass above $\sim 10^{12} M_{\odot}$. The relation between SMBH mass and stellar mass at this high mass end is caused by both AGN feedback and mergers, with neither mechanism dominant in establishing this relation.

3.4.2 Black hole accretion rates

In Figure 3.6 we show the black hole mass accretion rate distribution, showing its evolution with redshift and split by fuelling modes: the hot halo mode, starbursts triggered by mergers and starbursts triggered by disc instabilities (see Section 2.7). The hot halo mode becomes more dominant at later times, because the hot halo

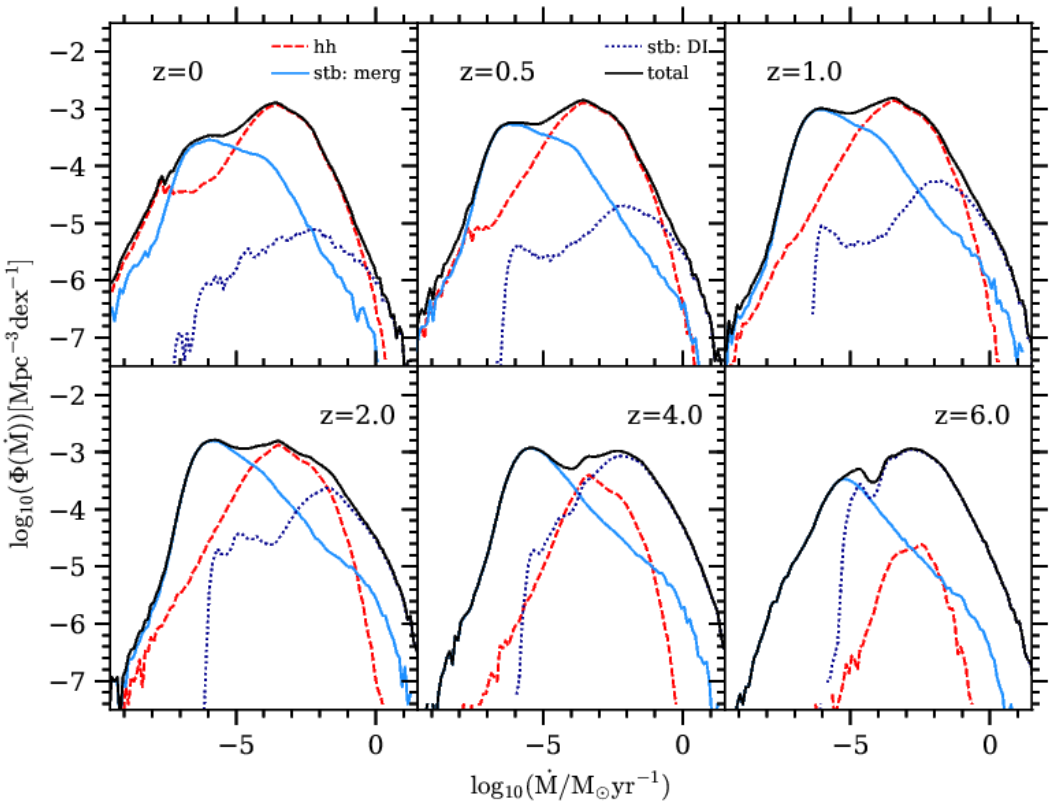

Figure 3.6: The distribution of black hole mass accretion rates for different redshifts (black solid line) split by contributions from hot halo mode (red dashed line), starbursts triggered by mergers (light blue solid line) and starbursts triggered by disc instabilities (dark blue dotted line). We have selected all black holes residing in galaxies of stellar mass, $M_{\star} > 10^{6} M_{\odot}$, which is above the completeness limit of the simulation.

mode requires long cooling times, and hence it occurs for massive haloes, and because dark matter haloes grow hierarchically, these large haloes only form at later times. The contribution from starbursts triggered by galaxy mergers peaks at $z \approx 2$. Starbursts triggered by mergers peak at a low mass accretion rate, as seen in Figure 3.6, albeit with a tail that extends to high $\dot{M}$. The peak at $\dot{M} \sim 10^{-6} M_{\odot}/\mathrm{yr}$ is mostly due to minor mergers with mass ratios $0.05 < M_2/M_1 < 0.3$ (mergers with mass ratios in this range cause about three quarters of the merger triggered starbursts at this mass accretion rate)[11]. These minor mergers involve a relatively small mass of gas, and so the gas mass accreted onto the SMBH is relatively small, leading to these lower mass accretion rates. The location of this peak may be sensitive to the value of f_{burst} adopted (which sets the threshold merger mass ratio for starburst triggering). For a higher value of f_{burst}, the mass accretion rate of this peak would increase. The contribution from starbursts triggered by disc instabilities increases as the redshift increases. Starbursts triggered by mergers typically have lower $\dot{M}$ values than starbursts triggered by disc instabilities. There are two reasons for this. First, the average stellar mass formed by bursts triggered by disc instabilities is higher than for bursts triggered by mergers, and this occurs because the average cold gas mass is higher for galaxies in which bursts triggered by disc instabilities occur. Secondly, the average bulge dynamical timescale for starbursts triggered by disc instabilities is smaller than for those triggered by mergers due to the average bulge size being smaller for starbursts triggered by disc instabilities. The combination of these effects accounts for the lack of starbursts triggered by disc instabilities at the very lowest $\dot{M}$ values. The galaxies that host such starburst episodes would be below the mass at which the simulation is complete.

In Figure 3.7 we show the evolution of the distribution of Eddington normalised mass accretion rate $\dot{M}/\dot{M}_{\mathrm{Edd}}$. We also show the predictions in different stellar mass ranges. Looking at the total distribution ($M_{\star} > 10^7 M_{\odot}$), for increasing redshift, the distribution shifts to somewhat higher values. This is seen as the number of objects with $\log(\dot{M}/\dot{M}_{\mathrm{Edd}}) < -2$ decreasing with increasing redshift, a peak at

[11]Note that a mass ratio of 0.05 is assumed to be the lower threshold for starburst triggering in galaxy mergers (Lacey et al., 2016)

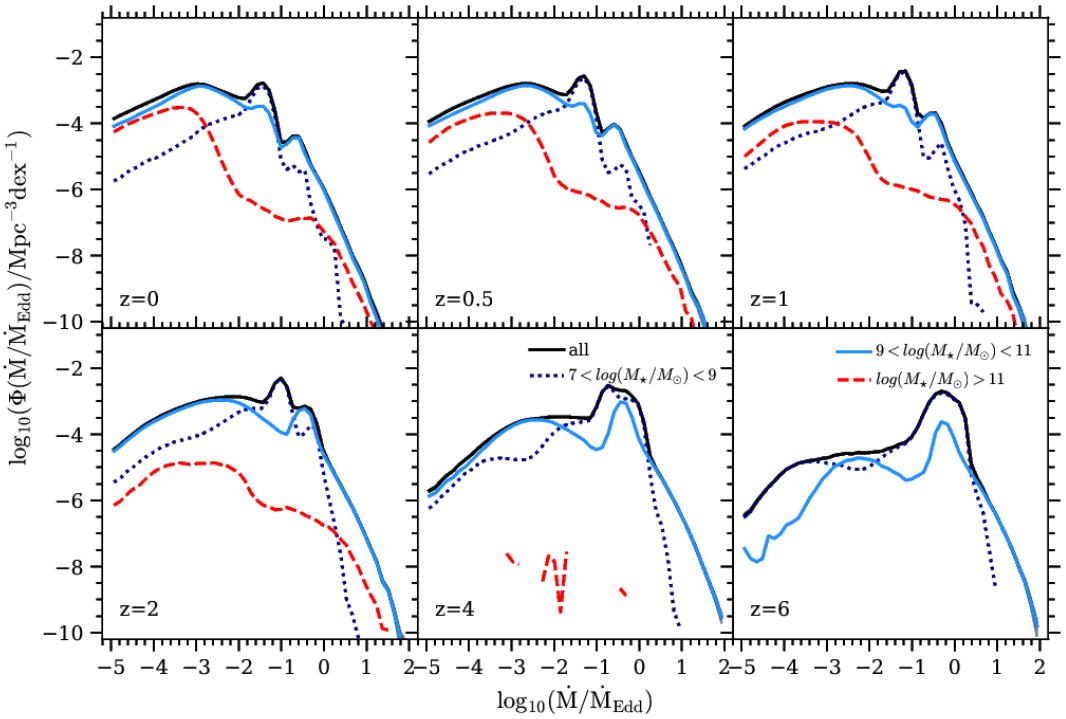

Figure 3.7: The distribution of Eddington ratio in terms of mass accretion rate, $\dot{M}/\dot{M}_{\rm Edd}$, evolving with redshift. Shown are all objects with stellar mass, $M_\star > 10^7 M_\odot$ (black solid line), objects with stellar mass $10^7 M_\odot < M_\star < 10^9 M_\odot$ (dark blue dotted line), objects with stellar mass $10^9 M_\odot < M_\star < 10^{11} M_\odot$ (light blue solid line) and objects with stellar mass $M_\star > 10^{11} M_\odot$ (red dashed line).

$\log(\dot{M}/\dot{M}_{\rm Edd}) \sim -1$ building up with increasing redshift and the number of objects with $\log(\dot{M}/\dot{M}_{\rm Edd}) > 0$ increasing with increasing redshift. The different bins of stellar mass have different distributions of $\dot{M}/\dot{M}_{\rm Edd}$, and evolve differently. At $z = 0$, the lowest bin in stellar mass ($10^7 M_\odot < M_\star < 10^9 M_\odot$) shows a broad distribution around a peak at $\log(\dot{M}/\dot{M}_{\rm Edd}) \approx -1.5$, the middle bin in stellar mass ($10^9 M_\odot < M_\star < 10^{11} M_\odot$) also shows a broad distribution, but with a peak at $\log(\dot{M}/\dot{M}_{\rm Edd}) \approx -3$ and also has features at $\log(\dot{M}/\dot{M}_{\rm Edd}) \approx -1.5$ and $\log(\dot{M}/\dot{M}_{\rm Edd}) \approx -0.5$. The distribution in the highest stellar mass bin ($M_\star > 10^{11} M_\odot$) peaks at lower value of $\log(\dot{M}/\dot{M}_{\rm Edd}) \approx -4$, but has fewer objects at high Eddington ratios than the lower stellar mass bins. The distribution in the highest stellar mass bin peaks at a lower Eddington ratio because this is where the hot halo mode is operational, so SMBHs are typically quiescently accreting.

As redshift increases, the $\dot{M}/\dot{M}_{\rm Edd}$ value of the peak in the $\dot{M}/\dot{M}_{\rm Edd}$ distribution for the lowest stellar mass bin increases, such that by $z = 6$, the peak for the lowest stellar mass bin and the middle stellar mass bin are both at $\log(\dot{M}/\dot{M}_{\rm Edd}) \approx -0.5$. The number of objects in the highest stellar mass bin decreases strongly at high redshift, so the hot halo mode is much less prevalent at higher redshift, $z > 3$.

We also have compared the predicted Eddington luminosity ratio, ($L_{\rm bol}/L_{\rm Edd}$) distribution at $z = 6$, to the observational data compiled in Wu et al. (2015) Figure 4. The $L_{\rm bol}/L_{\rm Edd}$ distribution at $z = 6$ from GALFORM has a median and 10-90 percentiles at $4.3^{+4.3}_{-3.0}$ for AGNs with $L_{\rm bol} > 10^{46}{\rm ergs}^{-1}$ and $8.6^{+3.5}_{-3.5}$ for AGNs with $L_{\rm bol} > 10^{47}{\rm ergs}^{-1}$, whereas the $L_{\rm bol}/L_{\rm Edd}$ median and 10-90 percentiles in Wu et al. (2015) is $1.0^{+1.8}_{-0.4}$ for a mixture of samples with $L_{\rm bol} > 10^{46}{\rm ergs}^{-1}$. The predicted $L_{\rm bol}/L_{\rm Edd}$ are somewhat larger than the observational estimate. One possible reason for the different distributions is systematic uncertainties in the black hole mass estimates in the observations. We plan to conduct a more detailed investigation in future work.

3.4.3 Black hole spins

In Figure 3.8 we show the SMBH spin distribution predicted by the model for both the prolonged and chaotic accretion modes. Note that a here represents the magni-

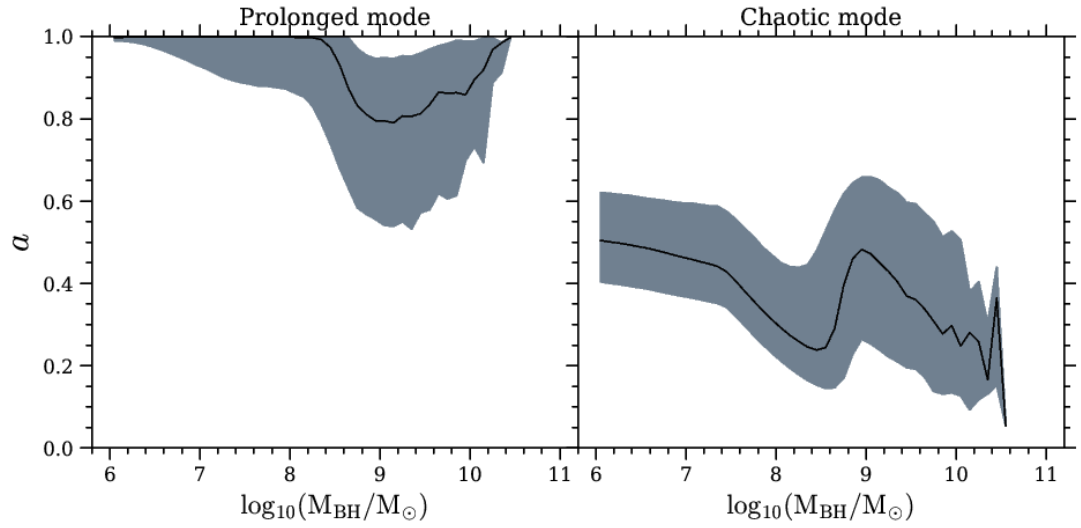

Figure 3.8: The predicted SMBH spin distributions at $z = 0$ for prolonged (left panel) and chaotic (right panel) accretion modes. The line represents the median value of the magnitude of the spin for that SMBH mass, and the shading represents the 10-90 percentile range of the distribution.

tude of the spin. The low mass end of the spin distribution ($6 < \log_{10}(M_{\rm BH}/M_{\odot}) < 8$) is dominated by accretion spinup whereas the high mass end ($8 < \log_{10}(M_{\rm BH}/M_{\odot}) < 10$) is dominated by merger spinup. For prolonged mode accretion, the coherent accretion spinup means that SMBHs quickly reach their maximum spin value, giving rise to a population of maximally spinning SMBHs at low mass. At high masses, the average spin value is lower because of SMBH mergers. This is because even if two maximally spinning SMBHs merge, the result is typically a SMBH with a lower spin value because of misalignment between the black hole spins and the orbital angular momentum. For chaotic mode accretion, the accretion direction is constantly changing and so the accretion spinup leads to SMBHs with lower median spin values ($a \approx 0.4$), compared to prolonged accretion. The spin values are not zero in the chaotic mode, as one may be tempted to expect, because the accretion spinup is more efficient if the accretion disc and SMBH spin are in the same direction compared to the case of anti-alignment (King et al., 2008). The mean value of the SMBH spin decreases with increasing black hole mass at this low mass end, for chaotic mode accretion as also reported in King et al. (2008). At the high mass

end, the increase in average spin at $M_{\rm BH} \sim 10^9 M_\odot$ is due to spinup by BH mergers. Two slowly spinning SMBHs typically form a higher spin SMBH when they merge, due to the angular momentum of the orbit between them.

One of the conclusions of Fanidakis et al. (2011) was that for chaotic mode accretion, smaller SMBHs will have lower spin values ($\bar{a} \approx 0.15$) whereas larger SMBHs will have higher spin values ($\bar{a} \approx 0.7 - 0.8$). Our new analysis predicts that for chaotic mode accretion SMBHs will generally have moderate spin values, $\bar{a} \approx 0.4$, yielding radiative accretion efficiencies of $\epsilon \approx 0.075$, not too dissimilar from the value of $\epsilon \approx 0.1$ required by the Soltan (1982) argument. However, the average radiative accretion efficiency implied by prolonged mode accretion is $\epsilon \approx 0.4$, in tension with the Soltan (1982) argument.

The chaotic mode spin distribution is different to that in Fanidakis et al. (2011) because the equations for SMBH spinup by gas accretion have changed from that paper (causing higher spin values at the low SMBH mass end) and because the directions for the spinup due to SMBH mergers are sampled from the surface of a sphere as opposed to the circumference of a circle, leading to lower spin values at the high SMBH mass end.

We then show the evolution of the SMBH spin distribution for the prolonged and chaotic modes in Figure 3.9. The black hole spin versus black hole mass relation shows negligible evolution for both modes, with the median black hole spin at any black hole mass approximately the same over the range $z = 0 - 6$. For both modes the scatter of the distribution decreases with increasing redshift, with the scatter for the prolonged mode decreasing much more than the scatter for the chaotic mode. For the prolonged mode, by $z = 6$, nearly all of the black holes with $M_{\rm BH} < 10^8 M_\odot$ have the maximal spin permitted by the model. Also, there is a lack of high mass, $M_{\rm BH} > 3 \times 10^8 M_\odot$, black holes at $z = 6$ for both modes. This is due to a low abundance of high mass galaxies at $z = 6$.

We show how typical black holes evolve in the chaotic mode (the standard choice for this analysis) for four different black hole masses in Figures in 3.10 and 3.11. When we generate each black hole history, we only follow the largest progenitor black hole back in time when two or more black holes merge. In the upper panel of

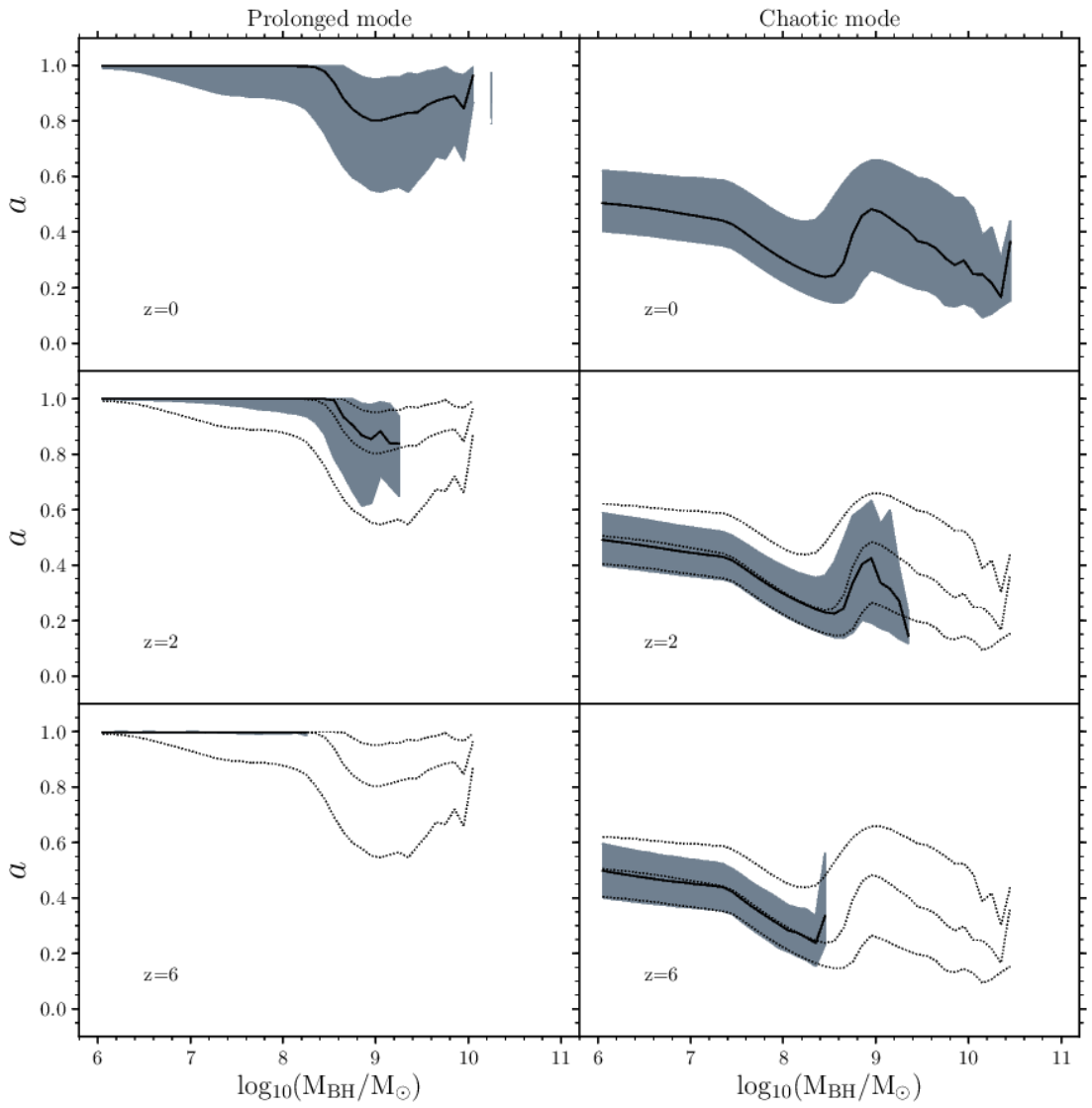

Figure 3.9: The predicted evolution of the SMBH spin distribution for prolonged mode (left panels) and chaotic mode (right panels). Results are shown for $z = 0, 2, 6$. The lines and shading have the same meaning as in the previous figure, with the dotted line representing the median and percentiles for that accretion mode at $z = 0$.

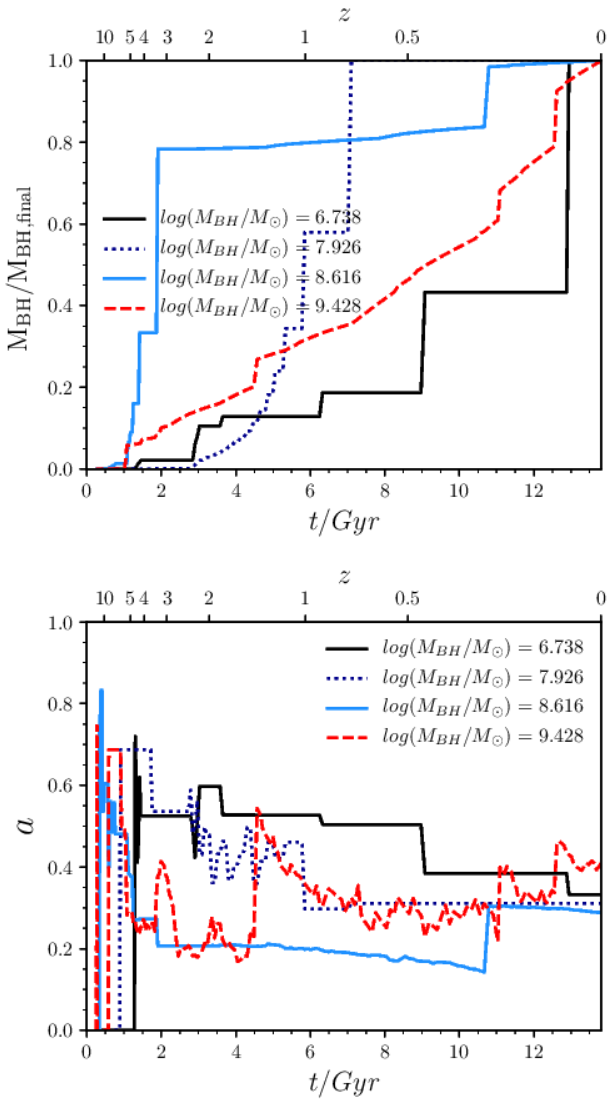

Figure 3.10: *Upper panel:* the evolution of the ratio of SMBH mass to the SMBH at $z = 0$ versus time. *Lower panel:* the evolution of SMBH spin versus time. In both panels we show examples of SMBHs with $z = 0$ masses of $M_{\rm BH} = 5.47 \times 10^6 M_\odot$ (black solid line), $M_{\rm BH} = 8.43 \times 10^7 M_\odot$ (dark blue dotted line), $M_{\rm BH} = 4.13 \times 10^8 M_\odot$ (light blue solid line), $M_{\rm BH} = 2.68 \times 10^9 M_\odot$ (red dashed line). The same objects are plotted in both panels.

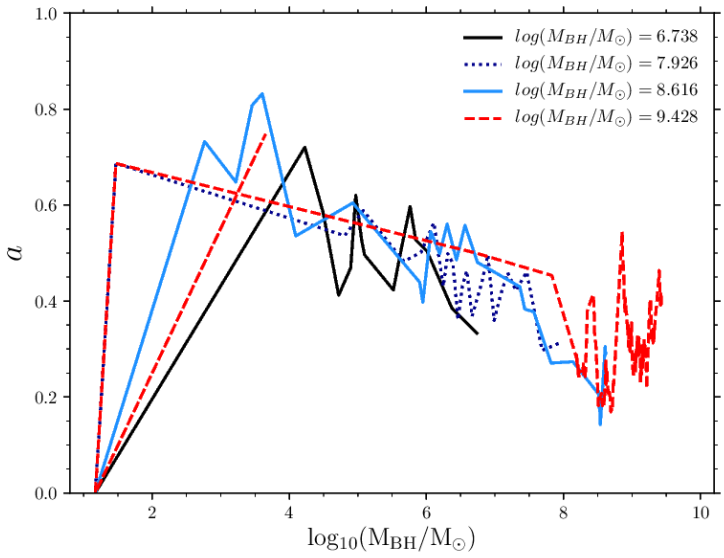

Figure 3.11: The evolution of four different mass SMBHs through the spin versus mass plane. The final SMBH masses at $z = 0$ are the same as plotted in Figure 3.10.

Figure 3.10 we show the evolution of the black hole mass through time evolution for these objects, where the time is measured from the Big Bang. Some of the features discussed for the black hole mass function in Figure 3.3 can be seen here, such as how most of the SMBH mass is assembled at early times, and how the very largest black holes build up gradually at late times. It can also be seen how the larger SMBHs generally grow their mass quickest, with smaller SMBHs generally growing later. This is seen in Figure 3.10 where the SMBH of mass $M_{\rm BH} = 5.47 \times 10^6 M_\odot$ reaches 40% of its final mass at 9 Gyr, whereas the SMBH of mass $M_{\rm BH} = 8.43 \times 10^7 M_\odot$ reaches 60% of its final mass at 6 Gyr, and the SMBH of mass $M_{\rm BH} = 4.13 \times 10^8 M_\odot$ reaches 80% of its final mass at 2 Gyr. However, the SMBH of mass $M_{\rm BH} = 2.68 \times 10^9 M_\odot$ grows more gradually.

In the lower panel of Figure 3.10 we show the evolution of SMBH spin through time. SMBHs of different masses generally show the same trends as their spin evolves through time. At early times, the black holes are smaller and so the spin values will change dramatically (with a changing between 0 and 0.8) if there is an accretion or merger event, whereas at later times, the spin values do not change as dramatically

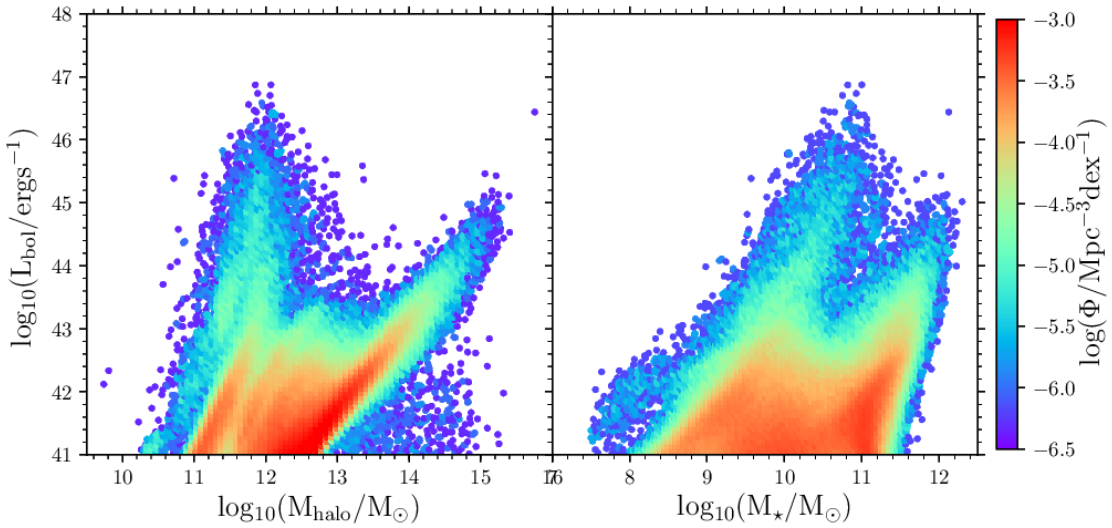

Figure 3.12: *Left panel:* a scatter plot of AGN bolometric luminosity versus halo mass at $z = 0$. The points are coloured by the density of objects in this plane, where red indicates a high density of objects while blue indicates a low density of objects. *Right panel:* as in the left panel but showing bolometric luminosity versus stellar mass.

(a only varies by about 0.1 for each event) with time. The spin values generally converge on a moderate value ($a \approx 0.2 - 0.6$) at late times.

In Figure 3.11, we show the evolution of the black holes through the spin versus mass plane. First, the black holes are spun up to high spins by mergers at small masses. Then the black holes of different masses generally show a similar evolution through the spin versus black hole mass plane as they evolve from high spins at lower black hole masses to lower spins at higher black hole masses, as they accrete gas by chaotic mode accretion. For the two largest black hole masses, there is an additional feature, as the black hole spin increases at the very highest masses. This is a result of the black holes merging with other black holes following their host galaxies merging.

3.4.4 AGN luminosities and black hole/galaxy properties

Before comparing the predicted AGN luminosity functions to observational estimates, we first show the dependence of AGN luminosities on some different galaxy

properties.

First in the left panel of Figure 3.12, we show the dependence of bolometric luminosity on halo mass, where the points are coloured by the density of points. Each halo mass can host an AGN up to $L_{\rm bol} \sim 10^{44}{\rm ergs}^{-1}$, with the brightest AGN not residing in the largest haloes, but instead in haloes of mass $M_{\rm halo} \sim 10^{12} M_{\odot}$. This is a result of how in the model, AGN activity is inhibited in the largest haloes due to AGN feedback (cf. Fanidakis et al., 2013a). The overall distribution is bimodal, which is a result of the two primary fuelling modes. The AGN at $M_{\rm halo} \lesssim 10^{12.5} M_{\odot}$ are mostly fuelled by starbursts triggered by disc instabilities, whereas the AGN at $M_{\rm halo} \gtrsim 10^{12.5} M_{\odot}$ are mostly fuelled by hot halo mode accretion. AGN fuelled by starbursts triggered by mergers make a minor contribution to both parts of this distribution. Hot halo mode accretion fuels the objects at the peak of the 2D distribution in this plane seen at $M_{\rm halo} \approx 10^{13} M_{\odot}$ and $L_{\rm bol} \approx 10^{42}{\rm ergs}^{-1}$. The peak of the distribution of objects fuelled by starbursts triggered by disc instabilities is at $M_{\rm halo} \approx 10^{11.5} M_{\odot}$ and $L_{\rm bol} \approx 10^{43.5}{\rm ergs}^{-1}$, while the peak in the distribution for starbursts triggered by mergers is at $M_{\rm halo} \approx 10^{11.5} M_{\odot}$ and $L_{\rm bol} \approx 10^{42}{\rm ergs}^{-1}$.

In the right panel of Figure 3.12, we show the dependence of bolometric luminosity on stellar mass. There is more of a correlation between bolometric luminosity and stellar mass than between bolometric luminosity and halo mass. The brightest AGN in the model do not live in the largest stellar mass galaxies, but rather reside in galaxies of $M_{\star} \sim 10^{11} M_{\odot}$. This distribution also shows a bimodality, where generally the objects at lower masses ($M_{\star} < 3 \times 10^{10} M_{\odot}$) are fuelled by the starburst mode, while objects at higher masses ($M_{\star} > 3 \times 10^{10} M_{\odot}$) are fuelled by the hot halo mode, although there is some overlap between the two. For the starburst mode, the peak of the distribution for starbursts triggered by disc instabilities and the peak of the distribution for starbursts triggered by mergers are both at stellar mass $M_{\star} \approx 3 \times 10^{9} M_{\odot}$. This peak is at $L_{\rm bol} \approx 10^{43}{\rm ergs}^{-1}$ for disc instabilities, whereas for mergers this peak is at $L_{\rm bol} \approx 10^{42}{\rm ergs}^{-1}$. Starbursts triggered by mergers do also occur for galaxies of stellar mass $M_{\star} > 10^{11} M_{\odot}$, whereas starbursts triggered by disc instabilities do not occur for galaxies of this mass.

In Figure 3.13, we show the dependence of AGN bolometric luminosity on the

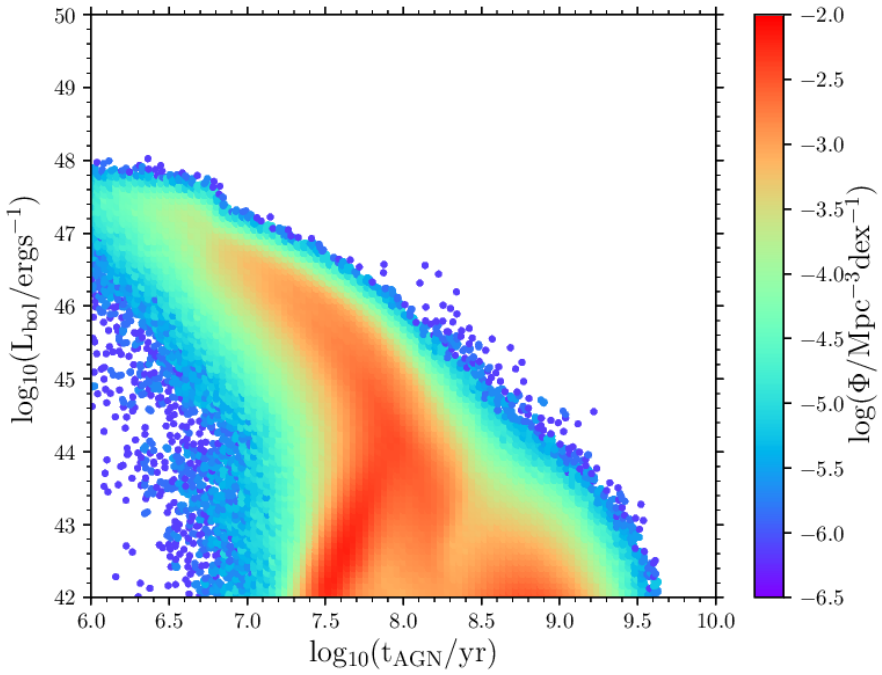

Figure 3.13: As in Figure 3.12 but showing the dependence of AGN bolometric luminosity on the duration of the AGN episode, for starburst mode fuelled AGN only.

duration of the AGN episode. The distribution peaks at $t_{\rm AGN} \approx 10^{7.5}$ yr and $L_{\rm bol} \approx 10^{42}{\rm ergs}^{-1}$, with objects with luminosities $L_{\rm bol} < 10^{44}{\rm ergs}^{-1}$ having a wide range of durations of the AGN episodes. However, the brightest objects at $L_{\rm bol} \approx 10^{48}{\rm ergs}^{-1}$ all have durations of $t_{\rm AGN} \approx 10^{6}$ yr with an anti-correlation between duration of the AGN episode and the AGN luminosity. This anti-correlation arises because in general, shorter AGN epsiodes lead to higher AGN luminosities.

3.5 Evolution of the AGN luminosity function at $z < 6$

We first discuss the evolution of the predicted AGN luminosity function, as it is the simplest to predict, and then the AGN luminosity functions at different wavelengths, which depend on bolometric and obscuration corrections.

3.5.1 Bolometric luminosity function

We present the predicted bolometric luminosity function compared to our observationally estimated bolometric luminosity function constructed from multiwavelength data. This observationally estimated bolometric luminosity function is described in Appendix A.3, and is compared to other observational estimates in Appendix A.3.

The model for SMBH evolution and AGN luminosity also involves some free parameters additional to those in the galaxy formation model, as shown in Table 3.1. We have calibrated the values of $f_{\rm q}$ and $\eta_{\rm Edd}$, and found that the best-fitting values are those adopted in Fanidakis et al. (2012). We show the effect of varying these parameters in Figures A.9 and A.10. We also slightly adjust the values of $\alpha_{\rm ADAF}$ and $\alpha_{\rm TD}$ from 0.087 to 0.1. This is for simplicity and to keep the values in line with MHD simulations (e.g. Penna et al., 2013). The value of $\delta_{\rm ADAF}$ has been updated from Fanidakis et al. (2012) (cf. Section 3.3.1)

In Figure 3.14, the predictions (where the black line is the sum of the contributions from all accretion modes) compare well to the observational bolometric luminosity function across the range of redshifts and for the luminosities shown.

Exceptions include the faint end at high redshift where the model overpredicts the observations by 0.5 dex for $L_{\rm bol} < 10^{46}{\rm ergs}^{-1}$ for $z > 4$, and the faint end at low redshift where the model underpredicts the observations for $L_{\rm bol} < 10^{45}{\rm ergs}^{-1}$ and $z < 0.5$ by 0.5 dex. The underpredictions at the faint end at low redshift may be because the ADAF radiative accretion efficiency is lower than the thin disc accretion efficiency, leading to lower luminosities (see Figure A.13 for a prediction using only a thin disc accretion efficiency for all values of $\dot{m}$). Alternatively, this discrepancy might be resolved by assuming an accretion timescale with a dependence on accreted gas mass or black hole mass. For a different model, Shirakata et al. (2018) obtain a better fit to the hard X-ray luminosity function at low luminosity and low redshift by doing this. In general, our model is a good match to these observations across a broad range.

We also show in Figure 3.14 the separate contributions to the AGN luminosity function from ADAFs ($\dot{m} < \dot{m}_{\rm crit,ADAF}$), thin discs ($\dot{m}_{\rm crit,ADAF} < \dot{m} < \eta_{\rm Edd}$) and super-Eddington objects ($\dot{m} > \eta_{\rm Edd}$). At low redshift, ADAFs dominate the faint end ($L_{\rm bol} < 10^{44}{\rm ergs}^{-1}$), thin discs dominate at intermediate luminosities ($10^{44}{\rm ergs}^{-1} < L_{\rm bol} < 10^{46}{\rm ergs}^{-1}$) and super-Eddington objects dominate the bright end ($L_{\rm bol} > 10^{46}{\rm ergs}^{-1}$). As we go to higher redshift, the ADAFs contribution to the luminosity function decreases: for $0 < z < 2$ the evolution is not that strong, although the contribution from ADAFs at each luminosity decreases slightly as we increase z in this range, whereas for $z > 2$, the evolution in the ADAF population is pronounced, and the number of ADAFs drops off sharply with increasing redshift. In contrast, the contribution from the thin disc population increases until $z \approx 2$, after which it remains approximately constant. At $z < 2$, there are not very many super-Eddington objects and so they make a fairly small contribution to the luminosity function but their contribution increases at $z > 2$. The distribution of super-Eddington objects is bimodal, and for $z < 4$, the higher luminosity peak has a higher number density, while for $z > 4$, the lower luminosity peak has a higher number density. The bimodality is not due to the bimodality in the fuelling modes, as all the super-Eddington objects are fuelled by starbursts triggered by disc instabilities, but it seems to be caused by a bimodality in the bulge stellar mass. We

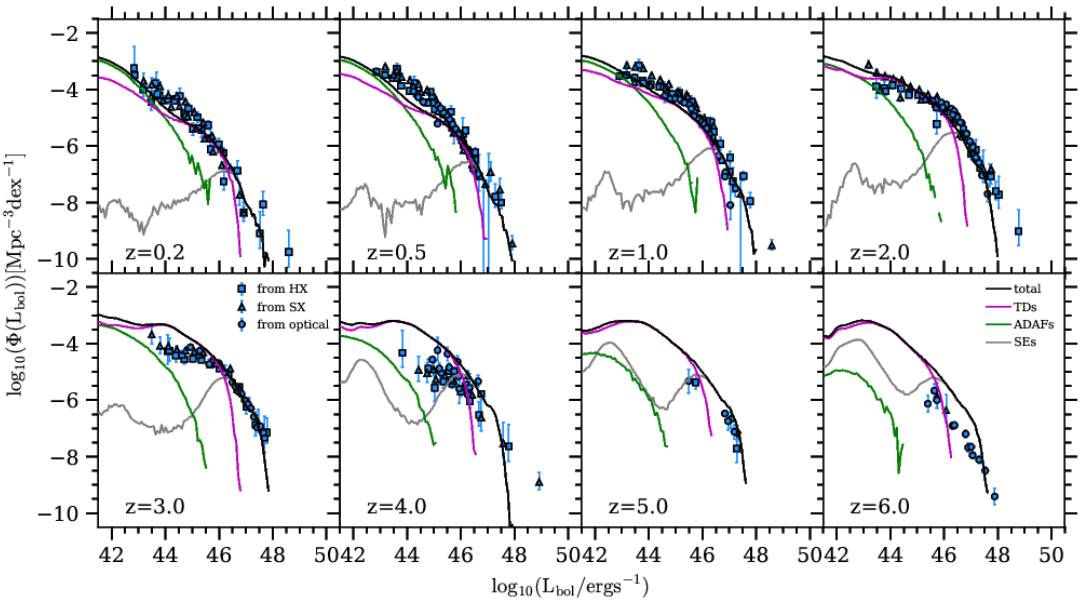

Figure 3.14: The AGN bolometric luminosity function predicted by our model (black line, with grey shading showing the Poisson errorbars) compared to our bolometric luminosity function constructed from the observations. We show the observational data indicating the wavelength of the data that was used to construct that particular point (squares - hard X-ray, triangles - soft X-ray, circles - optical). We split the total bolometric luminosity function by accretion mode into ADAFs (green), thin discs (purple) and super-Eddington objects (grey)

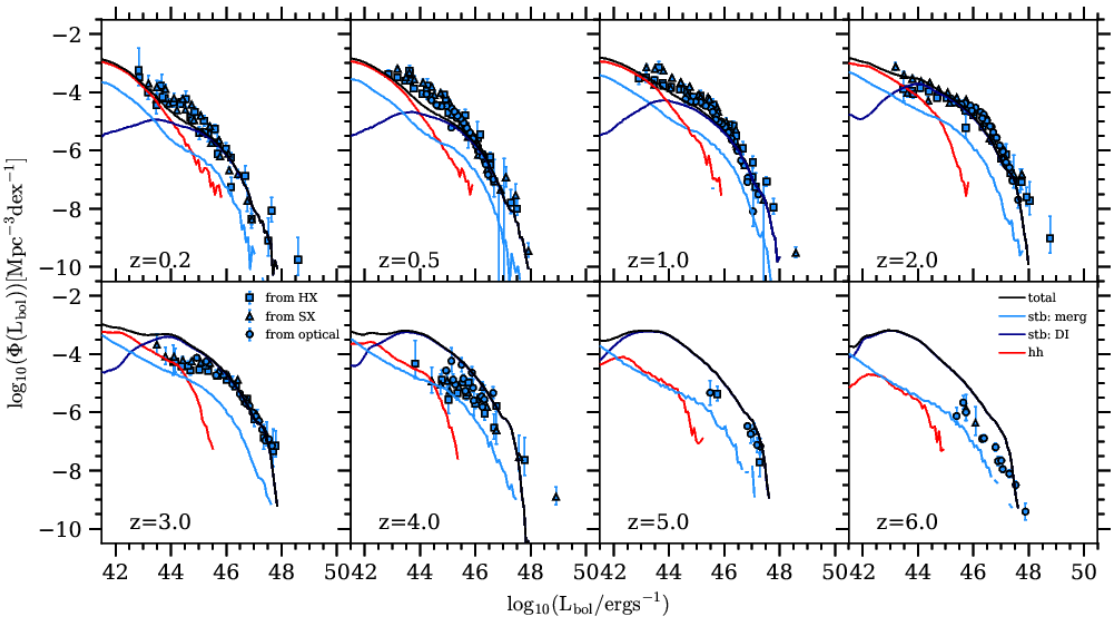

Figure 3.15: The AGN bolometric luminosity function as Figure 3.14, but split by the fuelling mode: starbursts triggered by mergers (light blue), starbursts triggered by disc instabilities (dark blue), hot halo mode (red).

plan to explore this issue in more detail in future work.

In Figure 3.15 we split the AGN luminosity function by contributions from the hot halo mode, starbursts triggered by mergers and starbursts triggered by disc instabilities. At low redshift ($z < 2$), the faint end is dominated by the hot halo mode, whereas the bright end is dominated by starbursts triggered by disc instabilities. Starbursts triggered by mergers make a small contribution to the AGN bolometric luminosity function at low redshift. Starbursts triggered by disc instabilities typically have higher values of $\dot{M}$ and so higher luminosities compared to starbursts triggered by mergers, which is why they dominate the bright end.

The hot halo mode only operates in the most massive haloes, and so it only begins to significantly contribute to the AGN luminosity function for $z < 3$. The hot halo mode does not strongly evolve for $0 < z < 2$. For $z > 2$, starbursts triggered by disc instabilities dominate the AGN luminosity function, with starbursts from mergers not significantly contributing. This implies that the inclusion of black hole growth via disc instabilities is significant for reproducing AGN luminosity functions

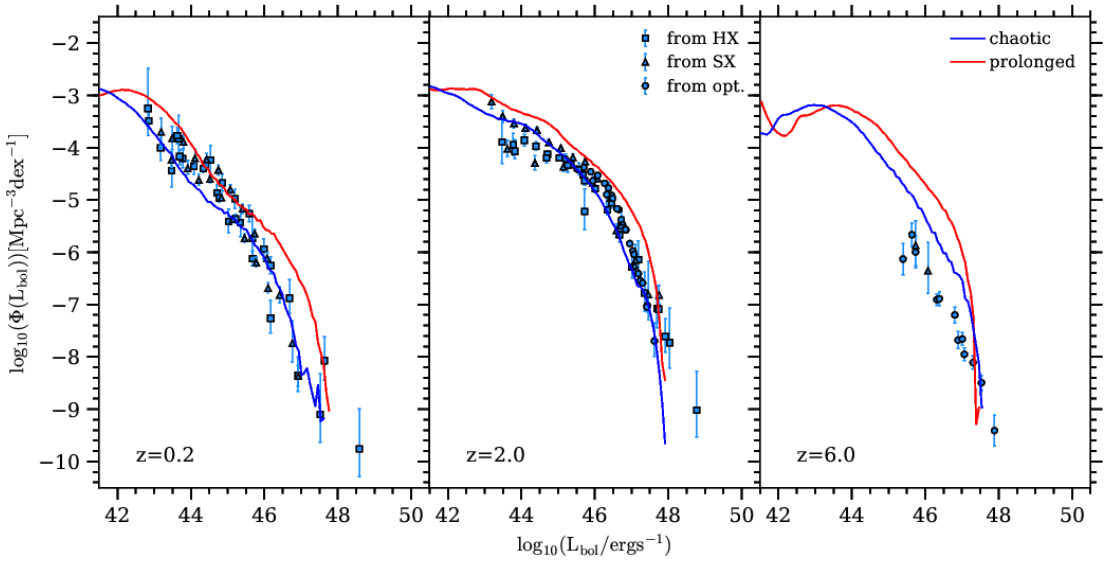

Figure 3.16: The effect of changing between chaotic (blue) and prolonged (red) mode on the AGN bolometric luminosity function at $z = 0.2, 2, 6$.

at high redshift.

A key aspect of the success of the GALFORM AGN model is the different channels of black hole growth, particularly the inclusion of disc instability triggered starbursts, that allow a good match to the AGN luminosity functions to be obtained. Other semi-analytic models do not necessarily include disc instabilities, which may explain why they do not reproduce AGN properties particularly well at high redshift (e.g. Bonoli et al., 2009; Menci et al., 2013; Neistein & Netzer, 2014; Enoki et al., 2014). The effect of disc instabilities on the AGN predictions at $0 < z < 6$ is shown in Figure A.11 and the effect on galaxy properties is shown in Lacey et al. (2016).

We show the effect on the AGN bolometric luminosity function of changing between chaotic mode (our standard choice) and prolonged mode in Figure 3.16. In the prolonged mode, SMBH spins are generally higher (see Figure 3.8), which results in a higher radiative accretion efficiency leading to higher bolometric luminosities.[12]

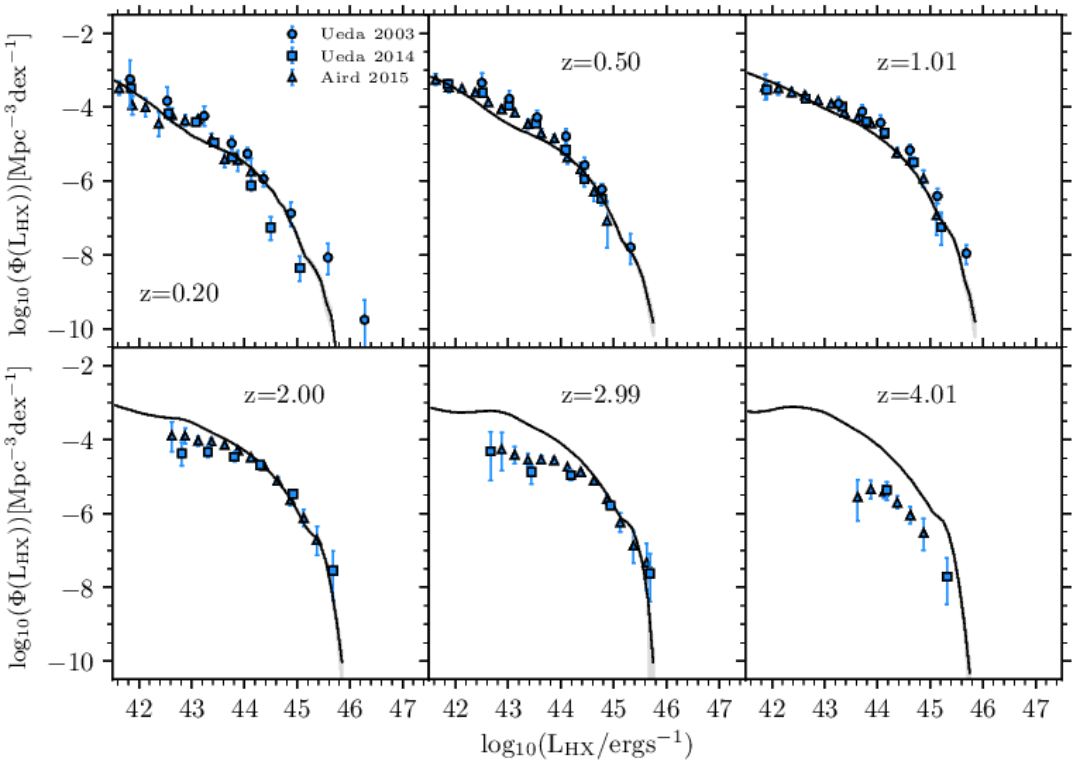

Figure 3.17: The rest-frame hard X-ray luminosity function predicted by the model (black line) compared to observational studies from Ueda et al. (2003) (circles), Ueda et al. (2014) (squares) and Aird et al. (2015) (triangles).

3.5.2 Luminosity functions at different wavelengths

We use the SED template described in Section 3.3.2 and visible fractions described in Section 3.3.3 to make predictions for the luminosity function in the rest-frame hard X-ray, soft X-ray and 1500Å bands. In Figure 3.17 we compare our hard X-ray predictions to observational data. The model is generally in good agreement with the observational data, particularly in the range $1 < z < 3$. For $L_{\rm HX} < 10^{44}{\rm ergs}^{-1}$ at $z < 0.5$, the model underpredicts the observations by about 0.5 dex, and for $L_{\rm HX} < 10^{44}{\rm ergs}^{-1}$ at $z > 3$, the model overpredicts the observations by about 1 dex. The former discrepancy corresponds to the model bolometric luminosity function underpredicting the observations in the same redshift and luminosity regime, and the latter also cooresponds to the bolometric luminosity function slightly overpredicting the observational estimates in that regime, but may also be influenced by our assumption that there is no obscuration for hard X-ray sources. This assumption may be not valid for the high redshift Universe; more observations are needed to constrain the obscuration effect on hard X-rays.

Our soft X-ray predictions are compared to observations in Figure 3.18. The predicted luminosity function without taking into account obscuration is shown alongside the model with the visible fractions of Hopkins et al. (2007), Hasinger (2008), Aird et al. (2015) and our observationally determined LZMH model. The luminosity functions with different visible fractions are very similar except for $L_{\rm SX} < 10^{44}{\rm ergs}^{-1}$. The LZMH model fits best to the observations in the range $1 < z < 2$. At higher redshifts and lower luminosities the visible fraction in the Hasinger (2008) model drops to zero, which causes the corresponding drop off in the luminosity function for that obscuration model.

Our 1500Å predictions are shown in Figure 3.19 compared to observational estimates. These have been converted to 1500Å - the conversions made are detailed in Appendix A.2. There is a strong dependence of the predictions on the assumed obscuration model. Our predictions are a good fit to observations at $z \approx 2$ if we adopt the Hasinger (2008) visible fraction, whereas our observationally determined

[12]Note that the shape of the luminosity function changes little between the two models.

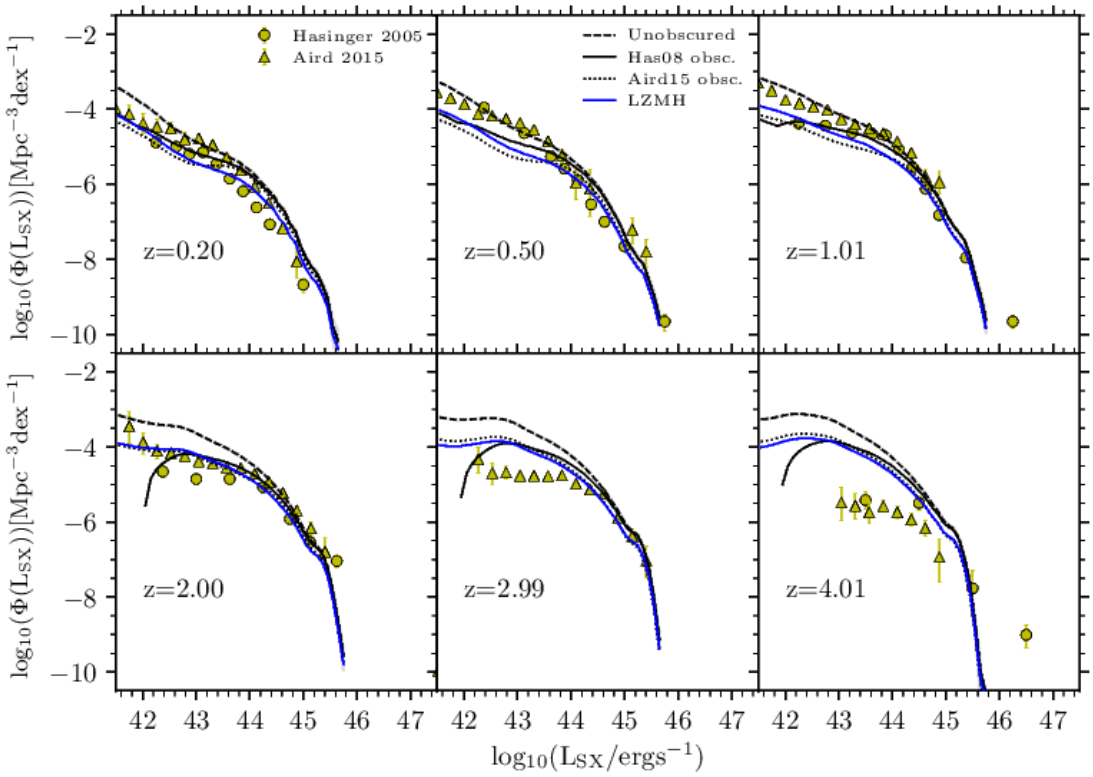

Figure 3.18: The predicted rest-frame soft X-ray luminosity function compared to observations. The dashed black line shows the prediction without accounting for absorption effects, the solid black line is the prediction using the Hasinger (2008) visible fraction, the dotted black line is using the Aird et al. (2015) visible fraction and the blue line is using our observationally determined LZMH visible fraction. The observations are Hasinger et al. (2005) (circles) and Aird et al. (2015) (triangles).

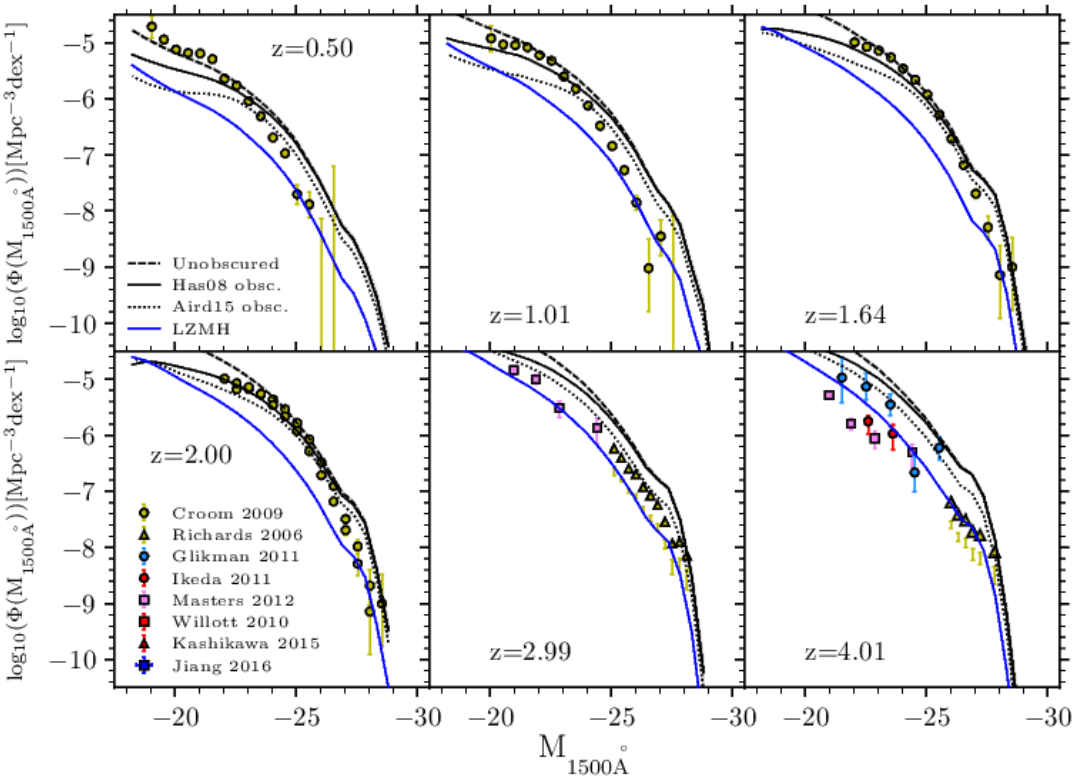

Figure 3.19: The predicted rest-frame 1500Å luminosity function compared to observations which have been converted to 1500Å. The dashed black line is the prediction without accounting for absorption effects, the solid black line is the prediction with the Hasinger (2008) visible fraction, the dotted black line is with the Aird et al. (2015) visible fraction and the blue line is with my observationally determined LZMH visible fraction. The observations are from SDSS DR3 Richards et al. (2006) (yellow triangles), 2SLAQ+SDSS Croom et al. (2009) (yellow circles), CFHQS+SDSS Willott et al. (2010) (red squares), NDWFS+DLS Glikman et al. (2011) (blue circles), the COSMOS field Ikeda et al. (2011) (red circles), Masters et al. (2012) (purple squares), Subaru Kashikawa et al. (2015) (red triangles) and SDSS Stripe 82 Jiang et al. (2016) (blue squares).

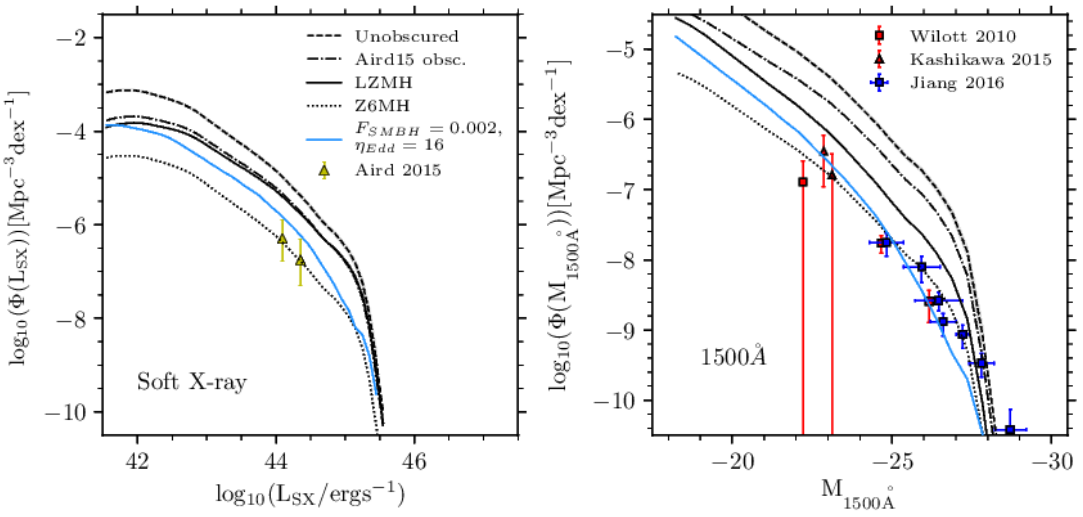

Figure 3.20: The rest-frame soft X-ray luminosity function (left panel) and the rest-frame 1500Å luminosity function (right panel), both at $z = 6$. We show predictions without obscuration (dashed black), with the Aird et al. (2015) visible fraction (dot-dash), with the 'low z modified Hopkins' (LZMH) visible fraction with the standard model (black solid), with the '$z = 6$ modified Hopkins' (Z6MH) visible fraction (black dotted) and with the 'low z modified Hopkins' visible fraction with the different parameters (blue solid). The observations for the soft X-ray band are from Aird et al. (2015) (yellow triangles), and for 1500Å are from Willott et al. (2010) (red squares), Kashikawa et al. (2015) (red triangles) and Jiang et al. (2016) (blue squares).

LZMH model fits best for $z \approx 4$. The reason for this difference is likely to be because Hasinger (2008) fitted their obscuration model at lower redshift whereas we are trying to fit for $z = 0 - 6$ with our LZMH visible fraction. Therefore, unsurprisingly, the different visible fractions are likely to fit better in different redshift ranges.

We present the soft X-ray and optical luminosity functions at $z = 6$ in Figure 3.20. The predicted soft X-ray luminosity function exceeds the observations at $z = 6$ as a result of the model bolometric luminosity function overpredicting the observations. For the optical luminosity function, while the model gives an acceptable fit to observations of the optical luminosity function at $z = 4$, it overpredicts the number of AGN compared to the observed luminosity function at $z = 6$. This is a

result of the model not strongly evolving in the redshift interval $z = 4 - 6$, while the observations indicate a stronger evolution in this redshift interval (Jiang et al., 2016). These discrepancies could be due to a variety of reasons. We suggest two possible explanations for this discrepancy and two corresponding variants on the model which provide a better fit to the observations at $z = 6$.

First, the discrepancy could be due to the obscuration model. At $z = 6$ the visible fraction is not constrained by any observations, and so in Figure 3.20 we present predictions with a lower visible fraction at $z = 6$, which give a better fit to the $z = 6$ optical luminosity function. We show predictions for the standard model with two obscuration models: the LZMH visible fraction and the Z6MH visible fraction (cf. Section 3.3.3). The Z6MH visible fraction needed to fit $z = 6$ is about a quarter of the LZMH visible fraction at $z < 6$. Thus $z > 6$ QSOs could be much more obscured than $z < 6$ QSOs.

Secondly, the discrepancy could be due to black hole accretion being less efficient at high redshift. While the model for black hole accretion has been calibrated at low redshift, the conditions for black hole accretion could be different at higher redshift. We therefore present a model with parameters that have been modified compared to the original calibration on observed data at low redshift. We change the parameter $f_{\rm BH}$, which sets the fraction of mass accreted onto a black hole in a starburst event and the parameter $\eta_{\rm Edd}$, which controls the degree of super-Eddington luminosity suppression. In the fiducial model, $f_{\rm BH} = 0.005$ and $\eta_{\rm Edd} = 4$. $f_{\rm BH} = 0.002$ and $\eta_{\rm Edd} = 16$ give a better fit to the observations of the 1500Å luminosity function at $z = 6$ in Figure 3.20. However, we note that $\eta_{Edd} = 16$ means that there is very little super-Eddington luminosity suppression, whereas the 'slim disc' model for super-Eddington sources predicts significant super-Eddington luminosity suppression. We refer to this model as the 'low accretion efficiency model'. In this model we use the LZMH visible fraction.

Both of these alternative models are in better agreement with observations of the 1500Å AGN luminosity function at $z = 6$ than our standard model, and so we will use them in the next Chapter investigating AGNs observed in future surveys.

3.5.3 Comparison with hydrodynamical simulations

An alternative theoretical approach for simulating galaxy formation is hydrodynamical simulations. A few of these simulations have been used to make predictions for the evolution of AGN luminosity functions through time. We give a brief comparison to some of these here.

The bolometric luminosity function predicted by the model in Hirschmann et al. (2014) over the redshift range $0 < z < 5$ is shown in their Figure 8. When compared to Hopkins et al. (2007), their model is a good fit to the observations at $z = 0.1$, but overpredicts the observations at the faint end at $z = 2$, and underpredicts the observations at $z = 5$. When comparing their results to the model presented here (cf. Figure 3.14), our model agrees similarly well with the observations for $z < 2$, and with better agreement to the observations for $z > 2$. For example, at $z = 4$, at $L_{\rm bol} = 10^{46}{\rm ergs}^{-1}$ (around the knee of the luminosity function at this redshift), our model agrees within 0.5 dex with the observed bolometric luminosity function, whereas the model of Hirschmann et al. (2014) underpredicts the observed bolometric luminosity function by 1 dex at this redshift and luminosity. The hard X-ray luminosity function predicted by EAGLE in Rosas-Guevara et al. (2016) is compared to the observational estimate of Aird et al. (2015) over the redshift range $0 < z < 5$ in their Figure 7. Their model fits well to the observations at $z = 0$, but by $z = 1$, the slope of the luminosity function in their paper is steeper than the observations. The model here is in similar agreement for $z < 1$, and in better agreement with the observations for $z > 1$. For example, at $z = 2$, at $\log(L_{\rm HX}) = 10^{44}{\rm ergs}^{-1}$ (around the knee of the luminosity function at this redshift), our model agrees within 0.5 dex with the observations, whereas the model of Rosas-Guevara et al. (2016) underpredicts the observations by about 1 dex. Finally, Weinberger et al. (2018) compare the bolometric luminosity function from IllustrisTNG to Hopkins et al. (2007) in the redshift range $0 < z < 5$. Their model underpredicts the observations at the faint and bright end of the bolometric luminosity function and overpredicts the observations at intermediate luminosities at $z = 0.5$, and overpredicts the observations at all luminosities at $z = 3$. Around the knee of the luminosity function at $z = 3$ ($L_{\rm bol} = 3 \times 10^{46}{\rm ergs}^{-1}$), our model agrees within 0.5 dex with the observations,

whereas the model of Weinberger et al. (2018) overpredicts the observations by 0.5 dex.

Overall, the AGN luminosity functions from the hydrodynamical simulations do not agree as well to the observational estimates as this model. The reasons for the differences in the AGN luminosity functions may be because the black hole mass accretion rates are calculated differently - in these simulations the Bondi-Hoyle approximation is used, as opposed to the calculation in Section 3.3.1 used in this Chapter.

3.6 Conclusions

In this Chapter we have presented predictions for SMBH and AGN properties from the model for $z < 6$, compared to a variety of observations. The model predictions are consistent with both the observed black hole mass functions and SMBH mass versus bulge mass correlations. We present the spin distribution of SMBHs in the simulation, for the chaotic and prolonged modes of accretion, and their evolution for $0 < z < 6$. The median SMBH spin in both the chaotic and prolonged modes evolves very little. For the prolonged mode, the scatter in the SMBH spin distribution decreases with increasing redshift. We also present examples of the evolution of spin and mass for typical SMBHs, and find that for most masses the evolution is similar, except at the highest masses, $M_{\rm BH} > 10^8 M_{\odot}$, where mergers cause the SMBHs to be spun up to higher spin values.

We compare the AGN luminosity functions in the redshift range $0 < z < 6$ to a wide range of observations at different wavelengths. The model is in good agreement with the observations. We split the luminosity functions by accretion mode (ADAFs, thin discs, super-Eddington objects) and by fuelling mode (hot halo or starbursts triggered by disk instabilities or mergers) to see the relative contributions. At low redshifts, $z < 2$, and low luminosities, $L_{\rm bol} < 10^{43}{\rm ergs}^{-1}$, the ADAF contribution dominates but at higher luminosities and higher redshifts, the thin disc and super-Eddington objects dominate the luminosity function. Hot halo mode fuelled accretion dominates at $z < 3$, and $L_{\rm bol} < 10^{44}{\rm ergs}^{-1}$, but at higher redshift and

higher luminosity, starbursts triggered by disc instabilities dominate the luminosity function.

We now extend this SMBH and AGN model within GALFORM to make predictions for $z \geq 7$, for future surveys conducted by space-based telescopes, which we present in the next Chapter.

Chapter 4

Predictions for JWST, EUCLID, ATHENA and Lynx

4.1 Introduction

Recent advances in observational capabilities have allowed us to investigate AGNs in the early Universe more thoroughly than ever before. At optical wavelengths, the Sloan Digital Sky Survey (SDSS, York et al., 2000) initiated the hunt for quasars out to redshift $z \sim 6$ (Fan et al., 2001; Fan et al., 2003; Fan et al., 2004; Jiang et al., 2009). Detections at $z \sim 6$ of fainter quasars have been made by the Canada-France High-z Quasar Survey (CFHQS, Willott et al., 2010), and a quasar has been detected at $z = 7.1$ in the United Kingdom Infrared Deep Sky Survey (UKIDSS, Lawrence et al., 2007) by Mortlock et al. (2011). Currently, the highest redshift quasar known is at $z = 7.64$, as discovered at optical/near-infrared wavelengths by mining three large area surveys (Bañados et al., 2018a), and the same object has also been observed at X-ray wavelengths using Chandra (Bañados et al., 2018b). Recent radio observations using the Giant Metrewave Radio Telescope have also been able to detect AGNs at high redshift, such as a radio galaxy at $z = 5.72$ (Saxena et al., 2018).

At $z \sim 6$, AGNs have been discovered with estimated black hole masses over a billion solar masses (e.g. Willott et al., 2010; De Rosa et al., 2011; Venemans et al., 2013; Wu et al., 2015). How these SMBHs could grow to such large masses

in such a short time is a puzzle. SMBHs grow from seed black holes, which could form from remnants of a first generation of (Population III) stars, or from gas clouds that form supermassive stars that eventually collapse to form a black hole, or from dense star clusters that collapse via stellar dynamical processes (e.g. Volonteri, 2010). These seeds are expected to be of mass $M_{\rm seed} = 10 - 10^5 M_\odot$ depending on the formation mechanism, with the remnants of Population III stars forming light ($\sim 10 - 100 M_\odot$) seeds, gas cloud collapse forming heavy ($\sim 10^{4-5} M_\odot$) seeds, and star cluster collapse forming seeds of intermediate ($\sim 10^3 M_\odot$) mass (Volonteri, 2010). SMBHs can then grow either by accretion of gas or by merging with other SMBHs. To form the observed high redshift SMBHs by gas accretion, these seeds require sustained accretion near the Eddington rate for several hundred Myr, which may be interrupted by feedback effects.

The next decade-and-a-half promise to be exciting for observing the high redshift Universe. The launch of the James Webb Space Telescope (JWST) in 2021 will pave the way for an increased understanding of the $z > 7$ Universe (e.g. Gardner et al., 2006; Kalirai, 2018). JWST, with its 6.5m diameter mirror, will make observations from the optical to mid-infrared (0.6 μm to 30 μm) to probe the earliest galaxies and the stars contained within them. EUCLID, also due for launch in 2021, with a 1.2m diameter mirror, is primarily a cosmology mission with the aim of constraining dark energy, but the surveys it will conduct at optical and near-IR wavelengths (0.5-2 μm) will also be useful for detecting high-redshift quasars (Laureijs et al., 2011). While JWST and EUCLID will probe similar wavelength ranges, the specifications of the missions are different. The sensitivity of JWST is better, but EUCLID will survey much larger areas of sky, which will lead to different samples of AGNs being detected by these two missions, as they will sample AGNs with different luminosities and space densities.

The Advanced Telescope for High-ENergy Astrophysics (ATHENA) (Nandra et al., 2013), scheduled for launch in 2031, will observe the high-redshift Universe at X-ray energies (0.5-10 keV). The Lynx X-ray observatory (The Lynx Team, 2018), which has a proposed launch date in 2035, will also observe the distant Universe at similar energies (0.2-10 keV). The science objectives of both missions include

determining the nature of SMBH seeds and investigating the influence of SMBHs on the formation of the first galaxies. The two missions have different capabilities: ATHENA has a larger field of view and larger effective area (which leads to better instrumental sensitivity) at 6 keV, but a worse angular resolution and lower effective area at 1 keV, compared to Lynx. The improved angular resolution of Lynx results in better sensitivity in practice, as sources that would be affected by source confusion when observed by ATHENA would be unaffected if observed by Lynx. Therefore, the two telescopes will detect different luminosity objects.

We are now entering an era in which the properties of SMBHs in the high redshift Universe ($z > 7$) during the first billion years of its evolution can be robustly probed. By comparing observations with simulations, we can test theoretical models of galaxy formation, and by comparing to the high redshift Universe, we can test these theoretical models in a regime that up to now is poorly constrained.

In this Chapter, we present predictions for the AGN population at $z \geq 7$ for comparison with observations from JWST, EUCLID, ATHENA, and Lynx. This Chapter is structured as follows. In Section 4.2 we outline the slight modification to the model used for this Chapter. In Section 4.3 we present predictions for black hole properties, and in Section 4.4 we present predictions for AGN luminosity functions for $z \geq 7$. In Section 4.5 we present predictions for AGNs detectable by future surveys using JWST, EUCLID, ATHENA and Lynx, and in Section 4.6 we give our conclusions.

4.2 Method

In this Chapter, we are using the same SMBH and AGN model within GALFORM as in Chapter 3, except with one small modification to the bolometric luminosities described below. We also use the three different variants of the model which are introduced at the end of Section 3.5.2 and compared in Figure 3.20. These three variants are (i) the fiducial model using the 'low z modified Hopkins (LZMH) visible fraction, (ii) the fiducial model using the '$z = 6$ modified Hopkins' (Z6MH) visible fraction, and (iii) the 'low accretion efficiency model', which uses the LZMH visible

fraction.

In Chapter 3, we gave the equations for bolometric radiative AGN luminosities in different accretion regimes: i) an Advection Dominated Accretion Flow (ADAF) state accreting via a physically thick, optically thin disc (Narayan & Yi, 1994), ii) a thin disc state accreting via a physically thin, optically thick disc (Shakura & Sunyaev, 1973), and iii) a super-Eddington state accreting via a slim disc (Abramowicz et al., 1988). We use these same equations in this Chapter, except for a slightly modified expression for the luminosity in the super-Eddington regime, where for Eddington normalised mass accretion rates $\dot{m} > \eta_{\rm Edd}(0.1/\epsilon(a))$, the bolometric luminosity is now given by:

$$L_{\rm bol} = \eta_{\rm Edd}\Big(1 + \ln\Big(\frac{\dot{m}}{\eta_{\rm Edd}}\frac{\epsilon(a)}{0.1}\Big)\Big)L_{\rm Edd}, \tag{4.2.1}$$

where $\epsilon(a)$ is the spin-dependent radiative accretion efficiency for a thin accretion disc, a is the dimensionless spin parameter, $\eta_{\rm Edd}$ is a free parameter, $\dot{m} = \dot{M}/\dot{M}_{\rm Edd}$ is the Eddington normalised mass accretion rate, and $L_{\rm Edd}$ is the Eddington luminosity.

4.3 Black hole mass function and accretion rates

In Figure 4.1 we show the black hole mass function predicted by the model over the range $6 < z < 15$. Black holes build up in the model as a result of galaxies forming in dark matter haloes, which build up hierarchically. In the model, for our simulation volume of $(800{\rm Mpc})^3$, some SMBHs of mass $10^8 M_\odot$ have already formed by $z = 9$, but at $z = 6$ there are no SMBHs with masses above $M_{\rm BH} = 3 \times 10^8 M_\odot$. This appears to be in conflict with observations of extremely massive SMBHs at $z = 6$ (e.g. Willott et al., 2010; De Rosa et al., 2011; Venemans et al., 2013; Wu et al., 2015), which find estimated masses up to $\sim (0.3 - 1) \times 10^{10} M_\odot$. The lack of these objects in this simulation may be because high-redshift surveys probe larger volumes than the volume of the simulation box in this thesis (e.g. the total survey volume for Bañados et al. (2018a) is of order 10 Gpc^3 compared to the volume of 0.5 Gpc^3 for this simulation), and so are able to detect rarer objects (e.g. Amarantidis et al., 2019). There are also uncertainties in the observational black hole mass

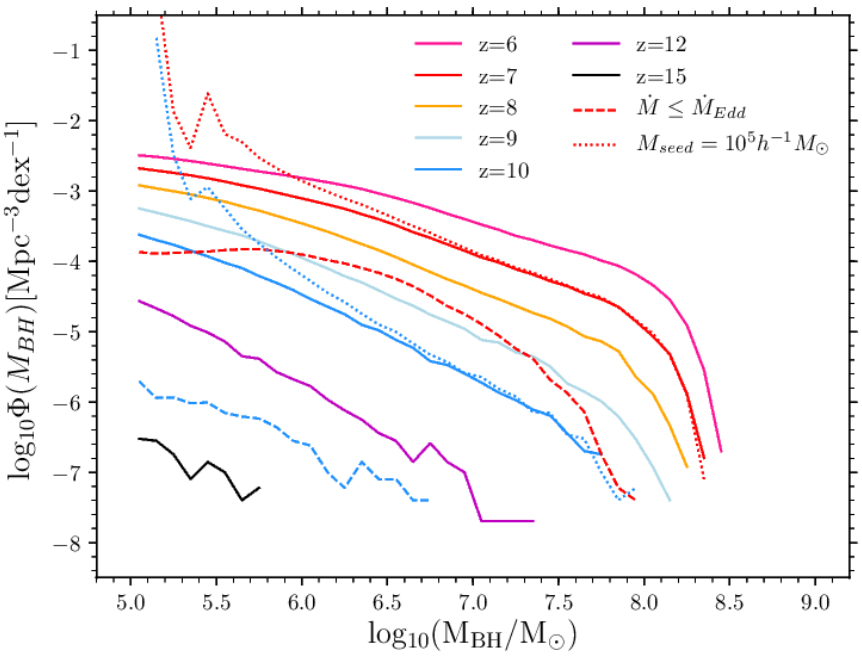

Figure 4.1: The black hole mass function in the fiducial model for $z = 6$ (pink solid line), $z = 7$ (red solid line), $z = 8$ (yellow solid line), $z = 9$ (light blue solid line), $z = 10$ (blue solid line), $z = 12$ (purple solid line), and $z = 15$ (black solid line). We also show the black hole mass functions when the gas accretion rate is not allowed to exceed the Eddington mass accretion rate for $z = 7$ (red dashed line) and $z = 10$ (blue dashed line). We show the black hole mass function for a seed mass of $10^5 h^{-1} M_\odot$, for $z = 7$ (red dotted line) and at $z = 10$ (blue dotted line).

estimates due to the use of observationally calibrated relations to determine black hole masses from observed emission line widths and luminosities. These errors are a mixture of random (these relations have an intrinsic scatter of a factor of about 3 (e.g. Vestergaard & Peterson, 2006)), and systematic (these relations are only constrained for certain luminosity ranges in the local Universe).

We also show in Figure 4.1 the predicted black hole mass function for the case in which gas accretion onto SMBHs in the model is not allowed to exceed the Eddington mass accretion rate (i.e. $\dot{M} \leq \dot{M}_{\rm Edd}$). In our standard model, SMBHs are allowed to accrete mass at super-Eddington accretion rates, and it can be seen that restricting SMBH accretion rates to the Eddington rate results in many fewer high-redshift SMBHs. At $z = 7$, restricting SMBH accretion in this way causes the number of SMBHs to decrease by about 1 dex at $M_{\rm BH} = 10^{6-7} M_{\odot}$, and by about 1.5 dex at $M_{\rm BH} = 10^{5} M_{\odot}$ and 2.5 dex at $M_{\rm BH} = 10^{8} M_{\odot}$. At $z = 10$, the effect of restricting SMBH growth is even more significant, with the number density of SMBHs decreasing by about 2 dex at $M_{\rm BH} = 10^{5-7} M_{\odot}$. This shows the importance of super-Eddington accretion in building up high-redshift SMBHs in our model.

We also show the black hole mass function at $z = 7$ and $z = 10$ when a seed mass, $M_{\rm seed} = 10^{5} h^{-1} M_{\odot}$ is adopted, instead of $M_{\rm seed} = 10 h^{-1} M_{\odot}$ as in the fiducial model. At both of these redshifts, there are a large number of black holes around the seed mass for this case, but at higher masses the black hole mass function converges to the same value as in the fiducial model. This shows how the SMBH masses are relatively unaffected by the choice of seed black hole mass for sufficiently high SMBH mass provided that the gas accretion rate is not Eddington limited.

In Figure 4.2 we show the number of objects as a function of Eddington normalised mass accretion rate ($\dot{M}/\dot{M}_{\rm Edd}$) predicted by the model at $7 \leq z \leq 15$, for SMBHs residing in galaxies with stellar masses above $10^{9} M_{\odot}$ or $10^{10} M_{\odot}$. At each redshift, the distribution is bimodal, with peaks at $\dot{M}/\dot{M}_{\rm Edd} \sim 0.001$, and $\dot{M}/\dot{M}_{\rm Edd} \sim 1$. The peak at $\dot{M}/\dot{M}_{\rm Edd} \sim 1$ is produced by AGNs fuelled by starbursts triggered by disc instabilities. The value of $\dot{M}/\dot{M}_{\rm Edd}$ at this peak increases slightly with redshift, which is a result of galaxy bulges having a smaller dynamical timescale at higher redshift, which results in shorter accretion timescales (cf. equa-

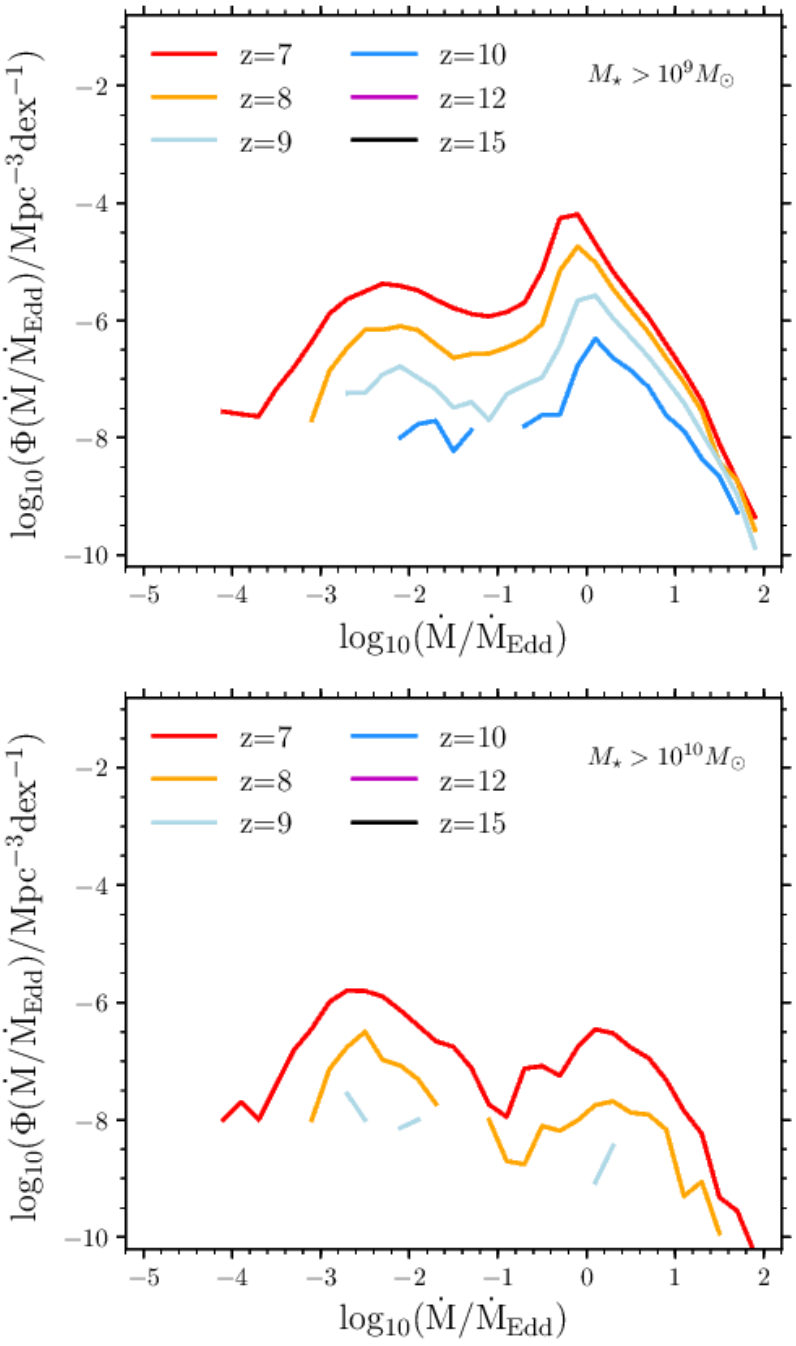

Figure 4.2: The number density of objects as a function of Eddington normalised mass accretion rate, $\dot{M}/\dot{M}_{\rm Edd}$, at $z = 7$ (red), $z = 8$ (yellow), $z = 9$ (light blue), $z = 10$ (dark blue), $z = 12$ (purple), and $z = 15$ (black). Only SMBHs residing in galaxies with stellar masses above $M_\star = 10^9 M_\odot$ are shown in the upper panel, whereas this stellar mass threshold is $M_\star = 10^{10} M_\odot$ for the lower panel.

tion (2.7.25)). Galaxies have lower masses at higher redshift, and so the mass of gas transferred in each disc instability episode is typically smaller at higher redshift, and SMBHs are smaller at higher redshift. The former decreases $\dot{M}/\dot{M}_{\rm Edd}$, while the latter increases $\dot{M}/\dot{M}_{\rm Edd}$, and these effects almost cancel out.

The peak at $\dot{M}/\dot{M}_{\rm Edd} \sim 0.001$ is produced by AGNs fuelled by hot halo accretion. There is also a minor contribution from AGNs fuelled by starbursts triggered by mergers with $\dot{M}/\dot{M}_{\rm Edd}$ values in the range 0.1-1. The peak at $\dot{M}/\dot{M}_{\rm Edd} \sim 1$ has more objects when the stellar mass cut is $10^9 M_\odot$, but the peak at $\dot{M}/\dot{M}_{\rm Edd} \sim 0.001$ has more objects when the stellar mass cut is $10^{10} M_\odot$. This is because AGNs fuelled by starbursts triggered by disc instabilities reside in lower stellar mass galaxies than AGNs fuelled by hot halo accretion. We allow SMBHs to accrete above the Eddington mass accretion rate in our model, and in this figure we see that there are objects that accrete at super-Eddington rates, but none above $\dot{M}/\dot{M}_{\rm Edd} = 100$.

4.4 Evolution of the AGN bolometric luminosity function at $z > 7$

In the left panel of Figure 4.3, we show the evolution of the AGN bolometric luminosity function for the fiducial model for $7 \leq z \leq 15$. As the redshift increases, both the number of objects and the luminosities decrease. By $z \approx 12$, there are almost no objects brighter than $L_{\rm bol} \sim 10^{46}{\rm ergs}^{-1}$ in our simulated volume of $(800{\rm Mpc})^3$.

We have investigated the effects of halo mass resolution on our predictions. In Figure B.1 we show the bolometric luminosity function for the standard model (with a halo mass resolution of $2.12 \times 10^9 h^{-1} M_\odot$) alongside the model with a halo mass resolution of $10^{10} h^{-1} M_\odot$. This comparison shows that the turnover in the bolometric luminosity function at low luminosity is due to halo mass resolution. The bolometric luminosity functions are converged for $L_{\rm bol} > 10^{43}{\rm ergs}^{-1}$.

In Figure B.2, we explore the effect of varying the black hole seed mass on the AGN bolometric luminosity function. We find that the AGN bolometric luminosity function is not sensitive to the choice of seed black hole mass for values in the range $M_{\rm seed} = (10 - 10^5) h^{-1} M_\odot$ for $L_{\rm bol} > 10^{42}{\rm ergs}^{-1}$ at $z = 7$, and for $L_{\rm bol} > 10^{43}{\rm ergs}^{-1}$

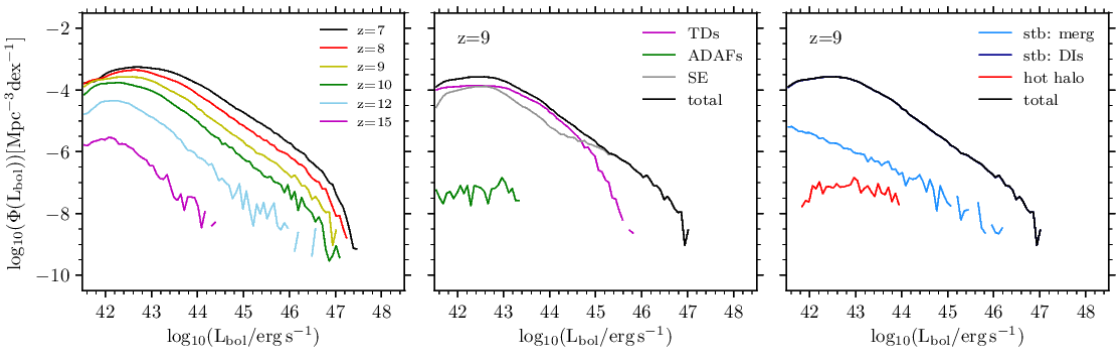

Figure 4.3: The predicted AGN bolometric luminosity function for the fiducial model at high redshift. *Left panel*: The evolution of the bolometric luminosity function for $z = 7$ (black), $z = 8$ (red), $z = 9$ (yellow), $z = 10$ (green), $z = 12$ (light blue), $z = 15$ (purple). The turnover at low luminosity is due to the halo mass resolution. *Middle panel*: The total AGN bolometric luminosity function at $z = 9$ (black) split into ADAFs (green), thin discs (purple) and super-Eddington objects (grey). *Right panel*: The total AGN bolometric luminosity function (black) at $z = 9$ split into objects fuelled by the hot halo mode (red), by starbursts triggered by mergers (light blue) and by starbursts triggered by disc instabilities (dark blue). Note that the dark blue line is under the black line.

at $z = 12$. For luminosities below this, the seed mass does affect the predictions.

In the middle panel of Figure 4.3 we split the AGN luminosity function at $z = 9$ into the contributions from ADAFs, thin discs and super-Eddington objects. Chapter 3 showed that at $z = 0$, the contribution from ADAFs dominates the predicted AGN luminosity function at low luminosities ($L_{\rm bol} < 10^{44}{\rm ergs}^{-1}$), while the contribution from thin discs dominates at intermediate luminosities ($10^{44}{\rm ergs}^{-1} < L_{\rm bol} < 10^{46}{\rm ergs}^{-1}$) and the contribution from super-Eddington objects dominates at high luminosities ($L_{\rm bol} > 10^{46}{\rm ergs}^{-1}$). As redshift increases, the contribution from ADAFs decreases, and the contribution from thin discs dominates at low luminosities, while the contribution from super-Eddington objects continues to dominate at high luminosities. This trend continues for $z > 0$, so that by $z = 9$, the contribution from ADAFs is extremely small. At low luminosities ($L_{\rm bol} < 10^{45}{\rm ergs}^{-1}$), the thin disc contribution just dominates over the contribution from super-Eddington objects, while at higher luminosities super-Eddington objects dominate. This implies that most of the QSOs (with $L_{\rm bol} > 10^{45}{\rm ergs}^{-1}$) that will be detectable by surveys conducted by future telescopes at $z = 9$ should be accreting above the Eddington rate. This prediction is not straightforward to test, as determining Eddington ratios requires estimations of black hole masses. Black hole masses can be estimated from measurements of emission line widths, or black hole masses and mass accretion rates can be determined by fitting theoretical SED models to multi-wavelength data (e.g. Kubota & Done, 2018). The black hole masses estimated using either of these methods will have some model dependencies.

In the right panel of Figure 4.3 we split the AGN luminosity function at $z = 9$ by gas fuelling mode, into hot halo mode, and starbursts triggered by galaxy mergers and disc instabilities. The dominant contributor at all luminosities at $z = 9$ is starbursts triggered by disc instabilities, so we predict that future high-redshift surveys will detect AGNs fuelled by this mechanism. This prediction contrasts with some other theoretical models. Some hydrodynamical simulations predict that gas may be driven into the centres of galaxies by high density cold streams for accretion onto the SMBH (e.g. Khandai et al., 2012; Di Matteo et al., 2017), while some other semi-analytical models simply assume that merger triggered starbursts dominate

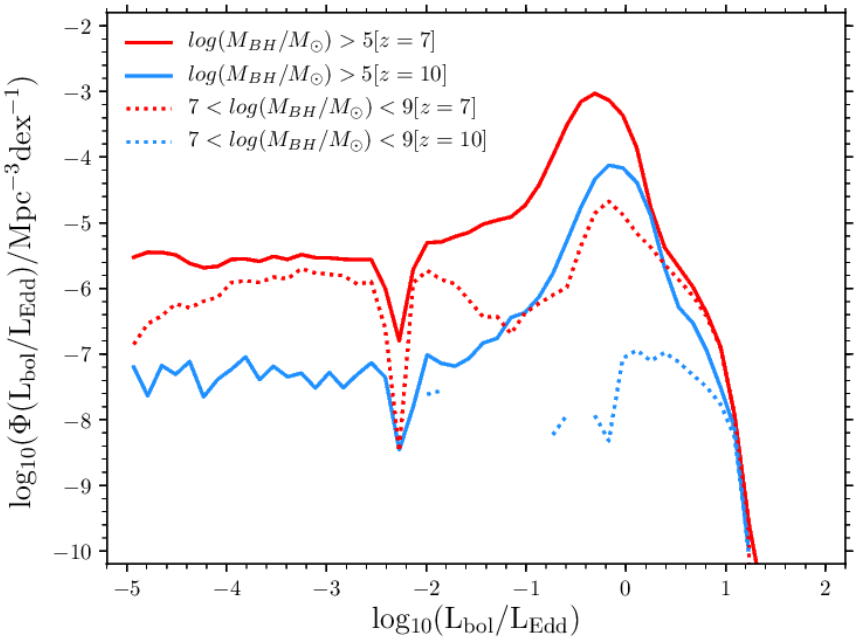

Figure 4.4: The number density of objects as a function of Eddington normalised luminosity, $L/L_{\rm Edd}$, predicted by the model at $z = 7$ (red) and $z = 10$ (blue), for SMBHs with mass $M_{\rm BH} > 10^5 M_\odot$ (solid lines), and for SMBHs with mass $10^7 M_\odot < M_{\rm BH} < 10^9 M_\odot$ (dotted lines).

SMBH growth at high-redshift (e.g. Ricarte & Natarajan, 2018).

In Figure 4.4, we present the number of objects as a function of $L/L_{\rm Edd}$ predicted by the model for $z = 7$ and $z = 10$ for black holes with $M_{\rm BH} > 10^5 M_\odot$. The distributions are flat for $L/L_{\rm Edd} < 0.1$, and peak at $L/L_{\rm Edd} \sim 1$. The $L/L_{\rm Edd}$ value of the peak of the distribution slightly increases with redshift. There are no objects with $L/L_{\rm Edd} > 10$ in our simulated volume at these redshifts, which is a result of there being no objects with $\dot{M}/\dot{M}_{\rm Edd} > 100$ combined with our luminosity suppression for super-Eddington sources (cf. equation (4.2.1)). The sharp dip around $L/L_{\rm Edd} = 0.01$ arises from the thin disc to ADAF transition not being continuous in luminosity.

We also show in Figure 4.4 the distribution of $L/L_{\rm Edd}$ predicted by the model for $10^7 M_\odot < M_{\rm BH} < 10^9 M_\odot$, alongside the distribution for $M_{\rm BH} > 10^5 M_\odot$. At $z = 7$, black holes in these two mass ranges have similar distributions of $L/L_{\rm Edd}$ values, while for $z = 10$, the number of black holes for $10^7 M_\odot < M_{\rm BH} < 10^9 M_\odot$

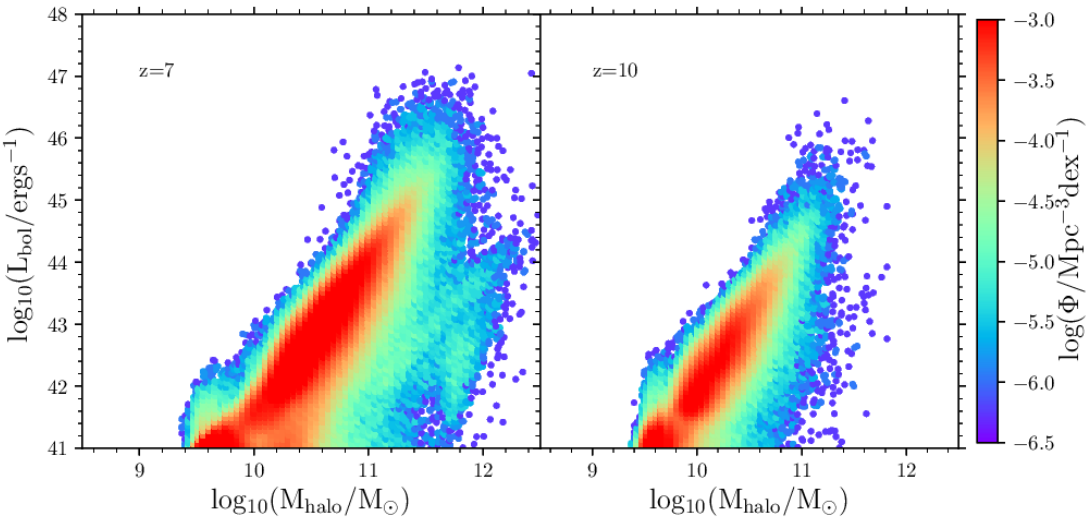

Figure 4.5: A scatter plot of AGN bolometric luminosity versus host halo mass for AGNs at $z = 7$ (left panel) and $z = 10$ (right panel). The colour indicates the number density of objects.

in our simulation is too small to draw any strong conclusion on the form of this distribution.

In Figure 4.5, we present the AGN bolometric luminosity versus host halo mass for objects in the model, colour-coded by the number density of objects. The objects mostly follow a relation between bolometric luminosity and halo mass, although there are some objects offset from this relation to higher halo masses at $z = 7$, but not at $z = 10$. The objects on the main relation are fuelled by starbursts triggered by disc instabilities, whereas the objects offset from the main relation at higher halo masses are fuelled by hot halo mode accretion. The brightest AGNs are not hosted by the most massive haloes at $z = 7$, but at $z = 10$ the brightest AGNs are hosted by the most massive haloes.

4.5 Predictions for high redshift surveys with future telescopes

We next employ our model to make predictions for the detection of AGNs at $z \geq 7$ with the future telescopes described in the Introduction. We use luminosity func-

Table 4.1: The sensitivities and solid angles covered by the possible surveys by JWST, EUCLID, ATHENA and Lynx. For ATHENA and Lynx, the survey area is assumed is that of a single field of view, whereas for JWST and EUCLID the survey area is assumed to be that of multiple fields of view. The integration time is the total for a survey in that band. For ATHENA and Lynx, the flux limits used are the estimated confusion limits. These flux limits, f_ν, can be related to apparent AB magnitudes by: $m_{\rm AB} = 31.40 - 2.5\log_{10}(f_\nu/{\rm nJy})$.

Instrument	Filter	$\lambda(\mu{\rm m})$ or E(keV)	Flux Limit	Survey Area	Assumed total integration time (ks)
JWST NIRCam	F070W	$0.6 - 0.8$ μm	22.5 nJy	9680 arcmin^2 (1000 FoVs)	10000
	F200W	$1.7 - 2.3$ μm	9.1 nJy	9680 arcmin^2 (1000 FoVs)	10000
	F444W	$3.8 - 5.1$ μm	23.6 nJy	9680 arcmin^2 (1000 FoVs)	10000
EUCLID (Deep Survey)	VIS	$0.55 - 0.9$ μm	91.2 nJy	40 deg^2 (70 FoVs)	$\sim$ 13000
	H	$1.5 - 2$ μm	145 nJy	40 deg^2 (70 FoVs)	$\sim$ 13000
EUCLID (Wide Survey)	VIS	$0.55 - 0.9$ μm	575 nJy	15000 deg^2 (26000 FoVs)	$\sim$ 120000
	H	$1.5 - 2$ μm	912 nJy	15000 deg^2 (26000 FoVs)	$\sim$ 120000
ATHENA WFI	Soft X-ray	$0.5 - 2$ keV	2.4×10^{-17}erg cm^{-2}s^{-1}	1600 arcmin^2 (FoV)	450
	Hard X-ray	$2 - 10$ keV	1.6×10^{-16}erg cm^{-2}s^{-1}	1600 arcmin^2 (FoV)	450
Lynx	Soft X-ray	$0.5 - 2$ keV	7.8×10^{-20}erg cm^{-2}s^{-1}	360 arcmin^2 (FoV)	15000
	Hard X-ray	$2 - 10$ keV	1.0×10^{-19}erg cm^{-2}s^{-1}	360 arcmin^2 (FoV)	15000

tions predicted by the model in the different wavelength or energy bands of these telescopes to predict the number of AGNs that should be detectable by surveys with these telescopes. We also describe the typical properties of the SMBHs detectable by the different telescopes. The survey parameters that we assume for JWST[1], EUCLID[2], ATHENA[3], and Lynx[4] are summarised in Table 4.1.

The number of AGNs detectable in a survey depends on both the flux limit and the survey area. The former affects the ability to detect low luminosity sources and the latter affects the number density of objects down to which one can probe. In practice, the emission from the host galaxy is likely to provide a more fundamental AGN luminosity limit for these surveys, but for this analysis we only consider the survey limitations.

From the predicted flux limits of the surveys, luminosity limits can be derived using $L = 4\pi d_{\rm L}^2 f$ for calculating broadband luminosities (ATHENA and Lynx) and $L_\nu = 4\pi d_{\rm L}^2 f_\nu/(1+z)$ for calculating a luminosity per unit frequency (EUCLID and JWST). Here, f is the flux, f_ν is the flux per unit frequency and $d_{\rm L}$ is the luminosity distance to the source, L is the luminosity in the rest-frame band or wavelength corresponding to the observed band or wavelength, and L_ν is the luminosity per unit frequency in the rest frame corresponding to the observed wavelength and redshift. We use these expressions to calculate luminosity limits (vertical lines) in Figures 4.6 to 4.11.

The luminosities shown in Figures 4.6 to 4.11 have been k-corrected to a fixed band in the observer frame. Our template SED for this calculation is that of Marconi et al. (2004), for which the ratio of X-ray to optical luminosity varies with bolometric luminosity. To calculate the luminosity in each band we input the bolometric luminosity and the redshift and then integrate the SED over frequency multiplied by the appropriate response function for the filter redshifted into the rest frame of the source. There is a one-to-one relation between bolometric luminosity and luminosity

[1] https://jwst-docs.stsci.edu/display/JTI/NIRCam+Sensitivity

[2] https://www.euclid-ec.org/?page_id=2581

[3] https://www.cosmos.esa.int/documents/400752/507693/Athena_SciRd_iss1v5.pdf

[4] https://wwwastro.msfc.nasa.gov/lynx/docs/LynxInterimReport.pdf

in a particular band.

The number density limit for a survey can be calculated via the following method. The number of objects per log flux per unit solid angle per unit redshift is given by:

$$\frac{\mathrm{d}^3N}{\mathrm{d}(\log f_\nu)\mathrm{d}z\mathrm{d}\Omega} = \frac{\mathrm{d}^2N}{\mathrm{d}(\log L_\nu)\mathrm{d}V}\frac{\mathrm{d}^2V}{\mathrm{d}z\mathrm{d}\Omega}, \tag{4.5.2}$$

where V is the comoving volume, $\mathrm{d}^2N/\mathrm{d}(\log L_\nu)\mathrm{d}V$ is the luminosity function in comoving units, and $\mathrm{d}^2V/\mathrm{d}z\mathrm{d}\Omega$ is the comoving volume per unit solid angle per unit redshift. We define $\Phi(X) = \mathrm{d}^2N/\mathrm{d}(\log X)\mathrm{d}V$ so the luminosity function can be written as $\Phi(L_\nu)$. For there to be an average of at least one object detectable in the survey per log flux per unit redshift, we therefore have the condition:

$$\frac{\mathrm{d}^2N}{\mathrm{dlog}L_\nu\mathrm{d}V} \geq \frac{1}{\frac{\mathrm{d}^2V}{\mathrm{d}z\mathrm{d}\Omega}\Delta\Omega}, \tag{4.5.3}$$

where $\Delta\Omega$ is the solid angle of sky covered by the survey. This condition allows us to construct the number density limits (horizontal lines) in Figures 4.6 to 4.11. Note that this limit is almost independent of redshift over the range $7 \leq z \leq 15$, as also seen for the JWST predictions of Cowley et al. (2018) for galaxies. The flux limits and survey areas adopted for the predictions for different telescopes are given in Table 4.1. These limits then allow us to predict the number of objects detectable by each survey, for the three different model variants, as given in Table B.1, and the properties of these objects, for the fiducial model, as given in Tables B.2, and B.3.

In general, the flux limit determines the lower luminosity limit of objects that can be detected, whereas the survey area determines the upper luminosity limit of objects that can be detected. The different flux limits and survey areas of the surveys conducted by the different telescopes therefore provide detections of different populations of AGNs.

4.5.1 Optical/near-IR surveys with JWST and EUCLID

JWST, planned for launch in 2021, will observe at wavelengths of 0.6-29 μm. It will have instruments for both imaging and spectroscopy, including the NIRCam for optical to near-infrared imaging (0.7-5 μm) and MIRI for mid-infrared imaging (5-29

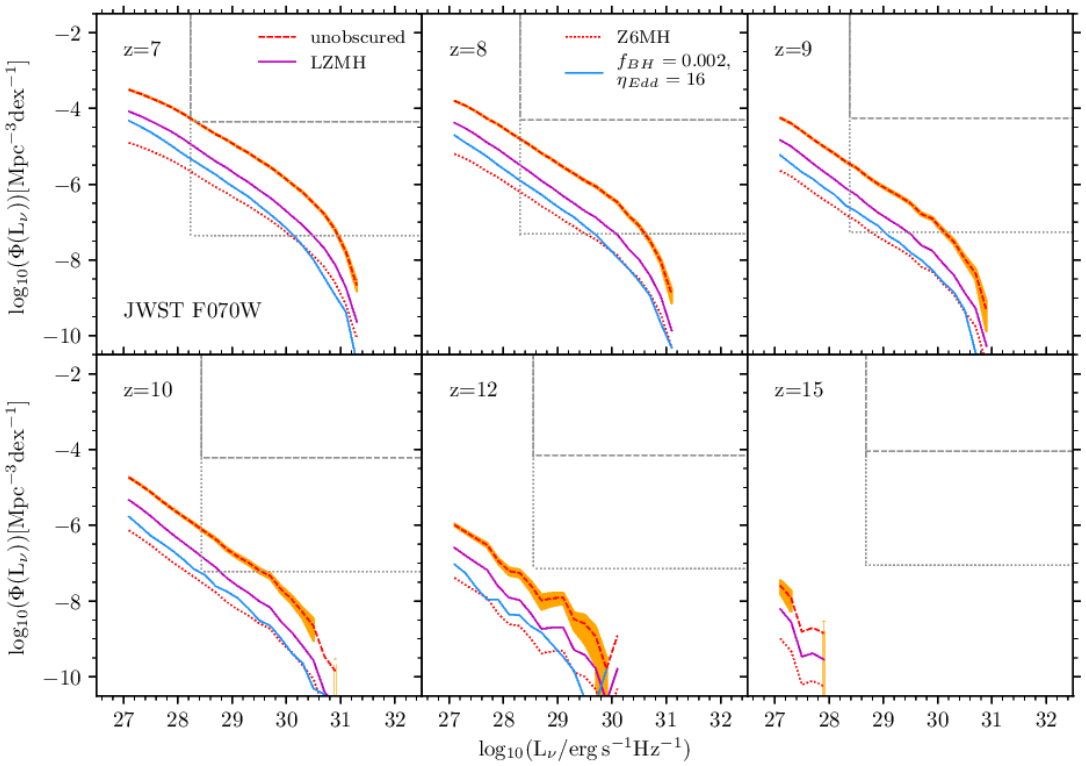

Figure 4.6: Predictions for the AGN luminosity function in the observer frame JWST NIRCam F070W (0.7μm) band. We show the luminosity function for the fiducial model without obscuration (red dashed) with Poisson errors (orange shading), the fiducial model with the 'low z modified Hopkins' (LZMH) visible fraction (magenta solid), the fiducial model with the '$z = 6$ modified Hopkins' (Z6MH) visible fraction (red dotted), and the low accretion efficiency model which uses the 'low z modified Hopkins' visible fraction (blue solid). The horizontal lines indicate the number density limit resulting from a survey area of one field of view (dashed), and the number density limit resulting from 1000 of these fields of view (dotted). The vertical lines show the luminosity limit resulting from the flux limit. The assumed flux limits and survey areas are given in Table 4.1. Detectable objects are above and to the right of these lines. These luminosities can be converted into absolute AB magnitudes via $M_{\mathrm{AB}} = 51.59 - 2.5\log(L_\nu/\mathrm{erg\,s^{-1}Hz^{-1}})$.

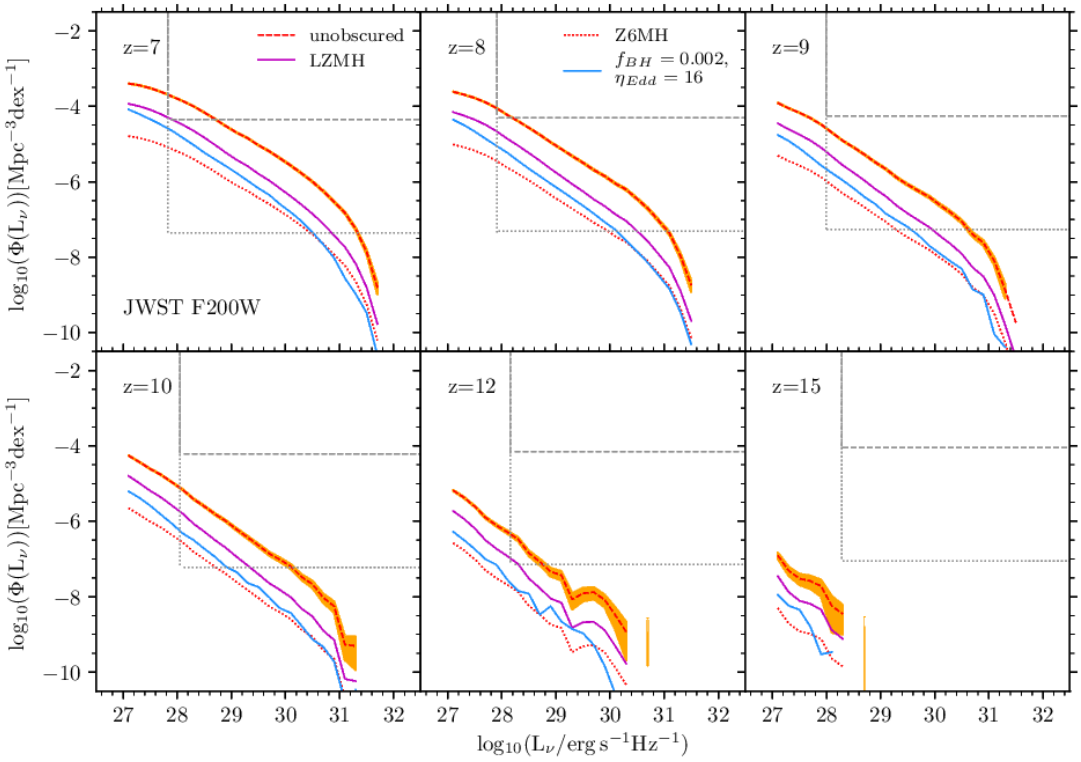

Figure 4.7: As in Figure 4.6 but for the observer frame JWST NIRCam F200W (2.0μm) band.

μm). We present predictions for three different NIRCam bands. We do not make predictions for MIRI, because our AGN model does not currently include emission from the dust torus, which would be necessary for modelling AGN emission in the mid-infrared. Figures 4.6 and 4.7 show predicted AGN luminosity functions in the observer frame F070W (0.7μm) and F200W (2.0μm) bands respectively. We also find that in the observer frame F444W (4.4μm) band, the predicted luminosity functions are similar to the observer frame F200W band. We present predictions for a survey composed of 1000 fields of view, each with a 10^4s integration time, giving a total integration time of 10^7s in each band. Figures 4.6 and 4.7 show that the effect of obscuration causes the predicted number of AGNs to be 0.04-0.2 of the predicted number of objects if obscuration is not taken into account. The effect of low accretion efficiency causes the predicted number of objects to be about 0.4 times lower than in the fiducial model if we are assuming the LZMH obscuration model. We predict that on average, < 1 AGN per unit z per field of view will be detectable by JWST for a 10^4s integration, once we allow for obscuration.

We give the predicted number of objects for each survey in Table B.1. For JWST we are assuming a survey of 1000 fields of view, each with a 10^4s integration time per band. We predict that $20 - 100$ AGNs (depending on which of the three models is used) will be observed at $z = 7$ in the F070W band, $90 - 500$ in the F200W band and $60 - 300$ in the F444W band. We predict that more objects will be detectable in the F200W band because the assumed flux limit for the F200W band is lower than for the F070W and F444W bands, which translates into a lower limit for the bolometric luminosity and higher number density. Predictions for the number of objects detectable at $z = 9$, $z = 10$ and $z = 12$ are given in Table B.1.

From the flux limits in these bands, limits in bolometric luminosity can be calculated. At $z = 7$, we predict that JWST will detect AGNs with bolometric luminosities in the range $(3 \times 10^{44} - 4 \times 10^{46})\,\mathrm{ergs}^{-1}$ (F070W), $(6 \times 10^{43} - 3 \times 10^{46})\,\mathrm{ergs}^{-1}$ (F200W), and $(1 \times 10^{44} - 4 \times 10^{46})\,\mathrm{ergs}^{-1}$ (F444W). For the assumed survey parameters, we predict that JWST will be able to detect AGNs out to $z = 9$ for all the optical/near-IR bands, with F200W being more favourable for detecting $z > 7$ AGNs than F070W and F444W. For F200W, we predict that about 60-90 times

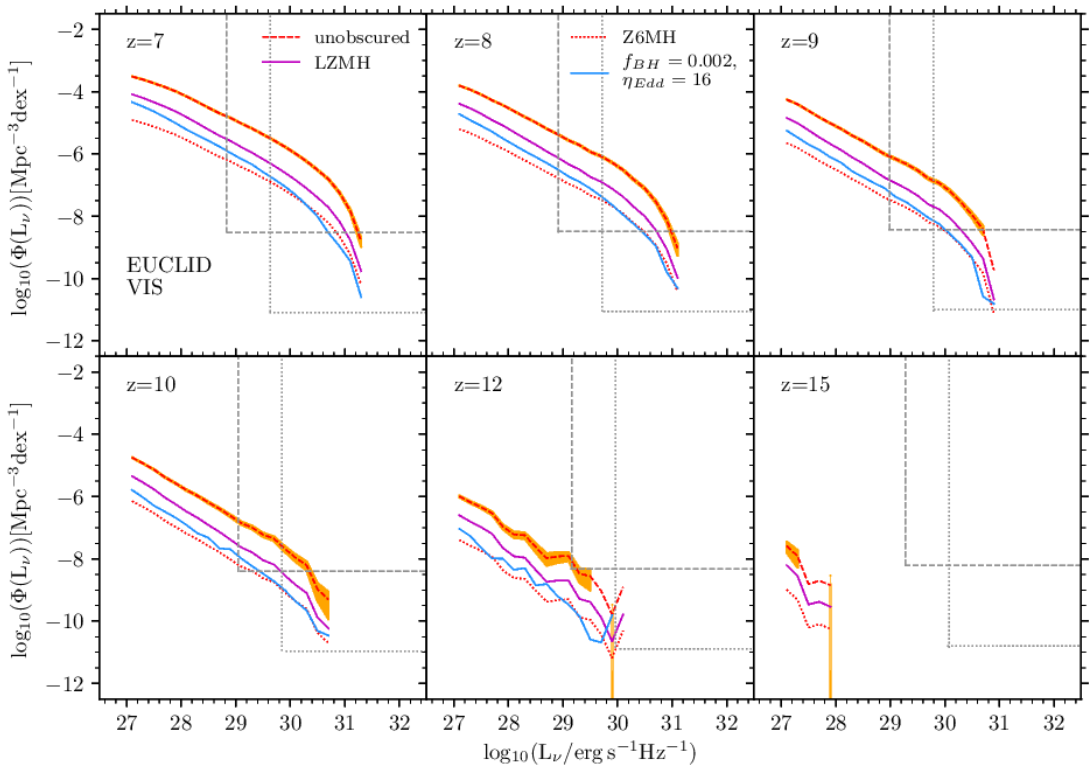

Figure 4.8: Predictions for the AGN luminosity function in the observer frame EUCLID VIS (550-900 nm) band. The dashed lines represent the sensitivity and survey volume limits of the EUCLID Deep survey and the dotted lines represent the sensitivity and survey volume limits of the EUCLID Wide survey.

fewer AGNs will be detectable at $z = 10$ than at $z = 7$. Considering even higher redshift objects, for $z > 10$ we predict that detection with JWST will become more difficult, as AGNs become extremely rare as well as very faint.

We explored whether a wide JWST survey composed of 1000 fields of view (as in Table 4.1) or a deep survey composed of one field of view for an integration time 1000 times longer (10Ms) would detect more objects. We found that the deep survey would detect more AGNs ($300-2000$) than the wide survey ($90-500$) in the F200W band at $z = 7$, although in practice the number of AGNs detectable by the deep survey would be reduced by contamination by light from their host galaxies.

EUCLID, due for launch in 2021, will use its visible and near-IR coverage (0.55-2 μm) of galaxies to probe the nature of dark energy, but these same surveys will also allow detections of high-redshift AGNs. EUCLID will conduct two surveys: a

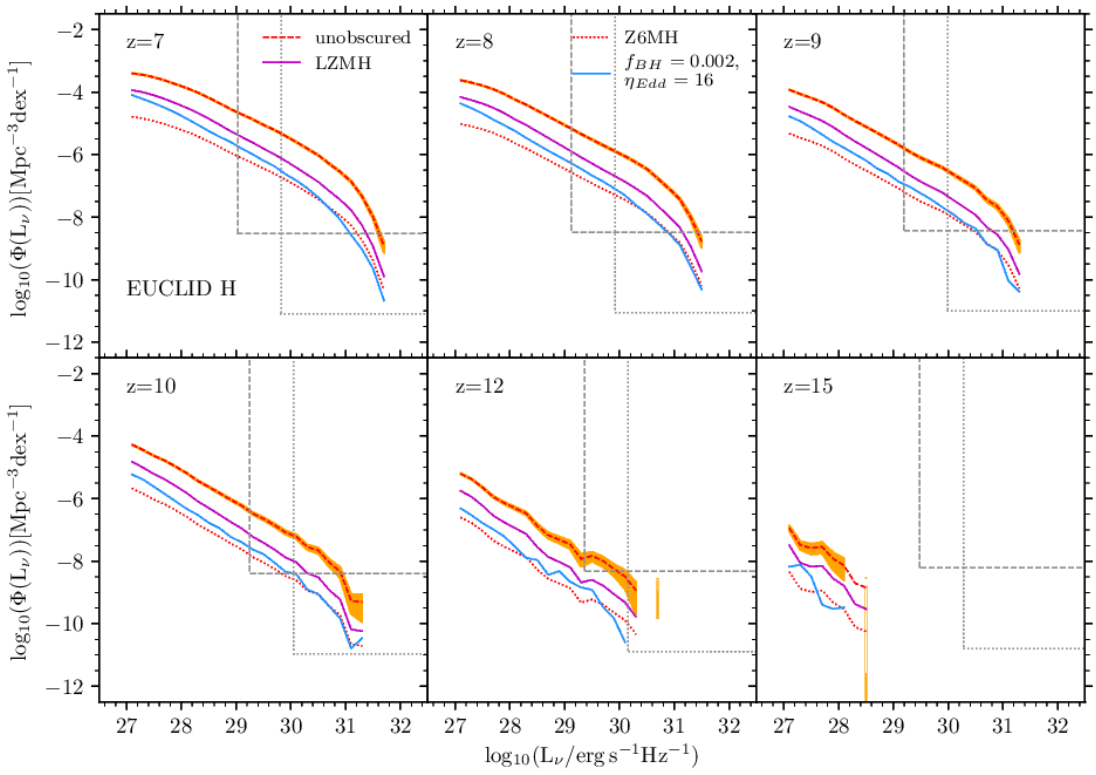

Figure 4.9: The same as Figure 4.8 but for the observer frame EUCLID H (1.5-2μm) band.

Wide Survey covering 15000 deg^2 of sky and a Deep Survey covering 40 deg^2 in three fields. The mission lifetime of EUCLID will be 6.25 years. The surveys will be conducted in four bands - one visible (VIS) and three near-IR (Y,J,H). We show predictions for the EUCLID VIS (0.55-0.9μm) band and the H (1.5-2μm) band in Figures 4.8 and 4.9 respectively. In these figures we show the sensitivity and survey volume limits for both the Deep and Wide surveys. The two surveys are seen to be quite complementary for detecting high redshift AGNs at different luminosities.

At $z = 7$, we predict that the EUCLID VIS band will detect AGNs with bolometric luminosities $L_{\rm bol} = (1 \times 10^{45} - 1.2 \times 10^{47})\,{\rm ergs}^{-1}$ for the Deep Survey, and with $L_{\rm bol} = (6 \times 10^{45} - 2 \times 10^{47})\,{\rm ergs}^{-1}$ for the Wide Survey. We therefore predict that the two EUCLID surveys and surveys by JWST will sample different parts of the AGN luminosity function.

At $z = 7$, we predict that a similar number of AGNs will be detectable in the EUCLID near-IR band compared to the visible band. For the EUCLID Deep survey, we predict that $90 - 400$ AGNs will be detectable in the VIS band compared with $100 - 600$ in the H band (depending on the model). For the EUCLID Wide survey at $z = 7$, we predict that $(5 - 20) \times 10^3$ AGNs will be detectable in the VIS band, and $(8 - 30) \times 10^3$ in the H band. At higher redshifts (e.g. $z = 10$), we predict that the EUCLID H band will detect more AGNs than the VIS band. For AGNs at $z = 7$, the peak of the observed SED is at 1μm, and so the luminosities in the VIS and H bands are similar, and because the flux limits are also similar, a similar number of AGNs should be detectable. At $z = 10$, the peak of the observed SED is at 1.3μm, and so the luminosities in the H band are higher, as they are closer to the peak of the AGN SED. Therefore, we predict that the H band will detect more AGNs than the VIS band at $z = 10$. A similar effect is seen when comparing the JWST F070W and F200W bands. It may be that such observations will reveal that the AGN SED shape at high redshift is different to the Marconi et al. (2004) SED used in this thesis.

According to our model, it will be impossible to detect very high redshift ($z = 15$) objects with EUCLID, so such investigation may have to wait until surveys after EUCLID. This is because despite the survey area being sufficiently large to probe

down to the required number densities, the sensitivity of EUCLID is not sufficient to detect these low luminosity AGNs.

The alternative models featuring a lower visible fraction or lower accretion efficiency predict fewer AGNs than the fiducial model, so observations using EUCLID and JWST may be able to differentiate between these models as well as constraining the form of the AGN SED and thus provide better understanding of the high redshift AGN population.

4.5.2 X-ray surveys with ATHENA and Lynx

Due for launch in 2031, ATHENA will make observations at 0.5-10 keV using two instruments: the X-ray Integral Field Unit (X-IFU) for high resolution spectroscopy and the Wide Field Imager (WFI) with a large field of view for surveys (Nandra et al., 2013). The Lynx X-ray observatory, with a proposed launch date of 2035, will make observations at 0.2-10 keV. Due to the effects of source confusion, Lynx will be able to probe down to lower luminosities than ATHENA as a result of its much better angular resolution.

We have calculated the sensitivity limits due to source confusion for ATHENA and Lynx. Source confusion occurs when multiple sources are separated by angles less than the angular resolution of the telescope and so appear merged together in images. To derive the confusion limits for ATHENA and Lynx, we use the commonly used Condon (1974) 'source density criterion', to obtain the cumulative number count per solid angle at the confusion limit ($N(> f_{\rm conf})$), for a given effective beam solid angle, $\Omega_{\rm beam}$, and number of beams per source $\mathcal{N}_{\rm beam}$:

$$N(> f_{\rm conf}) = 1/\mathcal{N}_{\rm beam}\Omega_{\rm beam}, \tag{4.5.4}$$

where the effective beam solid angle is related to the full width half maximum (FWHM) telescope beam width, $\theta_{\rm FWHM}$, by $\Omega_{beam} = \pi\theta^2_{\rm FWHM}/(4(\gamma-1)\ln 2)$ for a Gaussian beam profile, where γ is the slope of the power law relating differential number count and flux, given by:

Table 4.2: The values of γ used for calculating the confusion limits.

Telescope	Soft X-ray	Hard X-ray
ATHENA	1.5	1.32
Lynx	2.22	2.29

$$\frac{d^2N}{df\,d\Omega} \propto f^{-\gamma}. \tag{4.5.5}$$

We use $\mathcal{N}_{\rm beam} = 30$. Having calculated the cumulative number count at the confusion limit from equation (4.5.4), we can obtain the flux at the confusion limit by using a model that relates the cumulative number counts to the flux. For this, we use the Lehmer et al. (2012) empirical model, which is a fit to the number counts measured using Chandra assuming a double power law fit for the AGN contribution, and single power law fits for the galaxy and stellar contributions. For the Lynx sensitivities, we are extrapolating the Lehmer et al. (2012) model to 100-1000 times lower fluxes than observed by Chandra. For ATHENA, $\theta_{\rm FWHM} = 5\,$arcsec, whereas for Lynx, $\theta_{\rm FWHM} = 0.5\,$arcsec. The γ values that we use are slopes of the differential number counts from Lehmer et al. (2012) at the estimated confusion limits, and are given in Table 4.2. The fluxes calculated by this procedure are given in Table 4.1.

In Figure 4.10, we show predictions for these two telescopes in the soft X-ray (0.5-2 keV) band. Note that the turnover in the luminosity function seen at low luminosities is due to the halo mass resolution of the dark matter simulation (see Section 4.4). As the luminosity limit for Lynx for $z \leq 10$ is below the luminosity of this turnover, the predictions at low luminosities for $z \leq 10$ should be viewed as lower limits on the number densities. This figure also shows how Lynx will be transformational in the study of low luminosity AGNs, and will provide unique constraints and tests of our understanding of black hole physics and galaxy formation. This is a result of increased angular resolution of Lynx compared to ATHENA.

We do not include obscuration for these soft X-ray predictions because at the redshifts we are considering, the corresponding band in the galaxy rest frame lies at hard X-ray energies - a band for which we are assuming no obscuration. We show the fiducial model alongside the low accretion efficiency model ($f_{\rm BH} = 0.002$ and

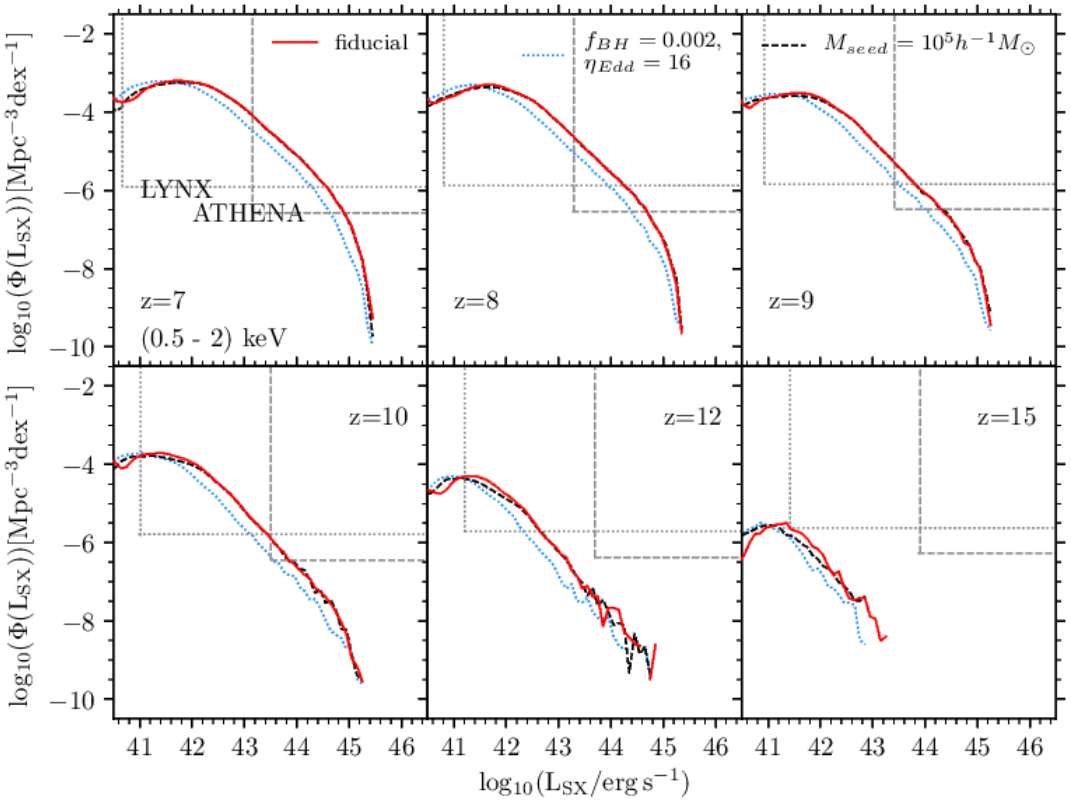

Figure 4.10: Predictions for AGN luminosity functions in the observer frame soft X-ray band. Shown are the fiducial model (red solid line), the low accretion efficiency model (blue dotted line), and the fiducial model with seed black hole mass $10^5 h^{-1} M_\odot$ (black dashed line). We also show the ATHENA (dashed) and Lynx (dotted) luminosity and number density limits (vertical and horizontal lines) for a single field of view and integration down to the estimated confusion limit, as in Table 4.1.

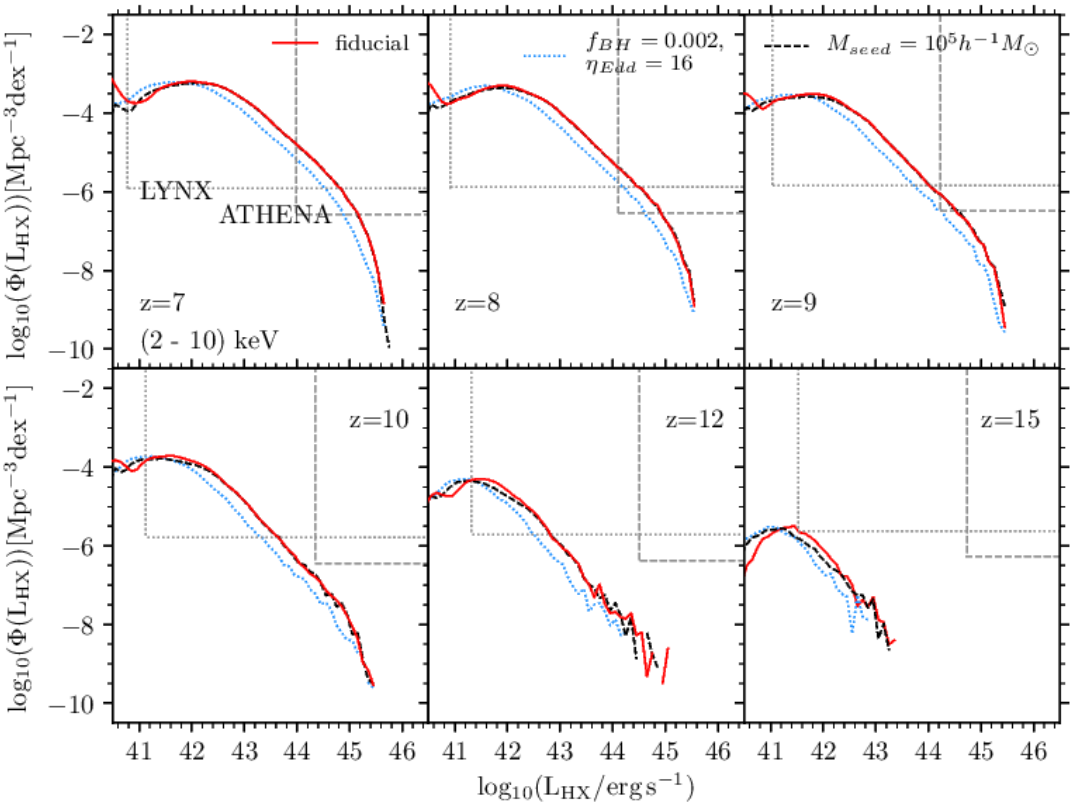

Figure 4.11: As for Figure 4.10, but for the observer frame hard X-ray band.

$\eta_{\rm Edd} = 16$) and also a model in which the black holes have a seed mass $M_{\rm seed} = 10^5 h^{-1} M_\odot$ (compared to the default value $M_{\rm seed} = 10 h^{-1} M_\odot$).

It can be seen how changing the seed black hole mass affects the soft X-ray luminosity function very little at $7 \leq z \leq 9$, and only by a small amount for $L_{SX} < 10^{42}{\rm ergs}^{-1}$ at $10 < z < 15$. This analysis suggests that even high sensitivity telescopes such as Lynx will struggle to differentiate between different seed masses at $7 \leq z \leq 9$ for our model assumptions, but measurements of the number densities of AGNs at low luminosities and very high redshifts ($L_{SX} < 10^{42}{\rm ergs}^{-1}$ and $10 < z < 15$), may be able to exclude models of SMBH seeding that involve high seed masses, although we predict that there will not be a substantial difference in the number densities between these two models.

In Figure 4.11 we show the predictions for ATHENA and Lynx in the hard X-ray (2-10 keV) band. For our template SED, an AGN emits more energy at hard than at soft X-ray energies, but the minimum luminosity of an object that can be detected is much higher for the hard X-ray band than for the soft X-ray band for ATHENA, while it is only slightly higher for Lynx. This has the effect that for ATHENA, we predict more AGNs will be detectable in the soft X-ray band compared to the hard X-ray band, whereas for Lynx, we predict that slightly more AGNs will be detectable in the hard X-ray band compared to the soft X-ray band.

For ATHENA, at $z = 7$ we predict that $30 - 80$ AGNs will be detectable per field of view in the soft X-ray band, and $5 - 20$ for the hard X-ray band (cf. Table B.1 for the number of objects predicted to be detectable by each survey). At $z = 10$, we predict that $0 - 2$ AGNs will be detectable in the soft X-ray band, and no objects in the hard X-ray band. For Lynx, at $z = 7$, we predict that about 800 AGNs per field of view will be detectable in the soft X-ray band, and about $800 - 900$ in the hard X-ray band. At $z = 10$, we predict that about 200 AGNs will be detectable per field of view for both the soft and hard X-ray bands. The low accretion efficiency model predicts fewer AGNs than the fiducial model across all luminosities and redshifts. According to our model, Lynx is the only telescope out of the four studied here that will be able to detect AGNs out to $z = 12$, with the possibility of detections at $z = 15$, depending on the model variant.

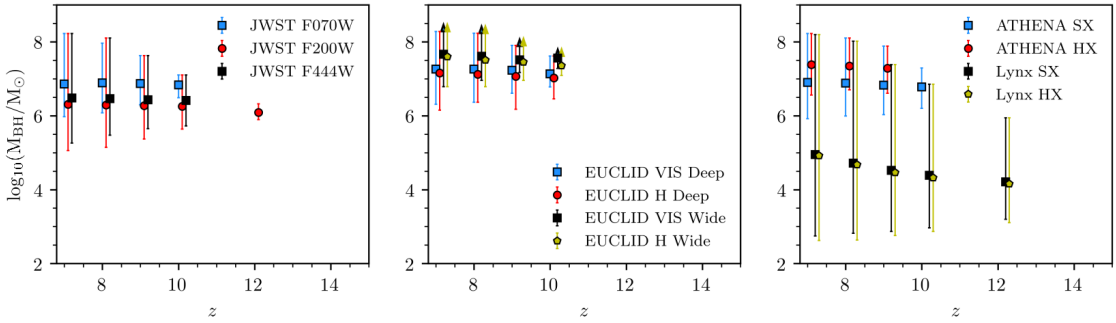

Figure 4.12: The predicted SMBH masses as a function of redshift for AGNs detectable by the surveys with the different telescopes for the fiducial model. Symbols and errorbars show the median and 0-100 percentiles of the distribution of SMBH masses at $z = 7, 8, 9, 10, 12$. *Left panel:* JWST F070W (blue squares), JWST F200W (red circles), and JWST F444W (black squares). *Middle panel:* EUCLID VIS and H for the Deep survey (blue triangles and red circles), and for the Wide survey (black squares and green pentagons). The maximum SMBH masses for EUCLID Wide are shown as upward pointing arrows because they are lower limits on the maximum SMBH masses that are detectable. *Right panel:* ATHENA soft and hard X-ray (blue squares and red circles), and Lynx soft and hard X-ray (black squares and green pentagons). In all panels, points for different surveys have been slightly offset in redshift for clarity.

However, we note that while we predict Lynx will detect more objects than ATHENA, this may be a result of the longer integration time of the proposed Lynx survey (15Ms) compared to the proposed ATHENA survey (450ks). If we assume a 15Ms ATHENA survey, we predict that in the soft X-ray band $1000 - 3000$ AGNs would be detected, compared to 800 by Lynx in that integration time (although this is a lower limit caused by the halo mass resolution). The different surveys by Lynx and ATHENA as 'deep' and 'wide' surveys respectively can provide different populations of detectable AGNs.

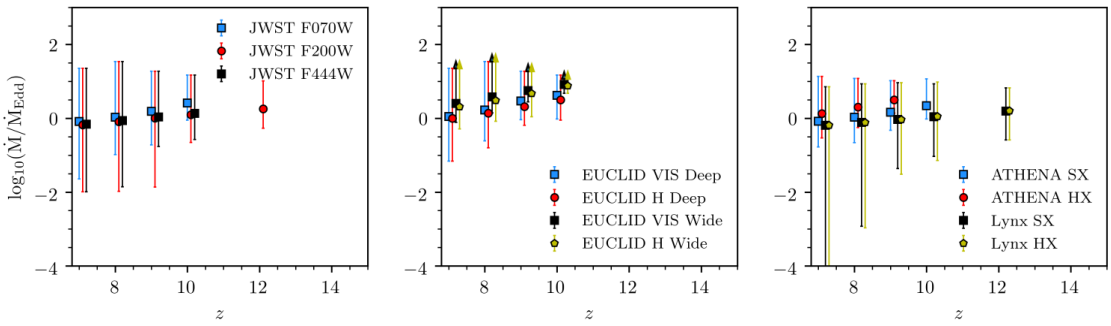

Figure 4.13: The Eddington normalised mass accretion rates as a function of redshift for the AGNs detectable by the surveys with the different telescopes. The lines are as in Figure 4.12.

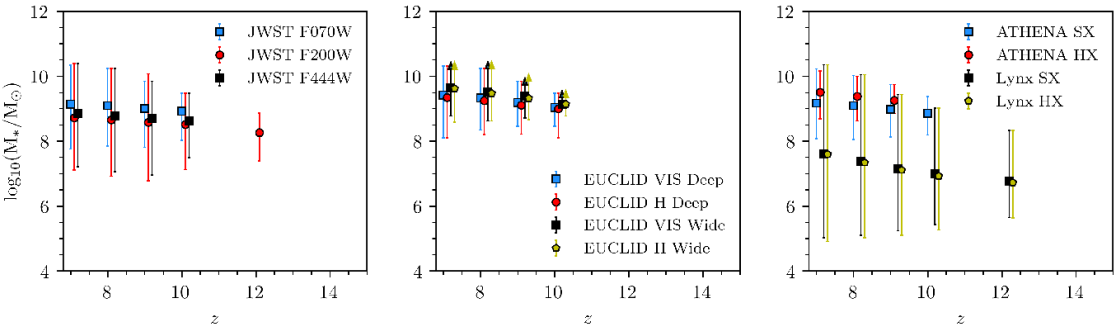

Figure 4.14: The host galaxy stellar masses as a function of redshift for the AGNs detectable by the surveys with the different telescopes. The lines are as in Figure 4.12.

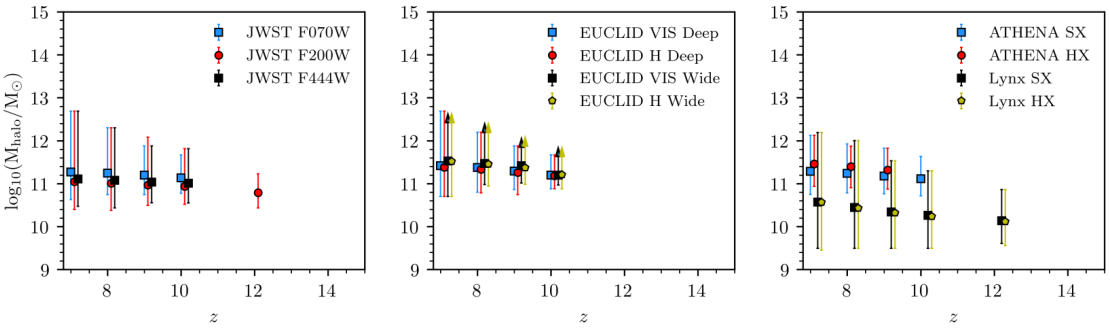

Figure 4.15: The host halo masses as a function of redshift for the AGNs detectable by the surveys with the different telescopes. The lines are as in Figure 4.12.

4.5.3 Properties of detectable AGNs and SMBHs in high-redshift surveys

We show the predictions for SMBH masses, Eddington normalised mass accretion rates, host galaxy stellar masses, and host halo masses for the AGNs detectable by each survey for redshifts $7 \leq z \leq 15$ in Figures 4.12, 4.13, 4.14, and 4.15 respectively. We constructed these plots by generating the number density distributions for each property for AGNs above the luminosity limit for the survey at that redshift, and then selecting the part of the distribution with number density above the survey limit, in the same way as we did for luminosity functions in the preceding sections. We then calculated the median, minimum, and maximum values of these distributions, which are plotted in the figures. We also list the median values of these quantities for $z = 7$ and $z = 10$ in Tables B.2 and B.3. The maximum SMBH masses, Eddington normalised mass accretion rates, galaxy masses, and host halo masses for the EUCLID Wide survey are shown as upward pointing arrows because they are lower limits on the maximum values that EUCLID Wide would detect. This is because the effective survey volume of EUCLID Wide at these redshifts is larger than the volume of the simulation box, and so there may be massive, rare black holes that the survey would detect, but which are not sampled by our simulation volume.

First we compare the optical/near-IR surveys. Compared to EUCLID Deep, we predict that JWST will probe SMBHs with masses about four times lower, in galaxies with stellar masses about three times lower, and in haloes with masses about two times lower, having Eddington normalised accretion rates about 1.4 times lower. We predict that the two different EUCLID surveys will detect slightly different populations of AGNs, with EUCLID Wide detecting SMBHs with masses about three times higher, in galaxies with stellar masses about two times higher, and in haloes with masses about 1.3 times higher, having Eddington normalised mass accretion rates about two times higher, compared to EUCLID Deep.

Now comparing the X-ray surveys, the properties of objects predicted to be detectable in the two ATHENA bands are similar to those predicted to be detectable

by EUCLID Deep, but the ATHENA soft X-ray band is predicted to detect SMBHs with masses about two times lower, in galaxies of stellar mass about two times lower, in host haloes about 1.3 times lower, and having Eddington normalised mass accretion rates about 1.3 times lower, compared to EUCLID Deep. Compared to ATHENA, we predict that Lynx will detect SMBHs with masses about 200 times lower, with galaxy stellar masses about 50 times lower, and in haloes of mass about 10 times lower, with Eddington normalised mass accretion rates about 2 times lower. For each survey, the AGNs detectable at $z = 10$ have somewhat lower black hole masses, lower host galaxy stellar masses, lower host halo masses, and higher Eddington normalised accretion rates than at $z = 7$.

Comparing all the distributions of the objects detectable by these surveys at $z = 7$, we predict that the objects detectable by the Lynx hard X-ray band will have the lowest median black hole mass, stellar mass, halo mass, and Eddington normalised mass accretion rate. On the other hand, we predict that the obects detectable by the VIS band for the EUCLID Wide survey will have the highest median black hole mass, stellar mass, halo mass, and Eddington normalised mass accretion rate.

We predict that Lynx will detect SMBHs that are substantially smaller than in the other surveys, and SMBH host galaxies that are substantially smaller than in the other surveys. Also, Lynx is the only survey that will be able to detect AGNs at $z = 7$ in the ADAF accretion state ($\dot{m} < 0.01$). The much lower black hole, galaxy, and halo masses probed by Lynx compared to the other telescopes are a result of it being able to detect AGN at much lower bolometric luminosities.

While Lynx is predicted here to detect AGNs with smaller black hole masses than the other surveys based on the survey parameters in Table 4.1, we explored whether AGNs with similarly low mass black holes could be detectable by a similarly long integration time with JWST. We considered a 15Ms integration time survey in the JWST F200W band, for a single field of view (compared to our standard assumption of a 10ks integration time in each of 1000 fields of view), assuming the survey is signal-to-noise limited. We predict that for this long integration time survey, JWST could detect objects at $z = 7$ down to an AGN bolometric luminosity

of $L_{\rm bol} = 2.8{\times}10^{42}{\rm ergs}^{-1}$, compared to $L_{\rm bol} = 3.8{\times}10^{41}{\rm ergs}^{-1}$ for the Lynx soft X-ray band. The smallest black holes at $z = 7$ that are detectable by this long integration time JWST survey are of mass $M_{\rm BH} = 4700M_{\odot}$, compared to $M_{\rm BH} = 560M_{\odot}$ for the Lynx soft X-ray band. JWST is therefore in principle as sensitive as Lynx to low luminosity, low SMBH mass AGNs at high redshift. However, this does not account for the 40 times smaller field of view of JWST compared to Lynx, which greatly reduces the survey volume, nor the greater difficulty of separating the light of the AGN from that of the host galaxy in optical/near-IR compared to X-rays.

The largest detectable SMBH is also different for each of these surveys. Surveys with larger survey areas can probe down to lower number densities, and so generally can detect higher mass SMBHs. However, because the black hole mass function decreases fairly steeply at the high mass end, increasing the survey area only slightly increases the mass of the largest SMBH detectable. For halo masses, a larger survey area does not necessarily correspond to detecting larger haloes from the AGNs they contain, because the largest haloes can host lower luminosity objects (see Figure 4.5). Therefore the maximum halo mass is also affected by the sensitivity limit, as seen for ATHENA and Lynx in the right panel of Figure 4.15. A similar argument can be applied for stellar masses as seen in Figure 4.14.

We also explored the effect of halo mass resolution in our simulation on the properties of objects detectable by these surveys (see Section 4.4). We find that if we degrade the halo mass resolution, as long as the objects have bolometric luminosities above the value at which the luminosity functions converge (i.e. $L_{\rm bol} > 10^{43}{\rm ergs}^{-1}$), the properties of the black holes are the same. The predictions of black hole properties for surveys by JWST, EUCLID and ATHENA are insensitive to this effect, but for Lynx the values given should be regarded as upper limits.

4.6 Conclusions

Recent advances in observational capabilities have opened up studies of the high-redshift Universe, but many uncertainties regarding the early stages of galaxy formation and evolution remain. The origin of supermassive black holes (SMBHs) and

their role in the early Universe still remains a mystery. Fortunately the next decade-and-a-half offers us exciting new opportunities to probe the high redshift Universe, especially given the plans for powerful new space-based telescopes such as JWST and EUCLID at optical/near-IR wavelengths, and ATHENA and Lynx at X-ray energies. These will offer us a multiwavelength view of the distant Universe and allow us to characterise physical processes in galaxy formation. The role of SMBHs and their growth in the distant Universe will be probed with much greater accuracy than ever before.

We present model predictions for the AGN bolometric luminosity function for $7 \leq z \leq 15$, finding that it evolves to lower luminosities and lower number densities at higher redshift as a result of hierarchical structure formation. When we split the bolometric luminosity function at these redshifts by accretion disc mode and gas fuelling mode, we find that the dominant accretion disc modes are thin discs at low luminosities ($L_{\rm bol} < 10^{45}{\rm ergs}^{-1}$), and super-Eddington objects at higher luminosities, and the dominant gas fuelling mode at all luminosities is starbursts triggered by disc instabilities. The model allows SMBHs to grow at mass accretion rates above the Eddington rate, so when we limit the SMBH gas accretion rate to the Eddington rate, the number of SMBHs at high redshift is significantly reduced. We also explore the effect of varying the SMBH seed mass on the bolometric luminosity function. We find that when we use a much larger seed black hole mass ($10^5 h^{-1} M_\odot$ compared to $10 h^{-1} M_\odot$ in the fiducial model), the luminosity functions are relatively unaffected, except for $L_{\rm bol} < 10^{43}{\rm ergs}^{-1}$ for $z > 10$.

We then present predictions for JWST, EUCLID, ATHENA, and Lynx, using sensitivities and survey areas for possible surveys with these telescopes. For example, we assume a 1.5×10^7s exposure for Lynx over a survey area of 360 arcmin^2 (1 field of view), whereas we assume a thousand 10^4s exposures for JWST over a total survey area of 9680 arcmin^2 (1000 fields of view). We find that the different surveys will probe down to different AGN bolometric luminosities and number densities, and hence sample different parts of the AGN population.

We also present predictions for two variants to the fiducial model that provide a better fit to the rest-frame UV and rest-frame soft X-ray luminosity functions of

AGNs at $z = 6$. In these models we vary either the amount of AGN obscuration or the SMBH accretion efficiency (defined here as the fraction of gas accreted onto the SMBH in a starburst). The resulting luminosity functions have lower number densities by factors of about 4 and 2 respectively. AGN obscuration and SMBH accretion efficiency are both uncertainties for the AGN population at high redshift. Comparing these predictions to observations should allow us to better both of these aspects at high redshift.

The properties of the SMBHs and AGNs detectable depend on the survey and wavelength. For our fiducial model, we predict that the AGNs detectable at $z = 7$ will have median black hole masses that vary from $8 \times 10^4 M_\odot$ to $5 \times 10^7 M_\odot$, and median Eddington normalised mass accretion rates that vary from $1 - 3$. These AGNs are predicted to reside in host galaxies with median stellar masses that vary from $4 \times 10^7 M_\odot$ to $4 \times 10^9 M_\odot$, and in haloes with median masses from $4 \times 10^{10} M_\odot$ to $3 \times 10^{11} M_\odot$. At $z = 10$, the AGNs detectable are predicted to have black hole masses that vary between $2 \times 10^4 M_\odot$ to $4 \times 10^7 M_\odot$, with Eddington normalised mass accretion rates that vary from $1 - 8$. The host galaxies of these AGNs are predicted to have masses that vary from $8 \times 10^6 M_\odot$ to $1 \times 10^9 M_\odot$, in haloes with masses that very from $2 \times 10^{10} M_\odot$ to $2 \times 10^{11} M_\odot$. The different telescopes will therefore provide different but complementary views on the $z > 6$ AGN population. For the survey parameters assumed here, Lynx is predicted to detect SMBHs with the lowest masses, in the lowest mass host galaxies and lowest mass host haloes, and so will provide the best opportunity to probe the nature of SMBH seeds. However, a similarly long integration (15Ms) in a single field of view with JWST could in principle detect similarly faint AGN at high redshift.

These future telescopes should therefore be able to detect SMBHs at very high redshift having masses $\sim 10^4 - 10^5 M_\odot$ that are comparable to those of the highest mass seed SMBHs that are envisaged in current scenarios, and put improved constraints on the physical mechanisms by which these seed SMBHs form.

In the last two Chapters we have made predictions from the model for AGN luminosities from near-IR to X-ray wavelengths. In the next Chapter, we make predictions for jet powers and radio luminosities. These quantities are calculated

using the SMBH spins, masses and mass accretion rates from the model.

Chapter 5

Jet powers and core radio emission

5.1 Introduction

Understanding the cosmic evolution of extragalactic radio sources has been of interest to the astrophysical community since the 1960s. Early work showed that the most luminous radio sources exhibited stronger cosmological evolution than the less luminous sources (Longair, 1966), but the lack of radio source redshifts in that work constituted a major uncertainty. Subsequent work showed that the comoving number density of powerful radio sources at $z \sim 2$ is ~ 1000 higher than for the local Universe, with a strong decrease in the number density from $z = 2$ to $z = 4$ (e.g. Peacock, 1985; Dunlop & Peacock, 1990), which was referred to as the high redshift 'cut-off'. Other works disputed this cut-off, with Jarvis & Rawlings (2000), Jarvis et al. (2001), and Willott et al. (2001) suggesting a more gradual evolution in the number density of high-redshift sources. In a more detailed analysis, Wall et al. (2005) confirmed the decrease in the number density of flat-spectrum radio sources for $z \geq 3$. More recent studies have also investigated the less powerful sources, which seem to show only a modest increase in number density of a factor ~ 2 from $z = 0$ to $z = 0.5$ (e.g. Sadler et al., 2007; Donoso et al., 2009), and also find that there is a decrease in number density for $z > 0.7$ (e.g. Rigby et al., 2011).

In this Chapter, we explore the evolution of jet powers and radio luminosities predicted by the model we are using here. While various previous theoretical studies have investigated the evolution of radio luminosities, using different mod-

Table 5.1: The values for the free parameters of the radio emission model used in this Chapter. $A_{\rm ADAF}$ and $A_{\rm TD}$ are the normalisations of the radio luminosity for ADAFs and thin disc, and have been calibrated to the radio luminosity function at $z = 0$.

Parameter	Adopted here
$A_{\rm ADAF}$	2×10^{-5}
$A_{\rm TD}$	0.8

elling techniques such as physical models of galaxy formation (e.g. Fanidakis et al., 2011; Hirschmann et al., 2014), or empirical galaxy evolution models (e.g. Kaiser & Alexander, 1999; Saxena et al., 2017), very few models base their radio luminosities on a self-consistent model for SMBH growth and spin evolution embedded in a physical model of galaxy formation.

The outline of this Chapter is as follows. In Section 5.2 we describe the model used. In Section 5.3 we present the predicted evolution of the jet powers and in Section 5.4 we present the predicted radio luminosity function evolution. In Section 5.5 we present our conclusions.

5.2 Model

5.2.1 Jet powers and radio luminosities

In this Chapter, we are using the same model as in the previous Chapters. The mechanisms by which SMBH mass builds up and the method by which mass accretion rates are calculated is given in Section 2.7, and the method by which SMBH spin evolution is calculated is given in Section 3.2. We calculate jet powers from black hole accretion discs following the model in Meier (2002), in which the jet power is sourced from the rotational energy of the black hole, as in the Blandford & Znajek (1977) (BZ) model for jet production. In the BZ model, the jet power, Q, also depends on the strength of the poloidal magnetic field, B_p:

$$Q \propto B_p^2 M_{\rm BH}^2 \, a^2. \tag{5.2.1}$$

The poloidal magnetic field in the accretion disc is then related to the azimuthal magnetic field strength, B_ϕ, via $B_p \approx (H/R)B_\phi$, where H/R is the ratio of disc half-thickness to the disc radius. For geometrically thick ADAFs, $H/R \sim 1$, whereas for (geometrically) thin discs, H/R is given by the thin disc equations. In our model, the SMBH is in the ADAF regime for $\dot{m} < 0.01$, and is in the thin disc regime for $\dot{m} > 0.01$. The poloidal magnetic field can then be related to accretion disc quantities by assuming the magnetic field pressure is limited by the maximum pressure of the accretion disc (Moderski & Sikora, 1996). This assumption of equipartition is likely to provide an upper limit on B_ϕ. The jet powers are then given by the expressions in Meier (2002):

$$Q_{\rm ADAF} = 2 \times 10^{45} {\rm ergs}^{-1} \left(\frac{M_{\rm BH}}{10^9 M_\odot}\right) \left(\frac{\dot{m}}{0.01}\right) a^2, \tag{5.2.2}$$

$$Q_{\rm TD} = 2.5 \times 10^{43} {\rm ergs}^{-1} \left(\frac{M_{\rm BH}}{10^9 M_\odot}\right)^{1.1} \left(\frac{\dot{m}}{0.01}\right)^{1.2} a^2, \tag{5.2.3}$$

where a is the black hole spin parameter. The coefficient for the thin disc case is lower than for the ADAF case as a result of the smaller values of H/R for thin discs, which reduce the poloidal magnetic field compared to the azimuthal magnetic field.

In this model, we calculate core radio luminosities, and assume that the total radio emission is dominated by the core emission. To calculate the core radio luminosity, $L_{\nu \rm R}$, at a particular frequency, we use the scaling model of Heinz & Sunyaev (2003), which relates the radio luminosity of core-dominated sources to the black hole mass and mass accretion rate, using scaling relations based on physical arguments. It gives $L_{\nu \rm R} \propto (M_{\rm BH}\dot{m})^{1.42}$ for ADAFs, and $L_{\nu \rm R} \propto M_{\rm BH}^{1.42}$, for thin discs[1]. By combining these relations with those for the jet powers, we obtain expressions for the radio luminosities[2]:

$$\nu_{\rm R} L_{\nu {\rm R,ADAF}} = A_{\rm ADAF}\, Q_{\rm ADAF} \left(\frac{M_{\rm BH}}{10^9 M_\odot}\right)^{0.42} \left(\frac{\dot{m}}{0.01}\right)^{0.42}, \tag{5.2.4}$$

[1]Following Fanidakis et al. (2011), we assume that $L_{\nu \rm R}$ depends on spin via $L_{\nu \rm R} \propto a^2$

[2]Note that equations (5.2.4) and (5.2.5) are different to Fanidakis et al. (2011) equations (44) and (45)

$$\nu_{\rm R} L_{\nu {\rm R,TD}} = A_{\rm TD}\, Q_{\rm TD} \left(\frac{M_{\rm BH}}{10^9 M_\odot} \right)^{0.32} \left(\frac{\dot{m}}{0.01} \right)^{-1.2}, \tag{5.2.5}$$

where $\nu_{\rm R}$ is the rest-frame frequency, and $A_{\rm ADAF}$ and $A_{\rm TD}$ are free parameters of the Heinz & Sunyaev (2003) model, as their scaling relations do not provide values for these A parameters. We allow $A_{\rm ADAF}$ and $A_{\rm TD}$ to vary independently, compared to Fanidakis et al. (2011) which required $A_{\rm ADAF}/A_{\rm TD} = 100$.

We choose the values of $A_{\rm ADAF}$ and $A_{\rm TD}$ to give the best agreement with the observed AGN radio luminosity function at $z = 0$, as we show in Figure 5.7 in Section 5.4. The values adopted for this study are given in Table 5.1. Following Fanidakis et al. (2011), and using equations (5.2.4) and (5.2.5), this results in a power law SED for the radio emission, $L_{\nu {\rm R}} \propto \nu^{-\alpha}$, with $\alpha = 1$[3]. This radio emission model in GALFORM has been used in Izquierdo-Villalba et al. (2018) to study predictions for the environments of radio galaxies, and in Amarantidis et al. (2019) in a comparison of AGN luminosity functions from different theoretical models. The model for jet powers has also been used in Ceraj et al. (2018), who compared it to their observational estimate of the evolution of the jet power density.

As stated above, we are assuming that the total radio emission is the same as the core emission, an assumption that is likely to be valid for lower radio luminosities, where most sources are core-dominated, but less valid for higher radio luminosities, where most sources are not core-dominated.

5.2.2 AGN heating and jet efficiency

In the hot halo mode of SMBH accretion, where AGN feedback is operational, the efficiency of SMBH heating of the halo gas is set to a constant value $\epsilon_{\rm heat} = 0.02$ as in equation (2.7.26). This is the efficiency of AGN feedback in the galaxy formation model, which we will refer to as the *AGN heating efficiency*. We also calculate jet powers from the SMBH spin, mass, and accretion rate in equations (5.2.2) and (5.2.3), from which an alternative efficiency, $\epsilon_{\rm jet} = Q/(\dot{M}c^2)$, can be calculated,

[3]We note that this is different to the $\alpha = 0$ value assumed for equations (5.2.4) and (5.2.5), as in Fanidakis et al. (2011)

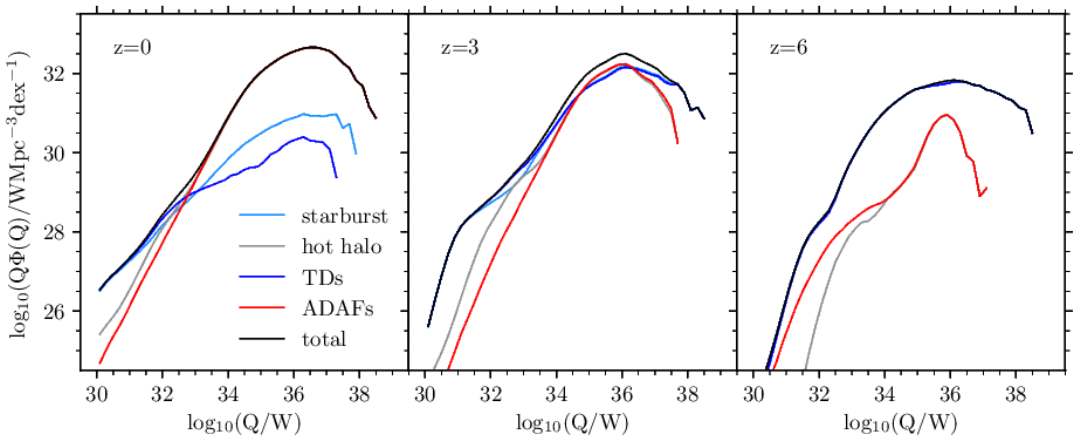

Figure 5.1: The product of the jet power and the comoving number density of objects at each jet power $Q\Phi(Q) = Qdn/d\log Q$, as a function of jet power, Q, for $z = 0, 3, 6$. We show the total (black line), the contribution from the starburst mode (light blue line), from the hot halo mode (grey line), the contribution from thin discs (blue line), and the contribution from ADAFs (red line).

which we will refer to as the *AGN jet efficiency*. If all of the energy in AGN jets were deposited in hot halo gas, one would expect $\epsilon_{\rm heat} = \epsilon_{\rm jet}$. In order to avoid modifying the underlying galaxy formation model, this condition was not imposed on $\epsilon_{\rm heat}$. However, we do explore in Section 5.3 whether the assumed AGN heating efficiency is similar to the average predicted AGN jet efficiency.

5.3 Evolution of jet power density

5.3.1 Predictions from the model

We first investigate the predicted evolution of the jet powers. In Figure 5.1, we show the product of the jet power and the comoving number density of objects at each jet power, $Q\Phi(Q)$, where $\Phi(Q) = dn/d\log Q$, for $z = 0, 3, 6$. This is shown split by accretion state into the contributions from thin discs and ADAFs, and separately by fuelling mode into contributions from starburst triggered accretion and hot halo accretion. This distribution shows us which jet powers and which contributions dominate the jet power density, as the integral of $Q\Phi(Q)$ with respect to $\log Q$ is

the jet power density. Note that our predictions for jet powers are independent of the model for radio emission.

The ADAF and hot halo mode contributions evolve similarly because the Eddington normalised mass accretion rate for objects in the hot halo mode is generally below 0.01 (cf. equation (2.4.20)). On the other hand, the thin disc and starburst mode contributions evolve similarly because the Eddington normalised mass accretion rate is generally above 0.01 for starburst mode accretion. This is because the mass accretion rate is typically higher for starburst mode accretion, and because the starburst mode typically occurs for smaller black holes in smaller haloes. At $z = 0$, for $Q \lesssim 10^{32}$W, the dominant contribution to $Q\Phi(Q)$ is from the starburst and thin disc contributions, whereas for $Q \gtrsim 10^{33}$W, the dominant contribution is from the hot halo and ADAF contributions. At $z = 3$, for $Q \lesssim 10^{34}$W, the starburst and thin disc contributions dominate, whereas at $Q \sim 10^{36}$W, the contributions to $Q\Phi(Q)$ from the starburst and hot halo modes contribute approximately equally. At $z = 6$, the dominant contribution to $Q\Phi(Q)$ at all jet powers is from the starburst and thin disc contributions. These predictions for the different contributions to the jet power distribution could be tested observationally, and so provide a simple test of the model.

The jet power density discussed below is dominated by objects in the peak of the $Q\Phi(Q)$ distribution. The dominant contribution to the jet power density comes from sources with $Q \sim 10^{36}$W, independent of redshift over the range $0 < z < 6$. Also, the peak in $Q\Phi(Q)$ occurs at roughly the same jet power for both starburst and hot halo modes, again roughly independent of redshift. This appears to be fortuitous, given the very different typical jet efficiencies for the starburst and hot halo modes as discussed below.

In the top panel of Figure 5.2 we show the evolution of the jet power density, $\rho(Q)$, where $\rho(Q)$ is given by the total jet power summed over all galaxies divided by the total comoving volume. We also split the jet power density evolution into contributions from thin discs and ADAFs, and separately into contributions from starburst triggered accretion and hot halo accretion. When comparing the fuelling modes, the hot halo mode contribution dominates the jet power density for $z <$

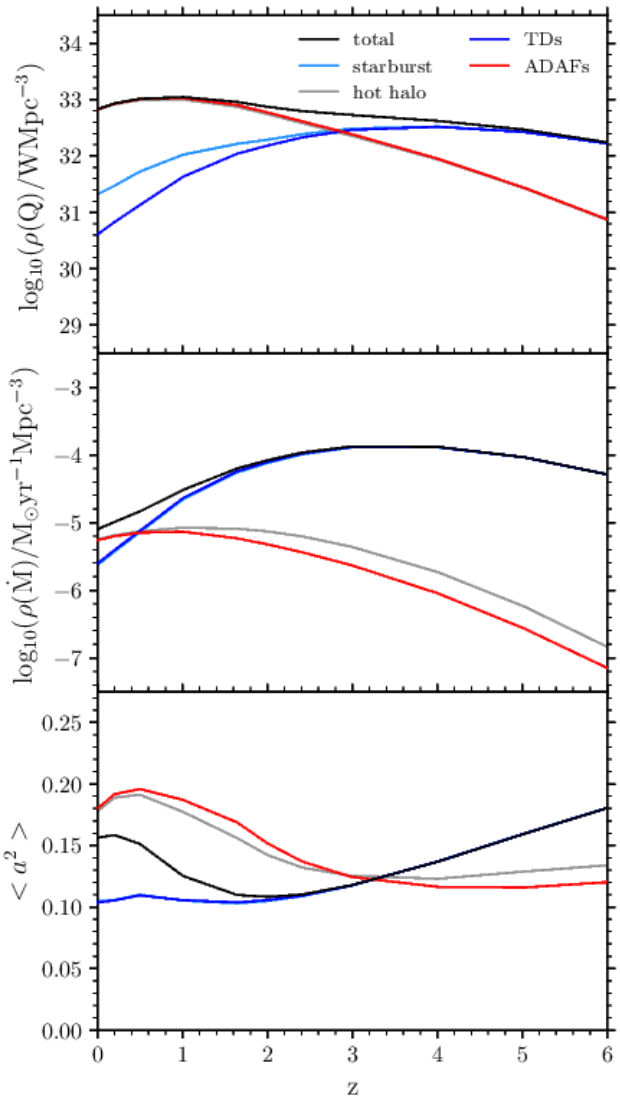

Figure 5.2: The evolution of the model with redshift. In each panel the model prediction (black line), is split into the contribution from starburst triggered accretion (light blue line), the contribution from hot-halo accretion (grey line), the contribution from thin discs (TDs, dark blue line) and the contribution from ADAFs (red line). *Top panel:* the predicted evolution of the jet power density with redshift. The solid grey line is underneath the red line. *Middle panel:* the evolution of the SMBH mass accretion rate density with redshift. *Bottom panel:* the evolution of the mass accretion rate weighted average mean square SMBH spin with redshift.

3, whereas the starburst mode contribution dominates for $z > 3$. The hot halo contribution peaks at $z \sim 1$, whereas the starburst contribution peaks at $z \sim 4$. When comparing the accretion disc states, the ADAF contribution dominates for $z < 3$, and the thin disc contribution dominates for $z > 3$.

In the middle panel of Figure 5.2, we show the evolution of the SMBH mass accretion rate density (the total mass accretion rate summed over all galaxies divided by the total comoving volume) with redshift. The total mass accretion rate density increases with redshift for $0 < z < 3$, has a peak around $z = 3-4$, and then decreases for $z > 4$. The mass accretion rate density is dominated by the contributions from AGNs fuelled by the starburst mode and accreting via the thin disc accretion state, except for $z < 0.5$ where the mass accretion rate density is dominated by the contribtions from AGNs fuelled by the hot halo mode and accreting via the ADAF accretion state.

In the bottom panel of Figure 5.2, we show the mass accretion rate weighted average mean square SMBH spin, $\langle a^2 \rangle$, calculated as the sum of the product of mass accretion rate and spin squared of the black holes, divided by the sum of the mass accretion rates (i.e. $\langle a^2 \rangle = \rho(\dot{M}a^2)/\rho(\dot{M})$). When considering all SMBHs together, $\langle a^2 \rangle$ decreases with redshift in the interval $0 < z < 2$, from about 0.15 to 0.1, before increasing for $z > 2$ to about 0.18 at $z = 6$. For $z < 4$, the hot halo and ADAF contributions have higher values of $\langle a^2 \rangle$ compared to the starburst and thin disc contributions. This is because for the AGNs fuelled by the starburst mode, the objects with the highest mass accretion rates have a low spin (around $a = 0.2$ at $z = 0$), whereas for the hot halo mode, the objects with the highest mass accretion rates have slightly higher spins ($a = 0.2-0.4$ at $z = 0$). For $z > 4$, $\langle a^2 \rangle$ is greater for the starburst mode and thin disc contributions because the highest mass accretion rate SMBHs in the starburst mode have higher spins ($a = 0.2 - 0.5$ at $z = 6$), compared to the hot halo mode (where $a = 0.2 - 0.4$ at $z = 6$). The method by which these SMBH spin distributions are calculated is given in Chapter 3.

By comparing Figure 5.2 to the expressions for the jet power in equations (5.2.2) and (5.2.3), we see that the dominance of the hot halo contribution to the jet power density at $z < 3$ is mainly due to the 80 times larger normalisation coefficient for

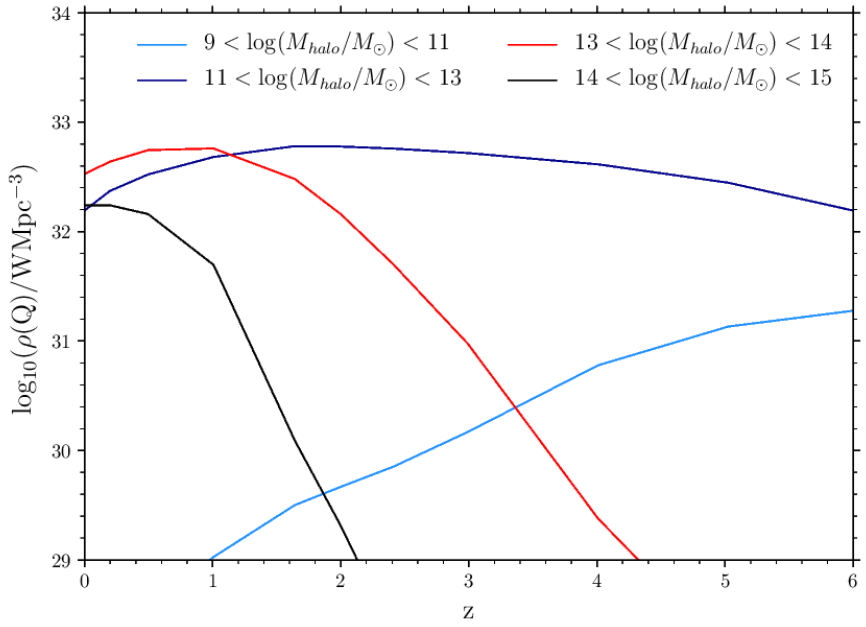

Figure 5.3: The predicted evolution of the jet power density split into different bins in halo mass: $9 < \log(M_{\rm halo}/M_\odot) < 11$ (light blue), $11 < \log(M_{\rm halo}/M_\odot) < 13$ (dark blue), $13 < \log(M_{\rm halo}/M_\odot) < 14$ (red), $14 < \log(M_{\rm halo}/M_\odot) < 15$ (black).

ADAFs compared to thin discs. The relative evolution of the jet power densities from the starburst and hot halo modes is therefore driven mainly by the differences in mass accretion rates and in the normalisations of the jet power relations (see equations (5.2.2) and (5.2.3)), with variations in the spin playing only a minor role.

In Figure 5.3, we present the jet power density split into the contribution from different halo masses. For $z < 1$, the jet power density is dominated by AGNs in haloes of mass $13 < \log(M_{\rm halo}/M_\odot) < 14$ (i.e. large galaxy groups and clusters), whereas for $z > 1$, the jet power density is dominated by AGNs in haloes of mass $11 < \log(M_{\rm halo}/M_\odot) < 13$ (i.e. individual galaxies and smaller groups).

In Figure 5.4, we show the evolution of the mean AGN jet efficiency, $\bar{\epsilon}_{\rm jet}$ (cf. Section 5.2.2), which is calculated as the ratio of the jet power density to the mass accretion rate density. The mean AGN jet efficiency is higher for the hot halo mode than for the starburst mode at all redshifts: this is mainly because the normalisation coefficient of the jet power for ADAFs is higher than for thin discs by a factor of 80 (see equations (5.2.2) and (5.2.3)), but this difference is slightly reduced by starburst

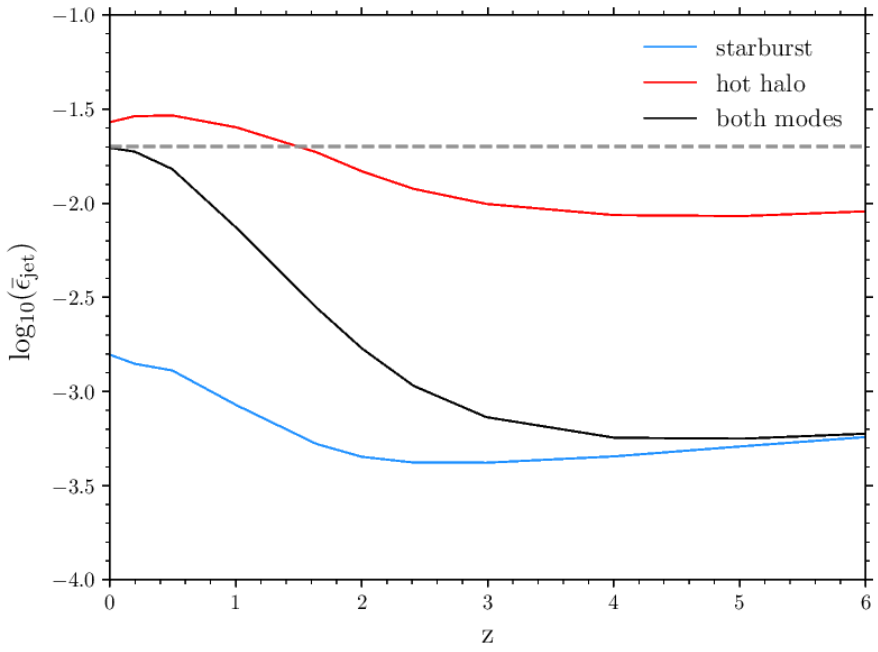

Figure 5.4: The predicted evolution of the AGN jet efficiency, $\bar{\epsilon}_{\rm jet} = \rho(Q)/\rho(\dot{M})c^2$ with redshift for the hot halo mode (red), for the starburst mode (blue), and for both modes combined (black). We also show the assumed constant AGN heating efficiency of the galaxy formation model, $\epsilon_{\rm heat} = 0.02$ (grey line).

mode AGNs having slightly higher spins, accreting at higher mass accretion rates, and having lower mass SMBHs. The jet efficiency of the two modes combined is similar to the hot halo mode jet efficiency for $z < 1$, and similar to that of the starburst mode for $z > 3$.

The mean AGN jet efficiency in either hot halo or starburst mode considered separately only varies moderately with redshift. In the hot halo mode, which is where AGN feedback is assumed to be active in the model, at lower redshift ($z < 2$) the AGN jet efficiency is $\bar{\epsilon}_{\rm jet} \approx 0.03$ whereas at higher redshift ($z > 2$) it is $\bar{\epsilon}_{\rm jet} \approx 0.01$, with an average over the history of the universe of 0.024. This time averaged value of the AGN jet efficiency is only 20% larger than the assumed constant value of the AGN heating efficiency, $\epsilon_{\rm heat} = 0.02$. The fact that the mean AGN jet efficiency for the hot halo mode only varies modestly with time suggests that the assumption that the AGN heating efficiency is constant through time is a reasonable approximation.

5.3.2 Comparison of jet power density to observational estimates

We now present the jet power density evolution of the model compared to the observational estimate of Ceraj et al. (2018). They obtain their estimate by measuring the evolution of the radio luminosity function at 1.4GHz, converting the 1.4GHz radio luminosities to jet powers using the Willott et al. (1999) relation, and then integrating over the subsequent jet power distribution. Ceraj et al. (2018) present their results both as data points in redshift bins, based on fitting an analytical luminosity function to data at that redshift, and also as a smooth function of redshift, obtained from an analytical pure luminosity evolution (PLE) model fit to their radio data.

The Willott et al. (1999) relation for jet power is derived using minimum energy arguments to estimate the minimum energy stored in the lobes given the observed synchrotron luminosity and combining with an estimate of the source age based on a dynamical model for the lobe expansion. This relation is expressed in terms of 1.4GHz luminosity in Heckman & Best (2014), and is given by:

$$Q = 4 \times 10^{35} \mathrm{W} \left(\frac{L_{\nu R, 1.4\mathrm{GHz}}}{10^{25} \mathrm{WHz}^{-1}} \right)^{6/7} (f_{\mathrm{W}})^{3/2}, \tag{5.3.6}$$

where f_{W} is a factor that accounts for uncertainties in the knowledge of the physics of radio sources (primarily the composition of the radio emitting plasma and the low energy cutoff of the electron energy distribution). Willott et al. (1999) estimate f_{W} to lie in the range $f_{\mathrm{W}} = 1 - 20$. Observational studies based on cavities in X-ray emitting hot gas around galaxies calculate the jet power from cavity volumes, cavity pressures, and an estimate of the lifetime of the cavity based on the buoyancy timescale (Rafferty et al., 2006; Bîrzan et al., 2008; Cavagnolo et al., 2010). Heckman & Best (2014) compiled these observational estimates of the jet power versus radio luminosity to find that they are consistent with the Willott et al. relation, with $f_{\mathrm{W}} = 15$. Using a different method based on estimating lobe expansion velocities using spectral ageing, Daly et al. (2012) also find radio luminosities and jet powers consistent with the Willott et al. relation, for a value of $f_{\mathrm{W}} = 4$. Other studies argue that other variables need to be considered in this relation, such as lobe size (because of radiative losses by the electron populations) (e.g. Shabala & Godfrey, 2013), the environment of sources (e.g. Hardcastle, 2018), and Fanaroff-Riley morphology (e.g. Turner & Shabala, 2015).

In Figure 5.5, we compare our predicted jet power density to the observational estimate of Ceraj et al. (2018). Comparing to their observational estimate using a value of $f_{\mathrm{W}} = 15$, our model is above their estimate by a factor of about 2 for $2 < z < 4$, and by a factor of about 4 for $z < 2$. Comparing to their observational estimate using a value of $f_{\mathrm{W}} = 20$, our model is above their estimate by a factor of about 1.5 for $2 < z < 4$, and by a factor of about 2.5 for $z < 2$. The jet power density in the model generally evolves a similar way to the observations, with both the model and observations showing an increase in jet power density with redshift for $z \lesssim 1$, and a decrease for $z \gtrsim 1$. However, the increase of the jet power density with redshift for $z \lesssim 1$ is slightly less steep in the model compared to the observations, and the model evolution is also slightly less steep compared to the observations for $z \gtrsim 3$.

While the model appears to be in some modest tension with the observations,

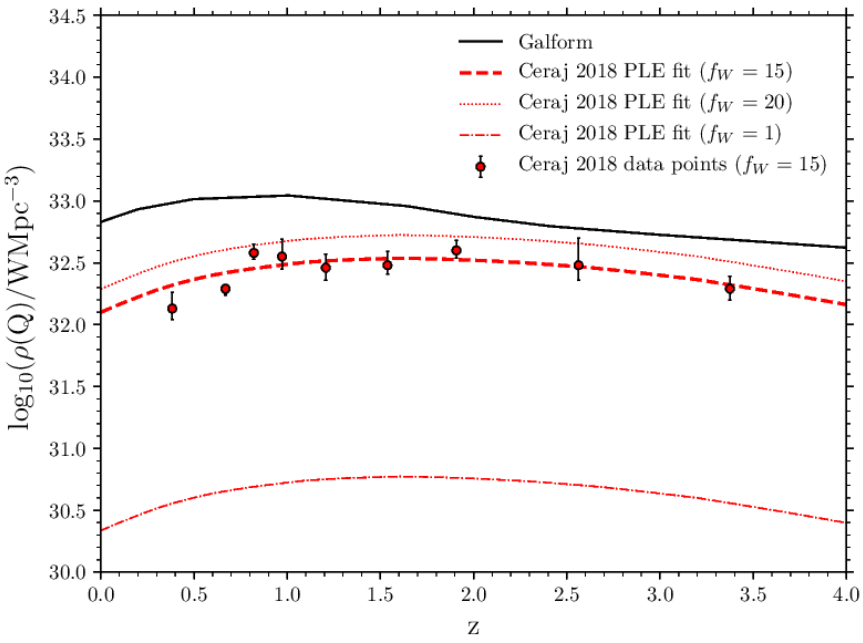

Figure 5.5: The predicted evolution with redshift of the jet power density in the model compared to the observational estimate from Ceraj et al. (2018). The model prediction (solid black line), is compared to the observational estimate from Ceraj et al. (2018) for $f_W = 15$, in redshift bins (red circles), and also using their pure luminosity evolution fit to the data (dashed red line). We also show the estimates for the jet power density evolution from Ceraj et al. (2018) for $f_W = 1$ (dot-dashed red line) and $f_W = 20$ (dotted red line). We only compare to the observational fit for $z > 4$, as at higher redshifts the fit is not well constrained by the data.

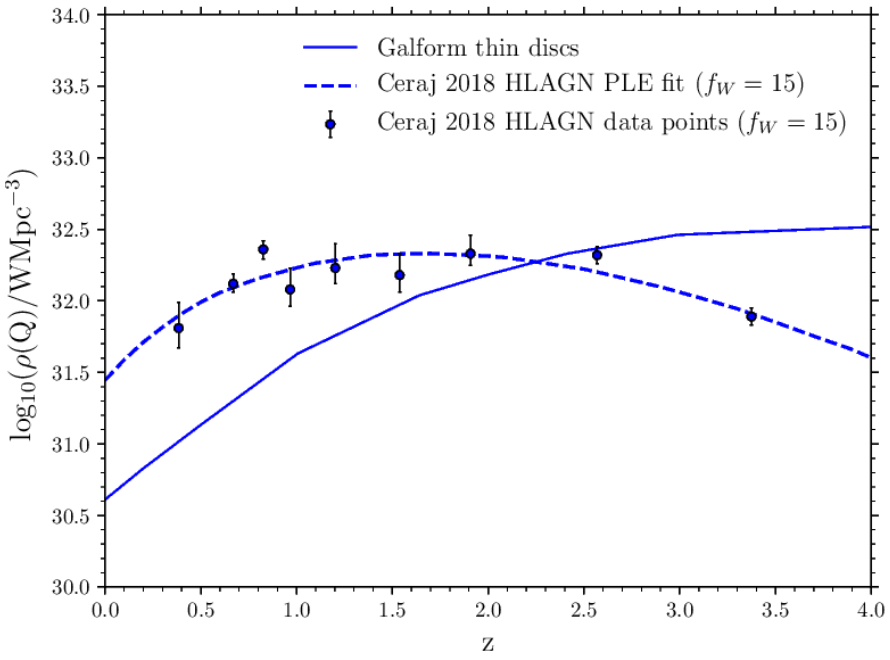

Figure 5.6: The predicted evolution of the jet power density from thin discs in the model (blue solid line) compared to the evolution of the jet power of 'HLAGN' from Ceraj et al. (2018) (the dashed blue line is the pure luminosity evolution fit to the data, and the blue points are the data in redshift bins). We only show the observational fit for $z > 4$.

there are several uncertainties in the observations to consider. First, there is uncertainty in the mean value of $f_{\rm W}$, which is estimated to take values in the range $1-20$ (Willott et al., 1999), and given that jet power depends on $f_{\rm W}$ as $Q \propto f_{\rm W}^{1.5}$, there are then significant uncertainties in the calculated Q values. Secondly, rather than each radio source having the same $f_{\rm W}$ value equal to the mean, it is likely that the radio source population has a distribution of $f_{\rm W}$ values around the mean, resulting in an increase in the derived jet power density due to the non-linear dependence of Q on $f_{\rm W}$. Overall, given the uncertainties, the model is reasonably consistent with the observations.

In Figure 5.6, we compare the predicted jet power density for AGNs accreting via a thin disc accretion state to the jet power density of 'moderate-to-high radiative luminosity AGN' (HLAGN) estimated from the observations by Ceraj et al. (2018).

In the observations, HLAGN are selected using a combination of (i) a threshold X-ray luminosity, (ii) mid-infrared colour-colour selection and (iii) template fitting to the spectral energy distributions (see Ceraj et al., 2018). While HLAGN in the observations do not exactly correspond to thin discs in the model, one would expect radio sources accreting via a thin disc accretion state to have relatively high radiative luminosities, and so this is an approximate comparison. We find that while the model underpredicts the observations for $z < 3$ and overpredicts the observations for $z > 3$, it reproduces the behaviour that the number density of these objects should increase with redshift for $0 < z < 2$. A more thorough application of these selections for HLAGN to the model in the future may give closer agreement with the observations. Similar comparisons to Figures 5.5 and 5.6 were done in Ceraj et al. (2018), based on a slightly earlier version of the model.

5.4 Evolution of the radio luminosity function of AGN

We now show our model predictions for the radio luminosity function of AGN at $z = 0$ compared to observational estimates, before analysing the evolution of the radio luminosity function in the model compared to observations. In the left panel of Figure 5.7 we present the radio luminosity function at $z = 0$ compared to observational estimates. The values of $A_{\rm ADAF}$ and $A_{\rm TD}$ were varied freely to give the agreement seen between the predictions and the observations at $z = 0$ in Figure 5.7, with the adopted values being given in Table 3.1. The model is able to match the observations very well, although there are some tensions between the different observational data, that we now describe.

First, at $L_\nu \sim 10^{25}{\rm WHz}^{-1}$, the Smolčić et al. (2009) and Smolčić et al. (2017) number densities are about 10 times higher than the Rigby et al. (2011) and Best et al. (2014) number densities. As discussed in Section 6.1.1 of Padovani et al. (2015), this discrepancy may be a result of the sample selection. Rigby et al. (2011)

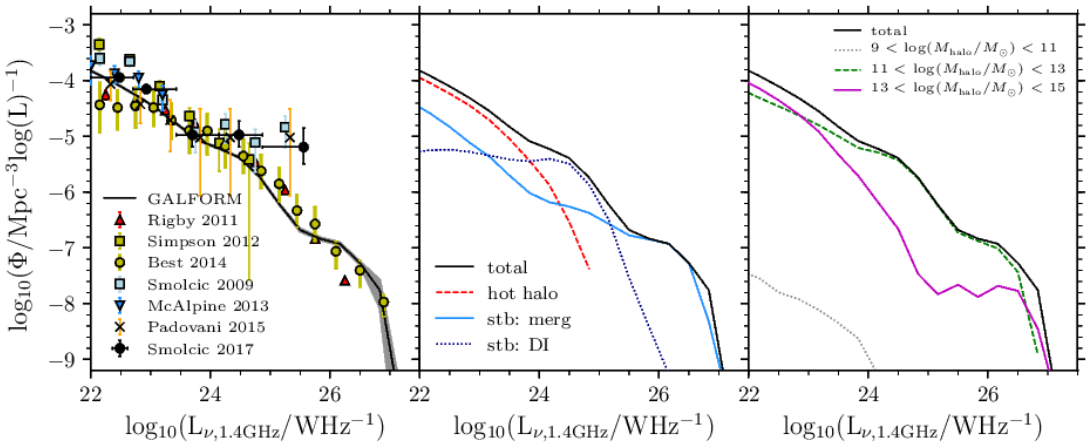

Figure 5.7: *Left panel:* the predicted 1.4GHz luminosity function of AGN at $z = 0$ compared to observational estimates from VLA-COSMOS (Smolčić et al., 2009) (light blue squares), CENSORS (Rigby et al., 2011) (red triangles), the Subaru/XMM-Newton Deep Field radio source sample (Simpson et al., 2012) (yellow squares), another VLA survey (McAlpine et al., 2013) (blue triangles), a sample from combining eight different surveys (Best et al., 2014) (yellow circles), the Extended CDF South VLA sample (Padovani et al., 2015) (crosses) and COSMOS 3GHz data (Smolčić et al., 2017) (black circles). The line is the GALFORM prediction, with the shaded region representing the Poisson errorbars. *Middle panel:* the predicted radio luminosity function at $z = 0$ (black solid line) split into contributions from the hot halo mode (red dashed line), starbursts triggered by mergers (light blue solid line), and starbursts triggered by disc instabilities (dark blue dotted line). *Right panel:* the the predicted radio luminosity function at $z = 0$ (black solid line) split into the contributions from haloes of mass $9 < \log(M_{\rm halo}/M_{\odot}) < 11$ (grey), $11 < \log(M_{\rm halo}/M_{\odot}) < 13$ (green) and $13 < \log(M_{\rm halo}/M_{\odot}) < 15$ (purple).

and Best et al. (2014) select a sample of steep-spectrum sources ($\alpha > 0.5$)[4], in a variety of surveys with smaller areas and smaller flux density limits, whereas Smolčić et al. (2009) and Smolčić et al. (2017) select their sample with only a flux density limit. This difference could also be caused by sample variance caused by large scale structure, with the volumes at $z \sim 0$ probed by the surveys in Smolčić et al. (2009) and Smolčić et al. (2017) being relatively small. The quoted observational errors at this luminosity are fairly large, with the errors for Smolčić et al. (2009), Best et al. (2014), and Smolčić et al. (2017) being about 0.5 dex. Our predictions follow Rigby et al. (2011) and Best et al. (2014) in this regime and to higher luminosities.

Secondly, for $L_\nu < 10^{23}\mathrm{WHz}^{-1}$, there is variation in the observational estimates spanning a range of about 1 dex, which may also be for the same reason as for $L_\nu \sim 10^{25}\mathrm{WHz}^{-1}$. Our model follows the data from McAlpine et al. (2013) and Smolčić et al. (2017) most closely. These two regimes may warrant further observational studies to constrain the radio luminosity function at these luminosities.

In the middle panel of Figure 5.7 we present the predicted radio luminosity function for AGN at $z = 0$ split by fuelling mode into contributions from the hot halo mode and from starbursts triggered by mergers and disc instabilities. The contribution from the hot halo mode is dominant for $L_\nu < 10^{24}\mathrm{WHz}^{-1}$, while for $10^{24}\mathrm{WHz}^{-1} < L_\nu < 10^{26}\mathrm{WHz}^{-1}$ the dominant contribution is from starbursts triggered by disc instabilties, and for $L_\nu > 10^{26}\mathrm{WHz}^{-1}$ the dominant contribution is from starbursts triggered by galaxy mergers.

In the right panel of Figure 5.7 we show the predicted radio luminosity function at $z = 0$ for AGN split into contributions from AGNs in different mass haloes. We find that for $10^{23}\mathrm{WHz}^{-1} < L_\nu < 10^{26.5}\mathrm{WHz}^{-1}$, the contribution from haloes of mass $11 < \log(M_{\mathrm{halo}}/M_\odot) < 13$ (individual galaxies and smaller groups) dominates, whereas for $L_\nu < 10^{23}\mathrm{WHz}^{-1}$, and $L_\nu > 10^{26.5}\mathrm{WHz}^{-1}$ the contribution from AGNs in haloes of mass $13 < \log(M_{\mathrm{halo}}/M_\odot) < 15$ (large galaxy groups and clusters) dominates. The $z = 0$ radio luminosity function at intermediate luminosities ($10^{23}\mathrm{WHz}^{-1} < L_\nu < 10^{26.5}\mathrm{WHz}^{-1}$) is therefore predicted to probe AGNs in different mass haloes

[4]This is for an assumed radio spectrum $S_\nu \propto \nu^{-\alpha}$

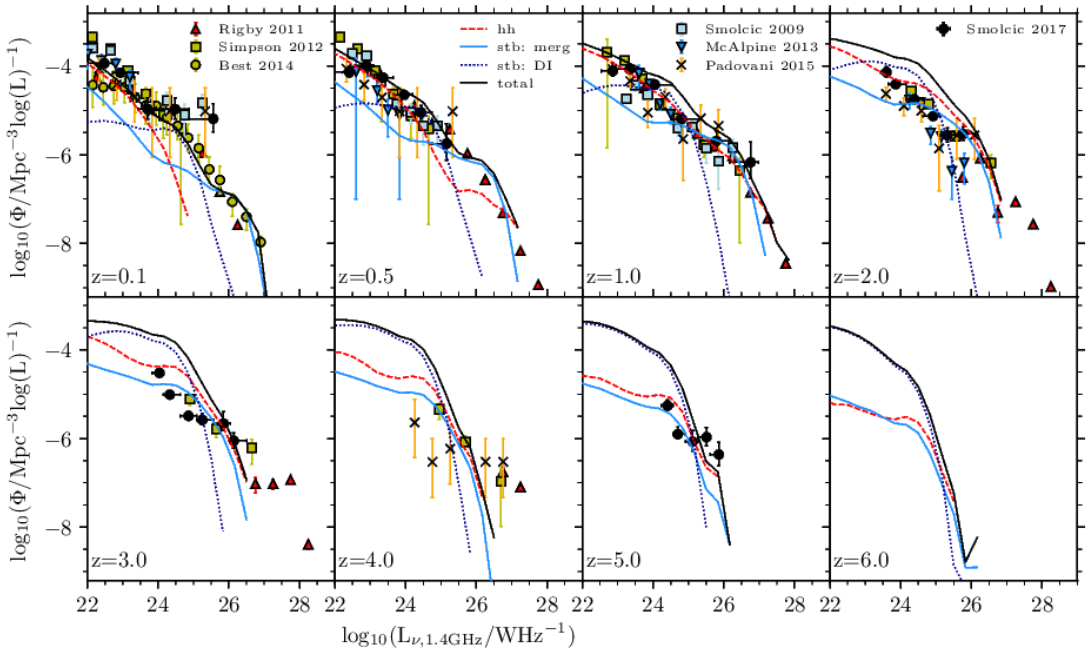

Figure 5.8: The evolution of the predicted rest-frame 1.4GHz luminosity function of AGNs compared to observational estimates. The symbols for the observations, and the linestyles for the different fuelling modes of the model are the same as for Figure 5.7.

to the jet power density at $z = 0$, which is dominated by AGNs in haloes of mass $13 < \log(M_{\rm halo}/M_{\odot}) < 15$.

In Figure 5.8 we present the predicted evolution of the AGN radio luminosity function for $0 < z < 6$ compared to observational estimates. The model prediction fits well to the observations at $z = 0$ as previously discussed, but evolves differently compared to the observations. At $z = 1$, for $L_{\nu} > 10^{26}$WHz^{-1} and for $L_{\nu} < 10^{24}$WHz^{-1}, the model prediction is still in good agreement with the observations. However, the model overpredicts the number of objects around $L_{\nu} \sim 10^{25}$WHz^{-1} by about 0.5 dex. As we look to redshifts $z > 3$, a trend emerges where the model overpredicts the luminosity function for low luminosities, underpredicts the luminosity function for high luminosities, but predicts a similar number density to the observations for intermediate luminosities. For example, at $z = 4$, the model overpredicts the number density for $L_{\nu} < 10^{25}$WHz^{-1}, underpredicts

the number density for $L_\nu > 10^{26}\mathrm{WHz}^{-1}$, and agrees with the observations for $10^{25}\mathrm{WHz}^{-1} < L_\nu < 10^{26}\mathrm{WHz}^{-1}$. This luminosity at which the model agrees with the observations decreases slightly with increasing redshift. The observations also have some uncertainties, for example at $L_\nu \sim 10^{25}\mathrm{WHz}^{-1}$ at $z = 4$, the Padovani et al. (2015) errors are about 1.3 dex, while the observed number densities from Simpson et al. (2012) and Padovani et al. (2015) are different by 1 dex.

In Figure 5.8 we also show the evolution of the contributions to the luminosity function from hot halo mode accretion and starbursts triggered by mergers and disc instabilities. At $z = 1$, similarly to $z = 0$, the hot halo mode contribution dominates the luminosity function for low luminosities ($L_\nu < 10^{24}\mathrm{WHz}^{-1}$), the contribution from starbursts triggered by disc instabilities dominates for intermediate luminosities ($10^{24}\mathrm{WHz}^{-1} < L_\nu < 10^{25}\mathrm{WHz}^{-1}$), and the contribution from starbursts triggered by mergers dominates for high luminosities ($10^{25}\mathrm{WHz}^{-1} < L_\nu < 10^{27}\mathrm{WHz}^{-1}$). The hot halo mode contribution also dominates at the very highest luminosities ($L_\nu > 10^{27}\mathrm{WHz}^{-1}$), unlike at $z = 0$, although this is the result of only a few objects. At $z = 3$, the contribution from starbursts triggered by disc instabilties dominates at low luminosities ($L_\nu < 10^{25}\mathrm{WHz}^{-1}$) and the hot halo mode contribution dominates at higher luminosities ($L_\nu > 10^{25}\mathrm{WHz}^{-1}$). This behaviour continues out to $z = 6$.

In the radio luminosity functions presented in Figures 5.7 and 5.8, we used the values of A_{ADAF} and A_{TD} from Table 5.1 to calculate radio luminosities which are most appropriate for core-dominated sources. We then assumed that the radio luminosity is dominated by the core emission for these comparisons. We now consider the effect on our results if we compare to a radio luminosity function of core-dominated sources.

To do this, we recalibrate the values of A_{ADAF} and A_{TD} to give good agreement with the core-dominated radio luminosity function of Yuan et al. (2018) at $z = 0$, finding that this requires $A_{\mathrm{ADAF}} = 3 \times 10^{-6}$ and $A_{\mathrm{TD}} = 0.2$. These recalibrated A values are both lower than the values for the fiducial model, and A_{ADAF} has been reduced by slightly more than A_{TD}. This reduction in the A values accounts for how the core-dominated luminosity function has a slightly lower number density at low luminosities (about 0.5 dex at $L_\nu \sim 10^{22}\mathrm{WHz}^{-1}$), and a reasonably lower number

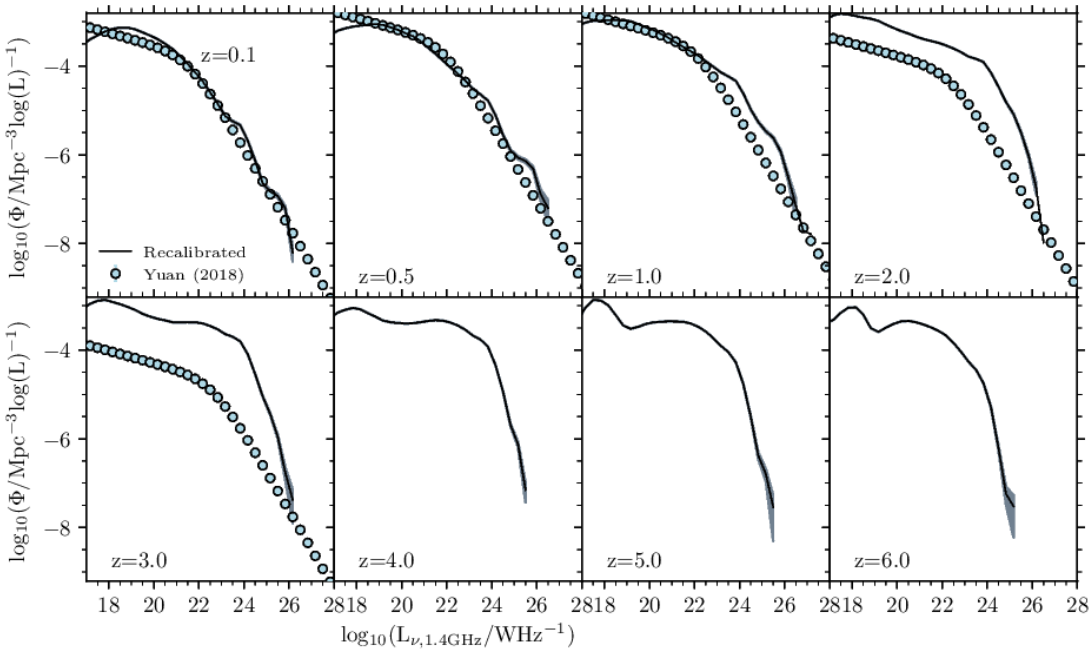

Figure 5.9: The evolution of the recalibrated ($A_{\mathrm{ADAF}} = 3 \times 10^{-6}$ and $A_{\mathrm{TD}} = 0.2$) rest-frame 1.4GHz AGN luminosity function for core-dominated sources (black line with shading for errorbars) compared to the observational estimate of Yuan et al. (2018) (black points).

density at high luminosities (about 1 dex at $L_\nu \sim 10^{26}\mathrm{WHz}^{-1}$).

In Figure 5.9, we present the evolution of this recalibrated model compared to the observational data from Yuan et al. (2018)[5]. The model is in good agreement with the observations at all luminosities at $z = 0.5$, and for $L_\nu < 10^{22}\mathrm{WHz}^{-1}$ at $z = 1$, but overpredicts the observations for $z = 2$ and $z = 3$. This occurs because the model number density is roughly constant with redshift for $1 < z < 3$, whereas the number density of the observations decreases over that redshift interval.

This overprediction of the recalibrated model for $z > 2$ may be caused by the double power-law form of the luminosity function of Yuan et al. (2018) not being a good fit to the actual luminosity function. Alternatively this may be because the simple model we are using for the core-dominated emission is not sufficiently detailed to capture the physical reason for the decrease in the number of core-dominated radio sources. By using a more detailed model for radio lobe growth, and investigating the core-dominated sources within that model, better agreement might be able to be obtained.

5.5 Conclusions

Observational estimates of the evolution of the radio luminosity function have greatly improved in recent years, and insights into the evolution of radio jets can be obtained by investigating the evolution of jet powers which can be determined from the radio luminosities. Understanding the evolution of radio AGN is important for understanding galaxy evolution, given the role they are believed to play in shutting off star formation via AGN feedback. In Chapter, we present predictions for the evolution of jet powers and radio luminosities from the model.

First, we predict the evolution of the jet powers. We present the distribution of jet powers (we show the product of jet power and comoving number density) of objects at $z = 0, 3, 6$, finding that the hot halo mode and ADAF accretion state contributions dominate for higher jet powers ($Q \gtrsim 10^{33}$) at lower redshift ($z = 0$),

[5]The observations from Yuan et al. (2018) have been corrected to 1.4GHz using a spectral index $\alpha = 0$

contribute approximately equally to the starburst mode and thin disc accretion state at $Q \sim 10^{36}$W at $z = 3$, but do not dominate the jet power distribution at the highest redshifts ($z = 6$). The starburst mode and thin disc accretion state contributions dominate at low jet powers and low redshift, and at all jet powers at higher redshifts. The peak of this distribution dominates the jet power density. We find that the peak of this distribution is at $Q \sim 10^{36}$W, independent of redshift for $0 < z < 6$. The distribution for the starburst and hot halo contributions also peaks at this jet power.

We then explore the predicted evolution of the jet power density. The jet power density is dominated by the contribution from haloes of mass $13 < \log(M_{\rm halo}/M_{\odot}) < 14$ for $z < 1$, and by the contribution from haloes of mass $11 < \log(M_{\rm halo}/M_{\odot}) < 13$ for $z > 1$. The mean AGN jet efficiency, which is the ratio of the jet power density to the mass accretion rate density, for the hot halo mode only varies modestly with time, suggesting that the assumption in the galaxy formation model that AGN heating efficiency is constant through time is reasonable. We then compare the jet power density evolution to the observational estimate of Ceraj et al. (2018) based on the measured radio luminosity function. The model prediction is slightly higher than the observational estimate, but reproduces the general shape of the jet power density evolution. The model evolves somewhat less steeply than the observations at low and high redshifts. Given the uncertainties in observationally estimating jet powers from radio luminosities, this tension may not be significant.

We then present the predicted radio luminosity function, where the two free parameters of the model relating radio luminosity to jet power are calibrated to the observed AGN radio luminosity function at $z = 0$. The model is able to give very good agreement with the observational estimates. We split the radio luminosity function at $z = 0$ into contributions from different gas fuelling modes, finding that the contribution from the hot halo mode dominates at low luminosities ($L_{\nu} < 10^{24}$WHz^{-1}), the contribution from starbursts triggered by disc instabilities dominates at intermediate luminosities (10^{24}WHz$^{-1} < L_{\nu} < 10^{26}$WHz^{-1}), and the contribution from starbursts triggered by mergers dominates at high luminosities ($L_{\nu} > 10^{26}$WHz^{-1}). We also find that the radio luminosity function at $z = 0$ at

intermediate luminosities ($10^{23}\mathrm{WHz}^{-1} < L_\nu < 10^{26.5}\mathrm{WHz}^{-1}$) is dominated by the contribution from AGNs in haloes of mass $11 < \log(M_{\mathrm{halo}}/M_\odot) < 13$, whereas at $L_\nu < 10^{23}\mathrm{WHz}^{-1}$ and $L_\nu > 10^{26.5}\mathrm{WHz}^{-1}$, the radio luminosity function is dominated by AGNs in haloes of mass $13 < \log(M_{\mathrm{halo}}/M_\odot) < 15$.

We present predictions for the evolution of the radio luminosity function in the redshift range $0 < z < 6$. The predictions evolve similarly to the observations, although at higher redshift the model luminosity function is steeper than that implied by observations. At the highest redshifts ($z > 3$) we find that the radio luminosity function is dominated by the contribution from starbursts triggered by disc instabilities for $L_\nu < 10^{25}\mathrm{WHz}^{-1}$ and by the contribution from the hot halo mode for $L_\nu > 10^{25}\mathrm{WHz}^{-1}$.

Finally, we present a recalibration of the model where we calibrate the two free parameters of the radio model to the core-dominated radio luminosity function of Yuan et al. (2018) at $z = 0$. We find that the model fits adequately out to $z = 1$, but overpredicts the observations for $z > 2$.

While the model generally provides a good fit to the observational data, and incorporates some key physics by calculating jet powers and radio luminosities using a prescription based on SMBH mass, accretion rate and spin, the model could be improved. The scaling model relating the radio luminosity to the jet power here was developed for core-dominated radio emission, however, in real radio AGNs there is also radio emission from extended lobe structures, which are particularly important at lower frequencies. In the next Chapter, we explore predictions for the evolution of extended radio lobes using an analytic model for the evolution of the dynamics of radio lobes and the radio emission.

Chapter 6

Extended radio emission

6.1 Introduction

Radio surveys have detected extended radio sources originating from Active Galactic Nuclei (AGNs) with a wide variety of sizes, luminosities and morphologies throughout the Universe, with some of these sources having sizes up to several Mpc (e.g. Muxlow & Garrington, 1991). Understanding these radio sources helps us to understand why there are such a large variety of radio sources observed. The energy required for these radio sources to propagate into their surrounding environment is provided by a jet, thought to originate from an accretion disc around a supermassive black hole (SMBH).

Our theoretical understanding of the evolution of extended radio sources has advanced greatly in recent years. Early works such as Blandford & Rees (1974) and Scheuer (1974) formulated models in which a collimated jet from the SMBH supplies energy to a 'hotspot', and where a 'cocoon' is inflated around the jet by the material flowing out of the hotspot. Following the work of Falle (1991), a great advance in the analytic models was made by Kaiser & Alexander (1997), where a model was presented in which the lobe grows self-similarly, i.e. the size of the lobe grows as a power law with time while the ratio of the length to the width of the lobe remains constant with time. A treatment of synchrotron emission and energy loss processes of the electron populations was then added in Kaiser et al. (1997) to make predictions for radio sources as their radio luminosities and sizes evolve. Many other related

analytic models for FRIIs have been developed (e.g. Blundell et al., 1999; Alexander, 2002; Manolakou & Kirk, 2002; Kaiser & Cotter, 2002; Kaiser & Best, 2007; Nath, 2010; Mocz et al., 2011; Hardcastle, 2018), and although they are less analytically tractable, analytical FRI models have also been developed (e.g. Wang et al., 2009; Luo & Sadler, 2010). For the models stated here, the FRII models assume that the jets are overpressured compared to their external medium, and hence cause a shock to form, whereas the FRI models assume that the radio source is in pressure balance with its environment. Some of the models suggest possible causes for the FRI/FRII transition, such as FRIs forming as a turbulent layer develops between the jet and lobe in FRIIs (Wang et al., 2011) or that FRIIs transition to FRIs when the velocity at the surface of the FRII cocoon becomes equal to the sound speed of the external medium (Turner & Shabala, 2015). Some observations have suggested that the two Fanaroff-Riley types are fundamentally different, with FRIs being composed of an energetically dominant proton population not present in FRIIs (Croston et al., 2018).

Alongside the analytic models, insights have also been gained from numerical simulations of jets, such as possible mechanisms for the FRI/FRII dichotomy (e.g. Krause et al., 2012; Ehlert et al., 2018), the role of environment in determining radio source properties (e.g. Hardcastle & Krause, 2013; Yates et al., 2018), and the role jets play in heating clusters (e.g. Weinberger et al., 2017). Some models also present radio emission predictions within the context of a galaxy formation model, either using an empirical model (e.g. Saxena et al., 2017), or using galaxy environments from a semi-analytic model of galaxy formation (e.g. Turner & Shabala, 2015), or by using SMBH and galaxy properties from a semi-analytic model of galaxy formation (e.g. Fanidakis et al., 2011; Raouf et al., 2017).

In this Chapter, we make predictions for extended radio sources in AGNs at $z = 0$ from the galaxy formation model GALFORM we are using in this thesis. The combination of a self-consistent SMBH spin evolution model and a detailed model for the evolution of extended radio sources has not been presented before, and we compare the model in detail to observed radio luminosity functions at different frequencies, radio lobe sizes, and FRI/FRII fractions for the first time. In this

Chapter, we compare to recent LOFAR Two-metre Sky Survey (LoTSS) data, and this model will be able to be compared to radio data from future surveys such as those with ASKAP or SKA.

This Chapter is structured as follows. In Section 6.2 we describe the model used. In Section 6.3 we show some examples of radio lobes in the model. In Section 6.4 we present the results from the model at $z = 0$. In Section 6.5 we present the effect on the results of varying different free parameters of the extended radio emission model. In Section 6.6 we give our conclusions.

6.2 The model

6.2.1 Jet powers and hot gas environment

We use the expressions for the jet power, Q, in Section 5.2.1, which are dependent on SMBH mass, mass accretion rate and spin. The hot halo gas profile into which the radio lobes grow is that of the GALFORM model, which is given by:

$$\rho(r) = \frac{\rho_0 r_c^2}{(r^2 + r_c^2)}, \tag{6.2.1}$$

where ρ_0 is the normalisation on the density, which is calculated from the hot gas mass as calculated in GALFORM, $M_{\rm hot}$, via:

$$\rho_0 = \frac{M_{\rm hot}}{4\pi r_c^3((\frac{r_{\rm vir}}{r_c}) - \tan^{-1}(\frac{r_{\rm vir}}{r_c}))}. \tag{6.2.2}$$

In these expressions, $r_c = 0.1 r_{\rm vir}$, and $r_{\rm vir}$ is the virial radius of the halo, as defined in equation (2.1.1).

6.2.2 The dynamics of lobe evolution

The analytic model of radio lobe evolution of Turner & Shabala (2015) brings together two different theoretical models for FRII and FRI sources respectively. The first of these is the theoretical model for FRIIs of Kaiser & Alexander (1997). In that model, a jet emerges from the region around the AGN with a constant opening angle. A reconfinement shock is assumed to form, which causes the jet to be

collimated, keeping a constant radius as it propagates outwards. The propagation of the jet at a speed above the sound speed of the external medium causes a bow shock to form. The jet interacts with the shocked material at the 'hotspot', from which material backflows to form a 'cocoon' around the jet. The cocoon is formed of relativistic plasma from the hotspot. This material then emits via synchrotron emission, so it is seen at radio wavelengths as a radio lobe. The cocoon is overpressured relative to the external medium, and the lobe grows as an ellipsoid in a self-similar way, with a constant axial ratio, A, which is the ratio of the semi-major axis of the ellipsoid to the semi-minor axis of the ellipsoid. In the second model, from Luo & Sadler (2010) which is for FRI sources, there is no bow shock, no hotspot, and the lobe is in pressure equilibrium with its external environment. This assumed pressure equilibrium means that in this regime, the lobe is not necessarily an ellipsoid.

The Turner & Shabala (2015) model makes several improvements over earlier models, by (i) combining FRII and FRI sources in a unified way, (ii) adopting a non-power law density profile, and (iii) including the effect of Rayleigh-Taylor instabilities. In the Turner & Shabala (2015) model, the radio lobe is divided into 'angular elements', which are the part of the lobe between θ and $\theta + d\theta$, where θ is the angle to the major axis of the lobe, as shown in the schematic of the radio lobe in Figure C.1. The evolution of the radius, velocity and pressure of each angular element are calculated separately. Each angular element of the lobe starts out as a 'supersonic' element, and the radio lobe is an ellipsoid, with a constant axial ratio when the expansion is highly supersonic and the slope of the density profile is the same for all angular elements. The model assumes that the bow shock is close to the cocoon (to keep the model analytically tractable). Once the velocity normal to the surface of the cocoon is equal to the sound speed of the external environment (the external medium has adiabatic index Γ_x), this angular element transitions into a 'subsonic' element, and the element follows the FRI evolution model described in Luo & Sadler (2010). Once one of the angular elements becomes subsonic, the lobe is no longer forced to be ellipsoidal in shape. Following Turner & Shabala (2015), when an angular element is subsonic, it becomes susceptible to Rayleigh-Taylor instabilities, which reduce the radio luminosity. This is because

as the cocoon becomes entrained by the surrounding medium, the energies of the synchrotron emitting electrons become collisionally reduced to the ambient energy level of the denser, surrounding environment, and therefore their radio emission is reduced. In the model, it is assumed that there is no radio emission from the parts of the cocoon where Rayleigh-Taylor mixing is occurring, which eventually causes the radio luminosity to fall to zero. The growth of Rayleigh-Taylor instabilities are quantified by the parameter, κ_{RT}. The equations for the lobe evolution are given in Appendix C.1.

Once the evolution of the radius, velocity, and pressure, has been calculated for each angular element, the total pressure is calculated as the volume weighted average of the pressures of all the angular elements. The total pressure and volume are then used to calculate the radio emission of the lobe. In this lobe expansion model, radiative loss processes are treated after the lobe size and pressure have been calculated, which is an assumption often used in theoretical models of radio lobe evolution (e.g. Kaiser & Alexander, 1997; Hardcastle, 2018).

6.2.3 The evolution of lobe synchrotron emission

The presence of highly relativistic electrons in a magnetic field causes the electrons to emit radiation by synchrotron emission. Following Turner & Shabala (2015), we adopt the prescription of Kaiser et al. (1997) for the radio emission. In this model, the magnetic field is assumed to be completely tangled, so an average over electrons moving at all pitch angles is taken, and electrons are assumed to emit only at their critical frequency. This yields an expression for the luminosity (cf. equation 2 of Kaiser et al., 1997):

$$L_\nu = \frac{4}{3}\sigma_T c u_B \frac{\gamma^3}{\nu} n(\gamma) V, \tag{6.2.3}$$

where σ_T is the Thomson cross-section, u_B is the magnetic energy density, γ is the Lorentz factor of the electron population, ν is the observed frequency, $n(\gamma)d\gamma$ is the number density of electrons with Lorentz factors between γ and $\gamma + d\gamma$, and V is the volume of the lobe. $n(\gamma)$ and u_B are assumed to be constant throughout the lobe.

A population of electrons is injected into the cocoon at an injection time, $t_{\rm i}$, with number density $n(\gamma_i, t_i) = n_0(t_i)\gamma_i^{-s} d\gamma_i$, where γ_i is the Lorentz factor of the injected electrons and $n_0(t_i)$ is the normalisation of this distribution, as calculated in Appendix C.2. This injected electron energy distribution is assumed to have low and high energy cutoffs at $\gamma_{i,min}$ and $\gamma_{i,max}$ respectively. This electron population evolves, as the electrons lose kinetic energy. The electrons lose energy by adiabatic losses (due to adiabatic expansion of the lobe), synchrotron losses (due to the synchrotron emission), and inverse-Compton losses (electrons scattering off CMB photons). The cocoon is assumed to be composed of three 'fluids': a relativistic electron fluid with energy density u_e, a magnetic field fluid with energy density u_B, and a thermal fluid of non-radiating particles with energy density u_T. The adiabatic index of the magnetic fluid is Γ_B. We define the ratios $k^t = u_T/u_e$ and $q_B = u_B/(u_e + u_T)$, which are free parameters of the model. Following the derivation in Kaiser et al. (1997) which we give in Appendix C.2, we obtain the expression for the luminosity per unit frequency for both lobes of a radio source:

$$\begin{aligned} L_\nu(t) = \int_0^t & \frac{4\sigma_T c q_B}{3\nu(q_B+1)} Q n_0(t_i) A^{2(1-\Gamma_c)/\Gamma_c} \\ & \times \gamma_i(t,t_i)^{2-s} \gamma(t_i) \Big(\frac{V(t)}{V(t_i)}\Big)^{(-\Gamma_B - 1/3)} dt_i, \end{aligned} \tag{6.2.4}$$

where A is the axial ratio, and Γ_c is the adiabatic index of the cocoon.

6.2.4 The duty cycle of the jets

The duration of the radio lobe events is important for determining the observed radio properties. For each object, we calculate a jet power from equation (5.2.2) or (5.2.3) based on its SMBH mass, mass accretion rate and spin. For the two different types of AGN gas fuelling from Section 2.7, we calculate the durations of the AGN events differently.

First, for the starburst mode, we assume that the starburst occurs over a timescale, $t_{\rm acc} = f_q t_{\rm bulge}$ where $t_{\rm bulge}$ is the dynamical timescale of the bulge and $f_q = 10$ is a free parameter. Secondly, for the hot halo mode, in which the SMBH is steadily accreting from the hot gas in the halo, we assume that the SMBH releases a jet

in a series of epsiodes. For simplicity, we assume that the switching on or off of a radio source is a random process, with the duration of each 'on' and 'off' phase for a particular radio source, $t_{\rm on}$ and $t_{\rm off}$, being randomly selected from exponential distributions with average values of $\bar{t}_{\rm on}$ and $\bar{t}_{\rm off}$ respectively. $\bar{t}_{\rm on}$ and $\bar{t}_{\rm off}/\bar{t}_{\rm on}$ are free parameters of the model.

In the hot halo mode, which is when AGN feedback is active, the SMBH mass accretion rate, $\dot{M}_{\rm hh,average}$, is calculated as the heating rate that heats the halo gas sufficiently to balance radiative cooling in the halo for an assumed constant heating efficiency. If the jet has 'off' phases then the mass accretion rate during the 'on' phase needs to be higher to balance cooling in the halo on average. We therefore set the accretion rate during the off phase to zero, and increase the mass accretion rate in the hot halo mode during the on phases, $\dot{M}_{\rm hh,on}$, by:

$$\dot{M}_{\rm hh,on} = (1 + \bar{t}_{\rm off}/\bar{t}_{\rm on})\dot{M}_{\rm hh,average}, \tag{6.2.5}$$

when the AGN jet is on. We emphasise that this duty cycle model is chosen for simplicity, and may require modification in the future.

6.2.5 Remnant phase

Once the AGN switches off, the jets stop supplying energy to the radio lobes, so electrons stop being injected into the lobe, and so the radio source fades. In this fading period, the pressure and volume of the lobe still evolve, and the electrons injected before the jet switched off can still emit synchrotron radiation. Therefore, in the model, once the jet is switched off, the pressure and volume of the lobe are assumed to evolve adiabatically. In equation (6.2.4), $Q = 0$ for all injection times greater than the time at which the source is switched off.

6.2.6 Radio lobes outside the halo

In GALFORM, gas falling into haloes is shock-heated to the virial temperature. Outside of the haloes, the gas is not in hydrostatic equilibrium, and so within this picture a radio lobe outside of the halo would cease to be pressure confined and hence ra-

dially expand, meaning that the electrons will quickly stop emitting synchrotron radiation. In the model this is implemented by setting the luminosity to zero for any lobe that grows longer than the virial radius of the halo. This only has a small effect on the predictions, as most lobes are shorter than the halo virial radius.

6.2.7 Calibrating the radio model

We list the free parameters of the extended radio emission model in Table 6.1. For the three parameters shown in the upper part of Table 6.1 (Γ_B, Γ_c, Γ_x), we adopt the values used in Turner & Shabala (2015). For the three parameters shown in the middle section of Table 6.1 ($\gamma_{i,max}$, κ_{RT}, and q_B), we explored the effect of varying the parameters on the model predictions shown in Section 6.4. We found that varying these parameters only negligibly affects the model predictions. Hence we use values from other studies and do not show the effect of varying these parameters in Section 6.5. The value of $\gamma_{i,max} = 10^{10}$ is similar to that of Turner & Shabala (2015) (which uses infinity, as obtained from private communication[1]), the value of $\kappa_{RT} = 0.05$ follows Turner & Shabala (2015), and the value of $q_B = 0.4$ follows Hardcastle (2018). For the six free parameters shown in the lower section of Table 6.1 (A, $\gamma_{i,min}$, k^t, s, $\bar{t}_{\rm on}$ and $\bar{t}_{\rm off}/\bar{t}_{\rm on}$), we explored their effect on the model predictions finding that they affect the model predictions reasonably. We show the effect of varying these parameters on the model predictions in Section 6.5. We calibrated these parameters on these observations. The calibration was done by-eye, using plots similar to that shown in Section 6.5. We give the observations that are most important in determining each parameter value in the right column of Table 6.1.

6.3 Example properties of radio lobes in the model

Before comparing predicted properties of the entire population of radio lobes with observations, we show some examples of radio lobe properties and evolution pro-

[1]Note that the dependence of luminosity on $\gamma_{i,max}$ in equation (C.2.25) is fairly weak for large values, and so for large values of $\gamma_{i,max}$, the predictions are relatively insensitive to the value adopted.

Table 6.1: The values of the free parameters of the extended radio emission model. The upper part of the table shows parameters where the values adopted are from other studies, the middle part of the table shows parameters which have been allowed to vary, but only make a small difference to the predictions, and the lower part of the table shows parameters which have allowed to freely vary, and significantly affect the predictions.

Parameter	Value	Range	Description	How chosen
Γ_B	5/3	-	Adiabatic index of magnetic field	Turner & Shabala (2015)
Γ_c	5/3	-	Adiabatic index of cocoon	Turner & Shabala (2015)
Γ_x	5/3	-	Adiabatic index of external medium	Turner & Shabala (2015)
$\gamma_{i,max}$	10^{10}	$10^6 - \infty$	High-energy cutoff of the injected electron energy distribution	Turner & Shabala (2015)
κ_{RT}	0.05	0.03-0.07	Rayleigh-Taylor growth parameter	Turner & Shabala (2015)
q_B	0.4	0.1-1	$u_B/(u_e + u_T)$	Hardcastle (2018)
A	2	2-6	Initial axial ratio of lobe	Sizes and FR fractions
$\gamma_{i,min}$	100	20-500	Low-energy cutoff of the injected electron energy distribution	1.4GHz Luminosity Function
k^t	10	0-10	u_T/u_e	1.4GHz Luminosity Function
s	2.1	2-3	Spectral index of the injected electron energy distribution	325MHz/20GHz Luminosity Functions
$\bar{t}_{\rm on}$	5×10^8 yr	$10^6 - 10^9$ yr	The mean 'on' phase duration	Sizes and FR fractions
$\bar{t}_{\rm off}/\bar{t}_{\rm on}$	2	0-10	The ratio of mean durations of 'off' to 'on' phases	Slope of 1.4GHz Luminosity Function

Table 6.2: The halo masses, hot gas masses and jet powers of the example radio sources. The evolution of size of the source represented by the light blue line is shown in Figure 6.1 and all the sources are shown in Figures 6.2 and 6.3.

Colour of line	Halo mass ($M_\odot$)	Hot gas mass ($M_\odot$)	Jet power (W)
Red	1.44×10^{12}	2.07×10^{11}	1.56×10^{34}
Light blue	4.93×10^{12}	7.59×10^{11}	1.02×10^{36}
Dark blue	1.39×10^{14}	2.01×10^{13}	1.91×10^{37}
Black	8.67×10^{13}	1.24×10^{13}	7.92×10^{37}

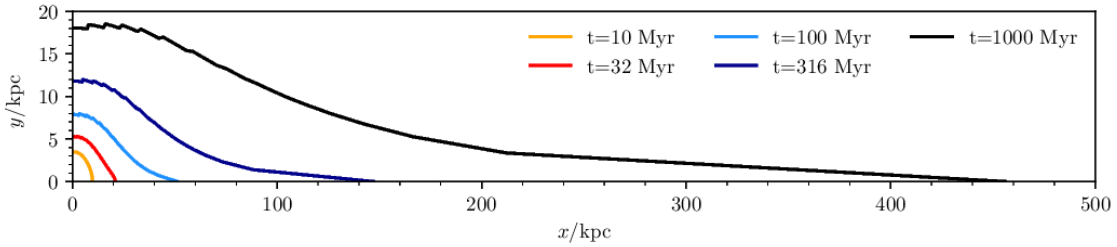

Figure 6.1: An example of the evolution of the shape of a radio source in the model at $z = 0$ with time. We show the projection of the source into the plane containing the major and minor axis. This source is the light blue line in Figures 6.2 and 6.3, with its halo mass, hot gas mass and jet power given in Table 6.2.

duced by the model. These examples were chosen to a span a range of luminosities. The halo masses, hot gas masses and jet powers of these radio sources are given in Table 6.2.

In Figure 6.1, we show the evolution of the shape of the lobe for one of the radio sources in the model, by showing the lobe projected onto a plane containing the major and minor axes. When this lobe has an age of 10Myr, it is an FRII source with all the angular elements of the lobe evolving into an external medium with the same slope, and so it has an assumed axial ratio $A = 2$. As this lobe ages, the major axis of the lobe expands into the region of the hot gas profile where the density decreases with radius ($\rho \propto r^{-2}$), compared to the rest of the lobe which is in a region of the hot gas profile where the density is constant with radius. The major

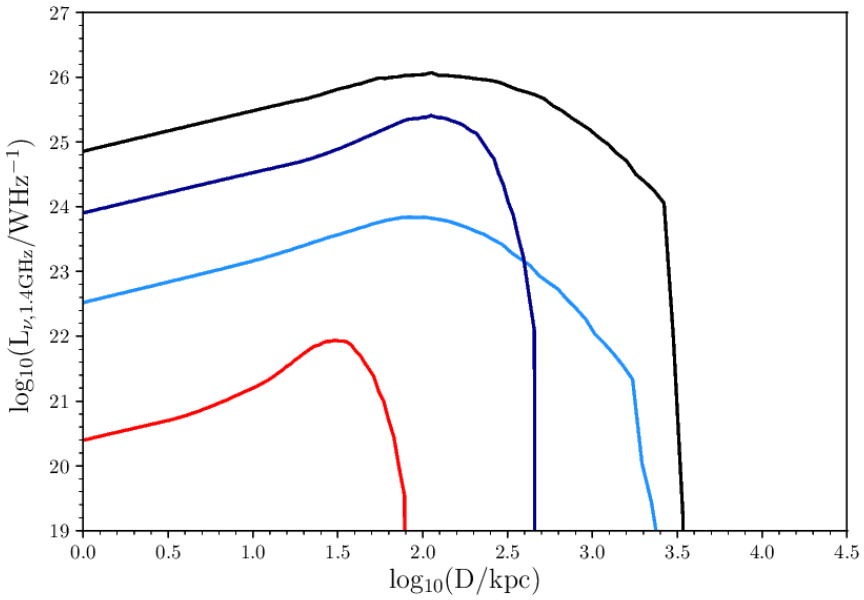

Figure 6.2: Examples of the evolution of radio sources from the model in 1.4GHz radio luminosity and size from the model at $z = 0$. The halo masses, hot gas masses and jet powers are given in Table 6.2.

axis of the lobe therefore propagates faster through the hot gas environment than the minor axis, and so the axial ratio of the lobe increases. This is a feature of the Turner & Shabala (2015) model, and is discussed in Section 5.1.1 of Turner et al. (2018b), where this evolution in axial ratio is compared to the axial ratio evolution from the numerical simulations of Hardcastle & Krause (2013).

Observational studies of extended radio sources often focus on the position of radio sources in a plot of radio power versus lobe size (often referred to as the P-D diagram), and analytic models of lobe evolution have been used to predict the evolution of sources through the P-D diagram (e.g. Kaiser et al., 1997), assuming a typical set of galaxy and radio lobe parameters in the model. In Figure 6.2 we show examples of the evolution through the L-D diagram (radio luminosity and radio power are related by $L_\nu = 4\pi P_\nu$) for four radio sources from the simulation. The four radio sources show the same general evolution, with each source increasing in luminosity with increasing size, until the luminosity begins to decrease with size. However, two of the sources (those shown by the light blue line and the black line)

are FRIIs for the full course of their evolution, their increase in luminosity for smaller sizes is caused by the flat density profile they are evolving through, and their decrease in luminosity at larger sizes is caused by the sources growing to a size where the density decreases with radius. The other two sources (shown by the red and dark blue lines) behave similarly to the other two when the lobes are fairly small, but then transition to FRI sources and so their luminosity increases briefly, before it decreases quickly due to Rayleigh-Taylor instabilities. The luminosity of a source increases when it transitions to an FRI due to changes in the evolution of its pressure and volume (see Appendix C.3 for the dependence of lobe luminosity on pressure and volume for the case of no radiative losses). When the source is an FRII in a constant density environment, its pressure is decreasing with radius, but its volume is increasing, and overall its luminosity gradually increases with size. When the source transitions to an FRI, it is assumed to be in pressure balance with its environment and its volume is still increasing, and so its luminosity increases more steeply with radius.

In Figure 6.3, we show examples of radio spectra of radio sources from the simulation. In general, the spectra of radio sources evolve such that when the radio source is young, the luminosity is a power law with frequency, $L_\nu \propto \nu^{(1-s)/2}$, whereas when the radio source is older, the luminosity shows a cutoff at high frequencies, as a result of higher energy electrons being more susceptible to radiative losses.

In Figure 6.4, we show the radio SEDs of radio sources generated by the simulation for different bins in luminosity. We show radio sources for $20 < \log(L_{1.4\mathrm{GHz}}/\mathrm{WHz}^{-1}) < 22$, $22 < \log(L_{1.4\mathrm{GHz}}/\mathrm{WHz}^{-1}) < 24$ and $24 < \log(L_{1.4\mathrm{GHz}}/\mathrm{WHz}^{-1}) < 26$. We find that the different luminosity bins have similar spectral shapes. At lower frequencies ($178\mathrm{MHz} < \nu < 1.4\mathrm{GHz}$) the spectra have a median spectral slope $\alpha = 0.61$[2], whereas for higher frequencies ($1.4\mathrm{GHz} < \nu < 20\mathrm{GHz}$), the spectra have a median spectral slope of $\alpha = 0.89$. At these higher frequencies, there is more of a variations in the spectral slopes than at lower frequencies, with some sources having the same spectral slope at all frequencies, and some sources having zero luminosity at higher

[2]This is for an assumed spectrum, $S_\nu \propto \nu^{-\alpha}$

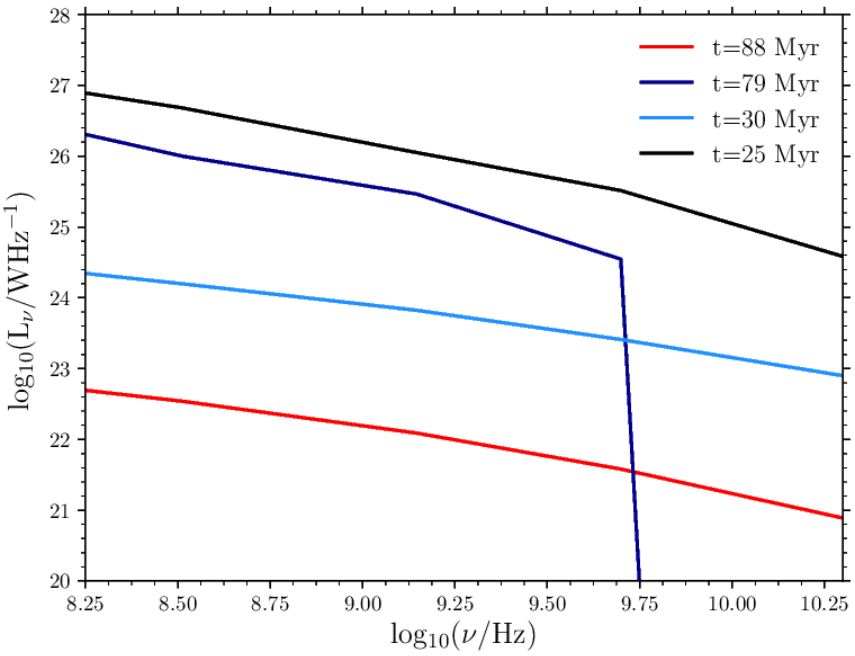

Figure 6.3: Examples of the spectra of radio sources from the model at $z = 0$. We show the radio luminosity at each frequency versus frequency. The objects and line colours are the same as in Figure 6.2. The halo masses, hot gas masses and jet powers of these objects are given in Table 6.2.

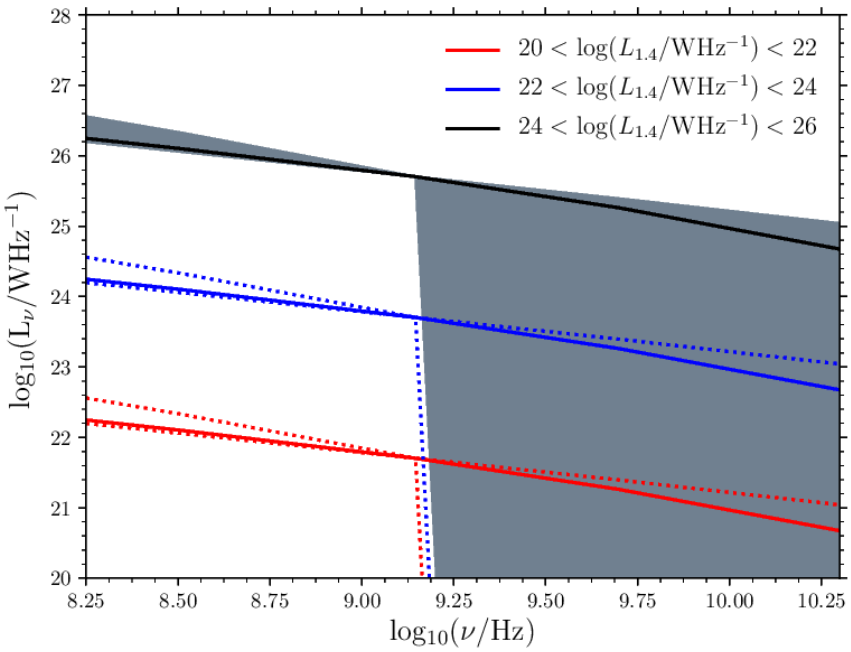

Figure 6.4: The average SEDs of the radio sources generated in the model for different bins in luminosity. We show the median and 10-90 percentiles of the SEDs of sources with luminosities $20 < \log(L_{1.4\mathrm{GHz}}/\mathrm{WHz}^{-1}) < 22$ (red solid line and red dotted lines), $22 < \log(L_{1.4\mathrm{GHz}}/\mathrm{WHz}^{-1}) < 24$ (blue solid line and blue dotted lines) and $24 < \log(L_{1.4\mathrm{GHz}}/\mathrm{WHz}^{-1}) < 26$ (black solid line and grey shading). The luminosities of objects in each luminosity bin have been rescaled to the luminosity at 1.4GHz at the middle of the bin in logspace.

frequencies.

6.4 Comparison to observations

We now show the predictions for the population of radio lobes generated by the fiducial model compared to a variety of observations at $z = 0$: radio luminosity functions, radio luminosities versus jet powers, radio luminosities split by stellar mass, Fanaroff-Riley fractions versus luminosity, and lobe sizes.

6.4.1 Radio Luminosity Functions

In Figure 6.5 we present the 1.4GHz radio luminosity function at $z = 0$ compared to observational estimates. The fiducial model is in very good agreement with the observations at all luminosities. We also show the contributions to the radio luminosity function from the different SMBH fuelling modes. The radio luminosity function is dominated by the contribution from objects fuelled by hot halo mode accretion. There is a small contribution from starbursts triggered by mergers for $L_\nu < 10^{26}\mathrm{WHz}^{-1}$, and an even smaller contribution from starbursts triggered by disc instabilities for $L_\nu < 10^{24}\mathrm{WHz}^{-1}$. In the model, hot halo mode accretion occurs when AGN feedback is active, so in the model the AGN only have significant radio luminosities when AGN feedback is active. The radio luminosity function is dominated by radio lobes of intermediate sizes ($10\mathrm{kpc} < D < 100\mathrm{kpc}$).

In Figure 6.6 we present the radio luminosity functions at 325 MHz and 20 GHz compared to observational estimates. We converted the observed luminosities in Sabater et al. (2019) from 150MHz to 325MHz assuming a radio spectrum with electron energy spectral index $\alpha = 0.7$. When calibrating the free parameters of the extended radio emission model, it was found that a value of the slope of the injected electron energy distribution of $s = 2.1$ provides best consistency between the different frequencies. This value of s gives a value of $\alpha = 0.55$ at injection.

The model is in slightly less good agreement at both of these frequencies than at 1.4GHz. At 325MHz, the model is in good agreement with observations of the luminosity function, except at $L_\nu \sim 10^{26}\mathrm{WHz}^{-1}$, where the model overpredicts the

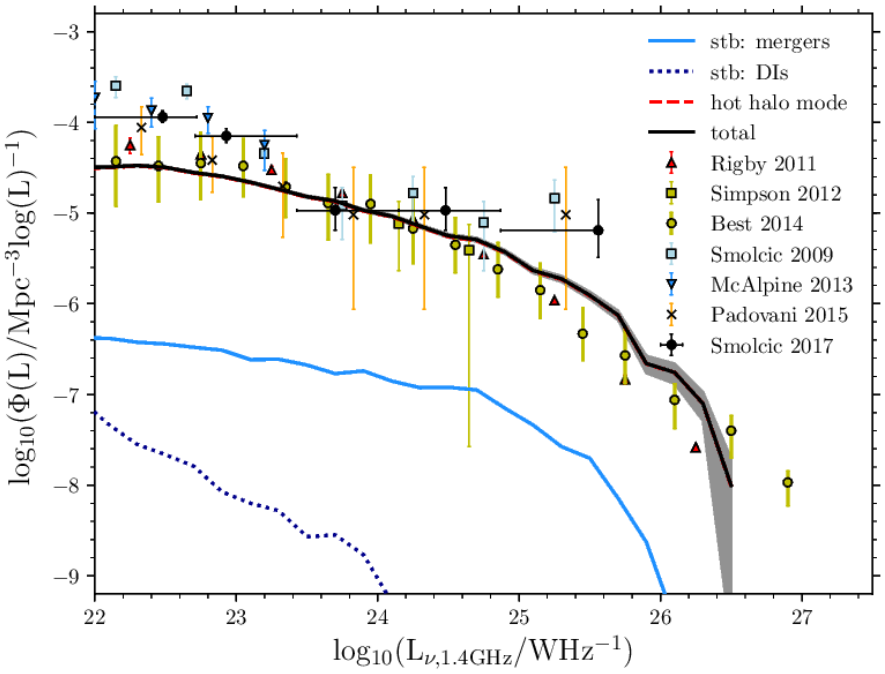

Figure 6.5: The 1.4GHz luminosity function at $z = 0$. The black line shows the prediction from our fiducial model, with the shading representing the Poisson errors, resulting from the finite number of objects in the simulation box. We show the contributions from the different SMBH fuelling modes: hot halo mode (red line - underneath the black line), starbursts triggered by mergers (light blue solid line), and starbursts triggered by disc instabilities (blue dotted line). Note that the red line is underneath the black line. The symbols represent observational estimates from Smolčić et al. (2009), Rigby et al. (2011), Simpson et al. (2012), McAlpine et al. (2013), Best et al. (2014), Padovani et al. (2015), and Smolčić et al. (2017).

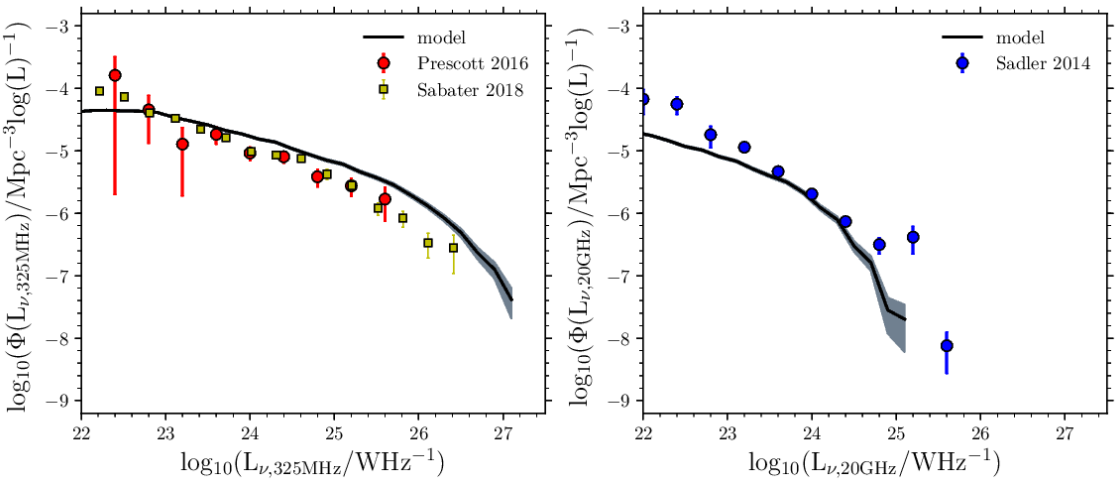

Figure 6.6: *Left panel:* the predicted radio luminosity function at 325MHz (black line) compare to observational estimates from Prescott et al. (2016) (red circles) and Sabater et al. (2019) (green squares). The latter has been converted to 325MHz from 150MHz assuming a spectral index $\alpha = 0.7$. *Right panel:*, the predicted radio luminosity function at 20GHz (black line) compared to observational estimates from Sadler et al. (2014) (blue circles).

observations by about 0.5 dex. At 20GHz, the model underpredicts the observations, although the number density predicted by the model at $L_\nu \sim 10^{24}$WHz^{-1} is similar to that observed. The observations may be an overestimate of the 20GHz luminosity function as a result of Doppler beaming.

Alongside the Fanaroff-Riley classification of radio sources, observed radio sources can also be classified into High/Low Excitation Radio Galaxies (HERGs and LERGs). This classification is based on optical emission line strength, with HERGs having stronger emission lines. HERGs are believed to correspond to AGN accreting via a physically thin, optically thick, thin disc accretion state (Shakura & Sunyaev, 1973), whereas LERGs are believed to correspond to the AGN accreting via a physically thick, optically thin Advection Dominated Accretion Flow (ADAF - Yuan & Narayan, 2014). In Figure 6.7 we present the predictions of the model split into the contribution from thin discs and ADAFs compared to observational estimates of the radio luminosity function from Best et al. (2014) and Pracy et al. (2016) split into the contribution from HERGs and LERGs.

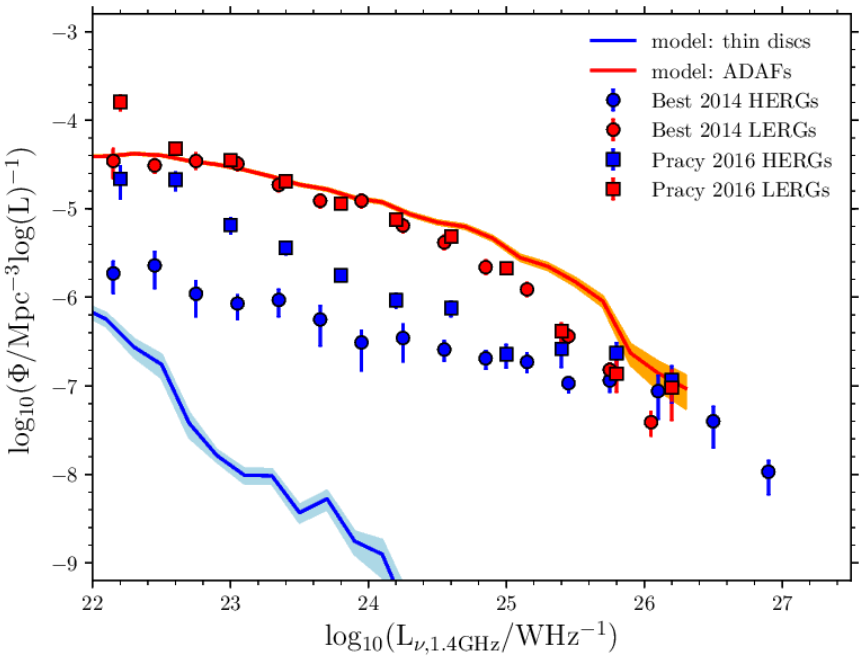

Figure 6.7: The 1.4GHz radio luminosity function at $z = 0$ predicted by the model split into the contribution from thin discs (blue line) and ADAFs (red line) compared to observational estimates from Best et al. (2014) (circles) and Pracy et al. (2016) (squares) split into contributions from HERGs (blue) and LERGs (red).

Both the model and the observations predict that the radio luminosity function is dominated by the contribution from ADAFs/LERGs. The contribution from ADAFs in this model is in very good agreement with the contribution from LERGs in the observational estimates. However, the number of thin discs in the model underpredicts the number of HERGs in the observations. While there is tension between the estimated contributions from HERGs between Best et al. (2014) and Pracy et al. (2016) at the low luminosity end, the model undepredicts both of these.

In Chapter 5, a 1.4GHz radio luminosity function from this GALFORM model was presented. In that model, the jet powers were calculated in the same way as here, but the radio luminosities were calculated from the jet powers using a scaling relation, rather than using the radio luminosity calculation here. That model also fits well to the radio luminosity function at $z = 0$, but the fuelling modes that dominate the radio luminosity function are different. In that model, for $L_\nu < 10^{24}\mathrm{WHz}^{-1}$, the hot halo mode dominates the radio luminosity function, whereas for $L_\nu > 10^{24}\mathrm{WHz}^{-1}$, the starburst mode dominates. This is different to the radio luminosity function from the model presented here, where the hot halo mode contribution dominates for all luminosities.

In this mode, the hot halo mode contribution may dominate because we calculate the durations of the radio sources differently for the two different modes. If the starburst mode sources were assumed to have longer durations, this could increase their luminosities, and so the split by fuelling mode would be more similar to that seen in Figure 5.7.

6.4.2 Relation of radio luminosities to jet powers

In Figure 6.8 we present the radio luminosity versus jet power relation, compared to observational estimates based on cavities in X-ray emitting hot gas from Rafferty et al. (2006), Bîrzan et al. (2008), and Cavagnolo et al. (2010) as compiled in Heckman & Best (2014). This observational sample is a sample of cavities from local giant elliptical galaxies and clusters with X-ray emission detected by Chandra. In the observations, the main uncertainty is in the jet power determination. The jet power is calculated by combining the cavity volume, pressure (assuming that the

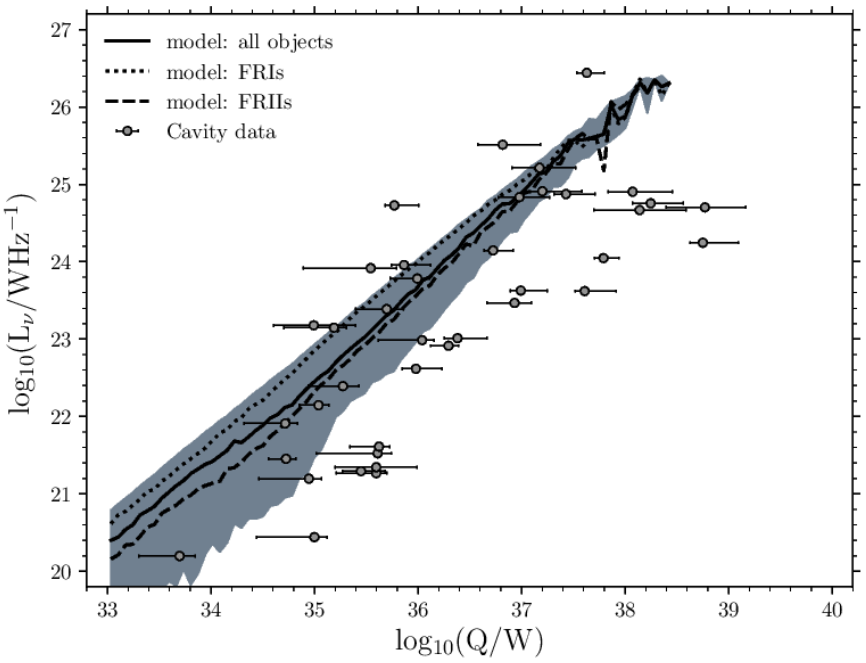

Figure 6.8: The relation between 1.4GHz radio luminosity and jet power. The solid line shows the median radio luminosity at a given jet power predicted by the model, with the shading representing the 10-90 percentiles of the distribution of radio luminosities for that bin in jet power. The median radio luminosity versus jet power for only FRIs (dotted line) in the model and for only FRIIs (dashed line) in the model are also shown. The model is compared to observational estimates from Rafferty et al. (2006), Bîrzan et al. (2008), and Cavagnolo et al. (2010) as compiled by Heckman & Best (2014) (grey circles).

cavity is in pressure equilibrium with its surroundings), and the duration of the jet. The latter is difficult to determine, and so the buoyancy age, i.e. the age of the source assuming the cavity is a buoyant bubble rising at the terminal velocity, is used for the duration of the jet. The model predicts a relation consistent with the observations. FRIs are predicted to have higher radio luminosities at a given jet power than FRIIs, as also seen in Turner & Shabala (2015).

6.4.3 Radio luminosities and galaxy stellar masses

In Figure 6.9, we present the fraction of galaxies hosting an AGN above a given radio luminosity for different ranges of stellar mass (which we will refer to as the radio fraction), compared to observational estimates from Best et al. (2005a) and Sabater et al. (2019). Both of these studies use SDSS for galaxy properties but cross-compare with different radio surveys, either FIRST and NVSS in Best et al. (2005a), and LOFAR Two-metre Sky Survey (LoTSS) data in Sabater et al. (2019).

The model is in good agreement for $L_\nu > 10^{23}\mathrm{WHz}^{-1}$ and $M_\star = 10^{11-11.5}M_\odot$, but at other luminosities and stellar masses, it does not match the observations well. For $L_\nu > 10^{23}\mathrm{WHz}^{-1}$, the model overpredicts the radio fraction for stellar masses, $M_\star > 10^{11.5}M_\odot$, and $M_\star < 10^{11}M_\odot$. For $L_\nu < 10^{23}\mathrm{WHz}^{-1}$, the predicted radio fraction at a given stellar mass flattens off for all the stellar mass bins. This is a different behaviour to the observations from Sabater et al. (2019), which show a power law increase in the radio fraction for decreasing luminosities, with radio fractions approaching unity at low luminosities for the high stellar masses.

This difference in behaviour may be caused by the observations, as the faint radio emission may not be from AGNs, but rather from star formation. Turning to the model, when we vary some of the free parameters from Table 6.1 (see Figure 6.17), we find that the model can be made to predict a radio fraction close to unity at low luminosities, but the flattening of the radio fraction happens for all parameter choices. We suggest three other potential changes that could be made to the model to avoid this flattening of the radio fraction. First, when a radio source is on, it has a fixed $\dot{M}$ value (and hence Q value), as opposed to a value randomly selected from a probability distribution. If we were to assume a distribution of $\dot{M}$ values, this would

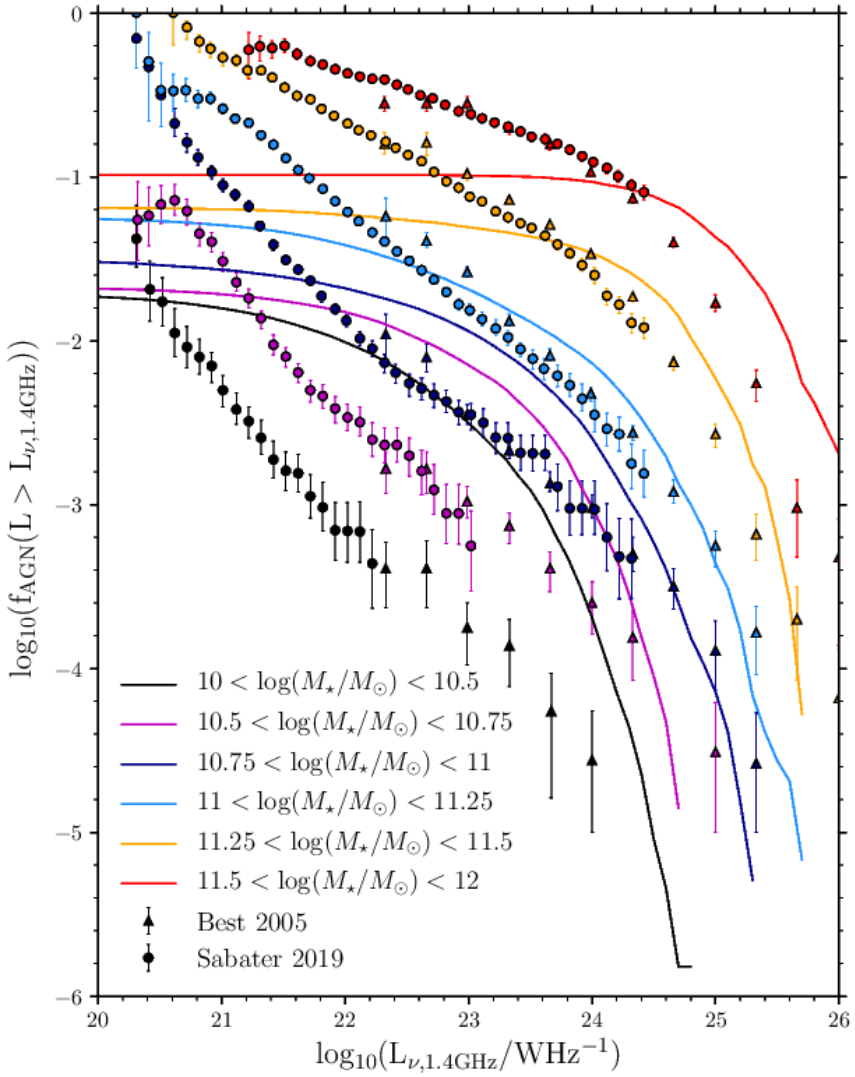

Figure 6.9: The fraction of galaxies hosting an AGN with a 1.4GHz radio luminosity above a given value for different bins in stellar mass (lines), compared to the observational data from Best et al. (2005a) (triangles) and Sabater et al. (2019) (circles).

produce more low luminosity sources which may stop the radio fraction flattening off. Secondly, the 'on' and 'off' times are drawn from an exponential distribution, which produces fewer short duration sources. By varying the distributions from which 'on' and 'off' times are generated (and perhaps allowing the 'on' and 'off' distributions to be different), better agreement with the observations might be able to be be obtained. Thirdly, our duty cycle model is independent of galaxy properties, the 'on' and 'off' times may depend on galaxy stellar mass or SMBH mass (e.g. Shabala et al., 2008).

6.4.4 Fanaroff-Riley fractions

While the physical reason for the dichotomy between the two Fanaroff-Riley types of sources is uncertain, we can test the model for FRI and FRII sources proposed by Turner & Shabala (2015) by comparing our predictions to observations. In this model, radio sources expand supersonically initially, but when the velocity of the surface of the cocoon becomes equal to the sound speed of the environment, that angular element of the source becomes subsonic. When a radio source has at least some supersonic angular elements, we classify it as an FRII, whereas when all the angular elements are subsonic, we classify it as an FRI. The velocity of the surface of the major axis is the highest of all the angular elements, and so this condition is equivalent to saying that if the major axis of the lobe is supersonic, the lobe is an FRII.

In Figure 6.10, we present the fraction of FRI and FRII sources in the model versus radio luminosity, compared to observational estimates from Gendre et al. (2013). The model shows a different trend to the observations. In the observations, the fraction of objects that are FRIIs increases with luminosity, from about 0.1 at $L_\nu \sim 10^{24}\mathrm{WHz}^{-1}$ to about 0.9 at $L_\nu \sim 10^{26}\mathrm{WHz}^{-1}$. This fraction stays roughly constant for luminosities above this. In the model however, the fraction of FRIIs gradually decreases from 0.6 at $L_\nu \sim 10^{23}\mathrm{WHz}^{-1}$ to 0.4 at $L_\nu \sim 10^{25}\mathrm{WHz}^{-1}$, and then strongly decreases to about 0.2 at $L_\nu \sim 10^{26}\mathrm{WHz}^{-1}$.

In the model, most of the radio sources at high radio luminosities are FRIs. This may be because sources increase in luminosity when they become FRIs (see

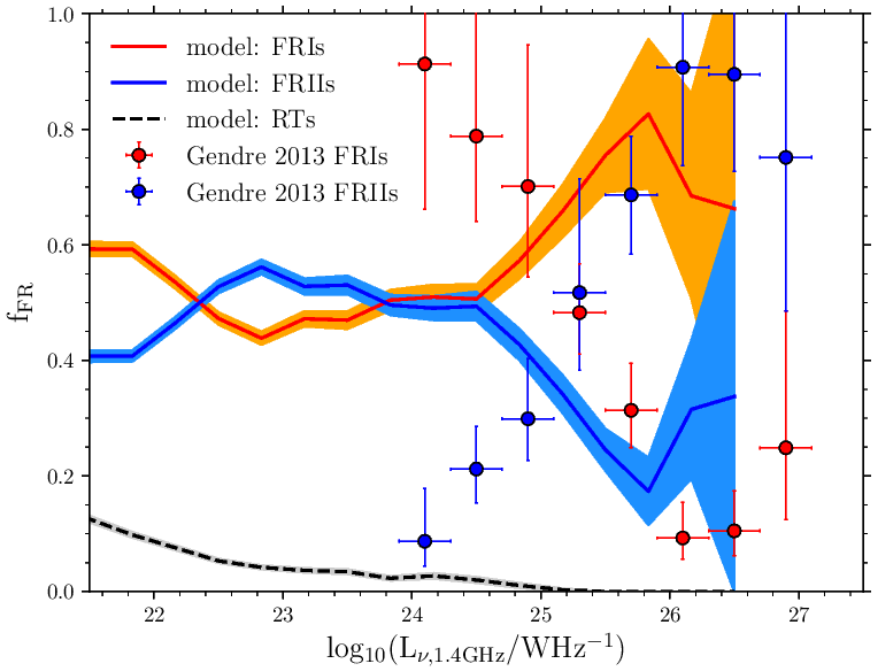

Figure 6.10: The fraction of radio sources of different Fanaroff & Riley (1974) morphological types versus 1.4GHz radio luminosity. Shown are the predicted fractions of FRI sources (red line), FRII sources (blue line). We also show the fraction of FRI sources with more than half of their luminosity reduced by Rayleigh-Taylor instabilities (RT sources - dashed black line). This is compared to observational estimates from Gendre et al. (2013) showing the fraction of FRI sources (red circles) and FRII sources (blue circles).

the luminosity evolution of the sources represented by the red and dark blue lines in Figure 6.2). FRIs have a higher luminosity at a given jet power, as seen in Figure 6.8. As discussed in Section 6.3, this increase in luminosity for FRI sources is a result of these sources reaching pressure equilibrium with their environments, and so it may be that the assumption that FRIs are in pressure balance with their environments is not correct, and allowing FRIs to be underpressured with respect to their external environment may provide better agreement. The discrepancy in Figure 6.10 may also be because the mechanism by which sources transition from FRIIs to FRIs is not correct, instead it may be the case that FRIs and FRIIs have different particle contents (e.g. Croston et al., 2018), and so should be modelled using different k^t values. Another reason for the discrepancy in Figure 6.10 may be the assumption of treating radiative losses after modelling the lobe expansion. If we were to treat radiative losses self-consistently within the lobe expansion, this may affect the luminosities of FRIs and FRIIs differently, and bring the model into better agreement here.

6.4.5 Radio lobe sizes

For our analysis, given that the galaxy formation model generates a population of galaxies and a population of radio lobes, we want to compare the predicted distribution of radio luminosities and sizes of the radio sources to observations. To do this, we need to take into account selection effects in the radio surveys. Observations of extended radio sources are limited by their surface brightness detection limit, where large but faint lobes can have surface brightness limits below the detection threshold of the radio survey.

We compare with observed size distributions for radio galaxies in the nearby Universe, using both the 3CRR survey[3] (Laing et al., 1983), and much more recent LOFAR Two-metre Sky Survey (LoTSS) data (Hardcastle et al., 2019). We compare to sources in the redshift range $0 < z < 0.5$, which is a redshift range chosen so that the cosmological evolution should not be too large. We compare the model

[3]The 3CRR data was retrieved from `https://3crr.extragalactic.info`

to these surveys in ranges of radio luminosity and lobe sizes from the bivariate number density of objects, $\Phi(L_\nu, D) = d^2n/d(\log L_\nu)d(\log D)$. To calculate the bivariate number density of objects in the $\log L_\nu, \log D$ plane, we use the '$V_{\rm max}$ method' (Schmidt, 1968), where we calculate the maximum volume over which the source could be observed, given the survey selection. For each object, we calculate the minimum redshift at which it could be observed $z_{\rm min}$ and the maximum redshift at which it could be observed, $z_{\rm max}$. From these, the volume over which a source could be observed, $V_{\rm max}$, can be calculated.

For each source in the 3CRR survey, $z_{\rm min}$ is determined by the maximum angular size at which the object could be detected (10 arcmin) and $z_{\rm max}$ is determined by the flux limit of the survey (10.9 Jy). For each source in LoTSS, $z_{\rm min}$ is determined by the maximum size of objects that can be detected (using the detection condition shown in Figure 8 of Hardcastle et al. (2019) at that luminosity), and $z_{\rm max}$ is the minimum of $z_{\rm max}$ due to the size $z_{\rm max,D}$ and $z_{\rm max}$ due to the luminosity $z_{\rm max,L}$. $z_{\rm max,D}$ is determined by the angular size below which that source would become unresolved (10 arcsec), and $z_{\rm max,L}$ is determined by the minimum luminosity of objects that can be detected (using the detection condition shown in Figure 8 of Hardcastle et al. (2019) at that lobe size). For each cell, the bivariate number densities of objects are calculated using:

$$n = \sum_{i=1}^{N} \frac{1}{V_{\rm i,max}}, \tag{6.4.6}$$

where N is the number of objects in that cell in $\log L_\nu$ and $\log D$. We show the number density of objects for 3CRR in the left panel of Figure 6.11, and for the LoTSS data in the left panel of Figure 6.13. If there are objects in this cell then the error on the number density is calculated using:

$$\sigma = \left(\sum_{i=1}^{N} \frac{1}{V_{\rm i,max}^2} \right)^{1/2}. \tag{6.4.7}$$

If there is not an object in a cell, then we calculate a 2σ upper limit for this cell. We assume that the number of objects in each cell follows a Poisson distribution with mean $\langle N \rangle$. The probability of there being r objects in this cell is therefore:

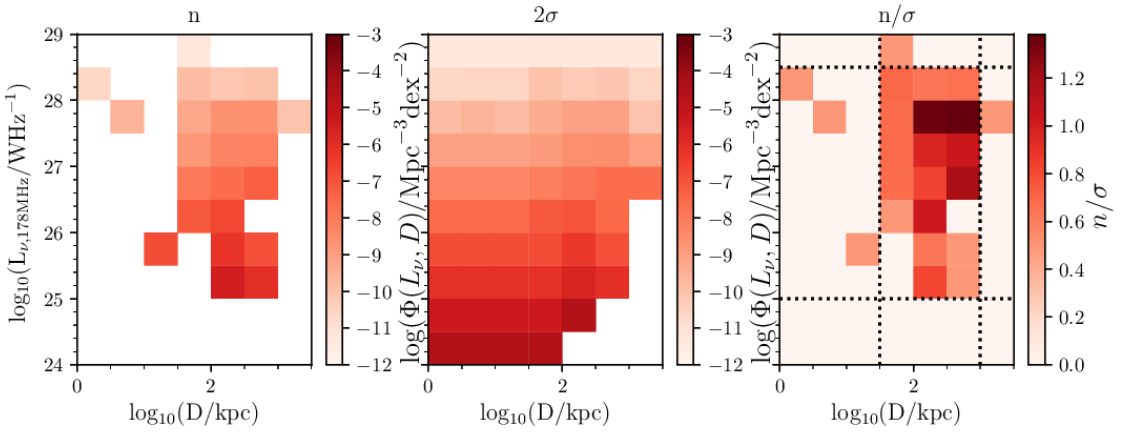

Figure 6.11: Radio luminosity versus lobe size for sources at $0 < z < 0.5$ in the 3CRR survey. *Left panel:* The bivariate number density, $\Phi(L_\nu, D)$, of objects detected in the 3CRR survey calculated using the $V_{\rm max}$ method, as indicated by the colour scale at the right of the panel. *Middle panel:* 2σ errors (if the cell has an object) or 2σ upper limits (if the cell does not have an object) on the number density of objects. *Right panel:* the ratio of the number densities and errors, where the luminosity and size range that we use for comparison with our model are shown as black dotted lines.

$$P_r = \exp(-\langle N \rangle)\frac{\langle N \rangle^r}{r!}. \tag{6.4.8}$$

To calculate the 2σ upper limit, we calculate the largest value of $\langle N \rangle$ for which the probability of finding no objects is greater than 0.05. Therefore we can derive an expression for $\langle N \rangle$:

$$\begin{aligned} &P(r = 0) \geq 0.05, \\ &\exp(-\langle N \rangle) \geq 0.05, \\ &\langle N \rangle \leq \ln 20. \end{aligned} \tag{6.4.9}$$

The 2σ upper limit of the number density is then given by:

$$n_{2\sigma,limit} = \frac{\langle N \rangle}{V_{\rm max}} = \frac{\ln 20}{V_{\rm max}}. \tag{6.4.10}$$

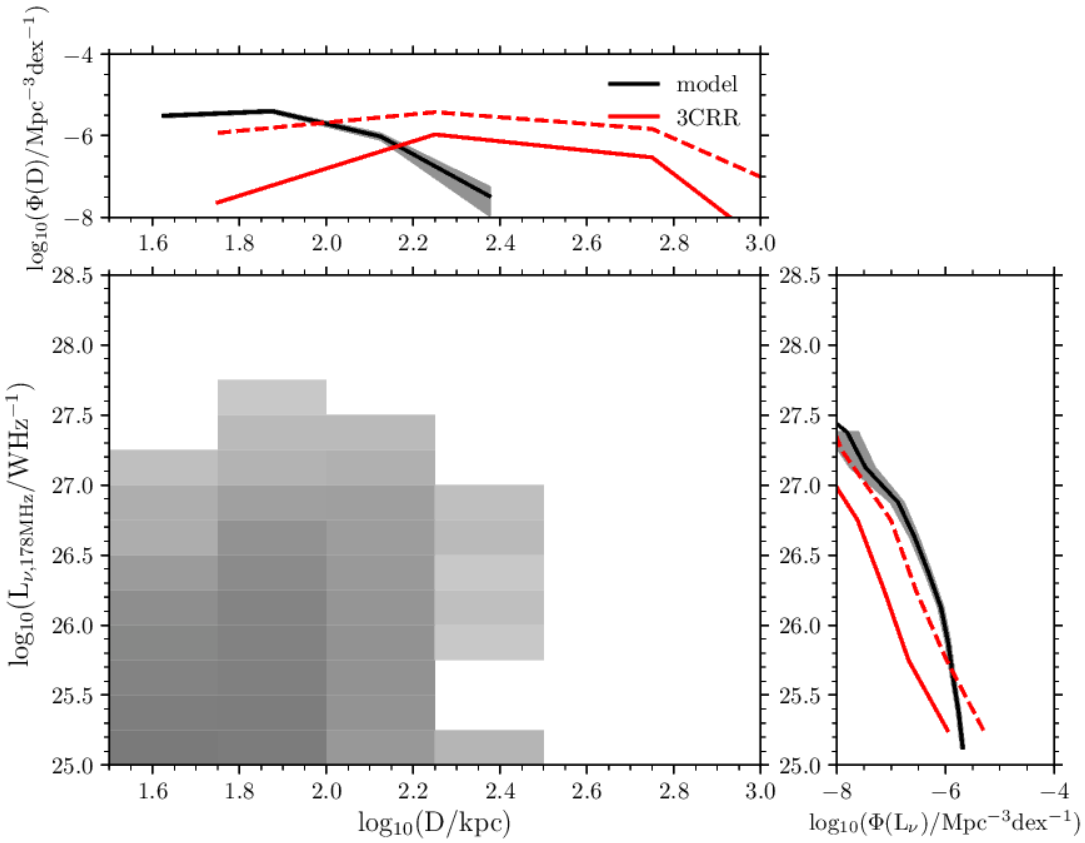

Figure 6.12: Comparing the bivariate number density $\Phi(L_\nu, D) = d^2n/d(\log L_\nu)d(\log D)$ in the model to the 3CRR survey in the luminosity and size range shown in Figure 6.11. The central plot shows the model predictions for the 2D distribution (grey). The plots above and to the right show the distributions of radio luminosity and size for the luminosity and size range considered. The model (black line), with associated 1σ errors (grey shading), is compared to the 3CRR survey (red line), with its associated errors (red dashed line). The lower limit of the errors for the 3CRR survey is below the range in number densities shown.

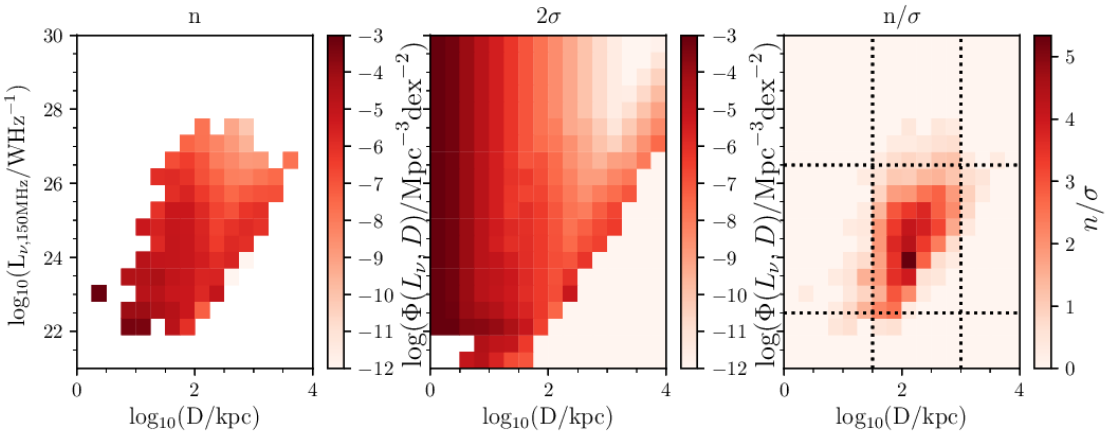

Figure 6.13: As for Figure 6.11 but for the LOFAR Two-metre Sky Survey (LoTSS) data. Note that the luminosity and size range used for comparison with the model are different for LoTSS and 3CRR.

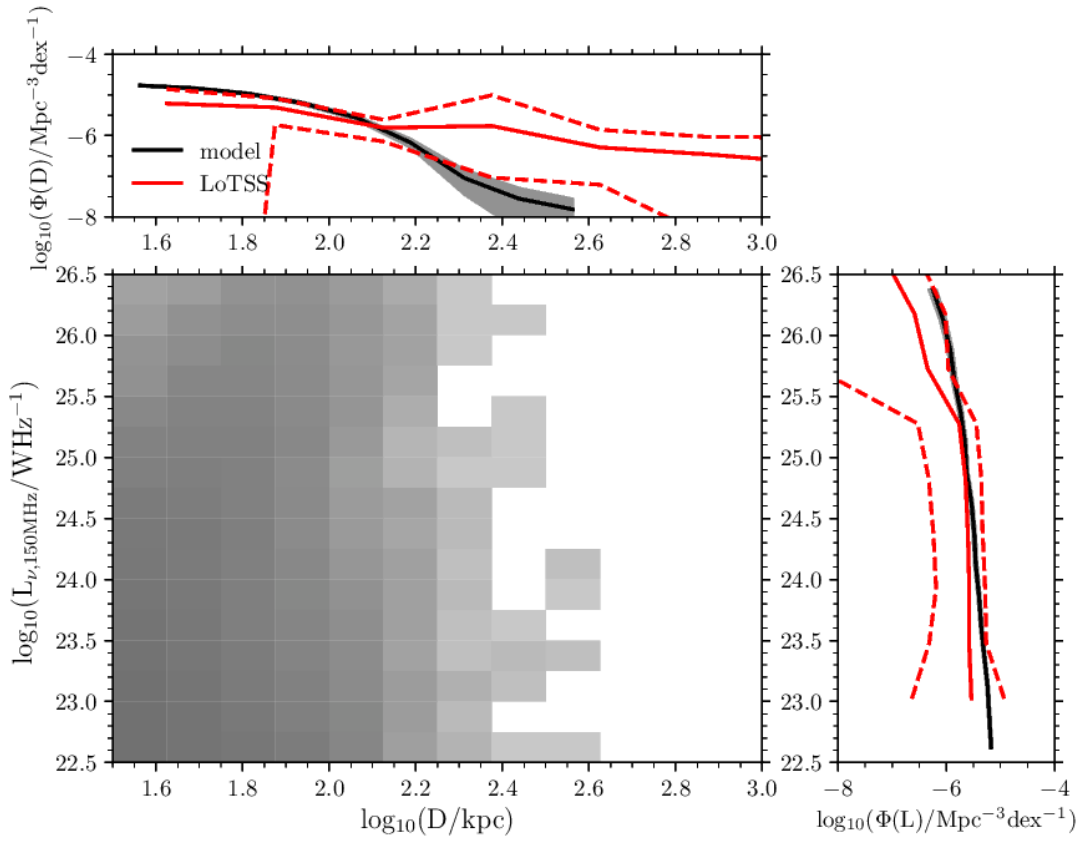

Figure 6.14: The comparison of LoTSS data (red) to the model (black) in the luminosity and size range shown in Figure 6.13.

We show these errors for the 3CRR and LoTSS data in the middle panels of Figures 6.11 and 6.13. We then select a rectangular region in the $\log L_\nu, \log D$ plane where the signal-to-noise, n/σ, is around 1.5 and above for the 3CRR data and around 3 and above for the LoTSS data. For the 3CRR data this results in selecting objects with radio luminosities $25 < \log(L_\nu/\mathrm{WHz}^{-1}) < 28.5$, and sizes $1 \log(D/\mathrm{kpc}) < 3$, and for the LoTSS data this results in selecting objects with $22.5 < \log(L_\nu/\mathrm{WHz}^{-1}) < 26$, and sizes $1.5 < \log(D/\mathrm{kpc}) < 3$. These regions are shown for the 3CRR and LoTSS data in the right panels of Figures 6.11 and 6.13 respectively.

The comparison between the model and this selection of the 3CRR survey is shown in Figure 6.12. The lobe sizes predicted by the model are on average a factor of two smaller than the lobe sizes in the 3CRR survey. In the right panel of Figure 6.12 the luminosity function predicted by the model in the given luminosity and size range is above the luminosity function we calculate from 3CRR. This is because we chose our model parameters to fit a range of observational estimates of the radio luminosity function at different frequencies and the 3CRR luminosity function falls below these other measurements.

We compare the model to the LoTSS data in Figure 6.14. We find that the predicted number of objects at each size are in better agreement with the LoTSS data than when the model is compared to 3CRR. However, the model predicts fewer large ($D > 200$kpc) sources than are seen in the LoTSS data. In the model, it is difficult to produce large radio sources, because there are several processes by which the luminosity of large lobes can decrease to zero. First, at large lobe sizes, inverse-Compton losses to the electrons energy become significant, and strongly reduce the lobe luminosity. Secondly, the density of the environment the large sources are in falls off with radius steeply, which causes the lobe to have a lower pressure causing the electrons to radiate with a lower luminosity. Thirdly, in the model, we assume once the radio lobes grow outside the halo, the lobe dissipates. When we modified the model so that radio lobes do not lose energy through radiative losses, evolve through a hot gas environment with no dependence of density on radius, and can grow outside of haloes, we still found that the large sources that are seen

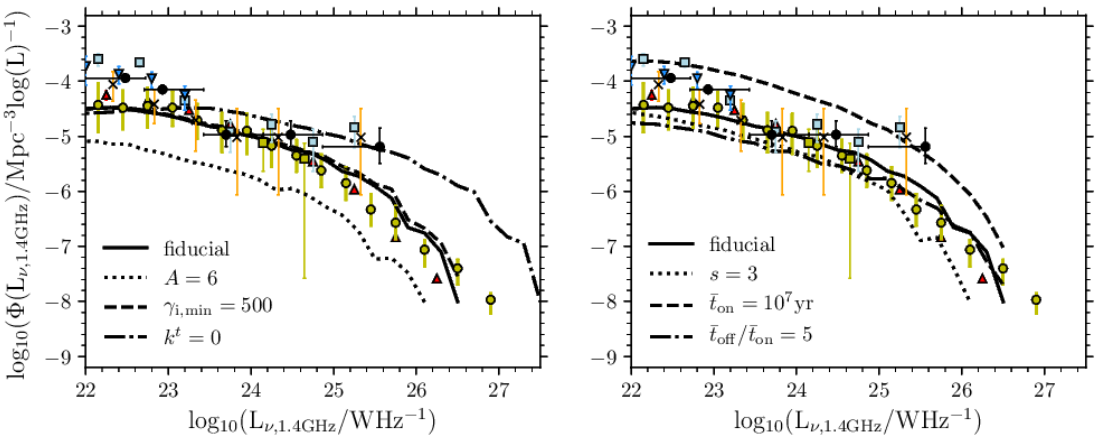

Figure 6.15: The 1.4GHz radio luminosity function at $z = 0$, showing the effect of varying free parameters of the extended radio emission model.

in the LoTSS data are not produced. One way to produce large lobes may be to have objects in the model with higher values of $\dot{M}$, which would cause lobes with higher energies to be produced. If the values of $\dot{M}$ were selected randomly from a probability distribution rather than with a fixed value, the model may produce the small number of large sources required.

6.5 Dependence of the predictions on free parameters of the radio model

In this Section, we explore varying the parameters of the extended radio emission model, which are given in Table 6.1. We will discuss the effect of the six parameters that most strongly affect the model predictions. We show the radio luminosity function at $z = 0$ in Figure 6.15, the radio luminosity versus jet power relation in Figure 6.16, the fraction of galaxies hosting an AGN above a given radio luminosity split by stellar mass in Figure 6.17, the fraction of FRII sources versus luminosity in Figure 6.18, and the size distribution of the radio sources in Figure 6.19.

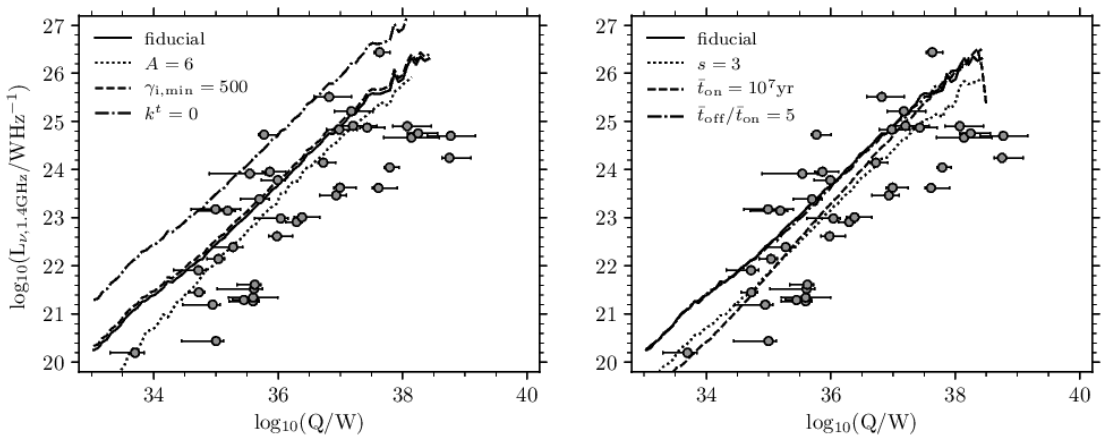

Figure 6.16: The relation between 1.4GHz radio luminosity and jet power at $z = 0$, showing the effect of varying free parameters of the extended radio emission model.

6.5.1 Initial Axial Ratio

First, we explore the effect of varying the initial axial ratio, A, of radio lobes in the simulation, where the axial ratio is the ratio of the semi-major axis of the lobe to the semi-minor axis of the lobe. In observational studies, the axial ratio of radio lobes is relatively straightforward to determine. These studies find that radio lobes have a variety of axial ratios, with an average axial ratio around $A \approx 4$, but with scatter, suggesting an allowed range of $A = 2 - 6$ (e.g. Leahy & Williams, 1984; Leahy et al., 1989; Kharb et al., 2008; Mullin et al., 2008). In our fiducial model, $A = 2$.

Equation (6.2.3) for the radio luminosity can be recast into an expression solely dependent on pressure and volume, as shown in Appendix C.3. Using equation (C.3.31), the lobe luminosity depends more strongly on the pressure than the volume, $L_\nu \propto p^{(s+5)/4}V$ (if radiative losses are neglected). For the value of $s = 2.1$ we adopt in our fiducial model, $L_\nu \propto p^{1.78}V$. When the assumed axial ratio increases, the model predicts that the total pressure of the lobes is slightly larger, but the total volume decreases, so overall, the luminosity decreases. This means that the luminosities of the lobes in the simulation are lower for $A = 6$ by about a factor of 2.5, compared to the fiducial model, as seen in the radio luminosity function in Figure 6.15. As the axial ratio does not affect the jet powers, increasing A causes the lobes in the

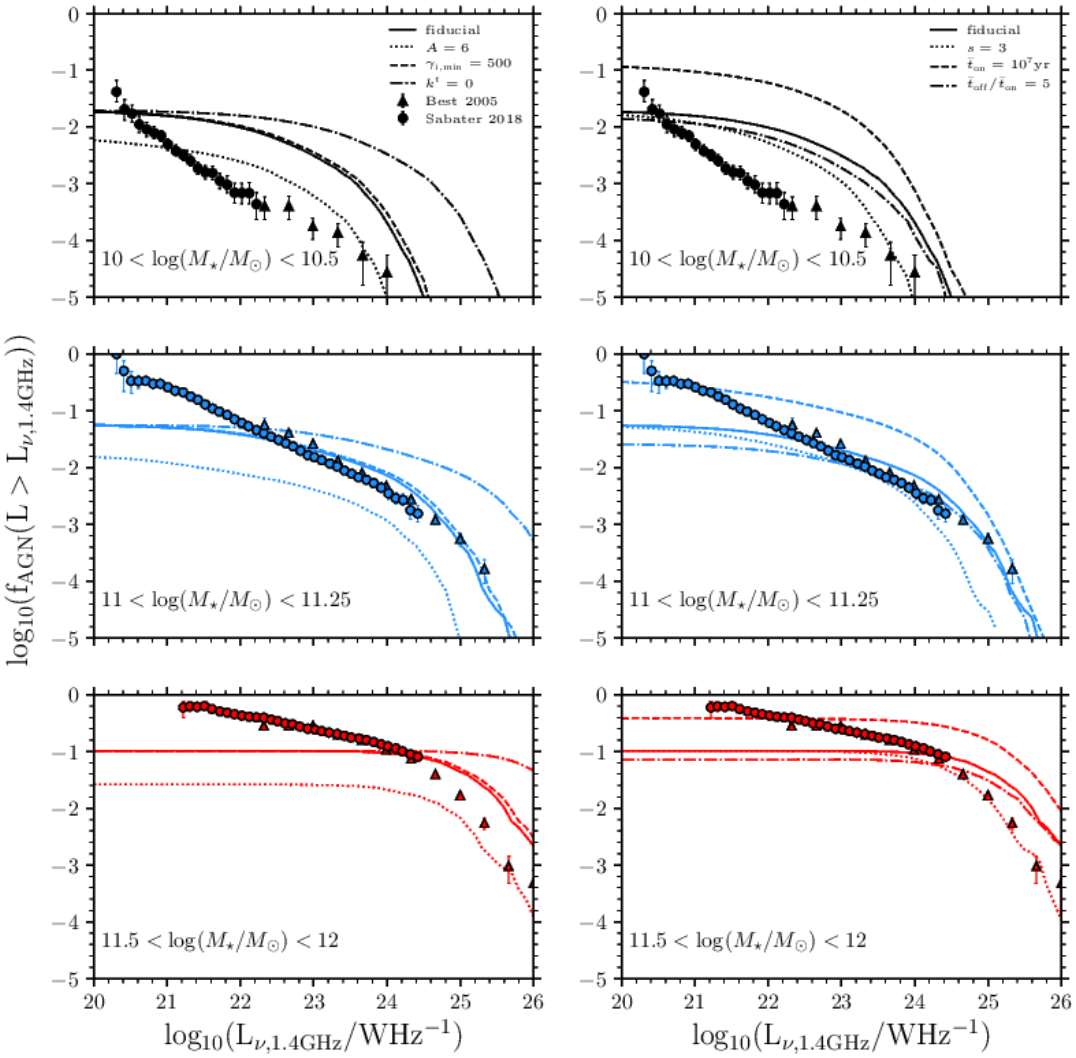

Figure 6.17: The fraction of galaxies hosting an AGN above a given 1.4GHz radio luminosity, in different stellar mass bins, showing the effect of varying free parameters of the extended radio emission model.

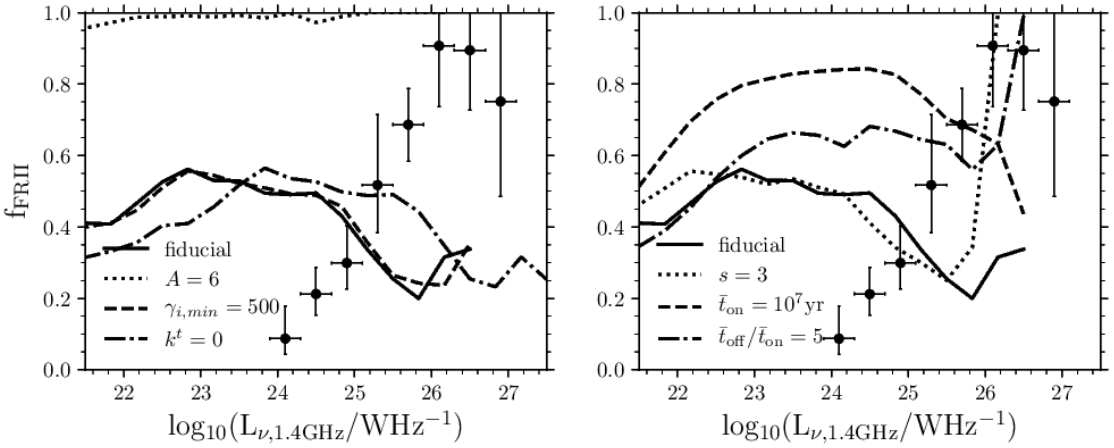

Figure 6.18: The fraction of sources that are FRIIs as a function of 1.4GHz radio luminosity, showing the effect of varying free parameters of the extended radio emission model.

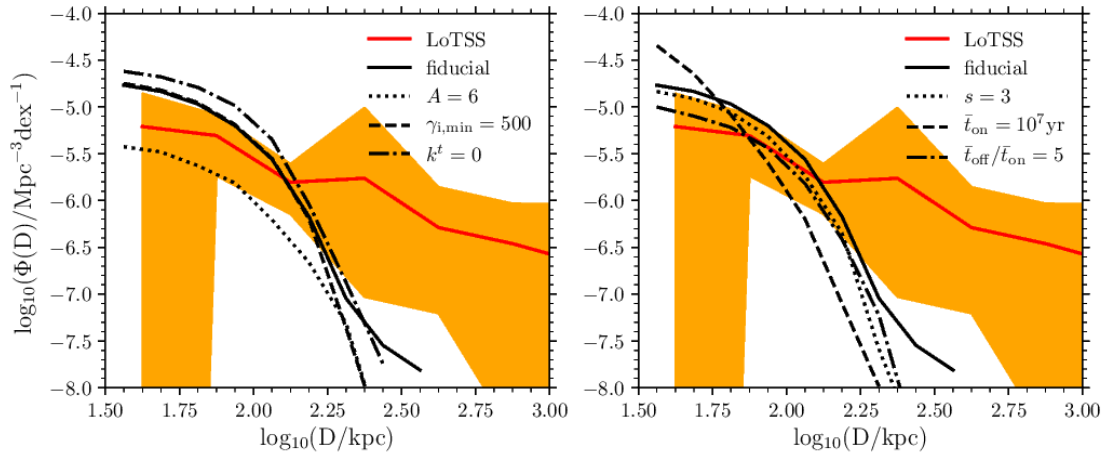

Figure 6.19: The size distribution of radio lobes predicted by the model compared to the LoTSS data (in the same range in L_ν and D as Figure 6.14), showing the effect of varying free parameters of the extended radio emission model.

model to have a lower radio luminosity at a given jet power, as seen in Figure 6.16. Similarly, as the stellar masses of galaxies are not affected by the axial ratios of lobes, when we increase A, the radio fraction decreases as seen in Figure 6.17, due to the luminosities decreasing.

Increasing A increases the number of FRII sources at all luminosities as seen in Figure 6.18. This is because when a lobe has a higher axial ratio, the lobe velocity on the major axis remains above the sound speed of the external medium for a longer time, and so it transitions to an FRI later in its evolution. Therefore, in the model, when A is increased, nearly all sources are FRIIs at the luminosities considered. Increasing A increases the sizes of radio lobes in the simulation, but it decreases the luminosities of the lobes. This means that as seen in Figure 6.19, fewer small lobes would be observed in the LoTSS data but a similar number of larger lobes would be observed.

6.5.2 Low energy cutoff of the electron energy distribution

The low-energy cutoff of the injected electron energy distribution, $\gamma_{i,min}$, can be inferred observationally in two ways. The first is from a reduction in radio luminosity at low frequencies, with studies of radio hotspots implying values of several hundred (e.g. Carilli et al., 1991; Godfrey et al., 2009). Secondly, $\gamma_{i,min}$ can be inferred from studies at X-ray energies investigating inverse-Compton scattered CMB photons (e.g. Tavecchio et al., 2000) with studies inferring values of about 10. Given this variety of possible values, we set the allowed range of $\gamma_{i,min}$ to be 20-500. In our fiducial model, $\gamma_{i,min} = 100$.

We explore the effect of changing $\gamma_{i,min}$ to 500 on the model predictions. The luminosity increases only modestly, by a factor of 1.3. This is because the luminosity only weakly depends on $\gamma_{i,min}$ for the fiducial value of the spectral index of the injected electron energy distribution, $s = 2.1$. The luminosity increases for a higher value of $\gamma_{i,min}$ because the electron population then has a higher average energy, and so the lobe has a higher luminosity. This effect on the radio luminosities is seen in Figures 6.15, 6.16, and 6.17. As increasing $\gamma_{i,min}$ only affects the luminosities, the sizes of the lobes and the FRI/FRII morphologies of the sources are not affected

by this change, and so the predictions are only slightly different from the fiducial model in Figures 6.18 and 6.19, as a result of the luminosities being slightly higher.

6.5.3 Fraction of energy density in thermal particles

Radio lobes contain relativistic electrons, which we see because of their synchrotron emission, but radio lobes are also likely to contain other particles such as protons and heavier ions, which contribute negligible synchrotron luminosity, but still contribute to the lobe pressure and energy. From radio and X-ray observations, the magnetic field strength and electron energy density can be calculated, which constrains the particle content. This is accounted for in the model via the parameter k^t, which is the ratio of the energy densities of the thermal particles to the energy density of the relativistic electrons at injection. A value of zero represents a lobe with no energy density in thermal particles. Observations suggest there is not an energetically dominant proton population (e.g. Croston et al., 2005; Hardcastle et al., 2016; Ineson et al., 2017), although there is some uncertainty. We therefore permit k^t values in the range 0-10 (cf. Figure 12 of Turner et al., 2018b). In our fiducial model, $k^t = 10$.

When a value of $k^t = 0$ is adopted, the energy density of the electrons is higher, and so the lobe has a higher luminosity. As the dependence of the lobe luminosity on k^t is $1/(k^t + 1)$, when the value of k^t is changed to 0, the luminosities increase by a factor of 11.

This increase in luminosities is seen in the radio luminosity function in Figure 6.15, and correspondingly increases the luminosities in the radio luminosity versus jet power relation in Figure 6.16 as well as increasing the radio fraction in Figure 6.17. Changing the energy density of the thermal particles does not affect the FRI/FRII morphology of sources, and does not affect their sizes, but this model variant does show differences in Figures 6.18 and 6.19 due to the increased luminosities.

6.5.4 Slope of the injected electron energy distribution

The electrons are injected into the lobe with a power law distribution in energy, with slope, s, as in Section 6.2.3. s relates to the spectral index (where $L_\nu \propto \nu^{-\alpha}$) via

$\alpha = (s-1)/2$, assuming no radiative losses to the electron population. Observations of radio sources, which will have been affected to some degree by radiative losses, favour a mean value of $\alpha = 0.7$, but values in the range $\alpha = 0.5 - 1$ are permitted (e.g. Smolčić et al., 2017). We therefore allow s to vary in the range $s = 2 - 3$. In our fiducial model, $s = 2.1$.

When a lobe has a higher value of s, more low energy electrons are injected into the lobe and so the average energy of the electrons is lower. This results in the lobe having a lower luminosity across all frequencies. A higher value of s also affects differently the luminosities at different frequencies, strongly reducing the luminosity at 20GHz, but only slightly reducing the luminosity at 325MHz.

When we increase the value of s in the model to 3, the luminosities decrease by a factor 3 at 1.4GHz, which reduces the number density of objects in the radio luminosity function in Figure 6.15. The radio luminosities at a given jet power are reduced as seen in Figure 6.16, and the radio fraction at a given stellar mass is reduced as seen in Figure 6.17. The FRI/FRII morphologies of sources are unchanged, but the FRII fractions are different in Figure 6.18 due to the changed luminosities. The size distribution of objects in Figure 6.19 is only negligibly changed, as the luminosities in that figure are at 178MHz, which is negligibly affected by this parameter change.

6.5.5 Mean 'on' phase duration

Observational estimates of the duration of the active phase, $t_{\rm on}$, of radio sources vary. Using measurements of curvature in the radio spectrum, Alexander & Leahy (1987) and Harwood et al. (2017) estimate $t_{\rm on}$ values for their sample of radio sources of a few 10^7 years. From the required energy injection rates to quench cooling, McNamara et al. (2005) estimate $t_{\rm on}$ of the order 10^8 years, and by comparing observed sources to a theoretical model, Hardcastle et al. (2019) constrains the active phase of some sources to be at least several 10^8 years. We therefore allow the mean 'on' phase duration of sources in the model, $\bar{t}_{\rm on}$, to vary in the range $10^6 - 10^9$ years. In our fiducial model, $\bar{t}_{\rm on} = 5 \times 10^8$yr.

When $\bar{t}_{\rm on}$ is decreased, the lobes have less time to grow, and so are shorter. In the

model, radio lobes start out as FRIIs, then transition to FRIs, and then are shredded by Rayleigh-Taylor instabilities, causing the lobe luminosity to fall to zero. When we decrease $\bar{t}_{\rm on}$ to 10^7yr, there are more FRIIs at every luminosity, the same number of high luminosity ($L_\nu > 10^{23}$WHz^{-1}) FRIs, and there are more low luminosity ($L_\nu < 10^{23}$WHz^{-1}) FRIs. The reason for the larger number of low luminosity FRIs is that they have not yet been shredded by Rayleigh-Taylor instabilities, whereas the high luminosity FRIs are less susceptible to Rayleigh-Taylor instabilities. Overall, the effect on the radio lumonsity function is that there are about 10 times more low luminosity sources, but only a factor of 4 more high-luminosity sources, as seen in the radio luminosity function in Figure 6.15. The increase in the number of low-luminosity sources then causes the median of the radio luminosity versus jet power relation to decrease, as seen in Figure 6.16. At higher luminosities, the relation is relatively unchanged.

The fraction of galaxies at a given stellar mass that host radio sources increases as a result of the number of objects increasing, as seen in Figure 6.17. The FRII fraction is increased in Figure 6.18, as a result of lobes in the model initially being FRIIs. When investigating the sizes of sources that would be detected in the LoTSS data, the increased number of sources and the decrease in sizes of sources causes the behaviour seen in Figure 6.19, where more small lobes, and fewer large lobes are predicted.

6.5.6 Ratio of 'off' phase duration to 'on' phase duration

The local radio loud fraction of a few percent (Best et al., 2005a; Sabater et al., 2019) suggests that radio sources spend an order of magnitude more time in a quiescent phase compared to their active phase. On the other hand, certain objects in which radio sources are observed inside of older radio lobes (double-double radio galaxies) suggest a quiescent phase duration that is an order of magnitude less than the active phase duration (e.g. Konar et al., 2013). The ratio of the durations of the active and quiescent phases, may vary between sources, and may depend on galaxy properties such as stellar mass (e.g. Shabala et al., 2008). We allow the ratio of the mean 'off' phase to the mean 'on' phase, $\bar{t}_{\rm off}/\bar{t}_{\rm on}$, to vary in the range 0-10. In our fiducial

model, $\bar{t}_{\rm off}/\bar{t}_{\rm on} = 2$.

When we increase $\bar{t}_{\rm off}/\bar{t}_{\rm on}$, to 5, this results in the model having fewer active sources. However, because we increase the mass accretion rate for each object when we increase $\bar{t}_{\rm off}/\bar{t}_{\rm on}$ (cf. equation (6.2.5)), and hence increase the jet power, the radio sources that are active have higher luminosities. This has the effect on the radio luminosity function, seen in Figure 6.15, that there are about a factor of 2 fewer sources at lower luminosities, but a similar number of sources at higher luminosities compared to the fiducial model. Increasing $\bar{t}_{\rm off}/\bar{t}_{\rm on}$ reduces the number of active sources, but once a source is active, it has the same luminosity at a given jet power as in the fiducial model, as seen in Figure 6.16. The radio sources have higher jet powers when $\bar{t}_{\rm off}/\bar{t}_{\rm on}$ is increased. The radio fraction behaves similarly to the radio luminosity function, with about a factor of 2 fewer objects at low luminosities, and a similar number of objects at higher luminosities, as seen in Figure 6.17.

When $\bar{t}_{\rm off}/\bar{t}_{\rm on}$ is increased, the increased jet powers lead to lobes expanding at higher velocities and so they remain as FRIIs for longer, so the FRII fraction is higher, as seen in Figure 6.18. The sizes and luminosities of radio lobes are both larger when $\bar{t}_{\rm off}/\bar{t}_{\rm on}$ is larger, but because there are fewer objects, the predicted distribution of radio lobe sizes in Figure 6.19 shows fewer objects at all sizes for this variant of the model compared to the fiducial model.

6.6 Conclusions

Large radio lobes with sizes up to several Mpc are observed throughout the Universe with a variety of sizes and morphologies. The energy required to create these radio lobes comes from the jets produced by supermassive black holes in the centres of galaxies.

We present predictions for the properties of radio AGN from the GALFORM semi-analytic model of galaxy formation. The jet powers are calculated from a Blandford-Znajek type model, and we use the analytic model of radio lobe evolution of Turner & Shabala (2015). In this model, radio sources start out as Fanaroff-Riley type II (FRII) sources, which then transition to Fanaroff-Riley type I (FRI) sources when

the expansion velocity of the surface normal the cocoon becomes equal to the sound speed of the external medium. These sources then become susceptible to Rayleigh-Taylor instabilities, which eventually shred the lobes.

We present the predictions from this model at $z = 0$. We compare to observational estimates of the radio luminosity function at 325MHz, 1.4GHz, and 20GHz, finding that the model is in very good agreement with the observations at 1.4GHz, but in less good agreement at 325MHz, and not in good agreement at 20GHz. The model may give better agreement with the observed 20GHz luminosity function if Doppler beaming is taken into account. We also split the radio luminosity function by accretion mode into the contribution from thin disc objects and ADAFs to compare to observational estimates of the contribution to the radio luminosity function from HERGs and LERGs. We find that the model is in good agreement with the observed contribution from LERGs, but appears to underpredict the contribution from HERGs. The model agrees that most radio galaxies should be ADAFs/LERGs.

The model also agrees well with observational estimates of the radio luminosity versus jet power relation. When comparing the model to the fraction of galaxies hosting an AGN above a given luminosity, split by stellar mass, it generally agrees for higher luminosities ($L_\nu > 10^{24}\mathrm{WHz}^{-1}$), but is in tension with the observations for lower ($L_\nu < 10^{24}\mathrm{WHz}^{-1}$) luminosities.

We also present predictions for the fractions of FRIs and FRIIs versus radio luminosity. The observations show an increase in FRII fraction with luminosity while the model shows a slight decrease in FRII fraction with luminosity. We also compare the model to observations of radio lobe sizes, comparing only to sources with sizes and luminosities for which surveys provide reliable estimates for number densities. When comparing the model to the 3CRR survey, the radio lobes in the model are on average two times larger than the 3CRR survey, but when comparing to more recent LOFAR Two-metre Sky Survey (LoTSS) data, the lobe sizes from the model agree better with the observations, except at the largest sizes ($D > 200$kpc), where the model predicts too few sources.

We also explore the effect of varying different free parameters of the extended radio emission model, showing how each parameter affects the different observables.

The luminosities of radio sources in the model are most strongly affected by the initial axial ratio of lobes, A, the ratio of the energy density of the thermal particles to the energy density of the electrons, k^t, and the slope of the injected electron energy distribution, s, where for modest changes of these parameters, the luminosities are affected relatively strongly. The fraction of FRII sources is most strongly affected by the value of A - for an increase in A by a factor of 3, causes virtually all sources to have an FRII morphology. The sizes of sources that would be detected by LOFAR are also most strongly affected by A.

Overall, we find that the model is generally in reasonable agreement with observations of radio AGN at $z = 0$, except for the fraction of galaxies with a radio AGNs at low luminosity, the fractions of FRI/FRII sources, and the number of the largest sources. In future work we plan to address some of these discrepancies. First, we could draw the value of $\dot{M}$ from a probability distribution rather than having a fixed value as we adopt here. This would produce a greater variety of luminosities of sources, and may address the lack of low luminosity sources and the lack of large size detectable sources. Secondly, we could explore changing the probability distribution from which the 'on' and 'off' times of the sources are calculated which may produce more short duration, low luminosity sources. We could adopt different probability distributions for the 'on' and 'off' times. Thirdly, the duration of the 'on' and 'off' times is currently independent of galaxy properties, in future we plan to explore a dependence of the duty cycle on stellar or black hole mass.

Finally, we would also like to explore the effect of changing the mechanism by which sources transition from FRIIs to FRIs, to explore if such a change to the model can give better agreement with observations. It may be that FRIs can become underpressured with respect to their external environments, unlike here where they are assumed to be in pressure balance, or it may be that FRIs and FRIIs have different particle contents.

The future comparison of this model to upcoming radio surveys such as those with MeerKAT, ASKAP and SKA may also give greater insights into the nature of the radio AGN population and AGN feedback.

Chapter 7

Overall Conclusions and Future Work

I now summarise the work presented in this thesis, and provide suggestions for future investigation.

Understanding the evolution of AGNs as they evolve across cosmological time has been of interest ever since they were discovered to reside outside of our own galaxy. Observational studies have been conducted across a range of wavelengths to explore the evolution of the AGN luminosity function, and theoretical models have sought to probe the physical mechanisms behind this evolution. AGNs are also believed to be important for understanding galaxy evolution via AGN feedback, which is thought to play an important role in the formation of the most massive galaxies. In this thesis, I have presented predictions for the evolution of SMBH and AGN properties from an existing theoretical model of galaxy formation, GALFORM.

In Chapter 2, I describe how the different physical processes relevant for galaxy formation are modelled in GALFORM, and the particular GALFORM model that I use. I have used the Lacey et al. (2016) GALFORM model as recalibrated by Baugh et al. (2019). The Lacey et al. (2016) model matches a wide variety of galaxy properties across a range of wavelengths and redshifts, and Baugh et al. (2019) introduces a recalibration of this model for a high resolution dark matter N-body simulation that uses the Planck cosmology. In the model, SMBHs grow by either (i) accretion of gas during starbursts, which are triggered by either galaxy mergers or galaxy disc

instabilities, (ii) accretion of gas from the hot gas atmospheres of massive haloes, or (iii) merging with other SMBHs.

In Chapter 3, I presented my new implementation of the spin evolution model used within GALFORM. In this model the SMBH spin evolves either by accretion of gas, or when merging with another SMBH. The model tracks the evolution of the angular momentum of the SMBH and the angular momentum of the accretion disc as gas is accreted. In this Chapter I presented SMBH and AGN properties from the model for $0 \leq z \leq 6$. I compared the SMBH masses to observational estimates of the black hole mass function, the active black hole mass function, and SMBH mass versus galaxy/bulge stellar masses. I then showed the predicted SMBH spin distributions and their evolution, and the evolution of mass and spin of some typical objects from the simulation. I then compared the predicted AGN luminosity functions in optical to X-ray bands to observed AGN luminosity functions. Overall, I found that the model is in good agreement with the observations. This model involves some free parameters, which are either adopted from other studies, or calibrated on the AGN luminosity functions presented in this Chapter. These parameters relate to the lifetimes of AGN epsiodes and the suppression of luminosity for super-Eddington mass accretion rates.

When splitting the AGN bolometric luminosity function by accretion disc state, I found that the contribution from objects accreting in an advection-dominated accretion flow state is dominant for $L_{\rm bol} < 10^{43}{\rm ergs}^{-1}$ and $z < 2$, while at higher luminosities and higher redshifts, the dominant contributor is from objects in a thin disc or super-Eddington accretion state. When splitting the AGN bolometric luminosity function by SMBH fuelling mode, I found that it is dominated by the contribution from quiescent hot halo accretion at low luminosities ($L_{\rm bol} < 10^{44}{\rm ergs}^{-1}$) and low redshifts ($z < 3$), but at higher luminosities and redshifts, the dominant contribution is from SMBHs fuelled by starbursts triggered by galaxy disc instabilities. Given the important role that disc instabilities are predicted to have in fuelling the high redshift AGN luminosity function, a more detailed investigation into the conditions under which disc instabilities occur would test the validity of this claim. A more accurate disc instability condition could be derived using high resolution

hydrodynamical simulations of isolated unstable galaxy discs (including physical processes such as gas cooling and feedback), and would improve the accuracy of the high redshift AGN luminosity function predictions.

In Chapter 4, I used this model to make predictions for $z \geq 7$, for surveys conducted by future telescopes. I presented predictions for surveys by JWST and EUCLID at optical and near-IR wavelengths, and for surveys by ATHENA and JWST at X-ray energies. I found that the different surveys will detect different samples of AGNs, as a result of the different wavelengths, flux limits, and sky areas for the different surveys, which result in different limits in bolometric luminosity and number density. When investigating the properties of objects predicted to be detected by these surveys, I predicted that Lynx will detect the smallest black holes, in the smallest mass host galaxies and haloes, accreting at the lowest Eddington normalised accretion rates. This is because of the improved angular resolution of Lynx compared to ATHENA, which improves the sensitivity limit due to the reduced source confusion, and hence lowers the luminosities of objects that can be detected. I predicted that the SMBH seed mass does not strongly affect the luminosity functions, although Lynx may be able to differentiate between some seeding models. For these predictions, each halo is seeded with a black hole of identical mass, but in future work one could explore introducing a more physical seeding mechanism, where SMBH seeds are produced from collapsing gas clouds or the remnants of the first (Population III) stars. Overall, comparing these predictions to results from these surveys will provide tests of these theoretical models in the early Universe.

In Chapter 5, I presented predictions for the evolution of jet powers and radio luminosities for $0 \leq z \leq 6$. The jet powers are calculated from the spin, mass, and mass accretion rate of the SMBHs, based on a Blandford-Znajek type model, and the radio luminosities are calculated from the jet powers using a published scaling relation. This radio emission model involves two free parameters, which we calibrate to the 1.4GHz radio luminosity function for AGN at $z = 0$. These radio luminosities are most appropriate for core-dominated sources. The jet powers predicted by the model were found to be dominated by the contribution from objects fuelled by starbursts and objects accreting via a thin disc state for jet powers $Q <$

10^{32}W at $z = 0$, and at all jet powers by $z = 6$. The total jet power density is dominated by objects with jet powers $Q \sim 10^{36}$W for $0 < z < 6$, and this is also the case for both the starburst and hot halo contributions. I then compared the evolution of the jet power density from the model to observational estimates, finding that while the model overpredicts the observations, there are observational uncertainties such that the tension between the model and the observations may not be significant. I then compared the predicted evolution of the radio luminosity function at 1.4 GHz to observations, finding that the model is in good agreement with the observations. I find that the radio luminosity function at $z = 0$ is dominated by SMBHs fuelled by hot halo accretion for $L_\nu < 10^{24}\mathrm{WHz}^{-1}$, by starbursts triggered by galaxy disc instabilities for $10^{24}\mathrm{WHz}^{-1} < L_\nu < 10^{26}\mathrm{WHz}^{-1}$, and by starbursts triggered by galaxy mergers for $L_\nu > 10^{26}\mathrm{WHz}^{-1}$. At higher redshifts ($z > 3$) the radio luminosity function is dominated by stabursts triggered by disc instabilities for $L_\nu < 10^{26}\mathrm{WHz}^{-1}$, and by quiescent hot halo accretion for $L_\nu > 10^{26}\mathrm{WHz}^{-1}$.

In Chapter 6, I presented predictions for the evolution of extended radio sources using an analytic radio lobe evolution model within the GALFORM model. In this analytic model, radio lobes start out as Fanaroff-Riley type II sources, and then transition into Fanaroff-Riley type I sources once they reach pressure balance with their environments. The Fanaroff-Riley type I sources are then susceptible to Rayleigh-Taylor instabilities, which eventually shred the lobes. I used the SMBH mass, mass accretion rate and spin dependent jet powers from Chapter 5, and a simple model for the jet duty cycle, separate for hot halo mode and starburst mode sources. This model predicts the luminosities at different frequencies, sizes, and Fanaroff-Riley types of the radio source population. I find that the model is in good agreement with a range of observations at $z = 0$, but the model (i) predicts too few low luminosity radio AGNs in high stellar mass galaxies, (ii) predicts a flat relation between the fraction of Fanaroff-Riley type II sources with luminosity, unlike the observations and (iii) predicts too few large ($D > 200$kpc) sources when compared to recent LOFAR Two-metre Sky Survey (LoTSS) data. The first and third of these shortcomings may be resolved by selecting SMBH mass accretion rate values from a probability distribution. This could create a greater variety in the energies of sources, to provide

low luminosity sources in high stellar mass galaxies, and to provide large lobes that would be detected in the LoTSS data. The second shortcoming could be resolved by modifying the mechanism by which sources transition from Fanaroff-Riley type IIs to Fanaroff-Riley type Is.

Alongside some of the possibilities for future work mentioned above, several other investigations could be conducted. First, the model presented here could be used to predict the spin of SMBHs detected by future gravitational wave detectors such as eLISA. By making predictions for both the chaotic and prolonged accretion modes, one could investigate whether eLISA would be able to distinguish between these two different accretion scenarios (e.g. Amaro-Seoane et al., 2013). One could also use predictions for eLISA to relate the actual merger rate of SMBHs to the merger rate detectable by eLISA.

Secondly, the SMBH spin predictions have been presented for either prolonged or chaotic modes, whereas some works use a mixture of the two (e.g. Bustamante & Springel, 2019), where SMBH spin can either evolve via the chaotic mode or the prolonged mode depending on the angular momentum. One could implement a similar scheme into the spin evolution model here.

Thirdly, the relation of AGN to environment in the model could be investigated. GALFORM has previously been compared to observations of the clustering of X-ray AGN to constain SMBH fuelling in Fanidakis et al. (2013b), and similar insights could be obtained at optical or radio wavelengths, using the models presented here.

Fourthly, while we have explored SMBH mass versus bulge stellar mass and galaxy stellar mass here, the relation of SMBH and AGN properties to other galaxy properties such as galaxy morphology and gas fraction could be investigated and compared to observational results.

Fifthly, some of this work investigating radio emission from galaxies from a semi-analytic model could also be applied to cosmological hydrodynamical simulations. The radio lobe evolution model used in Chapter 6 could be used as a subgrid model in such a galaxy formation simulation, and this may provide extra insights into the role of radio sources in galaxy evolution.

Finally, some more fundamental changes could be made to the galaxy formation

model. In GALFORM, the AGN feedback prescription is only radio mode AGN feedback, it would be interesting to introduce a prescription for quasar mode AGN feedback into the model. This could improve the AGN predictions, particularly at higher redshifts where quasar mode AGN feedback is believed to play an important role. Exploring the impact of quasar mode feedback on galaxy properties could allow for a better understanding of the role of AGNs in galaxy formation.

Appendix A

$z < 6$ SMBH and AGN properties

A.1 Effects of varying SMBH seed mass

In Figure A.1 we show the effect of varying the SMBH seed mass on the black hole mass function at $z = 0$. We show plots for SMBH seed masses of $10h^{-1}M_{\odot}$ (the default value), $10^{3}h^{-1}M_{\odot}$ and $10^{5}h^{-1}M_{\odot}$. Generally the black hole mass function reaches a converged value at about 100 times the black hole seed mass. We also plot as vertical lines $M_{\rm BH} = M_{\rm seed}$, $M_{\rm BH} = 2 \times M_{\rm seed}$ and $M_{\rm BH} = 3 \times M_{\rm seed}$. It can be seen that the spikes in the black hole mass function occur at these values due to SMBH seeds merging with other SMBH seeds.

This convergence in properties at around 100 times the seed mass can also be seen in Figure A.2, where the median of the SMBH mass versus bulge mass relation for seeds of mass $10^{5}h^{-1}M_{\odot}$ only converges with that for the other seed masses for SMBH masses above around $10^{7}M_{\odot}$.

A.2 Calculating broad-band optical magnitudes for AGN

We define the filter-averaged luminosity per unit frequency for a filter R in the observer frame at redshift z as:

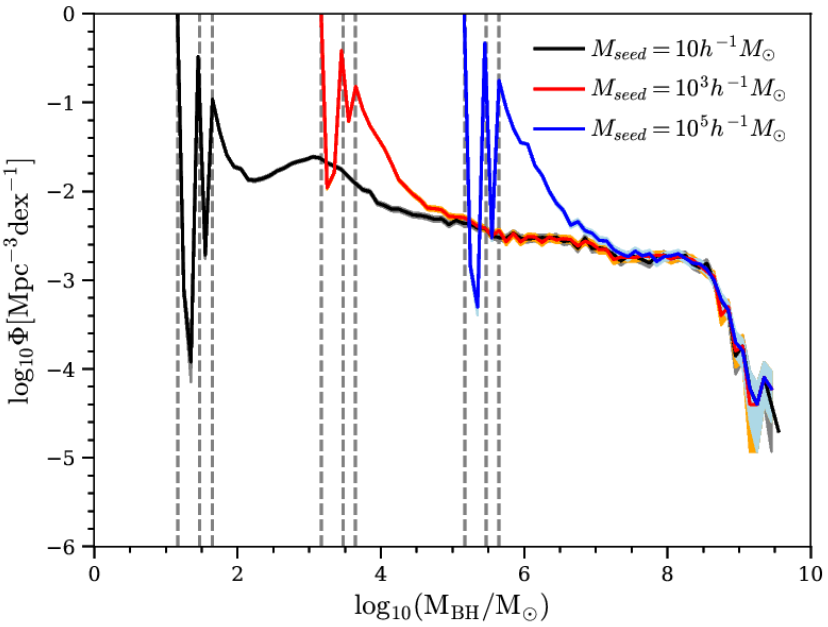

Figure A.1: The black hole mass function at $z = 0$ for seed masses of $10h^{-1}M_\odot$ (black), $10^3h^{-1}M_\odot$ (red) and $10^5h^{-1}M_\odot$ (blue).

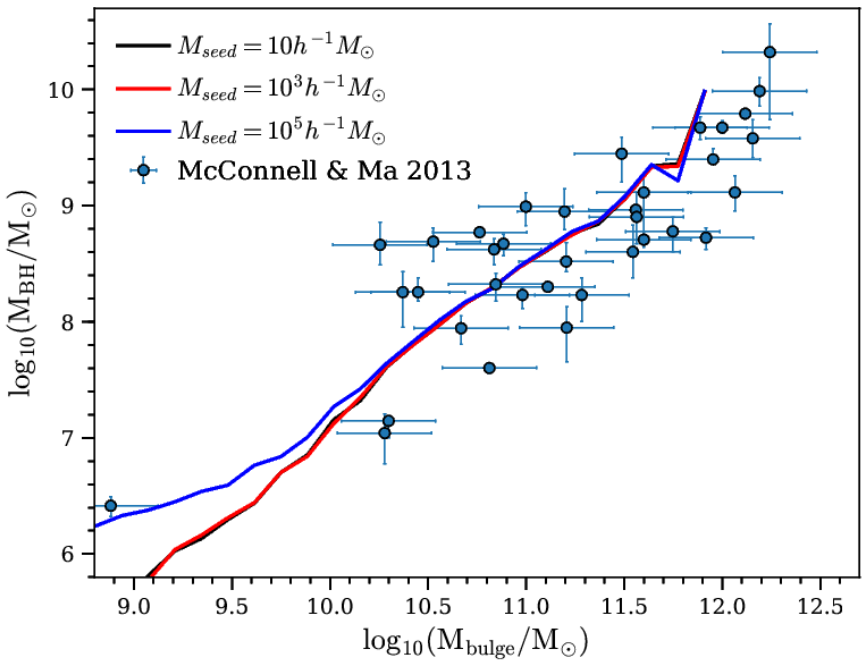

Figure A.2: The predicted SMBH mass versus bulge mass relation at $z = 0$ for seed masses of $10h^{-1}M_\odot$ (black), $10^3h^{-1}M_\odot$ (red) and $10^5h^{-1}M_\odot$ (blue) compared to McConnell & Ma (2013).

$$< L_\nu >_R^{(z)} = \frac{\int L_\nu((1+z)\nu_o)R(\nu_o)d\nu_o}{\int R(\nu_o)d\nu_o}, \tag{A.2.1}$$

where $L_\nu(\nu)$ is the luminosity per unit frequency in the rest frame, $R(\nu_o)$ is the response function of the filter at observed frequency ν_o. The absolute magnitude in the AB system in the observer frame band defined by the filter R for redshift z, is then defined as:

$$M_{AB,R}^{(z)} = -2.5\log_{10}\Big(\frac{< L_\nu >_R^{(z)}}{L_{\nu_o}}\Big), \tag{A.2.2}$$

where $L_{\nu_o} = 4\pi(10\mathrm{pc}^2) \times f_{\nu_o}$ with $f_{\nu_o} = 3631\mathrm{Jy}$, the flux corresponding to an apparent AB magnitude of 0, and L_{ν_o} the corresponding luminosity per unit frequency for an absolute AB magnitude of 0. We remind readers that monochromatic AB (Absolute Bolometric) apparent magnitudes are defined using the following relation (Oke & Gunn, 1983):

$$m_{\mathrm{AB}}(\nu) = -2.5\log_{10}\Big(\frac{f_\nu}{f_{\nu_o}}\Big), \tag{A.2.3}$$

where f_ν is the observed flux of the source, which is related to the luminosity per unit frequency in the rest-frame of the object as:

$$f_\nu(\nu_o) = \frac{(1+z)L_\nu((1+z)\nu_o)}{4\pi d_L^2}. \tag{A.2.4}$$

The apparent and observer frame absolute magnitudes for a filter R are then related by

$$m_{AB}(\nu) = -2.5\log_{10}\Big(\frac{< L_\nu >_R^{(z)}}{L_{\nu_o}}\Big) - 2.5\log_{10}(1+z) + 5\log_{10}(d_{\mathrm{L}}/10\mathrm{pc}). \tag{A.2.5}$$

We then use the following formulae to convert the observational data from the different wavelengths given to rest-frame wavelength 1500Å. Note that we are only comparing continuum luminosities in this study, which is consistent with the Marconi et al. (2004) template used throughout this paper. The data presented in the studies that we use have the contribution from the emission lines removed and so this is an

appropriate comparison. The results presented in Richards et al. (2006) are given in the K-corrected SDSS i band at $z = 2$, which we write as $M_i'(z = 2)$. This is given by $M_i'(z = 2) = M_i(z = 2) - 2.5\log(1 + z)$, where we define $M_i(z = 2)$ as the absolute magnitude at the rest-frame wavelength corresponding to the observed i-band at $z = 2$, as in equations (A.2.2) and (A.2.5). To convert from $M_i(z = 2)$ to 1500Å, we follow Richards et al. (2006) by using $L_\nu \propto \nu^{\alpha_\nu}$ but using a spectral index value of $\alpha_\nu = -0.44$ from Marconi et al. (2004) instead of $\alpha_\nu = -0.5$ in Richards et al. (2006). First we convert from $M_i'(z = 2)$ to $M_i(z = 0)$ using equations (A.2.1) and (A.2.2):

$$\begin{aligned} M_i(z = 0) &= M_i'(z = 2) + 2.5(1 + \alpha_\nu)\log(1 + 2) \\ &= M_i'(z = 2) + 0.668, \end{aligned} \tag{A.2.6}$$

where $M_i(z = 0)$ is the absolute magnitude at the central wavelength of the rest-frame i-band (7471Å) corresponding to equation (A.2.2) for $z = 0$. Then we relate $M_i(z = 0)$ to the absolute magnitude at rest-frame 1500Å, M_{1500}, to give the conversion to $M_i'(z = 2)$:

$$\begin{aligned} M_{1500} &= M_i(z = 0) + 2.5\alpha_\nu \log_{10}\Big(\frac{1500\text{Å}}{7471\text{Å}}\Big), \\ &= M_i(z = 0) + 0.767, \\ &= M_i'(z = 2) + 1.435. \end{aligned} \tag{A.2.7}$$

where in the last line we used equation (A.2.6). Jiang et al. (2009); Willott et al. (2010); Ikeda et al. (2011); Masters et al. (2012); Kashikawa et al. (2015) report observed absolute continuum magnitudes, M_{1450}, corresponding to rest frame 1450Å. These absolute magnitudes are defined without the extra redshift factor included in the Richards et al. (2006) definition. These absolute magnitudes at 1450Å, M_{1450}, can be converted to 1500Å using:

$$\begin{aligned} M_{1500} &= M_{1450} + 2.5\alpha_\nu \log_{10}\Big(\frac{1500\text{Å}}{1450\text{Å}}\Big), \\ &= M_{1450} - 0.016. \end{aligned} \tag{A.2.8}$$

Finally Croom et al. (2009) report observations in the SDSS g-band (4670Å) K-corrected to $z = 2$, so we use the correction in their paper:

$$M'_g(z=2) = M'_i(z=2) + 2.5\alpha_\nu \log\Big(\frac{4670\text{Å}}{7471\text{Å}}\Big), \tag{A.2.9}$$

and combine it with the above relation to give:

$$M_{1500} = M'_g(z=2) + 1.211. \tag{A.2.10}$$

A.3 Visible and obscured fractions for AGN

The AGN visible fractions (the fraction of sources at a particular luminosity and redshift that are unobscured) derived in this paper have been estimated by constructing an observational bolometric luminosity function from observed luminosity functions at X-ray and optical wavelengths. These luminosities were converted to bolometric using the Marconi et al. (2004) AGN SED, and then the observed number densities were converted to total number densities using visible fractions of a functional form similar to Hopkins et al. (2007) dependent only on $L_{\rm bol}$ (cf. equation (3.3.38)). We assumed that there is no obscuration for hard X-ray wavelengths. The coefficients in the expressions for the visible fractions were then selected (cf. equations (3.3.41), (3.3.42) and (3.3.43)) so as to minimise the scatter in the estimated bolometric luminosity function.

To construct a bolometric luminosity function from multiple sets of observations in different wavebands, different authors use different template SEDs. Some authors include reprocessed radiation from dust (its inclusion causes an 'IR bump' in the SED) whereas some do not. Including reprocessed radiation gives observed bolometric luminosities, whereas not including the IR bump gives intrinsic bolometric luminosities. The intrinsic bolometric luminosities are isotropic, while the observed bolometric luminosities are not isotropic because the obscuring torus is not isotropic. The observed bolometric luminosity functions of Hopkins et al. (2007) are given in terms of observed rather than intrinsic bolometric luminosities, so when we compare with these, we multiply the luminosities of Hopkins et al. (2007) by a factor 7.9/11.8

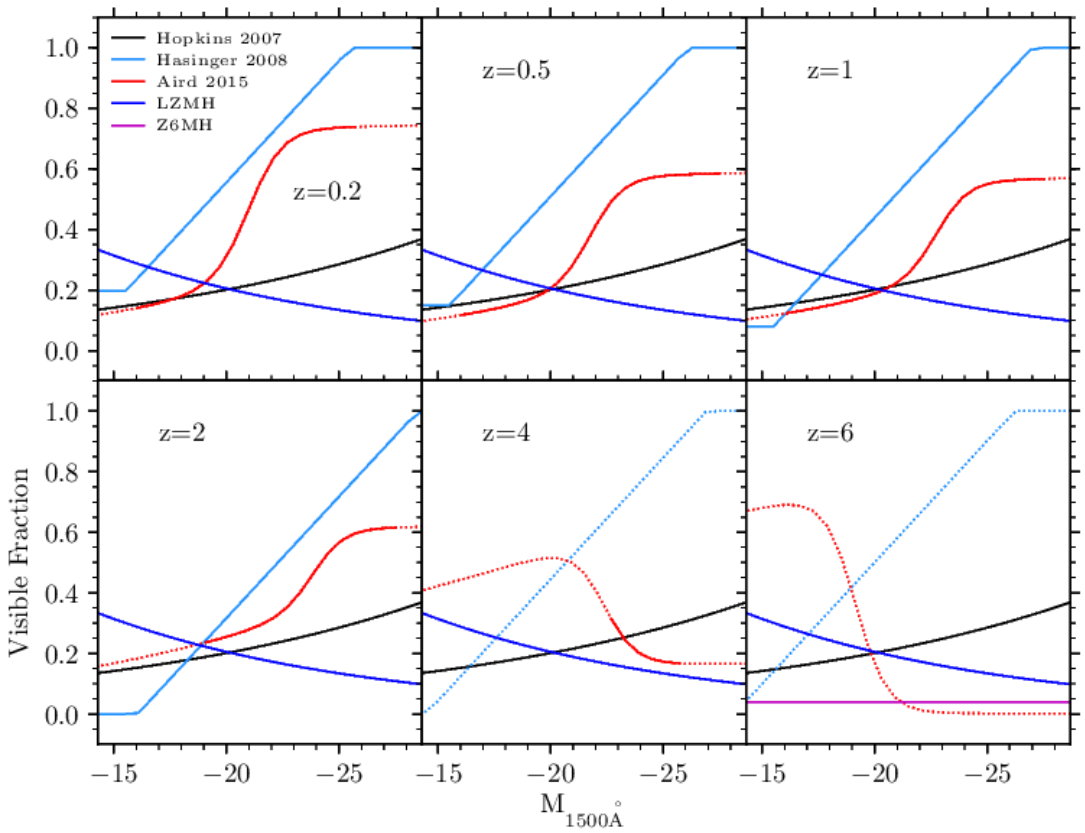

Figure A.3: Comparing the visible fractions for rest-frame 1500Å for different obscuration models. Shown are Hopkins et al. (2007) (black), Hasinger (2008) (light blue), Aird et al. (2015) (red), the LZMH model (dark blue) and the Z6MH model (purple). The solid lines for the observational visible fractions indicate the ranges where there is observational data, while the dotted lines indicate ranges where a functional form has been extrapolated.

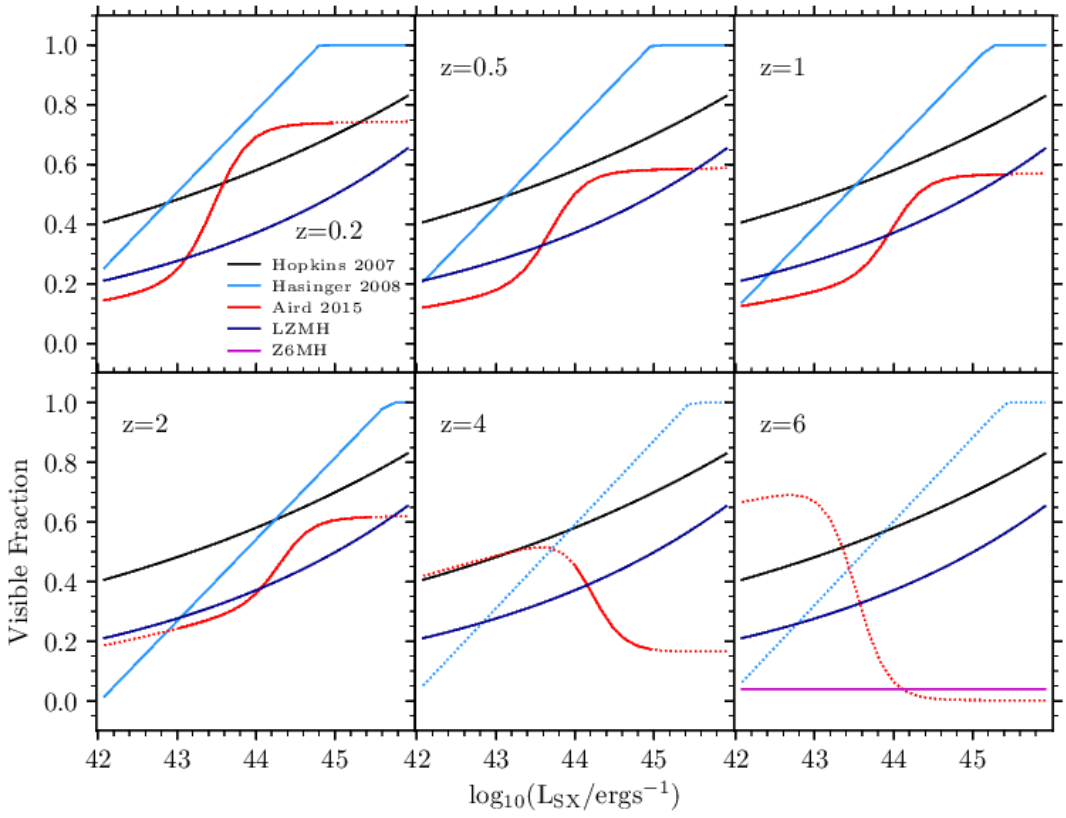

Figure A.4: The same as the previous plot, but for rest-frame soft X-rays.

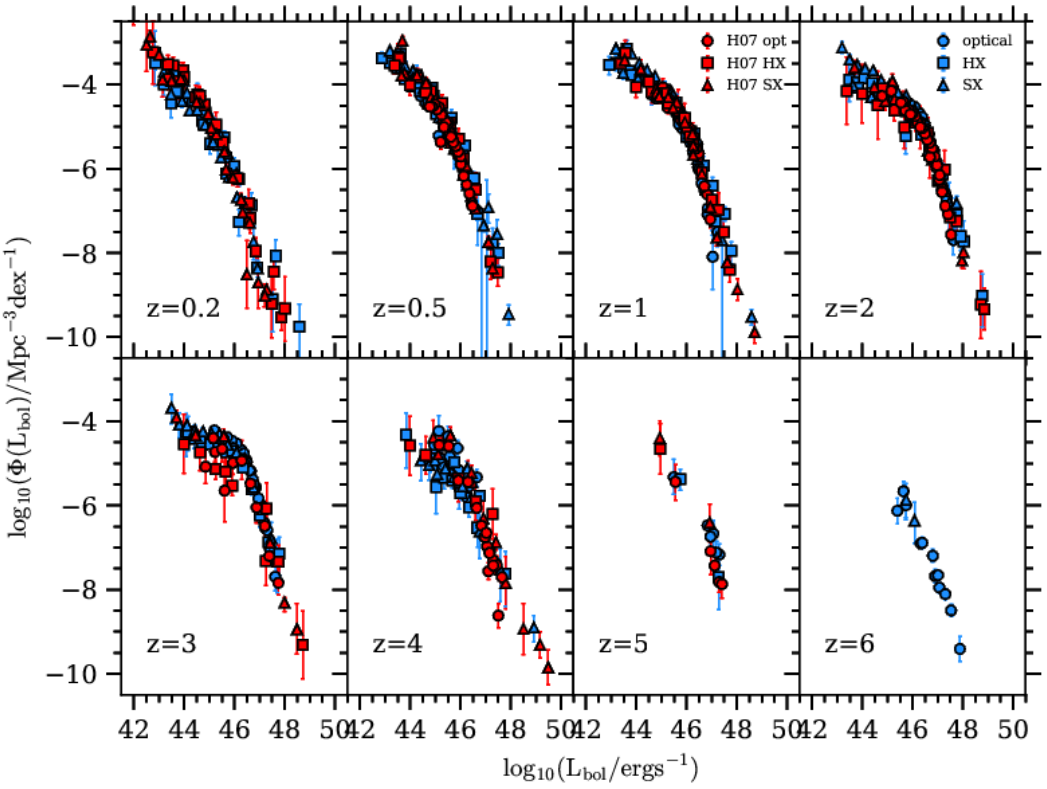

Figure A.5: The bolometric luminosity function derived in this work (blue) by using the Marconi et al. (2004) bolometric corrections, and by varying the coefficients of the visible fractions to obtain a bolometric luminosity function with the smallest scatter between points derived from data at different wavelengths, compared to the Hopkins et al. (2007) bolometric luminosity function (red). The Hopkins et al. (2007) bolometric luminosities have been multiplied by 7.9/11.8 to account for the different SED template used (see text).

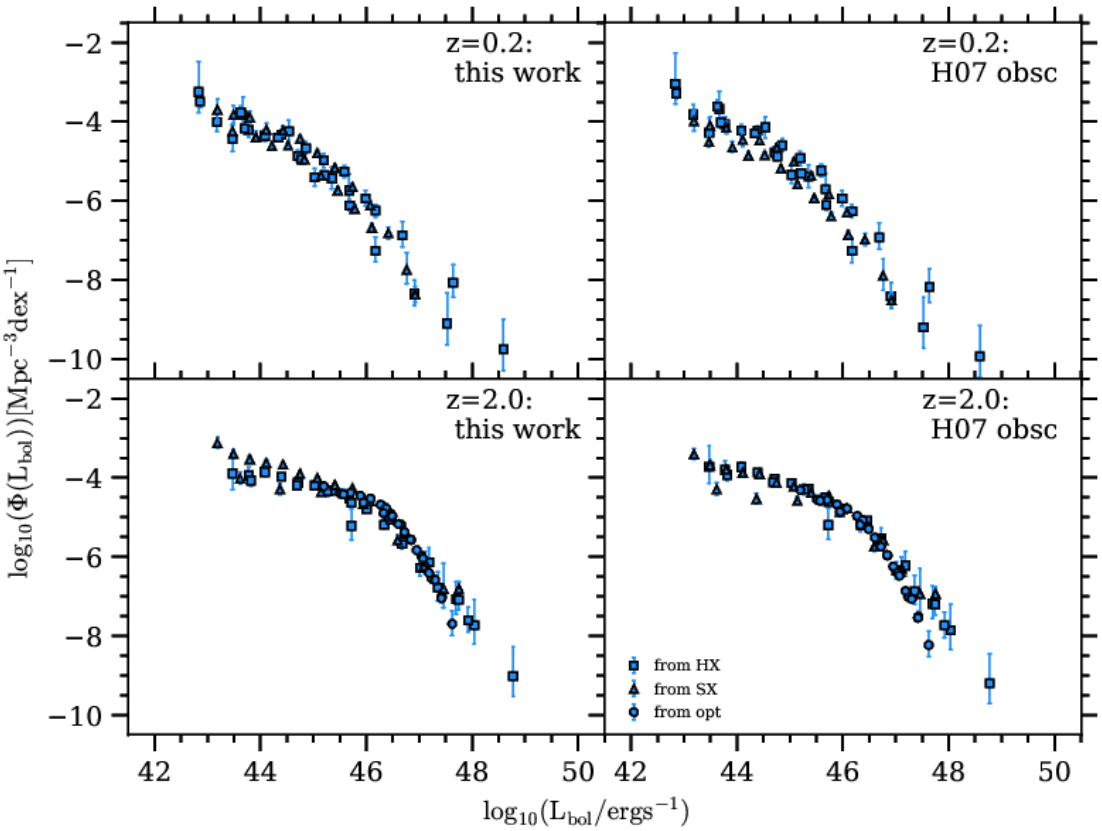

Figure A.6: Comparing the effect of using different obscuration models on the constructed bolometric luminosity functions. The left panels are obtained using the obscuration model presented in Section 3.3.3, while the right panels use the obscuration model of Hopkins et al. (2007). The upper panels are for $z = 0.2$ and the lower panels are for $z = 2$.

(cf. Marconi et al., 2004) to account for this effect.

We show a comparison of the different obscuration models at 1500Å in Figure A.3 and at soft X-ray energies in Figure A.4. The values from different studies are not all on a single curve, and so there is clearly still some uncertainty in the visible fraction.

Our bolometric luminosity function is shown compared to the bolometric luminosity functions estimated in Hopkins et al. (2007) in Figure A.5, and the two are in agreement. The bolometric luminosity function derived in this work is also similar to that determined by Shankar et al. (2009).

Our observationally estimated visible fractions are redshift independent by construction. We have explored whether a better fit could be obtained by including a redshift dependence. To obtain a better fit, the visible fraction needs to increase and then decrease with redshift (cf. the redshift dependence derived by Aird et al., 2015), but even with a functional form to allow this, the scatter in the bolometric luminosity function was only slightly less than for redshift independent versions of the visible fraction.

To quantify the effect of using the new visible fraction derived in this paper, we compare the bolometric luminosity function derived using the Hopkins et al. (2007) visible fraction, to the bolometric luminosity function derived using the visible fraction presented in this paper, in Figure A.6. The new visible fraction does improve the constructed bolometric luminosity function, this reduction in scatter can be seen particularly at $L_{\rm bol} \sim 10^{44}{\rm ergs}^{-1}$ at $z = 0.2$ and at $L_{\rm bol} \sim 10^{48}{\rm ergs}^{-1}$ at $z = 2$.

A.4 The effect of the time averaging method

In this appendix, we show the effect of varying $\Delta t_{\rm window}$ on the AGN luminosity function, as introduced in Section 3.3.4, and compare the luminosity function obtained using the time averaging method in Section 3.3.4 to a luminosity function constructed using the snapshot luminosities. In Figure A.7, the predicted luminosity function with a value of $\Delta t_{\rm window} = t_{\rm H}/10$ (the standard model), is compared to the predicted luminosity function with a value of $\Delta t_{\rm window} = t_{\rm H}/50$. The two are very

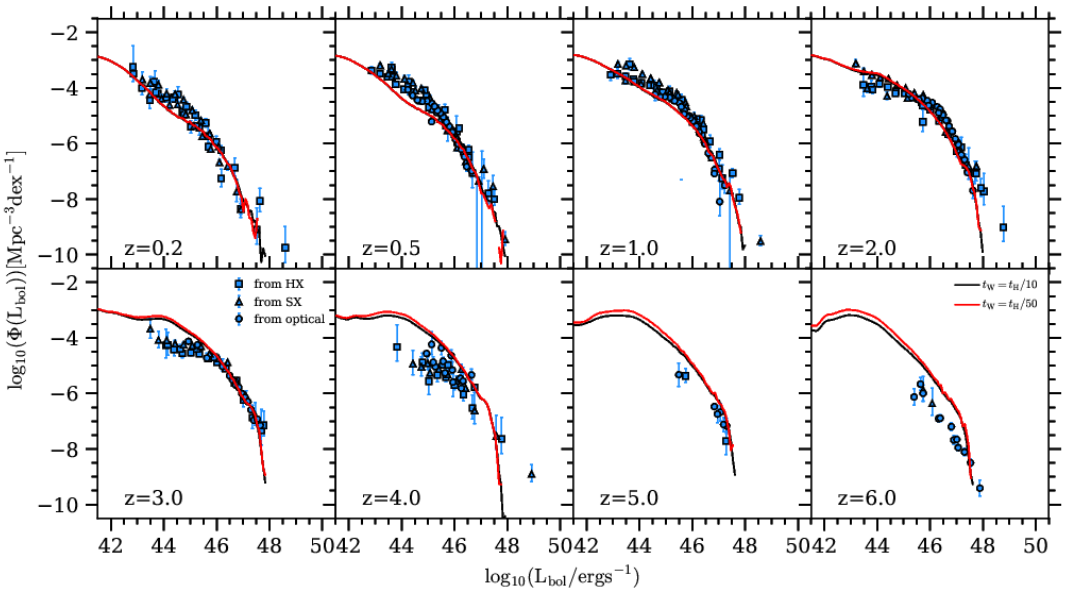

Figure A.7: Exploring the effect on the AGN bolometric luminosity function of varying $\Delta t_{\rm window}$, shown are $\Delta t_{\rm window} = t_{\rm H}/10$ (black) and $\Delta t_{\rm window} = t_{\rm H}/50$ (red).

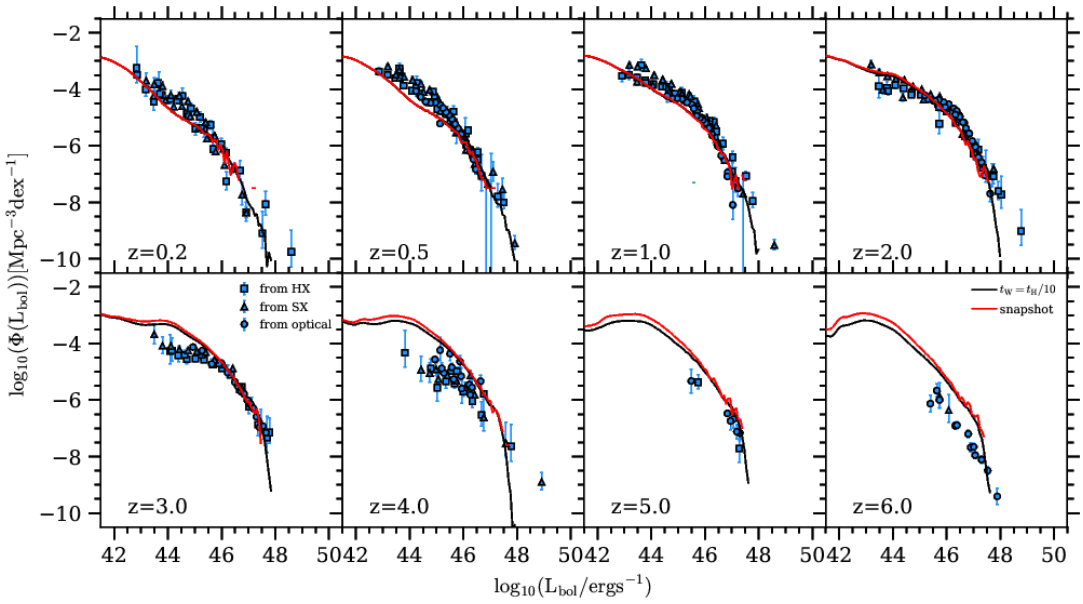

Figure A.8: Exploring the effect on the AGN bolometric luminosity function of varying $\Delta t_{\rm window}$, shown are $\Delta t_{\rm window} = t_{\rm H}/10$ (black) and using the snapshot luminosities (red).

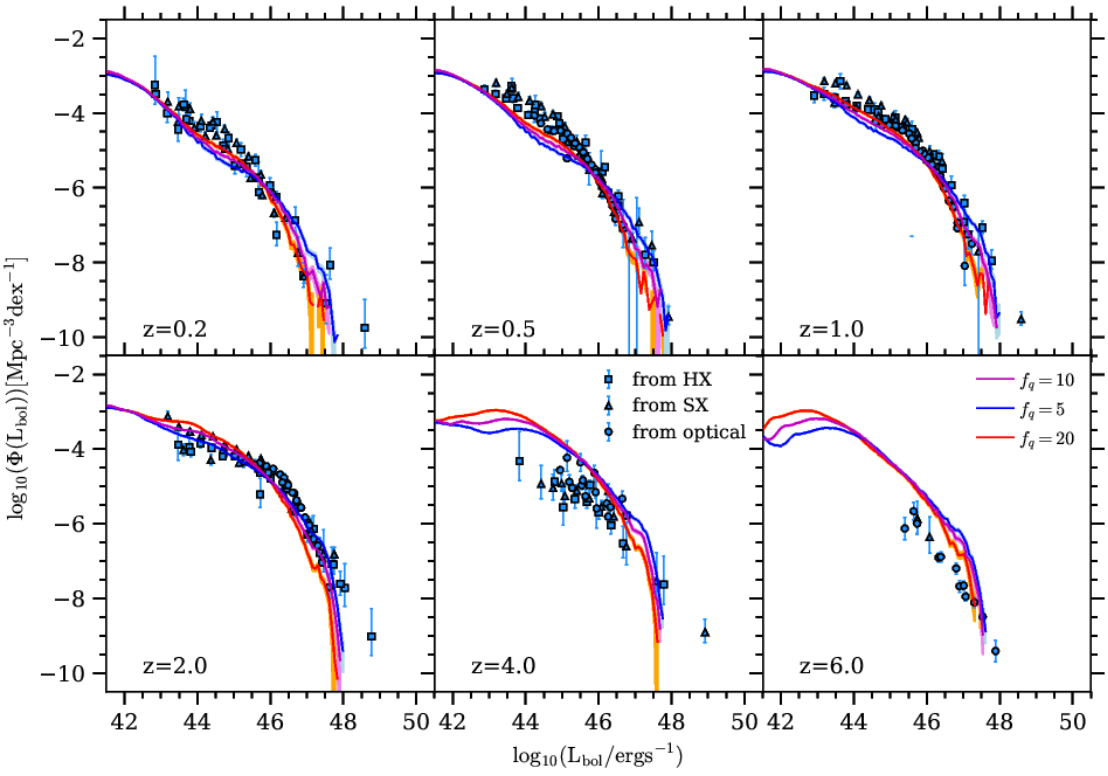

Figure A.9: Exploring the effect on the AGN bolometric luminosity function of varying the parameter $f_{\rm q}$. Shown are $f_{\rm q} = 5$ (blue), $f_{\rm q} = 10$ (purple, the fiducial model) and $f_{\rm q} = 20$ (red). The shading shows the Poisson errors of the distribution.

similar, except at low luminosities at high redshift, where there is a slight difference. The similarity shows that the value of $\Delta t_{\rm window}$ adopted does not strongly affect the luminosity function. In Figure A.8, the predicted luminosity function with a value of $\Delta t_{\rm window} = t_{\rm H}/10$ is compared to the luminosity function where only the snapshot luminosities are used to construct the luminosity function. It can be seen how the time averaging method allows predictions for much lower number densities than for the snapshot case. These two cases are very similar in the luminosity range where they overlap, showing that the time averaging method does not change the predicted luminosity function significantly.

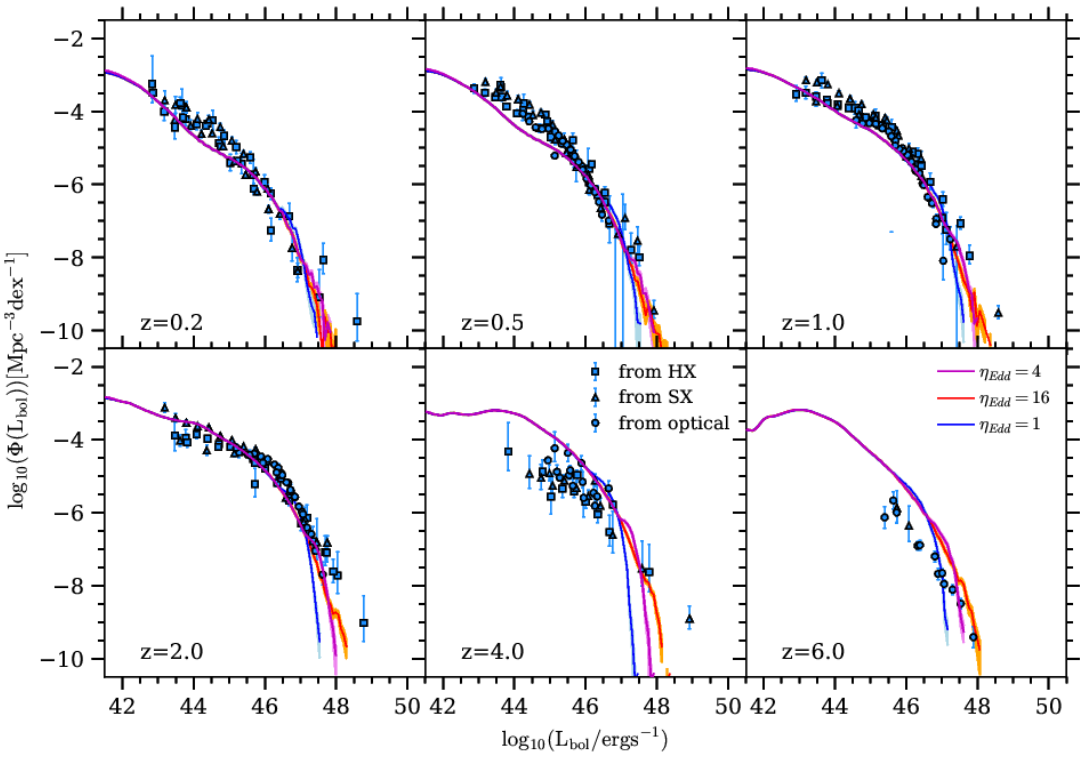

Figure A.10: Exploring the effect of varying $\eta_{\rm Edd}$. Shown are $\eta_{\rm Edd} = 1$ (blue), $\eta_{\rm Edd} = 4$ (purple, the fiducial model) and $\eta_{\rm Edd} = 16$ (red).

A.5 Exploring the effect of varying parameters

We show the effect on the bolometric luminosity function of varying some of the free parameters for SMBH and AGN used in the model; in Figure A.9, we show the effect of varying the parameter $f_{\rm q}$ (cf. equation (2.7.25)). $f_{\rm q}$ affects the value of $\dot{M}$ and therefore the AGN luminosities. One expects a higher value of $f_{\rm q}$ to lead to lower values of $\dot{M}$ and therefore a steeper luminosity function at the bright end, as we see in Figure A.9. At the faint end, a lower value of $f_{\rm q}$ results in a poorer fit to the observations at low redshift ($z = 0.2, 0.5, 1$) but is a better fit to the observations at high redshift ($z = 2, 4, 6$). At the bright end, a higher value of $f_{\rm q}$ seems to give a better fit to the observations at low redshift but gives a worse fit to the observations at high redshift (e.g. around $L_{\rm bol} \sim 10^{48}{\rm ergs}^{-1}$ at $z = 4$). With these considerations in mind, we decide to keep the Fanidakis et al. (2012) value of $f_{\rm q} = 10$ for our predictions in this paper.

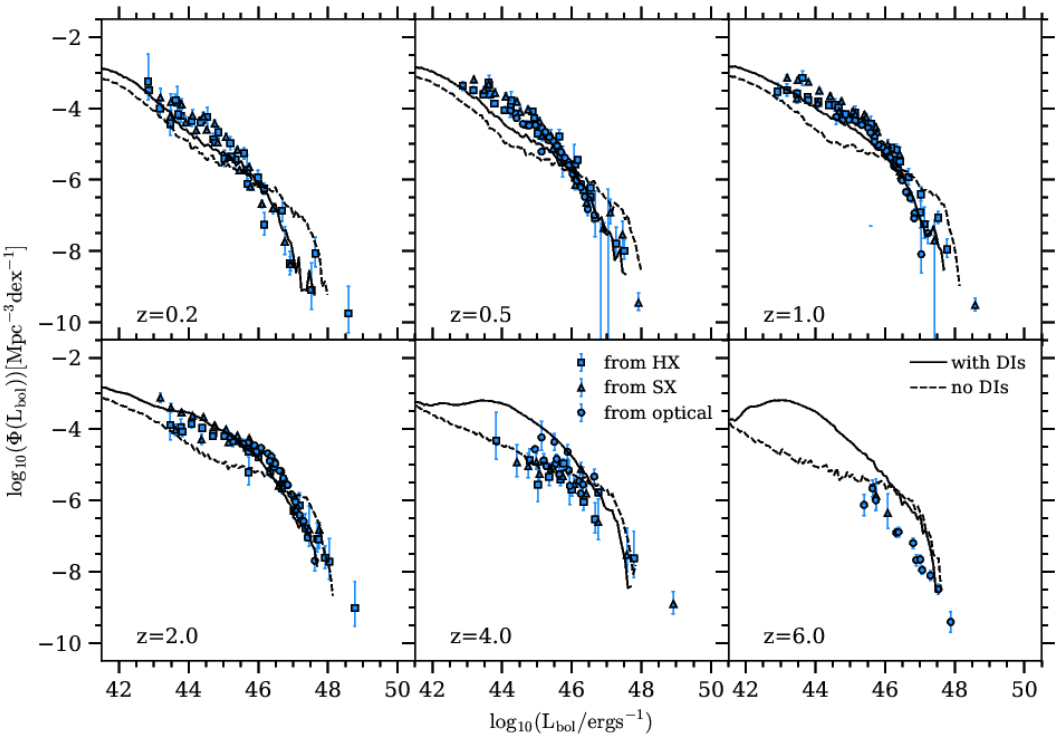

Figure A.11: Exploring the effect of switching off disc instabilities. Shown are the fiducial model (solid) and the model with disc instabilities switched off (dashed).

We show the effect of varying the parameter $\eta_{\rm Edd}$ (cf. equation (3.3.29)) in Figure A.10. $\eta_{\rm Edd}$ controls the suppression of the luminosity for super-Eddington accretion rates, where a low value of $\eta_{\rm Edd}$ corresponds to stronger luminosity suppression than a high value of $\eta_{\rm Edd}$. This parameter only affects the very bright end of the luminosity function, as we would expect. This parameter also has more of an effect at high redshift, where there are more super-Eddington sources. A value of $\eta_{\rm Edd} = 1$ gives a slightly better fit to the bright end observations at $z = 6$ but $\eta_{\rm Edd} = 16$ gives a better fit to bright end observations at $z = 2$ and $z = 4$. Therefore we once again opt to keep the Fanidakis et al. (2012) value of $\eta_{\rm Edd} = 4$ for our predictions in this paper.

We show the effect of switching off disc instabilities in Figure A.11. We show the fiducial model alongside a model in which all discs are stable and so no disc instability starbursts occur. Disc instabilities dominate the AGN luminosity function at $z > 2$, and so this is the regime where we expect turning off disc instabilities to

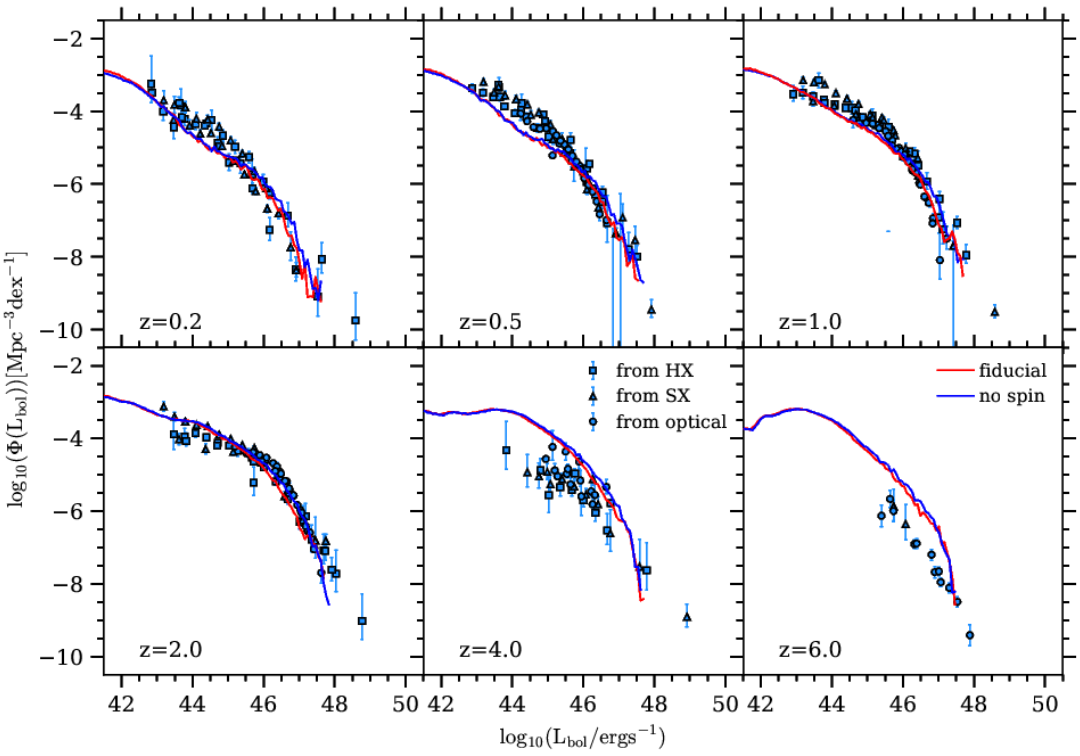

Figure A.12: Exploring the effect of turning off the SMBH spinup evolution: the model with chaotic mode accretion spinup and merger spinup (red) and the model with no accretion nor merger spinup with a thin disc accretion efficiency, $\epsilon_{TD} = 0.1$ (blue).

have the most effect. For $L_{\rm bol} < 10^{46}{\rm ergs}^{-1}$, at $z > 2$ switching off disc instabilities results in fewer starbursts and so there are fewer objects at these luminosities. For $L_{\rm bol} > 10^{46}{\rm ergs}^{-1}$, at $z > 2$ the two models are similar - this is because if we switch off disc instabilities, galaxy mergers trigger the starbursts that would have otherwise happened due to disc instabilities. At $z < 2$, switching off disc instabilities makes the luminosity function less steep.

We show the effect of switching off the accretion and merger spinup in Figure A.12. The radiative accretion efficiency given to the black holes is $\epsilon = 0.1$. The luminosity functions for the two models are generally similar, although the fiducial model has a slightly lower number density at high luminosities.

We show the effect of changing the assumptions for accretion efficiency, ϵ, in Figure A.13. We compare the fiducial model to a model in which the accretion effi-

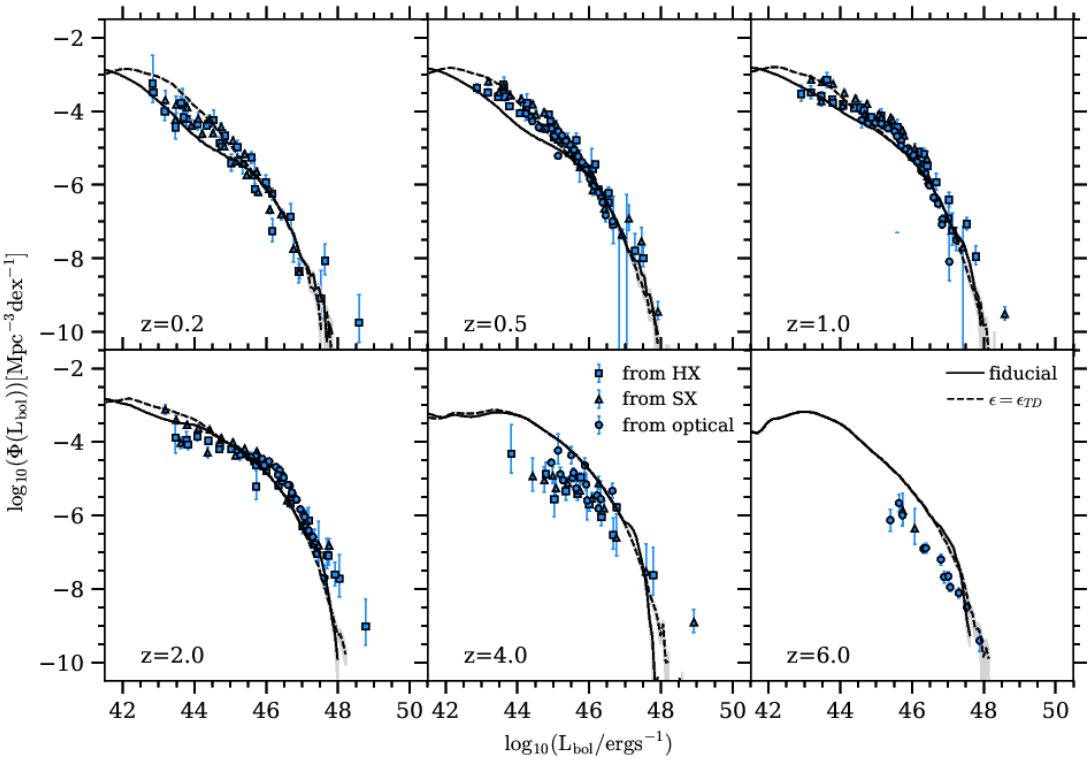

Figure A.13: Exploring the effect of changing the accretion efficiency ϵ: the model with $\epsilon = \epsilon_{TD}$ as the accretion efficiency for all $\dot{m}$ regimes (black dashed) and the fiducial model (black solid).

ciency is the thin disc accretion efficiency for all values of the specific mass accretion rate, $\dot{m}$. Interestingly, this result provides a slightly better fit to the bolometric luminosity function, particularly for $z < 0.5$ and $L_{\rm bol} < 10^{45}{\rm ergs}^{-1}$, where the fiducial model underpredicts the number density. This is the regime where ADAFs dominate the luminosity function, and so this test suggests that a better fit to the observed AGN luminosity function might be obtained if the radiative accretion efficiency for ADAFs is higher than the values assumed in our standard model.

Appendix B

High redshift AGN bolometric luminosity functions and the properties of objects detected

B.1 Effect of halo mass resolution

In Figure B.1 we show the predicted bolometric luminosity function at $z = 7$ and $z = 12$ for the fiducial model, which has a halo mass resolution of $2.12 \times 10^9 h^{-1} M_\odot$, and for a halo mass resolution of $10^{10} h^{-1} M_\odot$. The figure demonstrates that the turnover seen in the luminosity function at $L_{\rm bol} \sim 10^{43}{\rm ergs}^{-1}$ is due to the dark matter simulation only resolving haloes above a certain mass. The two bolometric luminosity functions are converged for $L_{\rm bol} \gtrsim 10^{43}{\rm ergs}^{-1}$ (depending somewhat on redshift), while the poorer halo mass resolution leads to fewer objects for $L_{\rm bol} < 10^{43}{\rm ergs}^{-1}$.

B.2 The effect of the SMBH seed mass

In Figure B.2 we show the AGN bolometric luminosity function at $z = 7$ and $z = 12$ for three different seed masses ($10 h^{-1} M_\odot$, $10^3 h^{-1} M_\odot$, and $10^5 h^{-1} M_\odot$). The luminosity functions for the three different seed masses are consistent with each other within statistical errors for $L_{\rm bol} > 10^{42}$ ergs^{-1} at $z = 7$, and consistent with

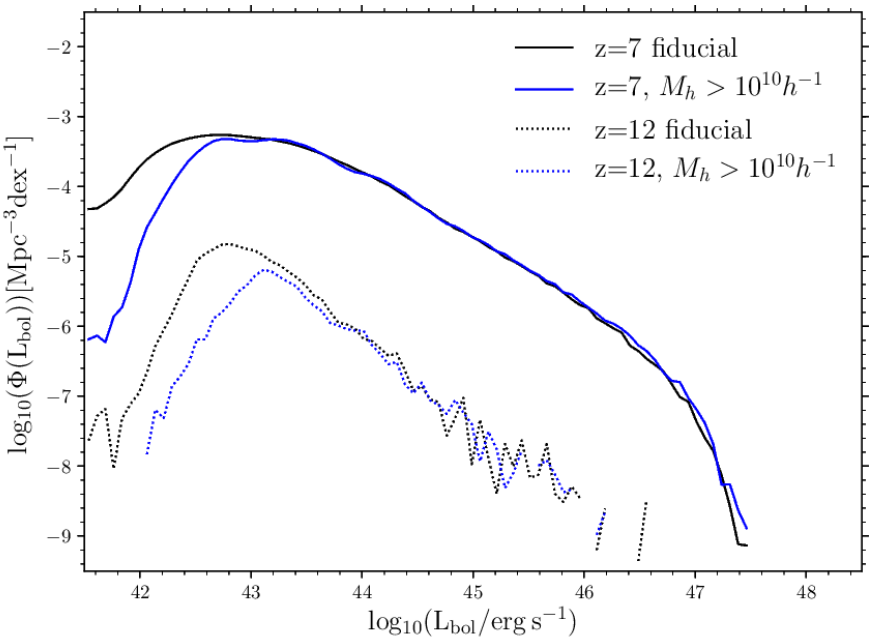

Figure B.1: The bolometric luminosity function at $z = 7$ (solid lines), and $z = 12$ (dotted lines) for the halo mass resolution of $2.12 \times 10^9 h^{-1} M_\odot$ as for the standard model (black lines) and for a halo mass resolution of $10^{10} h^{-1} M_\odot$ (blue lines).

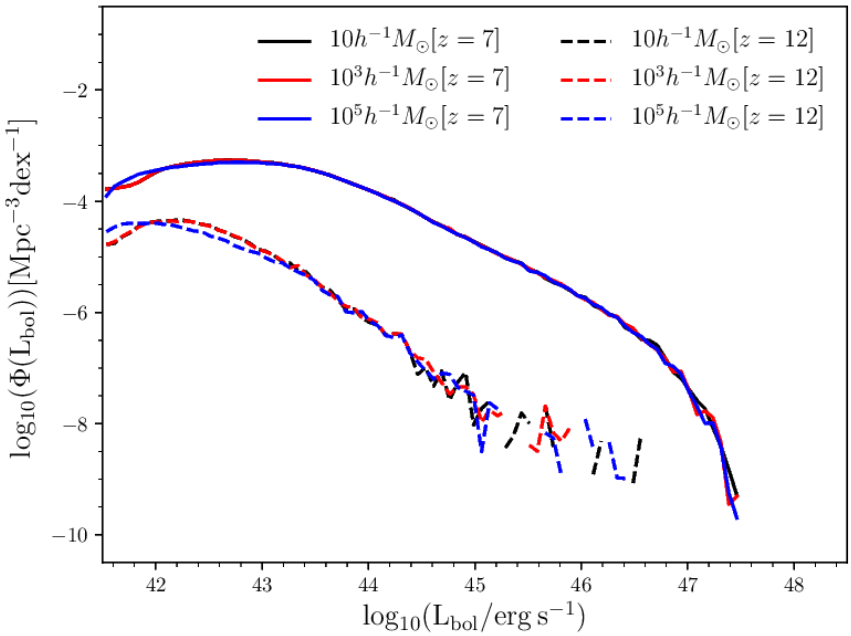

Figure B.2: The bolometric luminosity function at $z = 7$ (solid lines), and $z = 12$ (dashed lines) for seed masses of $10h^{-1}M_\odot$ (black), $10^3h^{-1}M_\odot$ (red) and $10^5h^{-1}M_\odot$ (blue). Note that the black lines are underneath the red lines.

Table B.1: Predictions for the number of AGNs expected to be detectable at different redshifts by the different telescopes, using the sensitivity limits and survey areas given in Table 4.1. The ranges of values correspond to the three different variants of the model: the fiducial model, which uses the LZMH obscuration fraction, the fiducial model using the Z6MH obscuration fraction, and the low accretion efficiency model.

Instrument	Filter	$z = 7$	$z = 9$	$z = 10$	$z = 12$
JWST	F070W	20-100	0-2	0	0
	F200W	90-500	5-30	1-8	0
	F444W	60-300	3-20	0-4	0
EUCLID Deep	VIS	90-400	2-10	0-1	0
	H	100-600	5-20	1-5	0
EUCLID Wide	VIS	5000-20000	100-400	20-70	0
	H	8000-30000	300-1000	70-300	1-4
ATHENA WFI	Soft X-ray	30-80	1-4	0-2	0-1
	Hard X-ray	5-20	0	0	0
Lynx	Soft X-ray	800	200-300	200	100-200
	Hard X-ray	800-900	200-300	200	100-200

each other for $L_{\rm bol} > 10^{43}$ ergs^{-1} at $z = 10$.

B.3 Number of detectable objects

In Table B.1 we show the number of objects detectable by each survey at $z = 7$, $z = 9$, $z = 10$, and $z = 12$, with sensitivities and survey areas as in Table 4.1.

B.4 Properties of detectable objects

In Tables B.2 and B.3 we show the median SMBH masses, Eddington normalised accretion rates, host galaxy stellar masses and host halo masses of AGNs detectable by the future surveys at $z = 7$ and $z = 10$. The assumed sensitivities and survey

Table B.2: The median SMBH masses, Eddington normalised mass accretion rates, host galaxy stellar masses, and host halo masses of the AGNs predicted to be detectable by JWST, EUCLID, ATHENA, and Lynx at $z = 7$ for our fiducial model, for the survey parameters given in Table 4.1.

Instrument	Filter	$M_{\rm SMBH}(M_\odot)$	$\dot{m} = \dot{M}/\dot{M}_{\rm Edd}$	$M_\star(M_\odot)$	$M_{\rm halo}(M_\odot)$
JWST	F070W	7.2×10^6	0.8	1.4×10^9	1.9×10^{11}
	F200W	2.0×10^6	0.7	5.2×10^8	1.1×10^{11}
	F444W	3.0×10^6	0.7	7.1×10^8	1.3×10^{11}
EUCLID	VIS	1.8×10^7	1.1	2.6×10^9	2.6×10^{11}
Deep	H	1.4×10^7	1.0	2.2×10^9	2.4×10^{11}
EUCLID	VIS	4.6×10^7	2.5	4.4×10^9	3.4×10^{11}
Wide	H	4.0×10^7	2.0	4.1×10^9	3.3×10^{11}
ATHENA	Soft X-ray	8.0×10^6	0.8	1.5×10^9	1.9×10^{11}
WFI	Hard X-ray	2.4×10^7	1.3	3.2×10^9	2.9×10^{11}
Lynx	Soft X-ray	8.9×10^4	0.6	4.1×10^7	3.7×10^{10}
	Hard X-ray	8.2×10^4	0.6	3.9×10^7	3.6×10^{10}

areas are given in Table 4.1.

Table B.3: The same as Table B.2, but at $z = 10$. We predict that the ATHENA hard X-ray band will not be able to detect any AGNs at $z = 10$.

Instrument	Filter	$M_{\rm SMBH}(M_\odot)$	$\dot{m} = \dot{M}/\dot{M}_{\rm Edd}$	$M_\star(M_\odot)$	$M_{\rm halo}(M_\odot)$
JWST	F070W	6.9×10^6	2.6	8.3×10^8	1.4×10^{11}
	F200W	1.8×10^6	1.2	3.2×10^8	8.6×10^{10}
	F444W	2.6×10^6	1.4	4.2×10^8	1.1×10^{11}
EUCLID	VIS	1.4×10^7	4.2	1.1×10^9	1.6×10^{11}
Deep	H	1.1×10^7	3.2	1.0×10^9	1.5×10^{11}
EUCLID	VIS	3.6×10^7	8.2	1.4×10^9	1.6×10^{11}
Wide	H	2.2×10^7	7.5	1.4×10^9	1.6×10^{11}
ATHENA	Soft X-ray	6.0×10^6	2.1	7.3×10^8	1.3×10^{11}
WFI	Hard X-ray	-	-	-	-
Lynx	Soft X-ray	2.4×10^4	1.1	9.8×10^6	1.8×10^{10}
	Hard X-ray	2.1×10^4	1.1	8.4×10^6	1.7×10^{10}

Appendix C

Modelling the evolution of lobe dynamics and luminsosity

C.1 Lobe Dynamics

In this Appendix, we present the model for the lobe dynamics from Turner & Shabala (2015). In the model, the jet from the SMBH causes a bow shock to form in the external medium, and the jet interacts with the shocked material at the hotspot. Relativistic plasma backflows from the hotspot to inflate a cocoon which, via synchrotron emission, is then visible at radio frequencies as a radio lobe. Radio lobes start out as constant pressure ellipsoids with axial ratio, A, and radius, R, for each angular element, as seen in Figure C.1. The angle between each angular element and the major axis of the lobe is θ. Each angular element is then assumed to evolve adiabatically (for both the supersonic and subsonic regimes). For the supersonic case this is:

$$\dot{p}\Delta V + \Gamma_c p \Delta \dot{V} = (\Gamma_c - 1) Q \Delta\lambda, \tag{C.1.1}$$

where Γ_c is the adiabatic index of the cocoon, p is the pressure at the surface of the cocoon, ΔV is the volume of the angular element, Q is the jet power, and $\Delta\lambda$ is the fraction of the jet power injected into that angular element. In the supersonic case, the pressure at the bow shock can be evaluated using the Rankine-Hugoniot jump conditions, and it is assumed that the surface of the cocoon is close to the bow

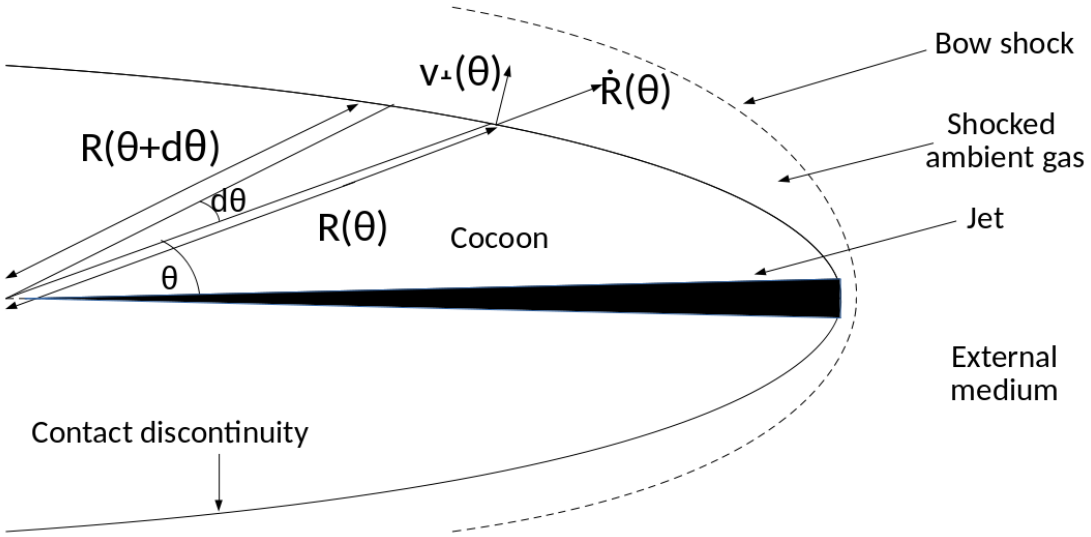

Figure C.1: A schematic of the structure of supersonic radio sources in the model. The subsonic radio sources are the same but there is no bow shock because the lobe is in pressure equilibrium with the external medium, and the lobe is not necessarily an ellipsoidal shape.

shock (this assumption keeps the model analytically tractable). The pressure of the cocoon for both the supersonic and subsonic cases is then given by:

$$p = \begin{cases} \frac{2\Gamma_x M_b^2 - (\Gamma_x - 1)}{\Gamma_x + 1} p_x, & \text{for } M_b > 1 \\ p_x, & \text{for } M_b < 1, \end{cases} \tag{C.1.2}$$

where p_x is the pressure of the external medium. The density profile of the external medium is divided into 100 segments, each with dependence on radius, $\rho(R) = kR^{-\beta}$. The pressure in the external medium is calculated from the density assuming a constant temperature $T_{\rm vir}$ (i.e. $\xi = 0$ in the notation of Turner & Shabala (2015)). Γ_x is the adiabatic index of the external medium, and M_b is the ratio of the component of the velocity of the surface of the cocoon normal to its surface, $v_\perp$, to the sound speed of the external medium, c_x. $v_\perp$ is related to $\dot{R}$ by $v_\perp = (\zeta/\eta)\dot{R}$, where $\zeta(\theta)$ is defined as the ratio of the component of the velocity normal to the surface to the expansion rate along the semi-major axis, and $\eta(\theta)$ is the ratio of the radius of the angular element to the radius of the lobe along the semi-major axis. These

geometrical factors are computed assuming that the cocoon is an ellipsoid with axis ratio A (even though the actual cocoon shape may depart from this during its evolution). $\zeta(\theta)$ and $\eta(\theta)$ are then given by:

$$\zeta(\theta) = \frac{v_\perp(\theta)}{v_\perp(\theta = 0)} = \sqrt{\frac{A^2 \sin^2\theta + \cos^2\theta}{A^4 \sin^2\theta + \cos^2\theta}}, \tag{C.1.3}$$

and

$$\eta(\theta) = \frac{R(\theta)}{R(\theta = 0)} = \frac{1}{\sqrt{A^2 \sin^2\theta + \cos^2\theta}}. \tag{C.1.4}$$

The sound speed of the external medium is given by:

$$c_x = \sqrt{\frac{\Gamma_x k_B T_{\rm vir}}{\mu m_p}} = \sqrt{\frac{\Gamma_x}{2}} V_{\rm vir}, \tag{C.1.5}$$

where k_B is the Boltzmann constant, $\mu = 0.6$ is the mean molecular weight, and $T_{\rm vir} = \mu m_p V_{\rm vir}^2 / 2k_B$, with $V_{\rm vir} = (GM/r_{\rm vir})^{1/2}$. The volume of each angular element of the cocoon is given in terms of its radial length, R, by:

$$\Delta V(\theta) = \frac{2\pi R^3(\theta)}{3} \sin\theta \Delta\theta. \tag{C.1.6}$$

We can then obtain expressions for the evolution of R for each angular element. For the supersonic case, using equation (C.1.2), the time derivative of the pressure is:

$$\begin{aligned} \dot{p} =& \frac{2k\left(\zeta/\eta\right)^2}{\Gamma_x + 1}\left(R^{-\beta} 2\dot{R}\ddot{R} - \beta R^{-\beta-1}\dot{R}\dot{R}^2\right) + \\ & \frac{\Gamma_x - 1}{2(\Gamma_x + 1)} k V_{\rm vir}^2 \beta R^{-\beta-1}\dot{R}, \end{aligned} \tag{C.1.7}$$

where β is treated as being constant. The time derivative of the volume from equation (C.1.6) is:

$$\Delta\dot{V} = 2\pi R^2 \dot{R} \sin\theta \Delta\theta. \tag{C.1.8}$$

Equations (C.1.2), (C.1.6), (C.1.7), and (C.1.8) can then be inserted into equation (C.1.1) to obtain:

$$\begin{aligned}\ddot{R} =& \frac{3(\Gamma_x+1)(\Gamma_c-1)QR^{\beta-3}\Delta\lambda}{8\pi\dot{R}(\zeta/\eta)^2 k\sin\theta\Delta\theta} + \frac{(\beta-3\Gamma_c)\dot{R}^2}{2R} \\ &+ \frac{(\Gamma_x-1)(3\Gamma_c-\beta)V_{\rm vir^2}}{8R(\zeta/\eta)^2}.\end{aligned} \tag{C.1.9}$$

The value of $\Delta\lambda(\theta)$ used for each angular element is the jet power required to maintain a constant axial ratio A when $M_b >> 1$ and β is fixed. It is given by:

$$\begin{aligned}\Delta\lambda(\theta) =& \frac{8\pi k\sin\theta\Delta\theta}{3(\Gamma_x+1)(\Gamma_C-1)Q}\Bigg[(3\Gamma_C-\beta)R^{2-\beta}\dot{R}^3 \\ &+ 2R^{3-\beta}\dot{R}\ddot{R}\Bigg]_{\theta=0} \times \eta^{3-\beta}\zeta^2.\end{aligned} \tag{C.1.10}$$

We keep the same $\Delta\lambda(\theta)$, even when the lobe is no longer highly supersonic and β is no longer constant (in which case we use the β value of the major axis). For the subsonic case, a similar differential equation can be written using the solution in Luo & Sadler (2010), where the radius evolves via:

$$\ddot{R} = \frac{(\beta-2)\dot{R}^2}{R}. \tag{C.1.11}$$

To solve these differential equations, we divide the density profile into 100 segments, each with constant β. We use a fourth-order Runge-Kutta integration method to solve these differential equations, using the R and $\dot{R}$ values from the previous segment at the initial conditions for the next one.

When an angular element is in the subsonic regime, it becomes susceptible to Rayleigh-Taylor instabilities at the interface between the cocoon and the external medium. Following Turner & Shabala (2015), the thickness of the Rayleigh-Taylor mixing layer, $h(t,\theta)$, can be calculated using the expression from Cook et al. (2004):

$$\frac{dh}{dt} = 2\sqrt{\frac{\kappa_{RT}(\rho_x-\rho_{coc})g_{\rm eff}h}{(\rho_x+\rho_{coc})}}, \tag{C.1.12}$$

where κ_{RT} is the Rayleigh-Taylor growth parameter, and ρ_x and ρ_{coc} are the densities of the external medium and cocoon respectively. We assume that $\rho_{coc} << \rho_x$ (the cocoon is composed of relativistic particles and so could be in pressure

balance with the external medium but have a lower density), so $(\rho_x - \rho_{coc})/(\rho_x + \rho_{coc})$ is set to 1, as in Turner & Shabala (2015). $g_{\rm eff}$ is the effective gravitational acceleration. This is calculated as the sum of the gravitational potential of the galaxy, $g_{\rm grav} = c_x^2\beta/\Gamma_x R$, calculated from the equation for hydrostatic equilibrium, and the acceleration of the cocoon, $g_{\rm c} = -\ddot{R}$. By integrating equation (C.1.12), using the condition that the mixing layer has zero thickness at the time at which the lobe becomes subsonic, we obtain:

$$h(t,\theta) = \kappa_{RT}\left(\int_{t_{\rm sub}}^{t}\sqrt{-\ddot{R} + c_x^2\frac{\beta}{\Gamma_x R}}\,dt\right)^2, \tag{C.1.13}$$

where $t_{\rm sub}$ is the time at which the angular element becomes subsonic. The radio luminosity from the mixing layer is assumed to be reduced to zero. The luminosity of the angular element is assumed to be reduced by a factor corresponding to the reduced emitting volume, for which the radius is assumed to be reduced from R to $R - h/2$, and therefore the luminosity of the cocoon is multiplied by the following factor when part of it is in the subsonic phase:

$$f_{vis} = \frac{\sum_{i=1}^{N}(R - h(t,\theta_i)/2)^3\sin\theta_i\Delta\theta}{\sum_{i=1}^{N}R^3\sin\theta_i\Delta\theta}, \tag{C.1.14}$$

where θ_i is each angular element, and N is the number of angular elements.

C.2 Radio Luminosity

The following derivation for the radio luminosity is based on the derivation given in Turner et al. (2018a), which is based on the derivation given in Kaiser et al. (1997). A population of electrons is injected into the cocoon at an injection time t_i, with number density $n(\gamma_i, t_i) = n_0\gamma_i^{-s}d\gamma_i$, where γ_i is the Lorentz factor of the electrons at injection, and s is the slope of the injected electron distribution. The cocoon is assumed to be composed of three 'fluids': a relativistic electron fluid with energy density u_e, a magnetic field fluid with energy density u_B, and a thermal fluid of non-radiating particles with energy density u_T. The pressure of the cocoon, p_c is therefore:

$$p_c = (\Gamma_c - 1)(u_e + u_B + u_T). \tag{C.2.15}$$

We define the ratios $k^t = u_T/u_e$ and $q_B = u_B/(u_e + u_T)$ so that the energy density of the electrons is given by:

$$u_e = \frac{p_c}{(\Gamma_c - 1)(k^t + 1)(q_B + 1)}, \tag{C.2.16}$$

and the energy density of the magnetic field is given by,

$$u_B = \frac{q_B p_c}{(\Gamma_c - 1)(q_B + 1)}. \tag{C.2.17}$$

The electrons are assumed to only emit synchrotron radiation at their critical frequency, $\nu = \gamma^2 \nu_L$, where γ is the Lorentz factor of the observed electrons, and ν_L is the Larmor frequency, which is given by:

$$\nu_L = \frac{eB}{2\pi m_e}. \tag{C.2.18}$$

Therefore γ is given by:

$$\gamma = \sqrt{\frac{\nu}{\nu_L}} = \sqrt{\frac{2\pi m_e \nu}{eB}}, \tag{C.2.19}$$

where ν is the observed frequency, m_e is the electron mass, e is the electron charge, and $B = \sqrt{2\mu_0 u_B(t_i)}$ is the magnetic field. The Lorentz factor of the electrons evolves by:

$$\frac{d\gamma}{dt} = \frac{a_p \gamma}{3\Gamma_c t} - \frac{4\sigma_T}{3m_e c}\gamma^2(u_B + u_C), \tag{C.2.20}$$

where the first term on the right-hand side represents adiabatic expansion losses, and the second term is the combination of synchrotron losses and inverse-Compton losses (the latter being from scattering with the CMB). $u_C = 4 \times 10^{-14}(1+z)^4 Jm^{-3}$ is the energy density of the CMB, and a_p gives the dependence of the cocoon pressure on time, $p_c(t_i) \propto t_i^{a_p}$, where a_p relates to β by $a_p = (4 + \beta)/(\beta - 5)$. a_p is evaluated from the pressure profile of the lobe at each injection time t_i. This expression can be integrated to give a relation between γ_i and the Lorentz factor of the observed electrons:

$$\gamma_i = \frac{\gamma t_i^{a_p/3\Gamma_c}}{t^{a_p/3\Gamma_c} - a_2(t,t_i)\gamma}, \tag{C.2.21}$$

where $a_2(t,t_i)$ is given by:

$$a_2(t,t_i) = \frac{4\sigma_T}{3m_e c}\Big(\frac{u_B(t_i)}{a_3} t_i^{-a_p\Gamma_B/\Gamma_c}(t^{a_3} - t_i^{a_3}) + \frac{u_C}{a_4}(t^{a_4} - t_i^{a_4})\Big). \tag{C.2.22}$$

In this expression, a_3 is given by:

$$a_3 = 1 + \frac{a_p}{\Gamma_c}(\Gamma_B + 1/3), \tag{C.2.23}$$

a_4 is given by

$$a_4 = 1 + \frac{a_p}{3\Gamma_c}, \tag{C.2.24}$$

and $n_0(t_i)$ is given by:

$$n_0(t_i) = \frac{u_e(t_i)}{m_e c^2}\Big(\frac{\gamma_{i,min}^{2-s} - \gamma_{i,max}^{2-s}}{s-2} - \frac{\gamma_{i,min}^{1-s} - \gamma_{i,max}^{1-s}}{s-1}\Big)^{-1}. \tag{C.2.25}$$

To calculate the luminosity of the lobe, we follow a clearer form of the derivation in Kaiser et al. (1997) equation (13). We consider a bubble at the hotspot with volume, δV_i, internal energy δU_i, and pressure p_h. The internal energy of the bubble is given by:

$$\delta U_i = \frac{p_h \delta V_i}{\Gamma_c - 1}. \tag{C.2.26}$$

We then allow this bubble to expand adiabatically into the cocoon over a time δt_i, to a pressure p_c. For adiabatic expansion, pV^{Γ_c} is a constant and therefore $V \propto p^{-1/\Gamma_c}$. The volume of the bubble, δV_f after a time δt_i is therefore given by:

$$\delta V_f = \delta V_i \left(\frac{p_h}{p_c}\right)^{1/\Gamma_c}, \tag{C.2.27}$$

and then by combining equation (C.2.27) with (C.2.26), this gives:

$$\delta V_f = (\Gamma_c - 1)\frac{\delta U_i}{p_c}\left(\frac{p_h}{p_c}\right)^{(1-\Gamma_c)/\Gamma_c}. \tag{C.2.28}$$

By then assuming the internal energy is given by $\delta U_i = Q\delta t_i$, this gives:

$$\delta V_f = \frac{(\Gamma_c - 1)Q\delta t_i}{p_c}\left(\frac{p_h}{p_c}\right)^{(1-\Gamma_c)/\Gamma_c}. \tag{C.2.29}$$

We then integrate over the different volumes of the electron populations by identifying δV_f in equation (C.2.29) with V in equation (6.2.3), which gives equation (6.2.4).

C.3 Lobe luminosity as a function of pressure and volume

In this Appendix, we recast equation (6.2.3) in terms of pressure and volume. We first give an expression for L_ν showing only the dependence on quantities related to the pressure and volume:

$$L_\nu \propto u_B \gamma^3 n(\gamma) V. \tag{C.3.30}$$

Equation (C.2.17) gives us the dependence of u_B on the pressure, p: $u_B \propto p$, and from equation (C.2.19), $\gamma \propto u_B^{-1/4} \propto p^{-1/4}$. If we assume (for simplicity) to neglect the effect of radiative losses, then $\gamma_i = \gamma$, and so $n(\gamma) \propto n_0 \gamma^{-s}$. Using equation (C.2.25), $n_0 \propto u_e \propto p$. Therefore, under this approximation, the luminosity depends on the pressure and volume via:

$$L_\nu \propto p^{\frac{s+5}{4}} V. \tag{C.3.31}$$

Bibliography

Abbott B. P. et al., 2016, PRL, 116, 061102

Abramowicz M. A., Czerny B., Lasota J. P., Szuszkiewicz E., 1988, ApJ, 332, 646

Aird J., Coil A. L., Georgakakis A., Nandra K., Barro G., Pérez-González P. G., 2015, MNRAS, 451, 1892

Alcock C. et al., 2000, ApJ, 542, 281

Alexander P., 2002, MNRAS, 335, 610

Alexander P., Leahy J. P., 1987, "MRAS", 225, 1

Alpher R. A., Bethe H., Gamow G., 1948, Physical Review, 73, 803

Amarantidis S. et al., 2019, MNRAS, 485, 2694

Amaro-Seoane P. et al., 2013, GW Notes, 6, 4

Bañados E. et al., 2018a, Nature, 553, 473

Bañados E. et al., 2018b, ApJL, 856, L25

Barausse E., 2012, MNRAS, 423, 2533

Bardeen J., 1970, Nature, 226, 64

Bardeen J. M., Petterson J. A., 1975, ApJl, 195, L65

Bardeen J. M., Press W. H., Teukolsky S. A., 1972, ApJ, 178, 347

Baugh C. M., Lacey C. G., Frenk C. S., Granato G. L., Silva L., Bressan A., Benson A. J., Cole S., 2005, MNRAS, 356, 1191

Baugh C. M. et al., 2019, MNRAS, 483, 4922

Becker R. H., White R. L., Helfand D. J., 1995, ApJ, 450, 559

Benson A. J., Bower R. G., Frenk C. S., Lacey C. G., Baugh C. M., Cole S., 2003, ApJ, 599, 38

Best P. N., 2009, Astronomische Nachrichten, 330, 184

Best P. N., Kauffmann G., Heckman T. M., Brinchmann J., Charlot S., Ivezić Ž., White S. D. M., 2005a, MNRAS, 362, 25

Best P. N., Kauffmann G., Heckman T. M., Ivezić Ž., 2005b, MNRAS, 362, 9

Best P. N., Ker L. M., Simpson C., Rigby E. E., Sabater J., 2014, MNRAS, 445, 955

Bigiel F., Leroy A., Walter F., Brinks E., de Blok W. J. G., Madore B., Thornley M. D., 2008, AJ, 136, 2846

Bîrzan L., McNamara B. R., Nulsen P. E. J., Carilli C. L., Wise M. W., 2008, ApJ, 686, 859

Blandford R. D., Payne D. G., 1982, MNRAS, 199, 883

Blandford R. D., Rees M. J., 1974, MNRAS, 169, 395

Blandford R. D., Znajek R. L., 1977, MNRAS, 179, 433

Blanton E. L., Randall S. W., Clarke T. E., Sarazin C. L., McNamara B. R., Douglass E. M., McDonald M., 2011, ApJ, 737, 99

Blitz L., Rosolowsky E., 2006, ApJ, 650, 933

Blundell K. M., Rawlings S., Willott C. J., 1999, AJ, 117, 677

Bondi H., 1952, MNRAS, 112, 195

Bonoli S., Marulli F., Springel V., White S. D. M., Branchini E., Moscardini L., 2009, MNRAS, 396, 423

Bournaud F., Combes F., Semelin B., 2005, MNRAS, 364, L18

Bournaud F., Elmegreen B. G., Elmegreen D. M., 2007, ApJ, 670, 237

Bower R. G., Benson A. J., Malbon R., Helly J. C., Frenk C. S., Baugh C. M., Cole S., Lacey C. G., 2006, MNRAS, 370, 645

Boyle B. J., Fong R., Shanks T., Peterson B. A., 1990, MNRAS, 243, 1

Brenneman L. W., Reynolds C. S., 2006, ApJ, 652, 1028

Bustamante S., Springel V., 2019, arXiv e-prints, arXiv:1902.04651

Carilli C. L., Perley R. A., Dreher J. W., Leahy J. P., 1991, ApJ, 383, 554

Cavagnolo K. W., McNamara B. R., Nulsen P. E. J., Carilli C. L., Jones C., Bîrzan L., 2010, ApJ, 720, 1066

Ceraj L. et al., 2018, A&A, 620, A192

Chen Y. M. et al., 2013, MNRAS, 429, 2643

Chiang C. Y., Fabian A. C., 2011, MNRAS, 414, 2345

Christodoulou D. M., Shlosman I., Tohline J. E., 1995, ApJ, 443, 551

Cole S., Lacey C., 1996, MNRAS, 281, 716

Cole S., Aragon-Salamanca A., Frenk C. S., Navarro J. F., Zepf S. E., 1994, MNRAS, 271, 781

Cole S., Lacey C. G., Baugh C. M., Frenk C. S., 2000, MNRAS, 319, 168

Collin-Souffrin S., Dumont A., 1990, A&A, 229, 292

Condon J. J., 1974, ApJ, 188, 279

Condon J. J., Cotton W. D., Greisen E. W., Yin Q. F., Perley R. A., Taylor G. B., Broderick J. J., 1998, AJ, 115, 1693

Cook A., CABOT W., L. MILLER P., 2004, Journal of Fluid Mechanics, 511, 333

Cora S. A. et al., 2018, MNRAS, 479, 2

Cowie L. L., Binney J., 1977, ApJ, 215, 723

Cowley W., Baugh C., Cole S., Frenk C., Lacey C., 2018, MNRAS, 474, 2352

Croom S. M. et al., 2009, MNRAS, 399, 1755

Croston J. H., Hardcastle M. J., Harris D. E., Belsole E., Birkinshaw M., Worrall D. M., 2005, ApJ, 626, 733

Croston J. H., Ineson J., Hardcastle M. J., 2018, MNRAS, 476, 1614

Croton D. J. et al., 2006, MNRAS, 365, 11

Croton D. J. et al., 2016, ApJS, 222, 22

Daly R. A., Sprinkle T. B., O'Dea C. P., Kharb P., Baum S. A., 2012, MNRAS, 423, 2498

Davis M., Efstathiou G., Frenk C. S., White S. D. M., 1985, ApJ, 292, 371

De Lucia G., Fontanot F., Wilman D., Monaco P., 2011, MNRAS, 414, 1439

De Rosa G., Decarli R., Walter F., Fan X., Jiang L., Kurk J., Pasquali A., Rix H. W., 2011, ApJ, 739, 56

de Vaucouleurs G., 1948, Annales d'Astrophysique, 11, 247

Di Matteo T., Croft R. A. C., Feng Y., Waters D., Wilkins S., 2017, MNRAS, 467, 4243

Done C., Jin C., Middleton M., Ward M., 2013, MNRAS, 434, 1955

Donoso E., Best P. N., Kauffmann G., 2009, MNRAS, 392, 617

Dubois Y. et al., 2014, MNRAS, 444, 1453

Dunkley J. et al., 2009, ApJS, 180, 306

Dunlop J. S., Peacock J. A., 1990, MNRAS, 247, 19

Efstathiou G., Lake G., Negroponte J., 1982, MNRAS, 199, 1069

Ehlert K., Weinberger R., Pfrommer C., Pakmor R., Springel V., 2018, MNRAS, 481, 2878

Eke V. R., Cole S., Frenk C. S., 1996, MNRAS, 282, 263

Elmegreen B. G., Bournaud F., Elmegreen D. M., 2008, ApJ, 688, 67

Enoki M., Ishiyama T., Kobayashi M. A. R., Nagashima M., 2014, ApJ, 794, 69

Event Horizon Telescope Collaboration et al., 2019, ApJL, 875, L1

Fabian A. C., Nulsen P. E. J., 1977, MNRAS, 180, 479

Fall S. M., Efstathiou G., 1980, MNRAS, 193, 189

Falle S. A. E. G., 1991, MNRAS, 250, 581

Fan X. et al., 2001, AJ, 122, 2833

Fan X. et al., 2003, AJ, 125, 1649

Fan X. et al., 2004, AJ, 128, 515

Fanaroff B. L., Riley J. M., 1974, MNRAS, 167, 31P

Fanidakis N., Baugh C. M., Benson A. J., Bower R. G., Cole S., Done C., Frenk C. S., 2011, MNRAS, 410, 53

Fanidakis N., Macciò A. V., Baugh C. M., Lacey C. G., Frenk C. S., 2013a, MNRAS, 436, 315

Fanidakis N. et al., 2012, MNRAS, 419, 2797

Fanidakis N. et al., 2013b, MNRAS, 435, 679

Fath E. A., 1909, Lick Observatory Bulletin, 149, 71

Feng Y., Di-Matteo T., Croft R. A., Bird S., Battaglia N., Wilkins S., 2016, MNRAS, 455, 2778

Ferrara A., Bianchi S., Cimatti A., Giovanardi C., 1999, ApJS, 123, 437

Font A. S. et al., 2011, MNRAS, 417, 1260

Fukugita M., Peebles P. J. E., 2004, ApJ, 616, 643

Gardner J. et al., 2006, SSRv, 123, 485

Gendre M. A., Best P. N., Wall J. V., 2010, MNRAS, 404, 1719

Gendre M. A., Best P. N., Wall J. V., Ker L. M., 2013, MNRAS, 430, 3086

Georgakakis A. et al., 2015, MNRAS, 453, 1946

Glikman E., Djorgovski S. G., Stern D., Dey A., Jannuzi B. T., Lee K. S., 2011, ApJ, 728, 26

Godfrey L. E. H. et al., 2009, ApJ, 695, 707

Gonzalez-Perez V. et al., 2018, MNRAS, 474, 4024

Guo Q. et al., 2011, MNRAS, 413, 101

Hardcastle M. J., 2018, MNRAS, 475, 2768

Hardcastle M. J., Krause M. G. H., 2013, MNRAS, 430, 174

Hardcastle M. J. et al., 2016, MNRAS, 455, 3526

Hardcastle M. J. et al., 2019, A&A, 622, A12

Häring N., Rix H. W., 2004, ApJ, 604, L89

Harwood J. J. et al., 2017, MNRAS, 469, 639

Hasinger G., 2008, A& A, 490, 905

Hasinger G., Miyaji T., Schmidt M., 2005, A& A, 441, 447

Hawley J. F., Gammie C. F., Balbus S. A., 1995, ApJ, 440, 742

Heckman T. M., Best P. N., 2014, ARAA, 52, 589

Heinz S., Sunyaev R. A., 2003, MNRAS, 343, L59

Helly J. C., Cole S., Frenk C. S., Baugh C. M., Benson A., Lacey C., 2003, MNRAS, 338, 903

Hirschmann M., Somerville R. S., Naab T., Burkert A., 2012, MNRAS, 426, 237

Hirschmann M., Dolag K., Saro A., Bachmann L., Borgani S., Burkert A., 2014, MNRAS, 442, 2304

Hohl F., 1971, ApJ, 168, 343

Hopkins P. F., Richards G. T., Hernquist L., 2007, ApJ, 654, 731

Hubble E. P., 1926, ApJ, 64, 321

Ikeda H. et al., 2011, ApJ, 728, L25

Ineson J., Croston J. H., Hardcastle M. J., Mingo B., 2017, MNRAS, 467, 1586

Izquierdo-Villalba D., Orsi Á. A., Bonoli S., Lacey C. G., Baugh C. M., Griffin A. J., 2018, MNRAS, 480, 1340

Jahnke K., Macciò A., 2011, ApJ, 734, 92

Jarvis M. J., Rawlings S., 2000, MNRAS, 319, 121

Jarvis M. J., Rawlings S., Willott C. J., Blundell K. M., Eales S., Lacy M., 2001, MNRAS, 327, 907

Jiang L., Helly J. C., Cole S., Frenk C. S., 2014, MNRAS, 440, 2115

Jiang L. et al., 2009, AJ, 138, 305

Jiang L. et al., 2016, ApJ, 833, 222

Johnston S. et al., 2008, Experimental Astronomy, 22, 151

Jonas J., MeerKAT Team, 2016, in Proceedings of MeerKAT Science: On the Pathway to the SKA. 25-27 May. p. 1

Kaiser C. R., Alexander P., 1997, MNRAS, 286, 215

Kaiser C. R., Alexander P., 1999, MNRAS, 302, 515

Kaiser C. R., Best P. N., 2007, MNRAS, 381, 1548

Kaiser C. R., Cotter G., 2002, MNRAS, 336, 649

Kaiser C. R., Dennett-Thorpe J., Alexander P., 1997, MNRAS, 292, 723

Kalirai J., 2018, Contemporary Physics, 59, 251

Kashikawa N. et al., 2015, ApJ, 798, 28

Kauffmann G., Haehnelt M., 2000, MNRAS, 311, 576

Kennicutt R. C. J., 1983, "ApJ", 272, 54

Kennicutt Robert C. J., 1998, ApJ, 498, 541

Kennicutt Robert C. J. et al., 2007, ApJ, 671, 333

Khandai N., Feng Y., DeGraf C., Di Matteo T., Croft R. A. C., 2012, MNRAS, 423, 2397

Kharb P., O'Dea C. P., Baum S. A., Daly R. A., Mory M. P., Donahue M., Guerra E. J., 2008, ApJs, 174, 74

King A., Pounds K., 2015, ARAA, 53, 117

King A., Lubow S., Ogilvie G., Pringle J., 2005, MNRAS, 363, 49

King A. R., Pringle J. E., Hofmann J. A., 2008, MNRAS, 385, 1621

Kinney A. L., Schmitt H. R., Clarke C. J., Pringle J. E., Ulvestad J. S., Antonucci R. R. J., 2000, ApJ, 537, 152

Komatsu E. et al., 2011, ApJS, 192, 18

Konar C., Hardcastle M. J., Jamrozy M., Croston J. H., 2013, MNRAS, 430, 2137

Krause M., Alexander P., Riley J., Hopton D., 2012, MNRAS, 427, 3196

Kubota A., Done C., 2018, MNRAS, 480, 1247

Lacey C., Cole S., 1993, MNRAS, 262, 627

Lacey C. G. et al., 2016, MNRAS, 462, 3854

Lagos C. D. P., Lacey C. G., Baugh C. M., Bower R. G., Benson A. J., 2011, MNRAS, 416, 1566

Lagos C. d. P., Tobar R. J., Robotham A. S. G., Obreschkow D., Mitchell P. D., Power C., Elahi P. J., 2018, MNRAS, 481, 3573

Laing R. A., Riley J. M., Longair M. S., 1983, MNRAS, 204, 151

Larson R. B., 1974, MNRAS, 169, 229

Laureijs R., Amiaux J., Arduini S. et al., 2011, arXiv: 1110.3193

Lawrence A. et al., 2007, MNRAS, 379, 1599

Leahy J. P., Williams A. G., 1984, MNRAS, 210, 929

Leahy J. P., Muxlow T. W. B., Stephens P. W., 1989, MNRAS, 239, 401

Lehmer B. D. et al., 2012, ApJ, 752, 46

Leroy A. K., Walter F., Brinks E., Bigiel F., de Blok W. J. G., Madore B., Thornley M. D., 2008, AJ, 136, 2782

Liu H. et al., 2013, ApJ, 764, 17

Longair M. S., 1966, MNRAS, 133, 421

Luo Q., Sadler E. M., 2010, ApJ, 713, 398

Lynden-Bell D., 1969, Nature, 223, 690

Magorrian J. et al., 1998, AJ, 115, 2285

Mahadevan R., 1997, ApJ, 477, 585

Malbon R. K., Baugh C. M., Frenk C. S., Lacey C. G., 2007, MNRAS, 382, 1394

Manolakou K., Kirk J. G., 2002, A&A, 391, 127

Maraston C., 2005, MNRAS, 362, 799

Marconi A. et al., 2004, MNRAS, 351, 169

Masters D. et al., 2012, ApJ, 755, 169

McAlpine K., Jarvis M. J., Bonfield D. G., 2013, MNRAS, 436, 1084

McConnell N. J., Ma C. P., 2013, ApJ, 764, 184

McCullagh N., Norberg P., Cole S., Gonzalez-Perez V., Baugh C., Helly J., 2017, arXiv: 1705.01988

McNamara B. R., Nulsen P. E. J., Wise M. W., Rafferty D. A., Carilli C., Sarazin C. L., Blanton E. L., 2005, Nature, 433, 45

Meier D. L., 2002, NAR, 46, 247

Menci N., Fiore F., Lamastra A., 2013, ApJ, 766, 110

Menci N., Gatti M., Fiore F., Lamastra A., 2014, A&A, 569, A37

Mo H. J., Mao S., White S. D. M., 1998, MNRAS, 295, 319

Mocz P., Fabian A. C., Blundell K. M., 2011, MNRAS, 413, 1107

Moderski R., Sikora M., 1996, MNRAS, 283, 854

Mortlock D. J. et al., 2011, Nature, 7353, 616

Mullin L. M., Riley J. M., Hardcastle M. J., 2008, MNRAS, 390, 595

Muxlow T. W. B., Garrington S. T., 1991, Observations of large scale extragalactic jets, Vol. 19. p. 52

Nandra K. et al., 2013, arXiv: 1306.2307

Narayan R., Yi I., 1994, ApJ, 428, L13

Natarajan P., Pringle J., 1998, ApJ, 506, 97

Nath B. B., 2010, MNRAS, 407, 1998

Navarro J. F., Frenk C. S., White S. D. M., 1997, ApJ, 490, 493

Neistein E., Netzer H., 2014, MNRAS, 437, 3373

Okamoto T., Gao L., Theuns T., 2008, MNRAS, 390, 920

Oke J. B., Gunn J. E., 1983, ApJ, 266, 713

Oort J. H., 1932, BAIN, 6, 249

Owen F. N., Ledlow M. J., 1994, in G.V. Bicknell, M.A. Dopita, P.J. Quinn, eds, The Physics of Active Galaxies. Astronomical Society of the Pacific Conference Series, Vol. 54, p. 319

Padovani P., Bonzini M., Kellermann K. I., Miller N., Mainieri V., Tozzi P., 2015, MNRAS, 452, 1263

Parkinson H., Cole S., Helly J., 2008, MNRAS, 383, 557

Peacock J. A., 1985, MNRAS, 217, 601

Peng C. et al., 2006, ApJ, 649, 616

Penna R. F., Sadowski A., Kulkarni A. K., Narayan R., 2013, MNRAS, 428, 2255

Penzias A. A., Wilson R. W., 1965, ApJ, 142, 419

Perlmutter S. et al., 1999, ApJ, 517, 565

Pracy M. B. et al., 2016, MNRAS, 460, 2

Prescott M. et al., 2016, MNRAS, 457, 730

Prestage R. M., Peacock J. A., 1988, MNRAS, 230, 131

Pringle J., 1981, ARAA, 19, 137

Rafferty D. A., McNamara B. R., Nulsen P. E. J., Wise M. W., 2006, ApJ, 652, 216

Randall S. W. et al., 2011, ApJ, 726, 86

Raouf M., Shabala S. S., Croton D. J., Khosroshahi H. G., Bernyk M., 2017, MNRAS, 471, 658

Rawlings S., Saunders R., 1991, Nature, 349, 138

Rezzolla L., Barausse E., Dorband E. N., Pollney D., Reisswig C., Seiler J., Husa S., 2008, PRD, 78, 044002

Ricarte A., Natarajan P., 2018, MNRAS, 474, 1995

Richards G. et al., 2006, AJ, 131, 2766

Riess A. G. et al., 1998, AJ, 116, 1009

Rigby E. E., Best P. N., Brookes M. H., Peacock J. A., Dunlop J. S., Röttgering H. J. A., Wall J. V., Ker L., 2011, MNRAS, 416, 1900

Roberts M. S., Rots A. H., 1973, A&A, 26, 483

Rosas-Guevara Y., Bower R. G., Schaye J., McAlpine S., Dalla Vecchia C., Frenk C. S., Schaller M., Theuns T., 2016, MNRAS, 462, 190

Rubin V. C., Ford W. K. J., Thonnard N., 1980, ApJ, 238, 471

Sabater J. et al., 2019, A&A, 622, A17

Sadler E. M., Ekers R. D., Mahony E. K., Mauch T., Murphy T., 2014, MNRAS, 438, 796

Sadler E. M. et al., 2007, MNRAS, 381, 211

Saha K., Cortesi A., 2018, ApJL, 862, L12

Sajina A., Yan L., Lacy M., Huynh M., 2007, ApJ, 667, 17

Salpeter E. E., 1955, "ApJ", 121, 161

Salpeter E. E., 1964, ApJ, 140, 796

Sargent W. L. W., Young P. J., Boksenberg A., Shortridge K., Lynds C. R., Hartwick F. D. A., 1978, ApJ, 221, 731

Saxena A., Röttgering H. J. A., Rigby E. E., 2017, MNRAS, 469, 4083

Saxena A. et al., 2018, MNRAS, 480, 2733

Schaye J. et al., 2015, MNRAS, 446, 521

Scheuer P. A. G., 1974, MNRAS, 166, 513

Schilizzi R. T., Dewdney P. E. F., Lazio T. J. W., 2008, in PROCSPIE. Society of Photo-Optical Instrumentation Engineers (SPIE) Conference Series, Vol. 7012, p. 70121I

Schmidt M., 1963, Nature, 197, 1040

Schmidt M., 1968, ApJ, 151, 393

Schulze A., Wisotzki L., 2010, A&A, 516, A87

Seyfert C. K., 1943, ApJ, 97, 28

Shabala S. S., Godfrey L. E. H., 2013, ApJ, 769, 129

Shabala S. S., Ash S., Alexander P., Riley J. M., 2008, MNRAS, 388, 625

Shakura N., Sunyaev R., 1973, A&A, 24, 337

Shankar F., Salucci P., Granato G. L., De Zotti G., Danese L., 2004, MNRAS, 354, 1020

Shankar F., Weinberg D. H., Miralda-Escudé J., 2009, ApJ, 690, 20

Sharma P. et al., 2007, ApJ, 667, 714

Sheth R. K., Mo H. J., Tormen G., 2001, MNRAS, 323, 1

Shimwell T. W. et al., 2017, A&A, 598, A104

Shirakata H. et al., 2018, arXiv: 1802.02169

Simha V., Cole S., 2017, MNRAS, 472, 1392

Simpson C. et al., 2012, MNRAS, 421, 3060

Slipher V. M., 1917, Lowell Observatory Bulletin, 3, 59

Smolčić V. et al., 2009, ApJ, 696, 24

Smolčić V. et al., 2017, A&A, 602, A6

Smolčić V. et al., 2017, A&A, 602, A1

Soltan A., 1982, MNRAS, 200, 115

Somerville R. S., Davé R., 2015, ARAA, 53, 51

Somerville R. S., Hopkins P. F., Cox T. J., Robertson B. E., Hernquist L., 2008, MNRAS, 391, 481

Springel V., White S. D. M., Tormen G., Kauffmann G., 2001, MNRAS, 328, 726

Springel V., Di Matteo T., Hernquist L., 2005, ApJ, 620, 79

Springel V. et al., 2005, Nature, 435, 629

Springel V. et al., 2018, MNRAS, 475, 676

Sutherland R. S., Dopita M. A., 1993, ApJS, 88, 253

Tavecchio F., Maraschi L., Sambruna R. M., Urry C. M., 2000, ApJl, 544, L23

The Lynx Team, 2018, arXiv e-prints, arXiv:1809.09642

Turner R. J., Shabala S. S., 2015, ApJ, 806, 59

Turner R. J., Rogers J. G., Shabala S. S., Krause M. G. H., 2018a, MNRAS, 473, 4179

Turner R. J., Shabala S. S., Krause M. G. H., 2018b, MNRAS, 474, 3361

Ueda Y., Akiyama M., Ohta K., Miyaji T., 2003, ApJ, 598, 886

Ueda Y., Akiyama M., Hasinger G., Miyaji T., Watson M. G., 2014, ApJ, 786, 104

Venemans B. P. et al., 2013, ApJ, 779, 24

Vestergaard M., Osmer P. S., 2009, ApJ, 699, 800

Vestergaard M., Peterson B. M., 2006, ApJ, 641, 689

Vikhlinin A. et al., 2009, ApJ, 692, 1060

Volonteri M., 2010, A&ARv, 18, 279

Volonteri M. et al., 2007, ApJ, 667, 704

Wall J. V., Jackson C. A., Shaver P. A., Hook I. M., Kellermann K. I., 2005, A&A, 434, 133

Wang Y., Kaiser C. R., Laing R., Alexander P., Pavlovski G., Knigge C., 2009, MNRAS, 397, 1113

Wang Y., Knigge C., Croston J. H., Pavlovski G., 2011, MNRAS, 418, 1138

Watarai K. y., Fukue J., Takeuchi M., Mineshige S., 2000, PASJ, 52, 133

Weinberger R., Ehlert K., Pfrommer C., Pakmor R., Springel V., 2017, MNRAS, 470, 4530

Weinberger R. et al., 2018, MNRAS, 479, 4056

White S., Frenk C., 1991, ApJ, 379, 52

White S., Rees M., 1978, MNRAS, 183, 341

Willott C. et al., 2010, AJ, 139, 906

Willott C. J., Rawlings S., Blundell K. M., Lacy M., 1999, MNRAS, 309, 1017

Willott C. J., Rawlings S., Blundell K. M., Lacy M., Eales S. A., 2001, MNRAS, 322, 536

Willott C. J. et al., 2010, AJ, 140, 546

Wu X. B. et al., 2015, Nature, 518, 512

Yates P. M., Shabala S. S., Krause M. G. H., 2018, MNRAS, 480, 5286

York D. G. et al., 2000, AJ, 120, 1579

Young P. J., Westphal J. A., Kristian J., Wilson C. P., Landauer F. P., 1978, ApJ, 221, 721

Younger J. D., Hopkins P. F., Cox T. J., Hernquist L., 2008, ApJ, 686, 815

Yuan F., Narayan R., 2014, ARAA, 52, 529

Yuan F. et al., 2003, ApJ, 598, 301

Yuan Z., Wang J., Worrall D. M., Zhang B. B., Mao J., 2018, ApJS, 239, 33

Zwicky F., 1933, Helvetica Physica Acta, 6, 110